

# Physics principles of inertial confinement fusion and U.S. program overview

O. A. Hurricane 

Lawrence Livermore National Laboratory, P.O. Box 808, L-472, Livermore, California 94550, USA

P. K. Patel

Focused Energy Inc., 11525-B Stonehollow Drive, Suite 200, Austin Texas 78758, USA

R. Betti, D. H. Froula , and S. P. Regan 

Laboratory for Laser Energetics and Department of Mechanical Engineering and Physics and Astronomy, University of Rochester, 250 East River Road, Rochester, New York 14623-1299, USA

S. A. Slutz, M. R. Gomez , and M. A. Sweeney

Sandia National Laboratories, Albuquerque, New Mexico 87185, USA

 (published 27 June 2023)

Inertial confinement fusion (ICF) has existed as a field of study since the 1970s, but the field was born out of the Cold War. In the decades since the 1960s, pioneering research developing the principles and technologies of ICF has culminated in the creation of three major Department of Energy facilities that still exist today: the National Ignition Facility (NIF) at Lawrence Livermore National Laboratory, the OMEGA laser at the Laboratory for Laser Energetics, and the Z pulsed power facility at Sandia National Laboratories. While the technology of ICF facilities themselves is interesting, this review concentrates upon the physics principles of the targets fielded on U.S. ICF facilities and upon results from the last decade of research. While there have been periods of frustration on the road to ICF ignition, recent research has demonstrated great leaps in understanding what aspects of the implosions need more control. Tangible progress in ICF is evident as burning plasmas and ignited plasmas have recently been generated, repeatedly, on the NIF stemming from decades of science and engineering understanding generated from work at the three previously mentioned facilities and in the international community.

DOI: [10.1103/RevModPhys.95.025005](https://doi.org/10.1103/RevModPhys.95.025005)

## CONTENTS

I. Fusion and Related Thermodynamic Processes	2	1. Hohlräum physics	13
A. Fusion fuels	3	C. Z-pinch-driven hohlraums	14
1. Reaction rates as a function of temperature $T$	3	D. Ablator physics	14
B. Pressure and internal energy in a DT plasma	3	E. Present status of results	17
1. Ignition temperature	4	1. Low-foot design: NIC during 2010–2012	18
2. Alpha-particle stopping range and areal density required to stop alpha particles	4	2. High-foot design: 2013–2015	19
3. Lawson’s criterion	6	3. Adiabatic-shaped design: 2014–2015	21
C. Self-heating without a magnetic field	7	4. Low-gas-fill hohlraum designs: 2016–present	21
II. How to Achieve a High-Energy-Density ICF Plasma	7	5. Experimental demonstration of burning plasmas and ignition	23
A. Hot-spot model, adiabatic implosion, and analytic solution for alpha heating	8	6. Alternate indirect-drive concepts	24
B. Principal physics parameters controlling ICF implosion performance	9	IV. Laser-Driven Implosions	25
C. Implosion acceleration and hydrodynamic instability	10	A. A history of direct drive	25
III. X-Ray-Driven Implosions	12	B. Key differences between direct- and indirect-drive ICF	27
A. History	12	1. Direct-drive scaling advantages	28
B. Indirect drive with lasers	13	2. Hydrodynamic instabilities in direct-drive implosions	29
		3. Initial nonuniformity seeding of hydrodynamic instabilities in direct-drive implosions	34
		4. Hot-electron preheat in direct-drive implosions	38
		5. Cross-beam energy transfer in direct-drive implosions	40

\*hurricane1@llnl.gov

C. Present status of direct-drive implosion performance and proximity to ignition	42
1. Hydrodynamic scaling from OMEGA to megajoule laser energies	43
2. Current OMEGA implosion performance and proximity to hydrodynamic scaled ignition	44
3. Polar direct drive	45
V. Magnetic-Drive Implosions	47
A. History of pulsed power fusion	47
1. Development of pulsed power	47
2. Electron-beam-driven fusion	48
3. Ion-beam-driven fusion	48
4. Z-pinch-driven indirect drive	49
B. Direct magnetic drive using the MagLIF concept	50
1. Basic principles	50
2. Experimental demonstration of MagLIF concepts	53
3. The effect of mix	54
4. Implosions instabilities	55
5. High yield and gain from MagLIF on future pulsed power machines	57
VI. Summary and Outlook	58
Acknowledgments	59
References	59

## I. FUSION AND RELATED THERMODYNAMIC PROCESSES

For many decades the running joke in fusion research has been that “fusion is 20 years away and always will be.” Yet, we currently find ourselves in a position where we can refer to the milestones of burning plasmas, fusion ignition, and target energy gain greater than unity (i.e., “scientific breakeven”) in the past tense, a situation that is noteworthy. In this review, we describe the three main inertial confinement fusion (ICF) paths that the U.S. chose to pursue (i.e., laser indirect drive, laser direct drive, and magnetic drive), and we tell some of the story of the applied physics and engineering challenges that needed to be overcome by the U.S. ICF program in order to achieve these milestones. To help understand the story, several key physics principles of inertial fusion are presented, and we show that much of the key ICF target physics can be understood from the standpoint of classical mechanics and thermodynamics. Moreover, classical mechanics and thermodynamic statements are what underpin the scientific definitions of the milestones of a burning plasma, an igniting plasma, and gain in the context of ICF research.

In particular, a “burning plasma” is one where a fusion plasma’s self-heating exceeds external sources of heating, which is a necessary but not sufficient condition for “ignition.” That condition occurs when a fusion plasma’s self-heating exceeds the sum of all the cooling mechanisms present in the plasma, resulting in a thermodynamic instability that sustains and rapidly increases fusion power output, for some interval of time. Fusion power integrated over sufficiently long times can result in energy gain. Since ICF systems are energy-density concentrators that have elements of successively smaller components of decreasing size nested inside each other, an “energy gain” can be defined for each layer of the system. The central most element of physical interest in an ICF system is the fusion fuel; thus, one can define a “fuel gain” ( $G_{\text{fuel}}$ ), which is the ratio of fusion energy produced over the net

energy that is externally delivered into the fusion fuel. The fusion fuel in an ICF system is carried inside a shell of material, the capsule; thus, “capsule gain” ( $G_{\text{cap}}$ ) defines the ratio of fusion energy produced over the net energy absorbed by the capsule. In the case of x-ray-driven ICF designs, a metallic outer structure, a “hohlraum,” surrounds the capsule, completing the ICF target, and thus one can define a “target gain” ( $G_{\text{target}}$ , or sometimes simply referred to as  $G$ ) that is the ratio of fusion energy produced as compared to the energy delivered into the hohlraum. For ICF schemes not involving a hohlraum, capsule gain and target gain are the same thing. None of these gain definitions account for the energy expended by the facility (usually orders of magnitude greater than the energy that is actually delivered to an ICF target). Thus, fuel gain, capsule gain, or target gain greater than unity do not imply net energy production. “Engineering gain” ( $G_{\text{engineering}}$ ) is usually defined to include the energy used by the facility; thus, an engineering gain  $>1$  would imply net energy gain in the practical sense of interest to the general public. No man-made facility system in existence has yet achieved  $G_{\text{engineering}} > 1$ .

$G_{\text{target}} \sim 1.5$  was recently achieved (Lawrence Livermore National Laboratory, 2022), where 3.15 MJ of fusion energy was produced by a target at the National Ignition Facility (NIF) with 2.05 MJ of energy delivered by the facility to the target (details will be forthcoming in future publications), while the NIF facility itself consumed several hundred MJ of energy. As a practical reference point, note that a 1 kilowatt hour (kWh) = 3.6 MJ and that the average U.S. household energy use is 30 kWh  $\approx$  108 MJ per day. Target gain and ignition are terms that are often conflated, even though the concepts and physics behind the terms are different. This conflation of terms was reinforced by a 1997 National Academy of Sciences (NAS) review committee (Koonin *et al.*, 1997) because, at the time of the 1997 NAS review, there was no point of consensus in the ICF community of what ignition was (and magnetic fusion community definitions were oddly ignored). To paraphrase, the NAS committee adopted an operative definition of ignition as  $G_{\text{target}} = 1$  for the purpose of their report based upon a (now known to be optimistic) calculated curve of fusion yield versus NIF laser energy; see Fig. 1 of Koonin *et al.* (1997). Nevertheless, the U.S. Department of Energy adopted the 1997 NAS definition and continues to use it to this day.

Since many decades of work have gone into putting ignition on a firm scientific foundation, this review treats target gain and ignition as separate concepts, as shown in the following sections, particularly Secs. II.A, III, and IV. However, as discussed in the physics development of Sec. I.B,  $G_{\text{fuel}}$ , which is more directly tied to thermonuclear fusion processes, and ignition are more directly connected.

Like many aspects of nuclear energy, large strides in understanding and harnessing thermonuclear fusion processes were made during the Manhattan Project era and the subsequent Cold War. A key member of the Manhattan Project driving fusion research was Edward Teller, in pursuit of his idea of a “super” bomb based upon thermonuclear fusion using deuterium. Cold War research and development resulted in the practical application of thermonuclear fusion, and

research on controlled fusion for peaceful purposes was initiated during the same period.

Based upon the work of G. Gamow (Gamow, 1928; d'Escourt Atkinson and Houtermans, 1929), it had been known from quantum mechanics that fusion reactions occur when particles tunnel across the Coulomb barrier, thereby bringing the nuclei into proximity. Moreover, it was known that under conditions approaching thermodynamic equilibrium the particles will have enormously greater penetrating power. Therefore, it was already known decades before the Cold War that significant thermonuclear energy cannot be obtained from particle beam to target configurations, since the incident energy is rapidly dissipated by ionization and x-ray emission losses. What is required instead is a completely ionized light element plasma that is either large volume or high density in order to have a high number of fusion reactions. Large volume fusion is naturally adapted to magnetic confinement fusion approaches such as the tokamak, while high-density fusion is naturally adapted to implosion-based concepts that today form the field of ICF.

Laboratory-scale ICF originated in the early 1960s (Nuckolls, 2006; Tarter, 2018) with the realization that “microfusion” explosions could be generated if sufficient compression could be achieved. However, like fusion itself the principles of the implosion technology that are key to ICF originated during the Manhattan Project. According to the recollections of key people involved in the Manhattan Project, the conceptual idea behind implosions has been credited to Richard C. Tolman and/or Seth Neddermeyer (Hoddeson *et al.*, 1993) in the 1942–1943 period, albeit the interest then was in fission-based implosion systems.

Basically, implosion systems entail surrounding a capsule material on all sides with a source of high pressure that exceeds the yield strength of the material and any internal pressure. The pressure difference will cause the capsule to “implode” inwardly upon itself, thereby increasing the density of the capsule shell and any internal fill (for instance, fusion fuel) as it is squeezed into a smaller volume. It is easier to describe in words what such an implosion is than to do it successfully since the difficulty of using the tactic increases exponentially with the desired degree of compression. To better appreciate the difficulty in making fusion implosions work, we estimate the extreme conditions needed, which are the topic of Secs. I.A–I.C.

The organization of this review is as follows. Sections I.A and I.B describe basic fusion fuel considerations illustrating why deuterium-tritium fusion is by far the most efficient reaction and also the importance of compression in limiting the energy cost of igniting a fusion fuel. Section I.C makes the connection between  $G_{\text{fuel}}$  and the “Lawson triple product” and introduces the key role of alpha-particle self-heating. Section II.A describes the highly nonlinear thermodynamics of fusion fuel inside an implosion, explaining why high implosion velocities are so critical for ICF. Section II.B provides a simple classical mechanics analog of an implosion that is quite effective for understanding the principle parameters that must be controlled in an ICF implosion, including the effect of asymmetry on an implosion. Section II.C describes the most essential hydrodynamic instability considerations for ICF that often conflict with the needs of high velocity and high compression in an ICF

implosion. Section III then focuses upon the indirect-drive ICF scheme, starting with a history, but focusing mostly upon the key works that have been pursued at the NIF over the past decade (Sec. III.E). Key topics for indirect drive are those of hohlraum physics and ablator physics, each discussed with some important scaling relationships in Secs. III.B and III.D, respectively. Since indirect drive can be generated using Z pinches in addition to lasers, Sec. III.C addresses this alternate way of making x rays. As part of the ablator physics discussion in Sec. III.D, the critically important yet obscure physics of “coast time” is emphasized. Laser direct drive is the focus of Sec. IV, starting with a history in Sec. IV.A, with key advantages and disadvantages compared to indirect drive described in Sec. IV.B. Section IV.C summarizes the present state of direct-drive theory and experiment. Section V.A describes a variety of Z-pinch concepts that have been examined, and Sec. V.B then focuses on the most recent studies using magnetized liner inertial fusion and associated physics and electrical engineering considerations. Section VI concludes this review with an outlook.

## A. Fusion fuels

Our understanding of what the most practical fusion reactions are has not really changed since early work on measuring the fusion reaction rates done by the F-3 group at Los Alamos National Laboratory in 1944 (Hoddeson *et al.*, 1993). It has long been recognized that the most favored reaction is deuterium (D) tritium (T) fusion,  $D + T \rightarrow n(14.1 \text{ MeV}) + {}^4\text{He}(3.5 \text{ MeV})$  (Post, 1956), because it is orders of magnitude more reactive for a given interparticle collisional energy than any other fusion reaction for thermal temperature  $T < 100 \text{ keV}$ . Put simply, the fewer protons in the reactants the less electric repulsion needs to be overcome in order to bring the nuclei into proximity for fusion. However, other reactions such as  $D + D \rightarrow n + {}^3\text{He}$ ,  $D + D \rightarrow p + T$ ,  $D + {}^3\text{He} \rightarrow {}^4\text{He} + p$ , and  $p + {}^{11}\text{B} \rightarrow 3 \times {}^4\text{He}$  are often used for experimentation in order to avoid directly handling radioactive tritium.

### 1. Reaction rates as a function of temperature $T$

Accurate analytic expressions for fusion reaction rates over a broad range of temperatures (see Fig. 1) can be cumbersome, so it is often useful and usually sufficient to use power-law fits over a limited range of temperature. Power-law expressions of the form  $\langle\sigma v\rangle_{\text{DT}} \sim T^{(2-5)}$  fit the DT reaction rate well, with the lower power of  $T$  decreasing as the temperature range of interest increases. A useful approximation to the DT reaction rate in the regime of present practical interest to ICF implosions is

$$\langle\sigma v\rangle_{\text{DT}} \approx 4.2 \times 10^{-20} T^{3.6}, \quad 3.5 < T < 6.5, \quad (1)$$

with  $T$  in keV and  $\langle\sigma v\rangle$  in  $\text{cm}^3/\text{s}$ .

## B. Pressure and internal energy in a DT plasma

Here we estimate the thermodynamic conditions that are expected for igniting an inertially confined fusion plasma using basic thermal considerations. Assuming nearly equal

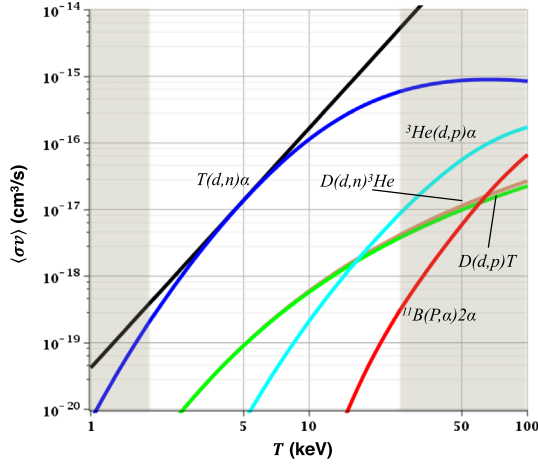


FIG. 1. The reaction rates of select reactions are plotted based upon formulas given by Bosch and Hale (1992) and Nevins and Swain (2000) in the case of  $p$ -boron. The temperature region  $2 < T < 20$  keV of practical interest to ICF is highlighted. The top curve is the DT reaction rate, while the tangent line is the power-law approximation [Eq. (1)] to the DT reaction rate.

ion and electron temperatures ( $T_{\text{ion}}$  and  $T_e$ , respectively), the plasma pressure ( $p$ ) is

$$p = \frac{\bar{Z} + 1}{\bar{A}} \frac{\rho}{m_p} k_B T, \quad (2)$$

where  $\bar{Z}$  is the effective average ionization,  $\bar{A}$  is the average atomic mass,  $\rho$  is the mass density,  $k_B$  is the Boltzmann constant, and  $T$  is the thermal temperature. Therefore, for a DT plasma of equal parts D and T,  $\bar{Z} = 1$  and  $\bar{A} = 2.5$ . Thus,

$$p = 0.77\rho T \quad (3)$$

in gigabars,  $\text{g}/\text{cm}^3$ , and keV. The heat capacity of a DT plasma is then  $c_{\text{DT}} = (3p)/(2\rho T) = 115 \text{ MJ}/(\text{g keV})$ , which is a key quantity for understanding fusion energy requirements for a given mass and temperature of heated DT. By comparison, with  $\bar{Z} = 3$  and  $\bar{A} = 6$  the heat capacity of fully ionized  $p$ -B $_{11}$  fuel is  $c_{p\text{-B}_{11}} = 555 \text{ MJ}/(\text{g keV})$ , a factor of  $\sim 5$  times that of DT. Note that in ICF, and fusion in general, the fusion plasma is not in thermal equilibrium with the radiation field, since the photon mean free path is long compared to the size of the plasma, so the blackbody energy ( $4\sigma T^4/c$ , where  $\sigma$  is the Stefan-Boltzmann constant and  $c$  is the speed of light) is not included in the heat capacity.

### 1. Ignition temperature

Any plasma heated to keV temperatures is a strong x-ray radiator and that radiation is a key cooling mechanism that must be overcome. For a mixture of atoms in local thermodynamic equilibrium, the volumetric bremsstrahlung x-ray (Heitler, 1954) emission power per unit mass (in grams) is (Zel'dovich and Raizer, 2002; Spitzer, 2006)

$$Q_{\text{brems}} = \frac{64}{3\sqrt{2\pi}} \frac{e^6 \rho}{m_e \hbar c^2} \sqrt{\frac{k_B T_e}{m_e c^2}} \frac{\bar{Z} \bar{Z}^2}{(\bar{A} m_p)^2}, \quad (4)$$

where  $e$  is the electron charge (in statcoulombs),  $m_e$  is the electron mass (in grams),  $\hbar$  is the conventional Planck's constant over  $2\pi$  (in erg s), and  $c$  is the speed of light (in cm/s). For a pure mixture of 50% D and 50% T, the bremsstrahlung emission per unit mass [Eq. (4)] reduces to

$$Q_{B,\text{DT}} = 3.1 \times 10^7 \rho \sqrt{T_e} \quad (5)$$

in GJ/(g s), with  $T_e$  in keV.

The ignition temperature ( $T_{\text{ign}}$ ) is defined as the temperature where the x-ray power lost due to bremsstrahlung emission just balances the fusion power (Post, 1956). The fusion power per unit mass in alpha particles for DT fusion is

$$Q_\alpha = 8.2 \times 10^{24} \rho \langle \sigma v \rangle \quad (6)$$

in GJ/(g s). The total fusion yield production rate for a mass of fuel  $m$  would then be  $dY/dt = 5mQ_\alpha$ , where the factor of 5 is due to the fact that only 1/5 of the DT fusion yield comes in the form of  $\alpha$  particles. Equating Eqs. (5) and (6) with  $T_e = T_{\text{ion}} = T_{\text{ign}}$ , using Eq. (1), and solving gives  $T_{\text{ign}} = 4.3$  keV. For fusion fuels other than DT,  $T_{\text{ign}}$  can be substantially higher than 4.3 keV and  $T_{\text{ign}}$  would also be higher for DT in the presence of impurities that rapidly increase x-ray emission, as reflected in the  $\bar{Z}$  and  $\bar{Z}^2$  terms of Eq. (4).

### 2. Alpha-particle stopping range and areal density required to stop alpha particles

To self-heat a mass of fusing plasma, some of the fusion by-products must be stopped by collisions in that plasma, thereby adding energy to the burn, which in turn increases the temperature and reaction rate. This argument has a fission chain-reaction analogy from the Manhattan Project days, as it was used to make the first estimates of the critical mass of fission material needed to stop fission neutrons. Generally, stopping 14 MeV fusion neutrons is not practical in ICF systems because of the high areal density required, so it is only the stopping of the  $\alpha$  particles that is practical.

To estimate the size and mass of fuel that will self-heat, the  $\alpha$ -particle stopping range ( $\lambda_{\text{DT}}$ ) is needed. A modern fit (Zylstra and Hurricane, 2019) to the Maynard-Deutsch (Maynard and Deutsch, 1985) calculation of ion stopping in a degenerate electron fluid is

$$\lambda_{\text{DT}} = \frac{1}{\rho} \frac{0.0171 T^{1.071}}{1 + 0.0113 T^{1.071}} \left[ 1 + 1.579 \left( \frac{\rho}{100} \right)^{0.199} \right], \quad (7)$$

where  $\lambda_{\text{DT}}$  is in centimeters,  $\rho$  is in  $\text{g}/\text{cm}^3$ , and  $T$  is in keV. Therefore, at the ignition temperature  $T = 4.3$  keV the areal density that must be assembled is

TABLE I. For a given energy delivery to the DT, the minimum density and minimum pressure required to bring a mass of DT of two ( $\mathcal{F} = 2$ )  $\alpha$ -particle stopping radii to 4.3 keV with the associated DT mass and total fusion yield (including charge particles and neutrons) estimated from  $Y \approx \phi(m_{\text{DT}}/2\bar{A}m_p) \times (17.6 \text{ MeV/reaction})$ , with a characteristic burn efficiency  $\phi \sim 0.2$  assumed.

$E_{\text{hot,DT}}$ (MJ)	$\rho_{\text{ign}}$ (g/cm <sup>3</sup> )	$p_{\text{ign}}$ (Gbar)	$m_{\text{DT}}$ ( $\mu\text{g}$ )	$Y$ (MJ)
1.0	7.4	25	2000	136
0.1	29	96	200	13.6
0.01	117	387	20	1.36
0.001	490	1622	2	0.136

$$(\rho\lambda_{\text{DT}})_{\text{ign}} = 0.077 \left[ 1 + 1.58 \left( \frac{\rho}{100} \right)^{0.2} \right] \quad (8)$$

in g/cm<sup>2</sup>. While a number of  $\alpha$ -particle stopping models exist (Brown, Preston, and Singleton, 2005; Singleton, 2008; Li and Petrasso, 2015), for the usual ICF conditions the impact of the different models is generally small (Zylstra and Hurricane, 2019). In addition to stopping  $\alpha$  particles, assembling a high areal density DT plasma has a beneficial reduction in electron condition heat losses from the burning region, as is seen following Eq. (14).

Assuming spherical geometry, the mass of DT needed to stop  $\alpha$  particles inside the burning volume is  $m_{\text{DT}} = (4\pi/3)[\mathcal{F}(\rho\lambda_{\text{DT}})]^3/\rho^2$ , where  $\mathcal{F} > 1$  is a ‘‘safety’’ factor that would guarantee that the  $\alpha$  particles are stopped inside the volume, rather than just at the edge. The mass can be related to the energy that needs to be delivered to the DT to ignite ( $E_{\text{hot,DT}}$ ) and the ignition temperature using the previously found heat capacity, and  $m_{\text{DT}} = E/c_{\text{DT}}T_{\text{ign}}$  gives an implicit expression for the ignition density using Eq. (8),

$$\rho_{\text{ign}} = \frac{0.97\mathcal{F}^{3/2}}{\sqrt{E_{\text{hot,DT}}}} \left[ 1 + 1.58 \left( \frac{\rho_{\text{ign}}}{100} \right)^{0.2} \right]^{3/2} \quad (9)$$

with the density in g/cm<sup>3</sup> and energy in MJ. Note the  $1/\sqrt{E_{\text{hot,DT}}}$  dependence in Eq. (9), which implies that the associated ignition pressure ( $p_{\text{ign}} = 0.77\rho_{\text{ign}}T_{\text{ign}}$ ) also has the same energy dependence. For a given value of  $E_{\text{hot,DT}}$ , Eq. (9) can be solved numerically and the result can be used to calculate the pressure, determine the mass, and give a fusion yield estimate, as shown in Table I. For  $E_{\text{hot,DT}}$  less than several hundred MJ, Eq. (9) results in DT fuel densities that are higher (usually by orders of magnitude for laboratory levels of energy) than the solid cryogenic density of DT (0.25 g/cm<sup>3</sup>), implying that some sort of density compression scheme is needed.

While based upon simple physics arguments, the numbers shown in Table I are representative of what is obtained from sophisticated modern multiphysics simulations of detailed ICF implosion designs. Moreover, the third row of Table I is representative of the near term goal and performance expectation for indirect-drive ignition on the NIF (Nicola *et al.*, 2019), and the energy, density, and pressure are characteristic of the goals for the central ‘‘hot spot’’ of the assembled

TABLE II. Fusion fuel gain for a given mass of fuel brought to the ignition temperature when  $T_e \approx T_{\text{ion}}$ . The result for  $p$ -boron fusion includes the recent reevaluation of the reaction cross section (Sikora and Weller, 2016) and ignition temperature (Putvinski, Ryutov, and Yushmanov, 2019) that are tens of percent more optimistic than past values.

Reaction	$k_B T_{\text{ign}}$ (keV)	$Q$ (MeV/reaction)	$G_{\text{fuel}}/\phi$
$\text{D} + \text{T} \rightarrow n + {}^4\text{He}$	4.3	17.6	1364
$\text{D} + \text{D} \rightarrow n + {}^3\text{He}$	35	3.25	31
$\text{D} + \text{D} \rightarrow p + \text{T}$	25	4.03	54
$\text{D} + {}^3\text{He} \rightarrow {}^4\text{He} + p$	28	18.3	175
$p + {}^{11}\text{B} \rightarrow 3 \times {}^4\text{He}$	300	8.7	5

implosions. It should be clear from Table I that heating a large mass of DT fusion fuel is energetically costly. Therefore, for facility-based ICF where only a small fraction of the driver energy can be coupled to the fuel, much smaller amounts of DT fuel are targeted for heating but then require extraordinarily high pressures and densities to be achieved (which implies that electron-ion collisions will be high, justifying the  $T_e \approx T_{\text{ion}}$  assumption made earlier).

The ‘‘fuel energy gain’’  $G_{\text{fuel}}$  (ratio of total fusion yield to the total energy in the DT) (Atzeni and Meyer-ter-Vehn, 2004) factor of  $\sim 136$  times implied by Table I appears to be attractive, but it can also be misleading if one does not appreciate that the energy delivered to the fusion fuel is much less (by 1 or 2 orders of magnitude) than the total energy used to get the fusion fuel to those conditions because of the natural inefficiency of ICF implosion systems. To make up for the total energy expended to start ignition, propagation of the burn into another mass of relatively cold fusion fuel is required. For example,  $G_{\text{fuel}} > 1$  was first achieved in 2014 (Hurricane *et al.*, 2014a), but the total energy gain (Rosen, 1999; Atzeni and Meyer-ter-Vehn, 2004)  $G$  as measured against the laser energy input was only  $\sim 1\%$ .

We now estimate the fuel energy gain for a variety of fusion fuels (see Table II) for burning a mass of fuel heated to the ignition temperature for that fuel. The fusion yield can be estimated as from a product of burn efficiency  $0 < \phi < 1$ , the number of possible fusions  $m/2\bar{A}m_p$ , and the energy released per fusion, traditionally denoted as  $Q$ , while the fuel energy  $E_{\text{fuel}}$  is the product of heat capacity, mass, and temperature (again assuming ion-electron equilibrium), so

$$G_{\text{fuel}} \equiv \frac{Y}{E_{\text{fuel}}} \rightarrow \frac{2\phi Q}{3(\bar{Z} + 1)k_B T_{\text{ign}}} \quad (10)$$

when  $T = T_{\text{ign}}$ . Since the somewhat misnamed ignition temperature is the minimum temperature needed for ignition, it is clear from Eq. (10) that low  $T_{\text{ign}}$  and low  $\bar{Z}$  in combination with high  $Q$  is highly desirable for a fusion fuel. As can be seen in Table II, DT fusion is orders of magnitude more attractive as a fusion fuel for any hope of having fusion output greatly exceed the energy consumed to get to fusion conditions because of the relatively low heat capacity and ignition temperature. Recognize that a subtlety in Eq. (10) in that  $E_{\text{fuel}}$  is the sum of energy from external drivers and any energy that comes from

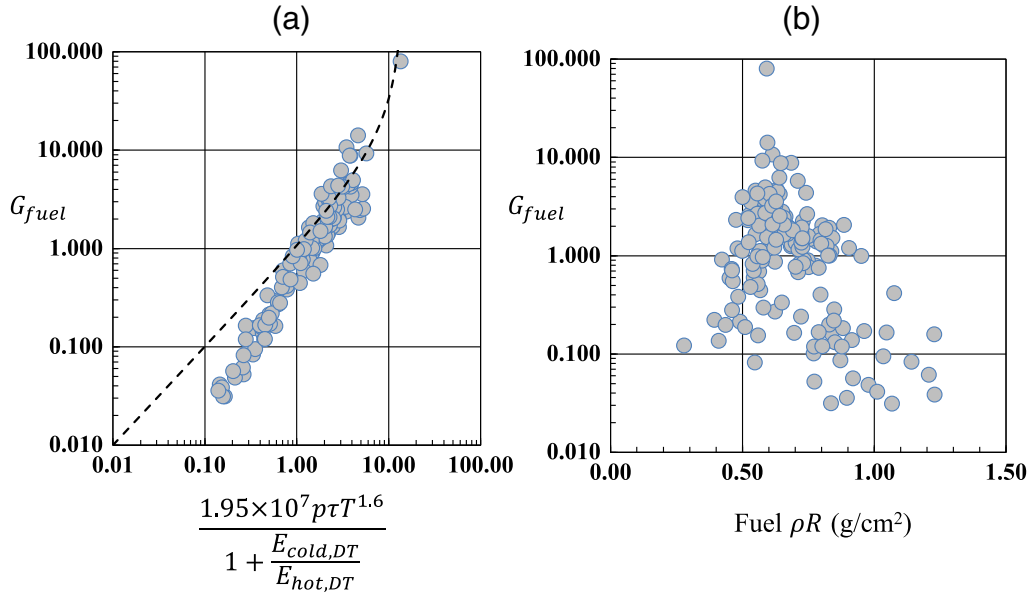


FIG. 2. (a) NIF DT implosion data (as of September 2021) plotted against Eq. (11) (dashed curve). Here  $G_{fuel}$  is calculated from the ratio of the fusion yield over the peak fuel kinetic energy (an approximation that neglects energy loss in the conversion of kinetic energy into internal energy at stagnation due to x rays or asymmetry). The low performing experiments that deviate from the theory expression are largely those from the National Ignition Campaign (see Sec. III.E.1), which experienced significant hydrodynamic instability and mixing: the enhanced bremsstrahlung emission that breaks the assumptions of Eq. (11). (b)  $G_{fuel}$  is plotted vs the measured burn-averaged DT fuel areal density (inferred via the neutron down-scatter ratio of 10–12 MeV neutrons over 13–15 MeV neutrons). As seen here, fusion performance rapidly falls off at low areal density (as expected since 1D inertial confinement is reduced), but surprisingly also at higher areal density (contrary to conventional wisdom; see Sec. III.E.1–III.E.3), and an apparent optimum exists for fuel  $\rho R \sim 0.6$ – $0.7$  g/cm<sup>2</sup>.

self-heating, so the fuel gain as measured against an external source of energy can be higher than Eq. (10) implies.

### 3. Lawson’s criterion

An alternate expression for  $G_{fuel}$  that accounts for the energy deposition of self-heating back into the fusion fuel shows a direct and important connection to ignited fusion requirements and fuel gain. Since from Eq. (6) we know that the total fusion yield produced by a mass of DT over a characteristic confinement-time  $\tau$  is  $Y \sim 5mQ_\alpha\tau$ , and since the internal energy in that DT is  $E_{hot,DT} = c_{DT}mT$ , the fuel gain can be written as

$$G_{fuel} = \frac{Y}{E_{pdV}} \approx \frac{Y/E_{hot,DT}}{1 + E_{cold,DT}/E_{hot,DT} - (q/10)(Y/E_{hot,DT})}, \quad (11)$$

with

$$\frac{Y}{E_{hot,DT}} \approx 4.6 \times 10^{26} p \frac{\langle \sigma v \rangle}{T^2} \tau, \quad (12)$$

where  $p$  is in gigabars,  $T$  is in keV, and  $\tau$  is in seconds. Note that  $E_{cold,DT}$  is the energy in the cold fuel, which is a fraction that depends upon fuel entropy, of the maximum kinetic energy acquired by the fuel during the implosion. In Eq. (11), the energy delivered (by external means) is determined from the hot and cold fuel (if present) energy at stagnation:  $E_{hot,DT}$

and  $E_{cold,DT}$ , respectively, minus a correction for additional energy retained by self-heating of the fuel and not lost as bremsstrahlung as measured by a “quality” factor  $q$ . Thus,  $E_{pdV} \approx E_{hot,DT} + E_{cold,DT} - qY/10$ , with  $0 \leq q \leq 1$ , where  $1/10$  is from  $1/5$  of the fusion energy being in  $\alpha$  particles over  $1/2$  the burn duration.

Albeit generally arrived at in a different fashion than we have discussed, the product  $p(\langle \sigma v \rangle/T^2)\tau$  is a Lawson-like (Lawson, 1957) product for ignition of an ICF implosion, which has been studied and restated in many alternate forms for decades (Zhou and Betti, 2009; Betti *et al.*, 2010; Tipton, 2015). Equation (11) makes it clear that fuel energy gain and the generalized Lawson product are directly related. Note that Lawson’s original analysis of a pulsed power producing a thermonuclear reactor determined that a function of  $\rho\tau$  (the “Lawson parameter”) and  $T$  was fundamental to ignition, later combined into a Lawson triple product,  $\rho\tau T$ , but some modification of these expressions is needed for ICF because of the dynamic nature of implosions, as discussed later.

Using Eq. (1) in Eq. (12) gives the simple expression

$$\frac{Y}{E_{hot,DT}} \sim 1.95 \times 10^7 p(\text{Gbar})T^{1.6}(\text{keV})\tau(\text{s}), \quad (13)$$

which makes it clear, with Eq. (11), that for high  $G_{fuel}$  the product of pressure, temperature, and confinement time should be maximized by whatever means. A plot of Eq. (11) is given in Fig. 2 for DT implosion experiments on the NIF.

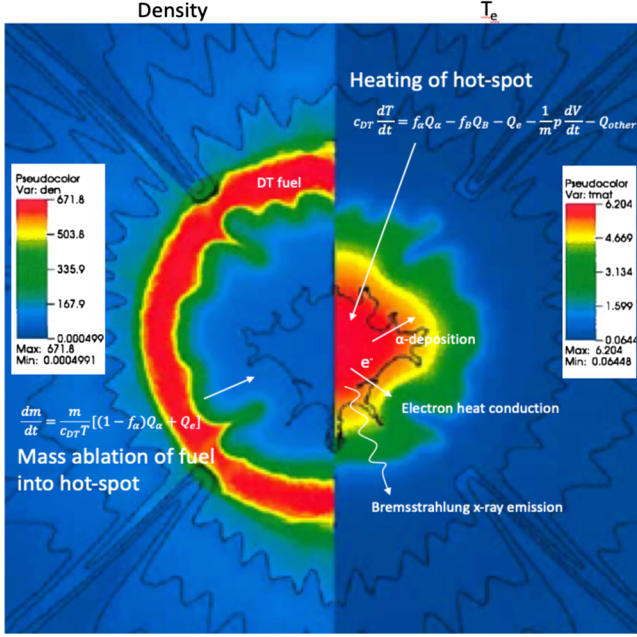


FIG. 3. Simulated image of a characteristic hot-spot ignition design implosion at peak compression illustrating what a configuration may look like. Black outlines illustrate material boundaries, and the breaking of perfect symmetry results from the input of realistic surface finishes and asymmetry breaking engineering features into the simulation; while initially small, these perturbations inevitably grow, as the tendency of an implosion is to act as an amplifier. Left half: density ( $\text{g}/\text{cm}^3$ ). Right half: electron temperature (keV). A few key processes are illustrated.

### C. Self-heating without a magnetic field

The temperature development of the DT fusion plasma in an ICF implosion is determined by a thermodynamic balance of energy sources and sinks; see Fig. 3. The source of fusion energy gain  $Q_\alpha$  [Eq. (6)] and one source of energy loss  $Q_B$  [Eq. (5)] have already been discussed. The complete power balance in an ICF plasma includes electron conduction losses and mechanical “ $p dV$ ” work,

$$c_{\text{DT}} \frac{dT}{dt} = f_\alpha Q_\alpha - f_B Q_{B,\text{DT}} - Q_e - \frac{1}{m} p \frac{dV}{dt} - Q_{\text{other}} \quad (14)$$

where  $Q_e = 5.4 \times 10^3 T^{3.2} / \rho^{0.8} R^2$  or  $Q_e = 5.9 \times 10^3 T^{7/2} / \rho R^2$  is the electron conduction loss in GJ/(g s) [assuming a SESAME conductivity form (Lyon and Johnson, 1995) or a Spitzer form (Spitzer and Härm, 1953), respectively] and  $R$  is the radius (assuming spherical geometry). The term  $f_B$  is the fraction of x rays lost to the hot plasma, which is  $< 1$  if the optical depth of the hot region is high enough to reabsorb x rays or  $> 1$  if the presence of high- $Z$  material enhances x-ray loss beyond that which pure DT would radiate. The quantity  $f_\alpha < 1$  is the fraction of alpha particles stopped in the hot DT plasma and is related to  $\lambda_{\text{DT}}$ ; for instance, with Eq. (7) the appropriate expression is (Zylstra and Hurricane, 2019)

$$f_\alpha = 1.0228 - 0.4254 \left( \frac{\rho \lambda}{\rho R} \right) + 0.07101 \left( \frac{\rho \lambda}{\rho R} \right)^2 - 0.004 \left( \frac{\rho \lambda}{\rho R} \right)^3. \quad (15)$$

In the presence of magnetic fields (see Sec. V), the  $f_\alpha$  and electron conduction terms are modified. The  $p dV$  work term [Eq. (14)] is a source of mechanical power injection into the plasma on implosion ( $dV/dt < 0$ ) or a loss term upon explosion ( $dV/dt > 0$ ) as the volume  $V$  surrounding the hot plasma changes. The loss term  $Q_{\text{other}}$  in Eq. (14) is associated with energy sinks that may exist in a real implosion that are not captured in the conventional thermodynamic power balance.

A tipping point in DT plasma self-heating can be obtained if the  $f_\alpha Q_\alpha$  term in Eq. (14) dominates over the other terms on the right-hand side of the power balance for a sufficient time. Once this tipping-point ignition is reached, thermal instability follows and  $T$  increases in a finite-time singular (explosive) fashion over the “bootstrapping” time-scale, which is dimensionally determined per Eq. (14) by the ratio of the heat capacity and the alpha-heating rate at stagnation (subscript  $s$ ), namely,  $dt/d \ln T \sim c_{\text{DT}} T / f_\alpha Q_\alpha \sim 2.9 \times 10^{-6} c_{\text{DT}} / f_\alpha \rho_s T_s^{2.6} \sim 30 - 60$  of picoseconds. Since ICF implosions are dynamic, thermodynamic instability is eventually terminated by expansion as the system blows itself apart.

## II. HOW TO ACHIEVE A HIGH-ENERGY-DENSITY ICF PLASMA

Equation (14) shows that ICF implosions are hydrodynamic systems that do mechanical work to compress the fusion fuel to reach a high-energy-density state in order to trigger thermonuclear reactions. In ICF a shell surrounding the fusion fuel is accelerated to high velocity inward upon itself (the aforementioned “implosion”) until there is nowhere to go (“stagnation”). At stagnation the built-up kinetic energy is turned into internal energy that increases the temperature and pressure in the DT. At the boundary of self-heating ( $f_\alpha Q_\alpha - f_B Q_B - Q_e \approx 0$ ), where x-ray and conduction losses balance alpha heating, the minimum characteristic velocity needed can be estimated from the balance between internal energy and kinetic energy, as seen in Eq. (14), assuming spherical symmetry and  $Q_{\text{other}} = 0$ ,

$$c_{\text{DT}} m T \leq \frac{1}{2} m_{\text{shell}} v_{\text{imp}}^2. \quad (16)$$

Taking  $T \approx T_{\text{ign}}$  in Eq. (16) gives a velocity estimate [noting that  $c_{\text{DT}} = 115 \times 10^3 \text{ (km/s)}^2/\text{keV}$ ]

$$v_{\text{imp}} (\text{km/s}) \geq 960 \sqrt{\frac{m}{m_{\text{shell}}}}. \quad (17)$$

For hot-spot ignition, where only a small fraction of the DT fuel is heated,  $m/m_{\text{shell}} \sim 1/10$ , so Eq. (17) gives  $v_{\text{imp}} \geq 320 \text{ km/s}$ . Designing the conditions needed to achieve these and higher velocities while controlling the tendency toward instability (a consequence of the significant

accelerations and decelerations and material density gradients involved in the implosion) and asymmetry requires great finesse and engineering control.

### A. Hot-spot model, adiabatic implosion, and analytic solution for alpha heating

Various implosion design strategies have been explored, but hot-spot ignition, where most of the DT fuel is compressed but not significantly heated (Nuckolls *et al.*, 1972; Lindl, 1995; Lindl *et al.*, 2004), is still the leading strategy using either indirect x-ray drive or direct laser drive. In hot-spot ignition, as the implosion heats, heat-conduction electrons and any alpha particles leaving the hot spot are stopped in the innermost DT fuel and the heating ablates the fuel (Gus'kov, Krokhin, and Rozanov, 1976) from the inside out, into the hot spot, increasing the hot-spot mass according to the following rate equation:

$$\frac{dm}{dt} = \frac{m}{c_{DT}T} [Q_\alpha(1 - f_\alpha) + Q_e]. \quad (18)$$

Equation (18) underestimates the mass ablation of the fuel into the hot spot due to a boundary layer effect in the electron conduction solution (Daughton *et al.*, 2023), but corrections to the electron conduction solution become less significant in the limit of  $Q_\alpha \gg Q_e$ . Since the energy in the hot spot is  $E_{hs} = c_{DT}mT = (3/2)pV$ , one can differentiate the expression for the hot-spot internal energy  $dE_{hs}/dt$  and then combine the result with Eqs. (18) and (14) to obtain an expression for hot-spot pressure, recovering a form popularized by Betti *et al.* (2002). After some algebra, one finds that

$$\frac{dp}{dt} + \frac{5p}{3V} \frac{dV}{dt} = \frac{2}{3} \rho (Q_\alpha - f_B Q_B - Q_{\text{other}}). \quad (19)$$

Since  $\alpha$  particles that leave the hot spot are stopped in the DT fuel, ablating the fuel and thus returning  $\alpha$ -particle energy to the hot spot,  $f_\alpha$  is not explicitly present in Eq. (19). Thus, Eq. (19) is insensitive to  $\alpha$ -stopping model uncertainties. Dropping  $Q_B$  and  $Q_{\text{other}}$ , Betti *et al.* (2002) noted that, assuming  $\langle \sigma v \rangle \sim T^2$  near stagnation ( $dV/dt \sim 0$ ), Eq. (19) takes the form of a Riccati equation, which has a finite-time singular solution. In particular, one finds that the pressure becomes singular when a normalized form of the Lawson criteria  $\chi_{\text{no-}\alpha} \sim p\tau/S(T)$  (“generalized Lawson criteria”) exceeds unity, with  $S(T)$  the hot-spot volume average of  $T^2/\langle \sigma v \rangle$  at stagnation; a number of other theoretical works have built upon this idea (Betti *et al.*, 2010, 2015; Chang *et al.*, 2010; Spears *et al.*, 2012; Cheng *et al.*, 2013; Christopherson, Betti, Bose *et al.*, 2018; Springer *et al.*, 2019).

Noting that  $\rho = 3p/(2c_{DT}T)$  and that  $\dot{p} + (5/3)(p/V)\dot{V} = p[d\ln(pV^{5/3})/dt]$  (the overdot denotes a time derivative) allows Eq. (19) to be integrated simply, we obtain (Hurricane *et al.*, 2019a)

$$\frac{pV^{5/3}}{p_{pv}V_{pv}^{5/3}} = \exp \left[ \int_0^t \frac{Q_\alpha - f_B Q_B - Q_{\text{other}}}{c_{DT}T} dt \right], \quad (20)$$

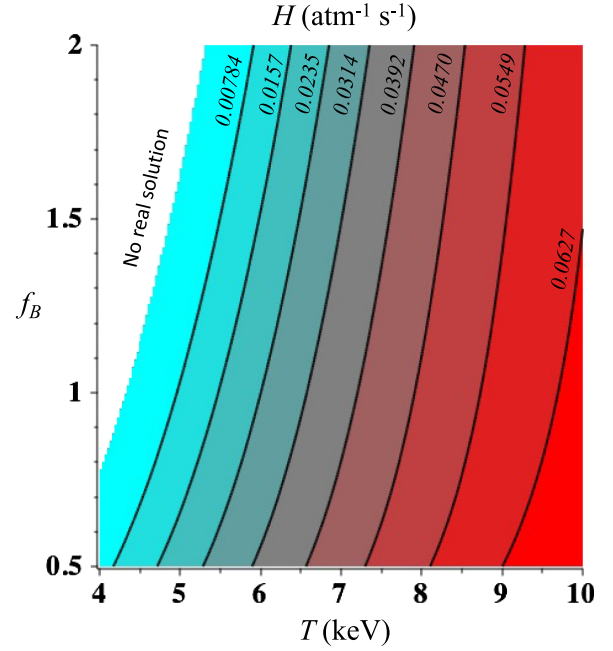


FIG. 4. Contour plot of  $H$  showing the dependence upon  $f_B$  and  $T$ . At fixed  $T$ , higher  $f_B$  lowers  $H$ , essentially reflecting the fact that enhanced bremsstrahlung cooling makes the ignition temperature higher than it would be for pure DT and this makes ignition more difficult to achieve. If the implosion can be engineered to have a high enough optical depth to reabsorb bremsstrahlung x rays ( $f_B < 1$ ), the ignition temperature is reduced.

where  $p_{pv}V_{pv}^{5/3}$  is an integration constant and the subscript refers to the conditions at peak velocity (pv). The assumptions leading to Eqs. (19) and (20) are good only if the 3D asymmetries are limited to low modes, Legendre modes  $\ell < 6$ , since for higher modes the hot-spot “bubbles” could be cold and the isobaric assumption becomes worse as flows in the hot spot become more significant.

A diagram version of Eq. (20) is  $pV^\gamma/p_{pv}V_{pv}^\gamma \sim \exp(E_\alpha/E_{hs}) \exp(-E_B/E_{hs})$ , where  $E_\alpha$  is the  $\alpha$ -heating energy and  $E_B$  is the energy lost to bremsstrahlung x rays. Since  $E_\alpha/E_{hs}$  has been identified as a key quantity for the ignition of 1D implosions (Christopherson, Betti, Howard *et al.*, 2018; Lindl *et al.*, 2018), it is expected that a rapid and nearly discrete jump in  $pV^\gamma$  is strongly related to fusion yield amplification and ignition as well. Equation (20) does not solve the pressure equation, because the integral depends upon  $p$  through the density dependence of the gain and loss terms, but Eq. (20) puts the equation into a form where, for high  $T$  ( $>4.3$  keV), an accurate but approximate solution can easily be found using the method of steepest descent (Hurricane *et al.*, 2019a, 2019b), without making any simplifying assumptions about the x-ray loss term or reaction rate. The resulting solution shows that many properties of the hot spot increase exponentially with another variation of a Lawson-like parameter, such as  $pV^{5/3}/p_{pv}V_{pv}^{5/3} \approx \exp[pH(T)\tau_{BW}]$ , where  $\tau_{BW} = \sqrt{T/\bar{T}}$  and  $H(T)$  is a complicated function of temperature (Hurricane *et al.*, 2021), with the property that  $H(T) > 0$  for  $T > T_{\text{ign}}$  and  $H(T_{\text{ign}}) = 0$ . Namely (see Fig. 4),

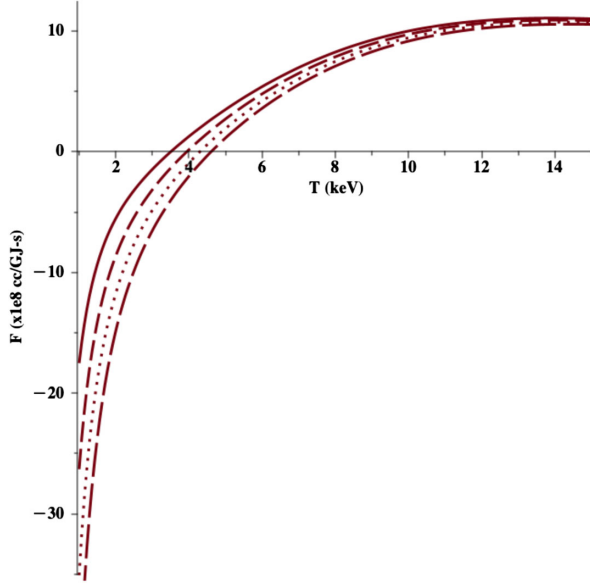


FIG. 5. Plot of  $F(T)$  for four different values of  $f_B$  (solid line, 0.5; dashed line, 0.75; dotted line, 1.0; long-dashed line, 1.25). A maximum in  $F(T)$  exists nearly independent of  $f_B \sim 14$  keV, and above 14 keV the temperature  $F(T)$  slowly declines due to the reaction-rate dependence.  $F(T)$  is positive only when alpha heating exceeds radiative loss, and for  $T \gg T_{\text{ign}}$  the sensitivity of  $F$  to radiative loss is of diminishing significance.

$$H(T) = \frac{\sqrt{\pi}F(T)}{\sqrt{2\gamma/(\gamma-1) + [2T/F(T)]\partial F/\partial T}}, \quad (21)$$

where  $\gamma = 5/3$  is the polytropic index and the function  $F(T)$  is a measure of the competition between alpha heating and bremsstrahlung cooling evaluated at peak hot-spot pressure,

$$F(T) = \frac{3Q_\alpha - f_B Q_B}{2\rho(c_{\text{DT}}T)^2}. \quad (22)$$

The parameter  $f_B$  reflects the DT bremsstrahlung enhancement at peak hot-spot pressure. Note that  $F = 0$  at the ignition temperature  $T_{\text{ign}} = 4.3f_B^{0.3}$  in keV. A maximum in  $F(T)$  exists near 14 keV nearly independent (within  $\sim 0.5$  keV) of the value of the radiation loss parameter  $f_B$ ; see Fig. 5. The  $T$  dependence of  $F(T)$  and  $H(T)$  illustrates why  $T \approx T_{\text{ign}}$  is insufficient for ignition and that a more sensible range of thermal temperatures to target in the design of an ICF implosion is where  $F(T)$  is nearly flat ( $\partial \ln F / \partial \ln T \ll 1$ ), maximal, and insensitive to radiation loss, namely,  $T \sim 8\text{--}14$  keV. Ignition based upon the Lawson-like formulation  $\rho H(T)\tau_{\text{BW}} > 1$  appears to be consistent across a variety of implosion designs (MacLaren *et al.*, 2021).

From Eq. (19) or (20) it can be seen that when  $(Q_\alpha - f_B Q_B - Q_{\text{other}})\tau \ll c_{\text{DT}}T$

$$\rho V^{5/3} \sim p_{\text{pv}} V_{\text{pv}}^{5/3}, \quad (23)$$

meaning that the pressure and volume in an ICF implosion will behave in an adiabatic fashion as the shell of the implosion

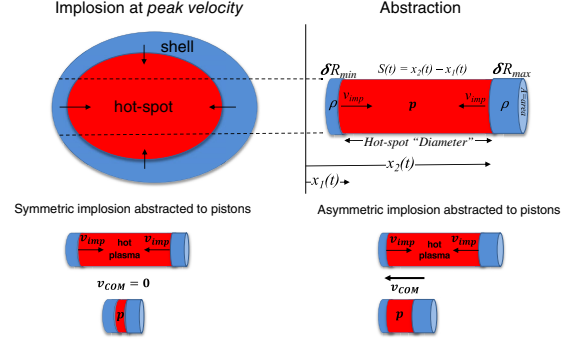


FIG. 6. An implosion with asymmetry at peak velocity is abstracted into an implosion of two asymmetric pistons. An analytic model constructed around this simple physical picture captures the principal impact of asymmetry on an implosion. Along the direction defined by the extremes of shell thickness variation (upper left image), the implosion is abstracted into an “apple core” of thin and thick pistons at opposing ends of the hot spot (upper right image). A symmetric configuration results in no center of mass motion (lower left image), while an asymmetric configuration has a net center of mass motion that carries kinetic energy. Adapted from Hurricane *et al.*, 2020.

decelerates from peak velocity to zero (stagnation); this relation reflects the pressure amplification nature of an ICF implosion. This adiabatic approximation is sufficient for obtaining a basic understanding of how important properties of an implosion scale with velocity, areal density, and measures of asymmetry.

## B. Principal physics parameters controlling ICF implosion performance

With Eq. (23) and a simple abstracted physical picture of a shell decelerating on hot DT (see Fig. 6), a useful model can be created (Hurricane *et al.*, 2020) for understanding the key parameters controlling an implosion. The asymmetric pistons, which represent segments of the implosion shell, are characterized by a minimum and maximum areal density ( $\rho\delta R_{\text{min}}$  and  $\rho\delta R_{\text{max}}$ ) and initially have the same implosion velocity. The pistons are incompressible and of constant mass, which neglects some of the physics details of a real ICF implosion shell as it stagnates on the hot spot, but as we later see, this classical mechanics model appears to be adequate for predicting several hot-spot properties.

The asymmetric pistons are separated by a “hot-spot” plasma that obeys Eq. (23). Combining the equations of motion for each piston together gives an autonomous nonlinear differential equation for the piston separation  $S$ ,

$$\ddot{S} = \frac{p_{\text{pv}}}{\rho\delta R_{\text{ave}}} \left( \frac{2}{1-f^2} \right) \left( \frac{S_{\text{pv}}}{S} \right)^{5/3}, \quad (24)$$

where the shell asymmetry fraction  $f$  is defined as a measure of areal density variation from the mean shell areal density,

$$f = \frac{\rho\delta R_{\text{max}} - \rho\delta R_{\text{min}}}{2\rho\delta R_{\text{ave}}}, \quad (25)$$

where  $p_{pv}$  is the pressure at peak velocity and  $S_{pv}$  is the piston separation at peak velocity. Data have corroborated (Rinderknecht *et al.*, 2020) that Eq. (25) is a relevant measure of asymmetry and that  $f$  is directly connected to alternate measures of asymmetry such as hot-spot drift velocity ( $v_{hs}$ ), which is calculated from the time-integrated neutron spectra (Ballabio, Källne, and Gorini, 1998) along multiple lines of sight that allow one to determine the bulk burn-averaged fluid velocity in the fusing plasma (Munro, 2016). The parameter  $f$  is related to the concept of residual kinetic energy (RKE) (Kritcher *et al.*, 2014) via the relationship  $f = v_{hs}/v_{imp} \approx \sqrt{RKE/[c(\alpha_{if})KE]}$ , where  $KE = (1/2)m_{shell}v_{imp}^2$  and  $c(\alpha_{if})$  is a fuel adiabat ( $\alpha_{if}$ ) compressibility factor;  $c(\alpha_{if}) = 1/(1 + 1.53/\alpha_{if}^{1.35}) \sim 0.66$  on average and typically ranges between 0.5 and 1 (Hurricane *et al.*, 2022). It is useful to note that, in an implosion shell, KE is split into a portion that compresses the hot spot and a portion that compresses the shell itself and that higher  $\alpha_{if}$  shifts more of the fuel KE into the hot spot, i.e.,  $E_{cold,DT}/E_{hot,DT} = 1/c(\alpha_{if}) - 1$ .

Equation (24) is analytically solvable and, from the solution expressions for a hot-spot diameter, the stagnation pressure, hot-spot energy at stagnation, inertial confinement time, Lawson product ( $p\tau$ ), hot-spot temperature, and fusion yield can be obtained when the levels of  $\alpha$ -particle self-heating are limited to levels of yield amplification  $Y_{amp} < 2$ . A subset of key scaling expressions is (Hurricane *et al.*, 2020)

$$P_{stag} \sim \frac{v_{imp}^5}{p_{pv}^{3/2}} \left[ \frac{2c(\alpha_{if})\rho\delta R_{ave}}{S_{pv}} (1 - f^2) \right]^{5/2}, \quad (26)$$

$$E_{hs} \sim A c(\alpha_{if})\rho\delta R_{ave} v_{imp}^2 (1 - f^2), \quad (27)$$

$$P_{stag}\tau \sim c(\alpha_{if})\rho R_{ave} (1 - f^2) v_{imp}, \quad (28)$$

where  $A = m_{shell}/(2\rho\delta R_{ave})$  is the piston cross-sectional area. The ratio of Eq. (28) to Eq. (26) gives the inertial confinement time. As implied by Eq. (17), Eqs. (26)–(28) reflect the importance of velocity. In addition to high  $v_{imp}$ , high  $\rho R_{ave}$ , low  $f$ , low  $p_{pv}$ , and low  $S_{pv}$  are seen to be desirable properties. A three-dimensional extension of the piston model indicates that the impact of mode-2 asymmetry can be captured in the previously mentioned relations by substituting for  $1 - f^2$  the ratio of the hot-spot area weighted harmonic mean (WHM) of  $\rho R$  to the area weighted average  $\rho R$  (Hurricane *et al.*, 2022). Namely,

$$\frac{\rho\delta R_{WHM}}{\rho\delta R_{ave}} = \frac{(\int dA)^2}{(\int dA/\rho\delta R)(\int \rho\delta R dA)}, \quad (29)$$

$$\frac{RKE}{c(\alpha_{if})KE} = 1 - \frac{\rho\delta R_{WHM}}{\rho\delta R_{ave}}, \quad (30)$$

where the integrals are taken over the hot-spot surface. Assuming a power-law fusion reaction-rate dependence  $\langle\sigma v\rangle \sim T^a$  then gives a fusion yield degradation (in the low alpha-heating limit) due to asymmetry of  $(1 - f^2)^a$  or  $(\rho\delta R_{WHM}/\rho\delta R_{ave})^a$ , respectively, for mode-1 or general

asymmetry. The asymmetry-induced yield degradation with significant alpha heating is more complicated, but a formula is available (Hurricane *et al.*, 2022). Other models have also pointed to the importance of the areal density harmonic mean (Woo and Betti, 2021). The key parameters for reaching ignition suggested by the piston model are the Lawson product [Eq. (28)], which reflects the importance of high shell (piston) areal density, high peak implosion velocity, and minimal asymmetry for a generic implosion.

Asymmetries can originate from capsule fabrication (Casey *et al.*, 2021) and/or from drive imbalances (MacGowan *et al.*, 2021). The fact that good symmetry is important for converting the implosion kinetic energy into useful thermal energy at stagnation is not surprising, as noted by many (Winterberg, 1968; Widner *et al.*, 1977; Bodner, 1995; Scott *et al.*, 2013; Gu *et al.*, 2014; Kritcher *et al.*, 2014; Chittenden *et al.*, 2016; Gatu Johnson *et al.*, 2016; Bose *et al.*, 2017, 2018; Cheng *et al.*, 2018; Woo *et al.*, 2018). However, there has been debate over which aspect of asymmetry is key (that is, hot spot, shell areal density, time dependent of either versus at stagnation, etc.). This piston model works well when compared against simulations and data (see Fig. 7), and it provides a concise statement of what aspect of asymmetry, namely, shell areal density asymmetry at stagnation, is most important. The essential physics of asymmetry illuminated by the piston model is that, in the lab frame of reference, some elements of the shell are still moving at the time of peak compression; thus, the kinetic energy of those moving elements is not converted into internal energy at peak compression.

### C. Implosion acceleration and hydrodynamic instability

Asymmetry is not the only potential degradation that impacts implosions. Inwardly accelerating shells of material to high velocity and then having them decelerate (see Fig. 8) as their central pressure builds puts the implosion at risk of unstable growth wherever the gradient in pressure  $\vec{\nabla}p$  is directed oppositely to the density gradient  $\vec{\nabla}\rho$ , i.e., wherever  $\vec{\nabla}p \cdot \vec{\nabla}\rho < 0$ . Any small imperfection can be amplified and, if the growth is severe enough, will defeat the ability of the implosion to effectively heat and compress DT because the shell that provides the inertial confinement gets shredded by the instability and will (in some cases) inject cold shell material into the central hot-plasma region, cooling that region by enhancing the bremsstrahlung emission due to the  $\bar{Z}$  dependence of Eq. (4).

The primary modes of concern are Rayleigh-Taylor (RT) instability (Rayleigh, 1883; Taylor, 1950) under continuously varying acceleration and Richtmyer-Meshov (RM) instability (Richtmyer, 1960; Meshkov, 1969) under impulsive accelerations. Magnetically driven implosions have additional instabilities to be concerned about, such as electrothermal and kink modes as well as the magnetohydrodynamic equivalent of RT (MRT) and RM modes; see Sec. V.B.4.

For linear instability (which assumes that the perturbation amplitude is less than the perturbation wavelength), the growth of the RT instability at the ablation front in an ICF implosion is a product of the effect of convergence [essentially

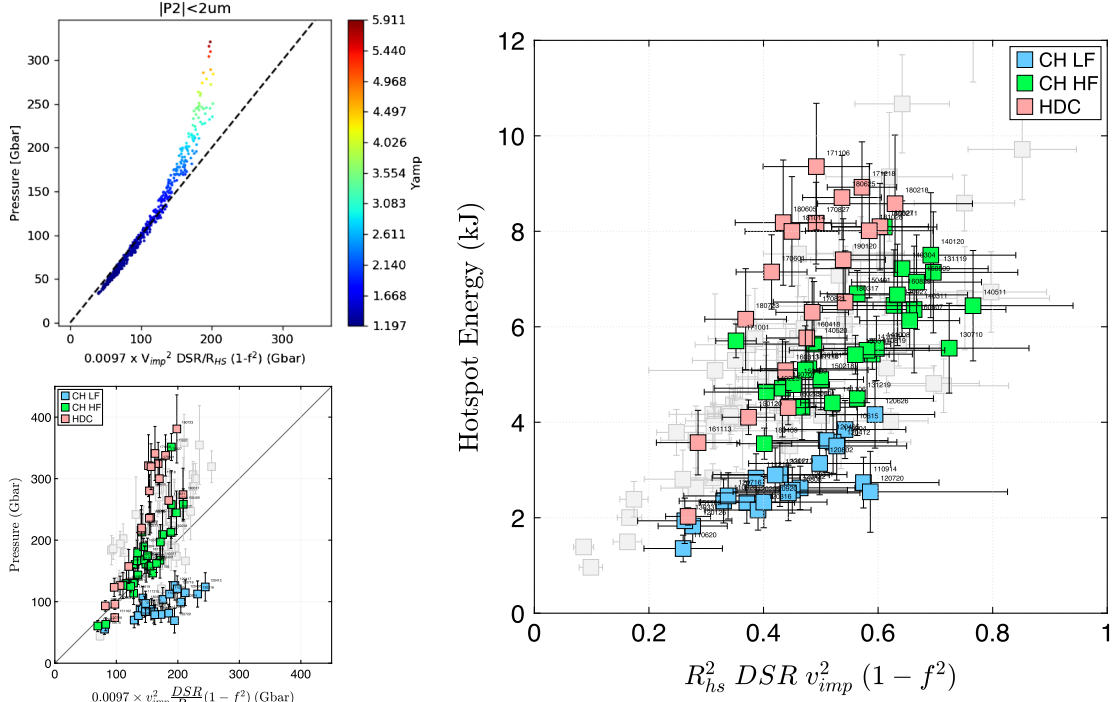


FIG. 7. Upper left panel: stagnation pressures from a suite of ensemble model simulations are plotted against the piston pressure formula  $P_{\text{stag}}(\text{Gbar}) = 0.0097 \text{ DSR}(\%) v_{\text{imp}}^2 (\text{km/s}) / R_{\text{hs}}(\mu\text{m})$ , which is a rewriting of Eq. (26) in terms of more directly measured variables. The ratio of 10–12 MeV fusion neutrons to 13–15 MeV fusion neutrons defines DSR, which is directly related to shell  $\rho R$ . Lower left panel: stagnation pressures from indirect-drive DT experiments at the NIF are plotted against the piston pressure formula. Right panel: hot-spot energy inferred from indirect-drive DT experiments at the NIF are plotted against the piston formula for hot-spot energy. Key implosion campaigns are in color, where LF refers to low foot, HF indicates high foot, and HDC refers to high-density carbon experiments on NIF. The data inference of stagnation pressure and hot-spot energy follows from a procedure first described by Cerjan, Springer, and Sepke (2013) and Springer *et al.* (2013). From Hurricane *et al.*, 2020.

mass conservation in a form known as the Bell-Plesset effect (Bell, 1951; Plesset, 1954)] and exponential growth.

The effect of convergence on the amplitude of perturbation growth is estimated as (Goncharov, McKenty *et al.*, 2000)

$$\eta_{\text{BP}} = C_R^{-1/4} \exp[\sqrt{2\ell}(\arcsin \sqrt{1 - 1/C_R} - \sqrt{1 - 1/C_R})], \quad (31)$$

where  $C_R > 1$  is the convergence ratio, which is the ratio of the initial to the final radius of the unstable region and  $\ell$  is the Legendre-mode number.

The exponential growth rate is given by (Betti *et al.*, 1998)

$$\gamma_{\text{A-RT}} = \alpha_2(\text{Fr}, \nu) \sqrt{\frac{kg}{1 + kL_\rho}} - \beta_2(\text{Fr}, \nu) kv_a, \quad (32)$$

where  $k = 2\pi\ell/R$  is the perturbation wave number,  $g$  is the shell acceleration,  $L_\rho = \rho/|\vec{\nabla}\rho|$  is the density gradient scale length of the ablation front,  $v_a$  is the velocity of ablation [a stabilizing term first identified by Bodner (1974) and described as fire polishing], while  $\alpha_2$  and  $\beta_2$  are parameters of the order of unity whose exact values depend upon a heat-conduction scale-length parameter  $\nu$  and the Froude number  $\text{Fr} = v_a^2/gL_\rho$ . Combining Eqs. (31) and (32) then

gives the total mode-dependent growth factor  $G(\ell)$  (ratio of the amplitude of final perturbation to the initial amplitude)  $G(\ell) \sim \eta_{\text{BP}} \exp[\int \gamma_{\text{A-RT}}(t) dt]$ . As a consequence of convergence and exponential growth, the degree of unstable perturbation growth is potentially many orders of magnitude; see Fig. 9.

In the low-mode limit  $kL_\rho \ll 1$ , a simple analysis of Eq. (32) suggests an important design parameter for controlling instability growth. Namely, taking  $\partial\gamma_{\text{A-RT}}/\partial k = 0$  gives the maximum growing mode ( $k_{\text{max}} \approx \alpha_2^2 g / \beta_2^2 v_a^2$ ) and maximum growth rate ( $\gamma_{\text{max}} \approx \alpha_2^2 g / 4\beta_2 v_a$ ). Noting that  $R \sim gt^2/2$  and  $2g\delta R \sim v_a^2$ , one finds that  $\int \gamma_{\text{max}} t \sim (\alpha_2^2 / 4\beta_2) \sqrt{\text{IFAR}}$ , where  $\text{IFAR} = R/\delta R$  is the “in-flight aspect ratio,” thereby highlighting the instability danger of accelerating a thin shell.

This form of Eq. (32) is from Betti *et al.* (1998), but numerous variations of Eq. (32) exist in the literature on this topic, and equations of that form are often referred to as the Takabe formula (Takabe, Montieth, and Morse, 1983; Takabe *et al.*, 1985). Equation (32) is enough to see that, given an initial condition of perturbation seeds, there are three principal ways to mitigate RT instability in an ICF implosion: increase the ablation velocity, increase the density gradient scale length, or reduce convergence.

Because the shell of an ICF implosion has a finite thickness, perturbation growth on the outside of the shell feeds through

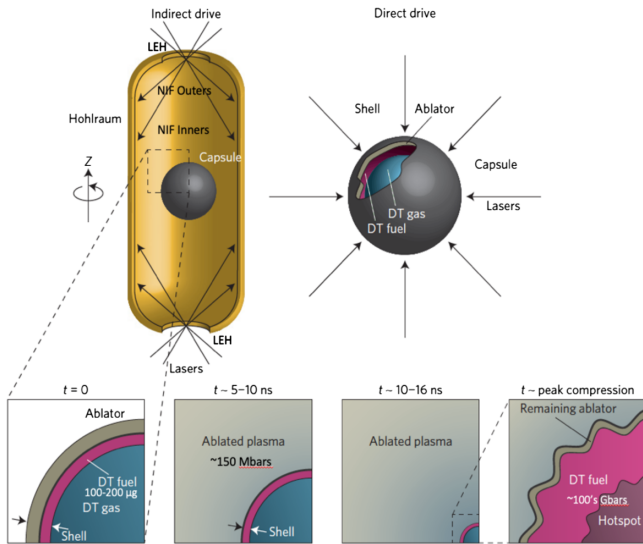


FIG. 8. Typical targets used in laser-driven ICF are (upper left image) indirectly driven (where the laser energy is incident on a hohlraum generating a bath of x rays) or (upper right image) directly driven (where the laser beams are directly incident on the capsule). In either case, a spherical capsule is prepared at  $t = 0$  with a layer of DT fuel on its inside surface. As the capsule surface absorbs energy and ablates, pressure accelerates the shell of the remaining ablator and DT fuel inward, thereby producing an implosion. By the time the shell is at approximately one-fifth of its initial radius, it is imploding at a speed of many hundreds of kilometers per second, as dictated by Eq. (17). By the time the implosion reaches minimum radius, a hot spot of DT has formed, surrounded by colder and denser DT fuel. The timescales shown in the row of frames at the bottom are characteristic of plastic ablaters. The timescales for higher-density ablaters like high-density carbon (HDC) are generally shorter owing to their reduced thickness. From Betti and Hurricane, 2016.

to the inside of the shell (and vice versa) as a consequence of shock imprinting, continuity (mass conservation), and the circulating flows inside the shell that buoyancy-driven instabilities generate. Post shock, for a given thickness of shell  $\delta R$ , any perturbation on one side of the shell develops on the other but is attenuated by a factor of  $\exp(-k\delta R)$  (Mikaelian, 1995), which can lead to a complex nonlinear interaction between the inside and outside of the shell.

Interfaces of the shell, such as the fuel-ablator interface, can be subject to high mode growth, with a growth rate  $\gamma \sim \sqrt{kA_t g}$ , if the density jump, as measured by the Atwood number (with  $A_t$  the density difference across an interface over the sum of densities across that same interface), is unfavorable. For nonlinear instabilities (modes with a perturbation amplitude greater than the perturbation wavelength), the amplitude growth is expected to asymptote to a free-fall scaling  $\sim gt^2$  (Dimonte *et al.*, 2004). While the instability behavior of ICF implosions can be understood analytically in special situations, computer simulations are usually used to assess the potential for instability growth and mixing (Fig. 9).

Like all areas of fusion research, controlling hydrodynamic instability growth is a major challenge. None of the three major ICF thrusts (laser indirect drive, laser direct drive, and

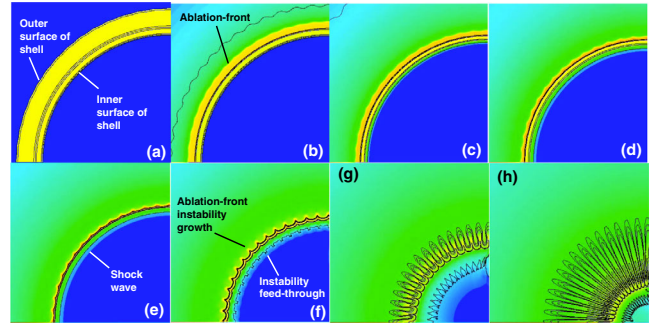


FIG. 9. A simulation of instability growth on an indirect-drive ICF gas capsule implosion is shown in a variable logarithmic density color scale that ranges from low (blue) to high (red). The particular implosion design is that of the “low foot”; see Sec. III.E.1. (a) A small amplitude mode-60 perturbation is imposed on the outside of the capsule at  $t = 0$ . (b) By  $t = 10$  ns the outer layer of the capsule has ablated away and the shell has been compressed. (c) By  $t = 15$  ns the shell begins to rapidly accelerate inward. (d) By  $t = 16$  ns perturbation growth on the outside of the capsule becomes visible. (e) By  $t = 18$  ns the shock wave that transited the ablator and entered the gas races inward ahead of the shell. (f) By  $t = 19$  ns instability growth on the inside of the shell develops. (g) By  $t = 20$  ns the amplitude of instability growth exceeds the thickness of the shell. (h) By  $t = 21$  ns the shell of the implosion has been shredded by instability.

magnetic direct drive) are immune from instability concerns. However, the idea of “starting over,” advocated by J. Nuckolls in the 1970s, with a smooth field of x rays driving a capsule was thought to be the best chance of minimizing instability problems and drove early work at Lawrence Livermore National Laboratory.

### III. X-RAY-DRIVEN IMPLOSIONS

#### A. History

At Lawrence Livermore National Laboratory (LLNL), the first laser fusion program, the “Q group” led by Ray Kidder, spanned the period of 1962–1972 (Nuckolls, 2006). It later became apparent that the Soviets also had an ICF program led by Nikolai Basov starting in this period. During that period the key target design simulation tool LASNEX (Zimmerman and Kruer, 1975) was developed and was the principal tool used to study ICF at LLNL for many decades. In 1971, elements of ICF began to be declassified and made public (but not the concept of x-ray drive); see Nuckolls *et al.* (1972). Some aspects of ICF remain classified even today.

From 1972 to 1992 a second laser fusion program existed. Centered around the 10-kJ-class Shiva laser system (1977–1982), it was on this laser system that the first indirect-drive ICF targets were demonstrated. A second higher energy and shorter wavelength laser system, Nova (operating from late 1984 to 1999) later replaced Shiva, as it became apparent that the laser wavelength was a key issue for mitigating deleterious laser-plasma interactions.

In 1993 plans were laid for the megajoule-class NIF laser system with the physics basis described by Lindl (1995).

Construction of the NIF began in 1997, with the laser fully completed about a decade later. The NIF is presently the primary indirect-drive experiment facility in the U.S. In principle, indirect-drive implosions should have an advantage at small spatial scales because the x-ray drive generated has a smoothing effect that mitigates high-mode asymmetry and fluid instabilities. The sacrifice made for the smoothing effect of x rays is in terms of energy coupled to the implosion because a large fraction of energy delivered to an indirect-drive target is absorbed by the walls of the x-ray-generating cavity known as the hohlraum since the capsule surface area is small compared to the hohlraum surface area.

## B. Indirect drive with lasers

A principal mechanism to drive an implosion inward upon itself and achieve high implosion speeds, which estimates suggest are needed [Eq. (17)], is to expose the outer surface of a shell of material (an “ablator”), to an intense bath of x rays; see Fig. 8. Absorption of x-ray energy by a thin layer of ablator material will ionize it and generate high pressures (on the order of hundreds of megabars), producing an inward-directed acceleration that literally rockets the remaining ablator and DT fuel to high velocity. The generation of ablation pressure is accompanied by the generation of inwardly directed shock waves (Guderley, 1942), the control of which are a key aspect of any modern design (Lindl, 1995; Landen *et al.*, 2010, 2011; Haan *et al.*, 2011; Robey *et al.*, 2012b). The implosion effectively amplifies the ablation pressure [Eq. (23)], as the volume shrinks to the levels required (Table I), but a majority of the x-ray energy is consumed in the process as the majority of the ablator (typically 90%–95%) is turned from a solid state into a plasma.

### 1. Hohlraum physics

As laser energy is deposited into the hohlraum, power balance determines the radiation temperature ( $T_r$ ) of any high-energy-density physics hohlraum,

$$P_{\text{laser}} = \sigma T_r^4 (1 - a_h) A_H, \quad (33)$$

where  $P_{\text{laser}}$  is the input power,  $\sigma$  is the Stefan-Boltzmann constant ( $1.03 \times 10^{11} \text{ MJ/cm}^2 \text{ s keV}^4$ ), and  $a_h$  is the hohlraum-wall albedo, which scales as (Lindl, 1995)

$$1 - a_h \sim T_r^{-2/3} t^{-1/2}, \quad (34)$$

where  $A_H$  is the inner hohlraum-wall area. Equation (33) reasonably assumes that losses are dominated by wall absorption rather than loss through apertures such as the laser entrance holes (LEHs) or to a capsule, assumptions that are not correct when the LEH area or capsule area are a significant fraction of  $A_H$ . Equation (34) reflects the fact that energy diffuses into the hohlraum wall in the form of a Marshak wave (Marshak, 1958); the most comprehensive modern treatment was given by Hammer and Rosen (2003).

Integrating Eqs. (33) and (34) gives a useful scaling of  $T_r$  with laser energy ( $E_{\text{laser}}$ ), namely,

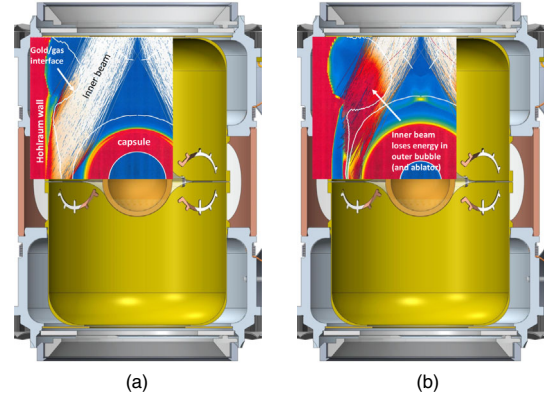


FIG. 10. Coupled hohlraum-capsule simulation images are inset on top of a typical indirect-drive target geometry. (a) At a time early in peak laser power, the shallow polar angle “inner” beams propagate to their intended location on the inner hohlraum wall unimpeded. (b) At a later time, a plasma bubble generated by the incidence of the large polar angle “outer” beams (not shown) interferes with the propagation of the inner beam, upsetting the intended x-ray symmetry inside the hohlraum. Insets: From Callahan *et al.*, 2018.

$$E_{\text{laser}} \sim T_r^{3.3} A_H \sqrt{t_{\text{laser}}}, \quad (35)$$

where  $t_{\text{laser}}$  is the duration over which laser power is applied. With a prescribed temporal history of laser power and with consideration of the details of capsule heat capacity and LEH losses, a more precise model of  $T_r(t)$  based upon Eq. (33) can be obtained that compares favorably to data and that is useful for scoping studies (Callahan *et al.*, 2020) because it has a much shorter time to solution than large computer simulations (Zimmerman and Kruer, 1975; Suter *et al.*, 1996; Marinak *et al.*, 2001), which are a primary tool in the field. The status of common baseline simulations for laser indirect drive was addressed by Clark *et al.* (2018) and Kritcher *et al.* (2018a).

The need to get laser energy into the hohlraum, while also minimizing x-ray energy losses back out the way that the lasers came in, leads to hohlraum geometries (see Fig. 10) and individual laser-beam pointings that greatly complicate the symmetry control of the implosion. The hohlraum can drive asymmetry because the sky of x-ray flux, as seen in the capsule, is nonuniform and changing in time. Much like hydrodynamic instability, an implosion is particularly sensitive to x-ray drive asymmetry during periods of peak acceleration (Masse *et al.*, 2019). Asymmetry is typically expressed by amplitudes of Legendre polynomials (with  $P_0$ ,  $P_2$ , and  $P_4$  standing for the amplitudes of Legendre modes 0, 2, and 4, respectively). Principal techniques of managing  $P_2$  and  $P_4$  symmetry control of hohlraum-driven implosions involve adjustments to beam pointing, rebalancing power between sets of beams [“cone fraction” (Glenzer *et al.*, 2010; Town *et al.*, 2011)], hohlraum gas fill (usually helium gas) and designing around plasma features inside the hohlraum (see Fig. 10) that evolve to obstruct the desired laser energy deposition (Callahan *et al.*, 2018; Ralph *et al.*, 2018).

Depositing laser energy into a hohlraum is often somewhat frustrated by laser-plasma instabilities (LPIs)

(MacGowan *et al.*, 1996), which occur when the laser wave beats resonantly with an outgoing scattered light wave and one or more plasma waves. When the laser wave vector  $\vec{k}_L$  and laser frequency  $\omega_L$  satisfy the phase-matching conditions  $\vec{k}_L = \vec{k}_s + \vec{k}_p$  and  $\omega_L = \omega_s + \omega_p$  (where  $s$  and  $p$  stand for a scattered wave and a plasma wave, respectively), unstable amplification of the scattered wave and plasma wave will occur (Kruer, 2003). The locations where the local electron plasma frequency  $\omega_{pe} = \sqrt{e^2 n_e / \epsilon_0 m_e}$  (with  $n_e$  the electron density and  $\epsilon_0$  the vacuum permittivity) match  $\omega_L$  define the “critical surface” and critical electron density  $n_c$ ; resonant absorption of laser energy occurs in the plasma with a number density at or below  $n_c$ . One-quarter critical density ( $n_c/4$ ) is the limiting density for electron plasma wave stimulated Raman scattering (SRS) and two-plasmon decay instabilities. Acoustic plasma wave stimulated Brillouin scattering (SBS), parametric decay, and filamentation instabilities can occur at densities up to and including  $n_c$ . The principal tactic for dealing with LPIs in ICF experiments is to keep  $n_e$  low (Hinkel *et al.*, 1998) and  $T_e$  (electron temperature) high in regions where the laser needs to propagate, which reduces the chance of LPIs occurring. In some cases LPIs, in the form of cross-beam energy transfer (CBET), can be used to intentionally direct energy from one set of beams to others, thereby changing the effective cone fraction (Michel *et al.*, 2009, 2011; Moody *et al.*, 2012; Kritcher *et al.*, 2018b), which can be a useful symmetry control tactic.

### C. Z-pinch-driven hohlraums

Lasers are not unique in their ability to generate x rays. Magnetic Z pinches are also ubiquitous x-ray sources and, moreover, they avoid LPIs. For example, the Z facility at Sandia National Laboratories is a pulsed power accelerator with 6 MJ of stored electrical energy that discharges in 120 ns. On Z, the peak currents delivered to the load approach 27 MA. Wire-array loads (see Sec. V.A.4) have been the main approach for producing x rays on Z for use in high-energy-density physics and inertial confinement fusion experiments. In particular, vacuum hohlraums (Hammer *et al.*, 1999), which are suitable for driving capsules, have achieved peak radiation temperatures ( $T_r$ ) of 90 eV. This temperature is achieved in a secondary hohlraum driven by a primary hohlraum containing a wire-array pinch. “Hybrid hohlraum” experiments have heated a small secondary hohlraum to  $T_r$  of about 145 eV (Olson *et al.*, 2001) but lack the control of illumination symmetry afforded by the vacuum hohlraum. In contrast, hohlraums at the OMEGA laser in Rochester, NY, regularly achieve 200 eV peak radiation temperatures, while at the NIF 300 eV is typical. Part of the problem in obtaining higher radiation temperatures using wire arrays is that they are not compact compared to laser-driven targets.

In wire-array loads, explosive resistive heating of the fine wires quickly generates a sheath of metal plasma as the Z machine discharges. This cylindrical sheath of conducting plasma is driven radially inward by the Lorentz force  $\mathbf{J} \times \mathbf{B}$  (with  $\mathbf{J}$  the current density and  $\mathbf{B}$  the magnetic field,

i.e., the z-pinch effect). As the plasma implodes on the  $z$  axis, x rays are produced, with approximately 10% variation from shot to shot. The radius of the plasma sheath  $R_p$  is related to the peak current  $I_p$  and the current rise time  $t_R$  through magnetohydrodynamic (MHD) force balance,  $\rho_s dR_p/dt = -\nabla(B^2/2\mu_0)$ , which yields the dimensional analysis scaling

$$R_p \sim \frac{\sqrt{I_p t_R}}{\rho_s^{1/4}}, \quad (36)$$

where  $\rho_s$  is the density of the plasma sheath. The energy imparted to the load must then scale as  $E \sim R_p^3 B^2 \sim I_p^{5/2} t_R^{1/2} / \rho_s^{1/4}$ .

From Eq. (33) and assuming a fixed hohlraum area, one finds that the radiation temperature scales as  $T_r \sim I_p^{5/8} \rho_s^{-1/16} t_R^{-1/8}$  for constant hohlraum albedo. Since the hohlraum albedo is generally not constant [Eq. (34)], a more accurate radiation temperature scaling is found to be

$$T_r \sim \frac{I_p^{3/4}}{\rho_s^{3/40}}, \quad (37)$$

which is independent of the current rise time. The sublinear scaling of  $T_r$  with current reflects the difficulty of obtaining high radiation temperatures in magnetically driven hohlraums. However, while any load design must adhere to the dynamical scaling of Eq. (36), higher radiation temperatures can, in principle, be obtained, thereby breaking the scaling of Eq. (37) by forcing the radiating plasma into a smaller primary or secondary geometry (Hammer, 2016).

### D. Ablator physics

The hohlraum generated x-ray energy is deposited into a unit area of ablator surface given by Planck’s expression for radiant energy flux  $\sigma T_{\text{rad}}^4$ . If the flow of radiation into the ablator is subsonic, which is generally the case in an x-ray-driven implosion, the x-ray energy flux onto the ablator, corrected for the ablator albedo ( $a_{\text{abl}}$ ), is balanced by the rate of work done in expanding the ablator plasma at the ablation pressure ( $p_{\text{abl},x}$ ),  $c_s p_{\text{abl},x} \sim \sigma T_r^4 (1 - a_{\text{abl}})$ , but here the speed is the sound speed of the isothermal rarifying plasma  $c_s \sim \sqrt{p/\rho} \sim \sqrt{[(\bar{Z} + 1)/\bar{A}] k_B T_e / m_p}$  with the use of Eq. (2). Therefore, assuming  $T_e \approx T_r$  in the ablator, the x-ray-driven ablation pressure scales as

$$p_{\text{abl},x} \sim \sqrt{\frac{\bar{A}}{\bar{Z} + 1}} (1 - a_{\text{abl}}) T_r^{7/2}. \quad (38)$$

This pressure generates the force that accelerates the implosion to high velocity, as described in Sec. II. To obtain the required implosion velocities, a good x-ray ablator must be a material that is fairly dense, readily ionizes, and is not too opaque to the incident x rays: a condition that generally excludes consideration of materials much above carbon on the periodic table. For realistic ablator materials, the effect of an albedo term is to reduce the  $T_r$  scaling in Eq. (38) from  $T_r^{3.5}$

TABLE III. Some useful characteristics of typical ablator materials. Initial room temperature density can vary with crystal grain size (for instance, nanoscale or microscale) and with the presence of any dopant atoms. Typical first shock pressure design target  $p_{1st}$  varies with the desired fuel adiabat but is usually chosen to minimally exceed the melt pressure  $p_{melt}$ . Owing to its amorphous nature, glow discharge polymer (GDP) plastic (also known as CH due to its atomic composition) allows for a large range of  $p_{1st}$ . The numbers here are associated with the low- and high-foot designs mentioned in Sec. III.E.

Ablator	Approx. $\rho_0$ (g/cm <sup>3</sup> )	$p_{1st}$ (Mbar)	$p_{melt}$ (Mbar)
GDP	1.1	1.7–3.4	1.0
Be	1.9	3.5	2.6
B <sub>4</sub> C	3.5	3.4	2.2
HDC	3.3 <sub>nano</sub> –3.5 <sub>micro</sub>	12–14	12

to  $T_r^{(2.4-2.9)}$ , depending upon the material (Lindl, Haan, and Landen, 2021).

Ablator materials start in the solid state and are then shock compressed and melted as the ablation pressure builds in response to the x rays incident upon the capsule. Melting the ablator upon initial shock without subsequent refreezing is an important aspect of implosion design, especially for crystalline materials. To guarantee a melted state, the pressure of the initial shock must exceed the melt pressure  $p_{melt}$ , and the postshock ablator material must subsequently maintain a high temperature. Table III lists the melt pressure for common indirect-drive ablator materials based upon the work of Benedict *et al.* (2014) and Fratantuono *et al.* (2016). An additional yet not completely understood complication of crystalline ablators is the effect of grain structure, which can generate post-shock-front velocity perturbations (Ali *et al.*, 2018) that seed hydrodynamic instability, perturbations that are minimized with a complete transition to melt before the implosion proceeds.

Early in the implosion when the central pressures are small, the trajectory of the implosion is well approximated using a simple rocket model (Saillard, 2006), namely,

$$m_{shell} \frac{dv_{imp}}{dt} = -4\pi R_{shell}^2 p_{abl,x}, \quad (39)$$

$$\frac{dm_{shell}}{dt} = -4\pi R_{shell}^2 \dot{m}_a, \quad (40)$$

where  $R_{shell}$  is the ablation-front radius,  $v_{imp} = \dot{R}_{shell}$  is the mean implosion velocity of the remaining capsule shell, and  $\dot{m}_a = k_m p_{abl} / \sqrt{T_r}$  is the mass ablation rate per unit area ( $k_m$  is a numerical constant). Note that in Eq. (39) the reduction in x-ray absorption efficiency due to the capsule surface area shrinking in time ( $\sim R_{shell}^2$ ) is compensated for by mass ablation ( $m_{shell}$  also declines in time), so acceleration at late times can still be significant even though the capsule radius is small. If  $T_r$  (and therefore  $p_{abl,x}$ ) is constant in time over the duration of the implosion, then Eqs. (39) and (40) have a simple “rocket-equation” solution, which is  $v_{imp} = (\sqrt{T_r}/k_m) \ln[m_{shell}(0)/m_{shell}(t)]$ ; that is, high velocities are obtained by ablating most of the shell and/or by having a high  $T_r$  in the hohlraum. The ratio of late-time shell mass  $m_{shell}(t)$  to the initial shell mass  $m_{shell}(0)$  is the fractional “mass remaining,” which plays a key role in managing the integrity of the implosion as the need for high velocity is traded off against the need for hydrodynamic stability control and good inertial confinement at stagnation. In the thin-shell approximation, the replacement  $p_{abl,x} \rightarrow p_{abl,x} - p$  in Eq. (39), coupled with Eqs. (14) and (18) or (19), provides a complete 1D dynamic model of a DT implosion and hot spot with the deceleration and explosion phases.

In typical indirect-drive designs,  $p_{abl,x}$  is not constant in time, as assumed in the previously discussed solution, but is instead more typically a triangular-shaped function (see Fig. 11),

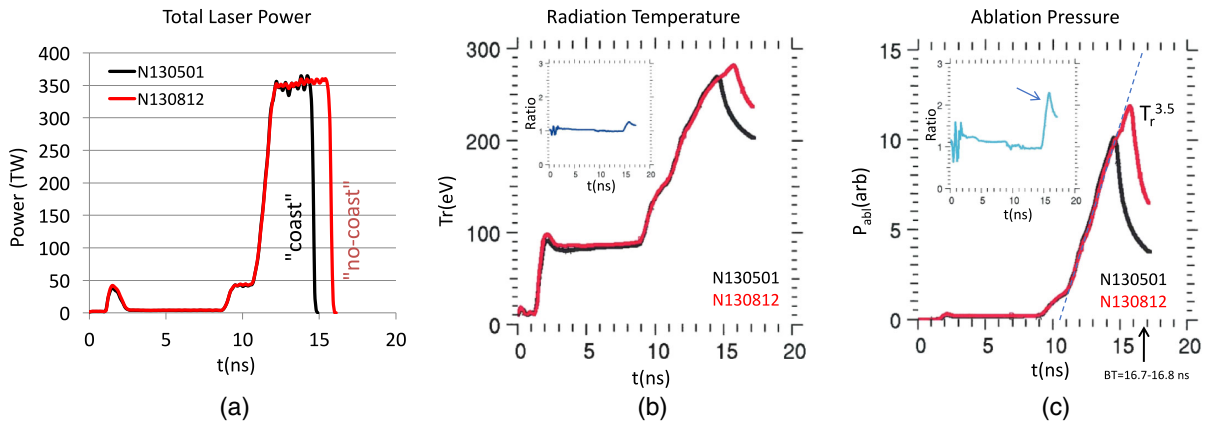


FIG. 11. Examples of laser pulse shapes, hohlraum radiation temperatures, and ablation pressures for two indirect-drive experiments at the NIF. (a) Laser power vs time for the “coasting” 1.3 MJ pulse N130501 and the “no-coasting” 1.7 MJ pulse N130812. The colloquial terms coast and no coast are misnomers since both of the pulse shapes shown result in implosions that coast. It is just that the longer duration pulse results in less coasting. (b) The resulting simulated hohlraum radiation temperatures for shot N130501 and shot N130812, with the ratio of the two shown in the inset. (c) The ablation pressure (arbitrary units) that results from  $T_{rad}^{7/2}$ , with the ratio of the two shown in the inset. The shape of the ablation pressure in time is nearly triangular with a near-linear rise and fall. Time duration between the bang time and the peak in ablation pressure is the coast time. Insets: From Hurricane *et al.*, 2017b.

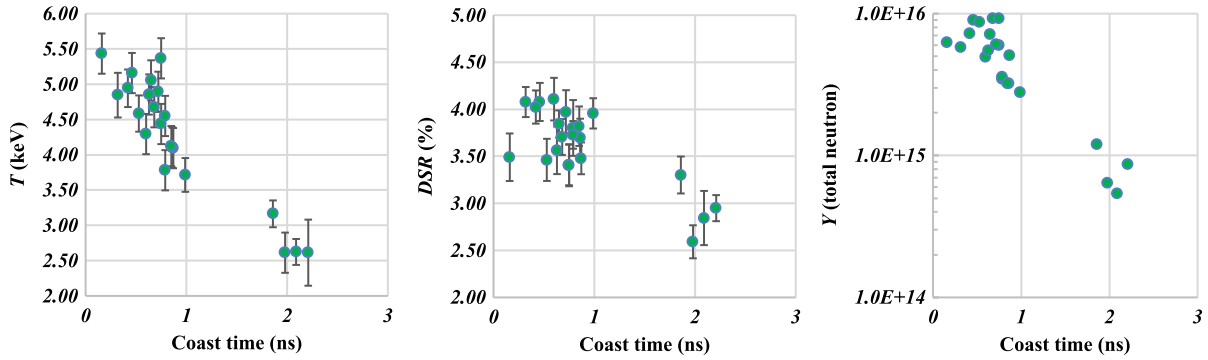


FIG. 12. Data from the high-foot series of experiments (2013–2014) show a clear correlation between burn-average hot-spot ion temperature as measured by neutron time-of-flight detectors (left frame), the neutron down-scatter ratio (DSR), which is the ratio of 10–12 MeV fusion neutrons to 13–15 MeV fusion neutrons and is therefore a measure of compression (middle frame), and the total fusion neutron yield (right frame).

resulting in a more complex solution to Eqs. (39) and (40) than the rocket-equation solution. In dimensionless radius and time terms, the solutions of Eqs. (39) and (40) are determined by three dimensionless parameters  $4\pi R_0 p_{\max} t_{\max}^2 / m_{\text{shell}}(0)$ ,  $4\pi R_0^2 k_m p_{\max}^{6/7} t_{\max} / m_{\text{shell}}(0)$ , and  $p_{\max} / \dot{p}_{\text{cool}} t_{\max}$ , where  $R_0$  is the initial shell radius,  $p_{\max}$  is the peak ablation pressure,  $t_{\max}$  is the rise time of peak ablation pressure, and  $\dot{p}_{\text{cool}}$  is the rate of ablation pressure decline after peak pressure that results from hohlraum cooling. The time duration between when  $p_{\text{abl},x}$  peaks and the implosion stagnates is called coast time, albeit that definition is not unique. The coast time is an important aspect of an implosion design since experimentally short coast times strongly correlate with many measures of improved hot-spot performance (see Fig. 12) and compression (Zylstra *et al.*, 2014), such as the stagnation pressure (Hurricane, 2016; Hurricane *et al.*, 2016, 2017b; Döppner *et al.*, 2020) (see Fig. 13) and the total areal density (Landen *et al.*, 2012, 2020; Robey *et al.*, 2013; Lindl *et al.*, 2014). Reducing the coast time results in less sensitivity to  $\dot{p}_{\text{cool}}$ , a reduction in the radius at which peak velocity is achieved (Hurricane *et al.*, 2022), for

instance, a reduction in the  $S_{\text{pv}} \sim 2R_{\text{pv}}$  term in Eq. (26), and this results in a higher deceleration rate and an increased rate of mechanical power transfer as kinetic energy is converted into internal energy (Callahan *et al.*, 2020). For example, a key metric for ignition is the product of hot-spot stagnation radius and pressure  $p_{\text{stag}} R_{\text{hs}}$  (which is equivalent to the product of hot spot  $\rho R$  and  $T$ ), and this quantity rapidly increases with reduced  $R_{\text{pv}}$  (Hurricane *et al.*, 2022),

$$p_{\text{stag}} R_{\text{hs}} \sim \frac{m_{\text{shell}} c_s^2}{4\pi R_{\text{pv}}^2} (1 - f^2) c(\alpha_{if}), \quad (41)$$

where  $c_s$  is the hot-spot plasma sound speed. In Eq. (41), it was assumed that there is enough alpha heating to offset x-ray loss cooling in addition to the plasma heating that results from compression. Equation (41) is a form of a kinetic energy areal density, and we note that  $p_{\text{stag}}^2 E_{\text{hs}} = 2\pi (p_{\text{stag}} R_{\text{hs}})^3$ , indicating the importance, via Eq. (41), of large  $m_{\text{shell}}$  and small  $R_{\text{pv}}$  for ignition. For a coast time much less than the cooling time of the

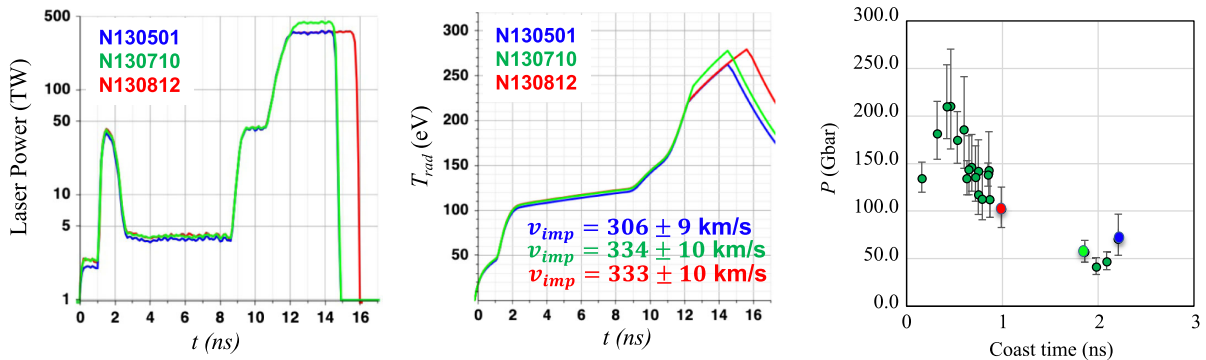


FIG. 13. The first high-foot DT implosion experiment N130501 formed a baseline to study the impact of increasing implosion velocity with different choices of coast time. Left frame: experiment N130710 increased implosion velocity by increasing laser power relative to N130501, while experiment N130812 maintained the same laser power as N130501 but extended the duration of peak laser power, therefore significantly reducing the coast time. Middle frame: experiments N130710 and N130812 were designed to have identical peak hohlraum radiation temperature and implosion velocity, but the N130812 experiment has a higher late-time hohlraum radiation temperature. Right frame: the three experiments N130501, N130710, and N130812 gave the first indications that hot-spot pressure would increase with reduced coast time, as was later proven through a series of high-foot experiments where the coast time was systematically decreased in steps. At short coast time, the hot-spot pressure was observed to drop from its maximum value: a failure mode speculated to be due to a rupture in shell caused by an asymmetry-induced perforation at low remaining mass (Hurricane *et al.*, 2016).

TABLE IV. Indirect-drive implosion designs at the NIF tested over various time periods accompanied by the motivations for design.

Design	Motivation	Approx. year(s)
Low foot (LF), also known as NIC	Demonstrate ignition and high gain using a four-shock low-adiabat design with a CH ablator.	2010–2013
High foot (HF)	Using LF targets, trade away any possibility of ignition to obtain a more ablation-front Raleigh-Taylor stable implosion with fewer (three) shocks, with the goal of better simulation-data agreement (i.e., establish a base camp). Obtain velocity and energy (for instance, coast time) scaling. Test for performance cliffs.	2013–2015
Low-foot adiabat shaped	Demonstrate that high-foot stability and the high-foot Au-lined depleted uranium (DU) hohlraum can be used on a four-shock lower adiabat to obtain higher convergence.	2014
High-foot adiabat shaped	Demonstrate that high-foot stability and the high-foot Au-lined DU hohlraum can be used on a three-shock lower adiabat to obtain higher convergence.	2015
High-density carbon (HDC) three-shock high gas fill	Test to determine whether a HDC ablator offers any advantage using an otherwise HF-type design	2014–2015
HDC two-shock vacuum	Test an HDC ablator in a vacuum (VAC) hohlraum with different case-to-capsule ratios. Look for improvements in symmetry control and energy coupling.	2015–2017
Be low gas fill	Test a beryllium ablator implosion in a low-gas-fill (LGF) hohlraum with two different picket tactics.	2015–2017
CH low gas fill	Test a high-foot plastic ablator implosion in a LGF hohlraum with two different capsule scales. First tests using cross-beam energy transfer (CBET) in a LGF hohlraum.	2015–2018
HDC LGF	Leverage the short pulse length of HDC to better utilize a LGF hohlraum and test the limits of symmetry and velocity.	2016–2019
BigFoot	Test unconventional tactic of colliding shocks in the DT fuel, trading off compression for extra stability and minimal pulse length (for improved symmetry control).	2016–2018
Two-shock CH	Test a minimal asymmetry and minimal instability (i.e., 1D) implosion by making the shell thick, slow, high adiabat. Compare the results against simulations (MacLaren <i>et al.</i> , 2018).	2016–2017
Hybrid B–E designs	Increase energy coupling to implosion via capsule scale while maintaining symmetry, high implosion speed, and low coast time. Recognizing the limited predictive capability of hohlraum simulations for symmetry control, use an empirical-based model to guide design. Integrate BigFoot and HDC elements into one design (Hybrid-B), attempt to control CH implosion symmetry in LGF hohlraums using CBET (Hybrid-C), and test Be ablator implosions (Hybrid-D). Efforts converged to HDC ablators with CBET (Hybrid-E).	2018–present
I-raum and Frustrum	Test different hohlraum geometries, literally <i>i</i> -beam cross-section and frustrum shapes, respectively, for managing the symmetry control of large-radius capsules.	2018–present

hohlraum ( $\tau_{\text{cool}}$ ),  $R_{\text{pv}}$  saturates at a minimal value due to hot-spot back pressure, generally of the order of 100–200  $\mu\text{m}$ .

### E. Present status of results

The National Ignition Campaign (NIC) (Lindl and Moses, 2011) focused upon demonstrating ignition and thermonuclear burn in the laboratory based upon a “point design” that was thought to be capable of ignition and burn based upon a decade of work on the Nova and OMEGA facilities. Post-NIC, progress on the laser indirect-drive approach to ICF at the NIF (Moses *et al.*, 2016) has come in steps, as new design strategies address limiting the physics issues identified as the experimental program at the NIF has unfolded; see Table IV. These new design strategies (“base camp”) are then

pushed to their maximum performance limits using the implosion control parameters of velocity, coast time, or adiabat [a measure of DT fuel entropy before stagnation (Haan *et al.*, 2011)] while one tries to manage hydrodynamic instabilities, symmetries, and laser backscatter. Exploring the performance limits of these new designs identifies performance-limiting factors, which inform the next generation of designs, while focused science experiments delve into the details of the performance limiters, and simulations models are updated to capture these factors. Over the past decade of indirect-drive ICF experiments at the NIF, the fusion yields have increased by a factor of  $\sim 1000$  times, recently entering the burning-plasma (Ross *et al.*, 2021; Kritcher *et al.*, 2022a; Zylstra *et al.*, 2022a) and ignition regimes (Abu-Shawareb *et al.*, 2022; Kritcher *et al.*, 2022b; Zylstra *et al.*, 2022b).

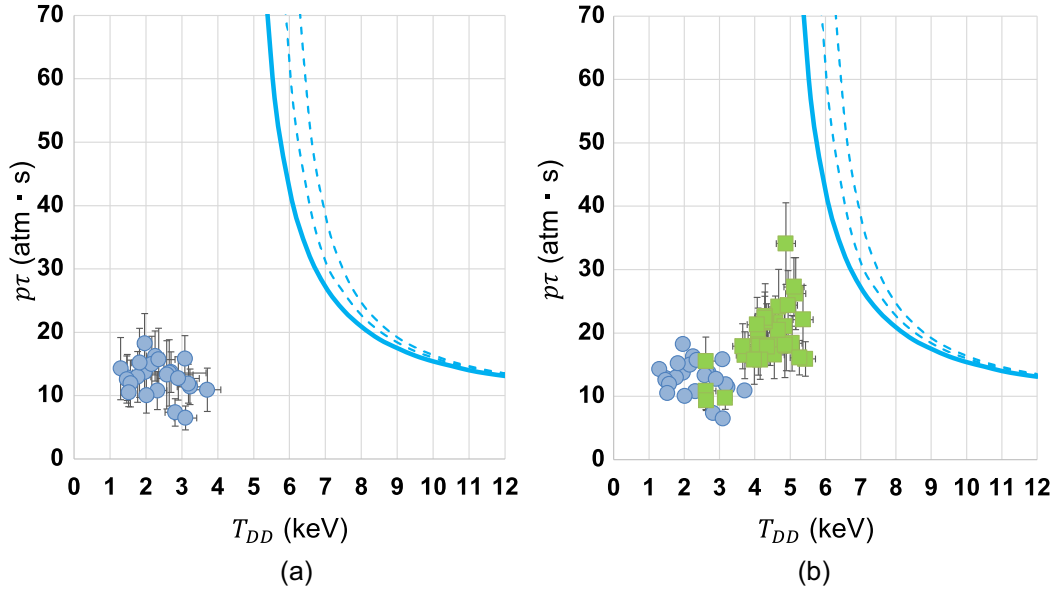


FIG. 14. NIF DT shot data (dots) are plotted in the space of the inferred Lawson parameter and hot-spot (thermal) temperature. The curves denote the ignition boundary estimated from  $p\tau H(T) \geq 1$  and Eq. (21). The dotted and dashed curves show how the ignition boundary moves to higher temperature under different assumptions of mixing of high-Z material into the DT, resulting in enhancement of bremsstrahlung x-ray losses. Solid curves,  $f_B = 1$ ; dotted curves, a 50% increase in bremsstrahlung:  $f_B = 1.5$ ; dashed curves, a 100% increase:  $f_B = 2.0$ . (a) Data from the low-foot series (circles). (b) Data from the high-foot series (squares). In this analysis, the neutron time of flight (NTOF) inferred DD ion temperature  $T_i(\text{DD})$  is used as an estimate of thermal temperature since it is less sensitive to Doppler broadening effects, as previous work (Jarrott *et al.*, 2018) measuring electron temperature ( $T_e$ ) has shown that  $T_e \approx T_i(\text{DD}) \leq T_i(\text{DT})$  for these types of implosions.

The following discussion chronicles the steps that led to these achievements.

### 1. Low-foot design: NIC during 2010–2012

The initial low-foot (LF) design used a high helium gas-fill hohlraum ( $\sim 1 \text{ mg/cm}^3$ ) to hold back the ingress gold hohlraum-wall plasma over the long,  $\sim 20 \text{ ns}$  pulse lengths to produce high gain with a high 1D margin via a low adiabat. These targets were sensitive to a number of failure modes (Lindl *et al.*, 2014), primarily due to the mix at 330 km/s implosion speeds caused by high ablation-front RT instability growth (Ma *et al.*, 2013; Regan *et al.*, 2013), which resulted in hot-spot performance far from what is required for ignition; see Fig. 14(a). In addition to measured  $T$  below  $T_{\text{ign}}$  and fusion yields in the low kilojoule instead of the megajoule range, a key data inference of burn-averaged stagnation pressure using burn-averaged measurements and imaging data, essentially via the formula  $p \sim \sqrt{T^2 Y / \langle \sigma v \rangle V \tau}$ , was developed during this period (Cerjan, Springer, and Sepke, 2013; Springer *et al.*, 2013) that gave pressures  $\sim 1/3$  of what was understood to be necessary for ignition.

However, the LF design was used in commissioning platforms (Landen *et al.*, 2011) at the NIF for (1) the laser system (Moses *et al.*, 2016), (2) shock timing (Robey *et al.*, 2012a, 2012b), (3) early-time symmetry (Dewald *et al.*, 2011), (4) implosion velocity (Hicks *et al.*, 2010), (5) in-flight symmetry (Rygg *et al.*, 2014; Town *et al.*, 2014), (6) hot-spot symmetry (Kyrala *et al.*, 2010, 2011), and (7) cryogenic layered implosions (Glenzer *et al.*, 2012). The LF campaign also demonstrated (1) precision pulse

shaping and four staged shocks leading to high fuel areal densities, for coast times  $< 1 \text{ ns}$  [as measured using the neutron DSR (the ratio of 10–12 MeV neutrons to 13–15 MeV neutrons)  $\sim 6\%$ ] (MacKinnon *et al.*, 2012); (2) wavelength separation ( $\Delta\lambda$ ) between the inner and outer laser cones was an effective means of controlling  $P2$  symmetry (Michel *et al.*, 2009; Glenzer *et al.*, 2010) and, between the  $23^\circ$  and  $30^\circ$  cones, to control  $M4$  symmetry in a high-gas-fill (HGF) hohlraum (Michel *et al.*, 2011; Moody *et al.*, 2012); and (3) gold-lined depleted uranium (DU) hohlraums effectively gave a 7% higher x-ray drive (Callahan *et al.*, 2012) than pure Au hohlraums. However, regardless of the hohlraum material, these high-gas-fill hohlraum designs had problems with strong time-dependent asymmetries, as well as significant SRS and missing energy (compared to radiation hydrodynamics simulations) (Kline *et al.*, 2013). This motivated the development of the view-factor platform (MacLaren *et al.*, 2014) that confirmed the apparent drive deficit and inaccuracy in simulations of the LEH region of the hohlraum.

It was clear at the end of the NIC that a number of problems existed in both the low-foot implosions themselves (hydrodynamic instability, mixing, low-mode asymmetry, etc.) and the coupling of the hohlraum to the implosions. Most of the observed problems were anticipated before the NIC (Lindl, 1995; Lindl *et al.*, 2004), but what was not expected was the inability to manage these problems with the choices made in the point design of the low-foot implosion, the veracity (or lack thereof) of computer simulations used in the design, and the real level of control over the laser and target engineering. A different strategy

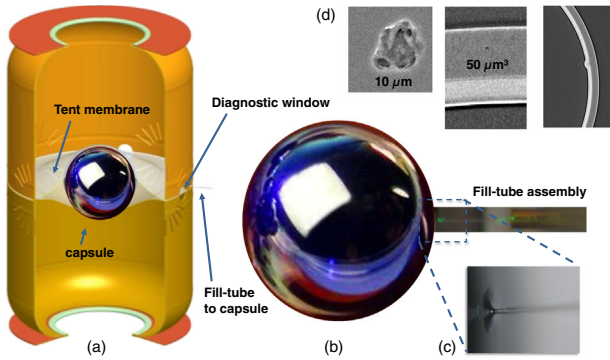


FIG. 15. (a) Schematic indirect-drive target showing basic engineering elements. The tent membrane, which holds the capsule in the center of the hohlraum, is a Formvar material of thickness 15–100 nm. The most typically used tent thickness is 45 nm, which balances fragility with desire to minimize any potential hydrodynamic perturbation. (b) A fill tube through which the capsule is fueled extends out of a hole drilled through the ablator. Fill tubes range in diameter from 2 to 30  $\mu\text{m}$ , depending upon the capsule material and target type. For plastic and beryllium capsules 10  $\mu\text{m}$  diameter fill tubes have been standard, while for HDC capsules 5  $\mu\text{m}$  diameters are standard. (c) The fill tube is epoxied to the capsule, where the two components contact each other and the drill hole around the tube is also grouted with epoxy. (d) Defects typically for HDC capsules are, from left to right, particles (or pits) on the outer surface of the ablator, voids in the through thickness of the ablator, and residue on the inner surface of the capsule. These defects are all potential seeds for inwardly directed hydrodynamic jets of ablator material.

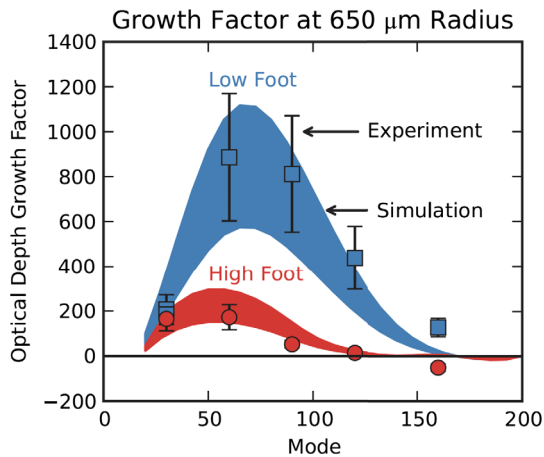


FIG. 16. Observed and simulated growth of an imposed perturbation on the outside surface of the capsule is plotted against the mode number of the perturbation. In this case the capsule has converged from its initial outer radius of 1137 to 650  $\mu\text{m}$ . The perturbation amplitude growth is measured in terms of an increased optical depth variation using a face-on radiography technique. As shown, the predicted instability growth is largely in agreement with the data, except for the highest modes, and the high-foot implosion indeed has much less ART growth than the low-foot implosion across all modes, proving the key assertion about the high-foot tactic. From Peterson, Casey *et al.*, 2015.

was needed, one that addressed the observed problems and then addressed anticipated problems that would later reveal themselves, like peeling away the layers of an onion, and thus the incremental base-camp strategy was born (Hurricane, 2015). In the base-camp strategy, one steps back from directly trying for ignition and instead solves problems in steps; thus, an ignition design was created by evolution over time and, in this case, that took a decade. The first base camp was the high-foot implosion.

## 2. High-foot design: 2013–2015

The high-foot (HF) design (Dittrich *et al.*, 2014), which mitigated ablation-front RT instability, obtained an order-of-magnitude-better fusion yield performance than the low-foot design (Hurricane *et al.*, 2014a, 2014b; Park *et al.*, 2014). As it was a lower-convergence, higher-adiabat design with a higher early-time hohlraum  $T_r$ , the high-foot design was able to resist ablation-front RT (ART) instability by increasing the two key stabilizing terms in Eq. (32), namely,  $L_\rho$  and  $v_a$ ; see Fig. 17 for a simulation demonstration of the improved stability. Better controlling ART instability allowed access to much higher implosion speeds without mixing (Ma *et al.*, 2015) than the low-foot design, and the high-foot experiments showed that the fusion yield rapidly increased with gold-equivalent laser energy ( $Y \sim E_{\text{laser}}^{5.5-7.9}$ ) (Callahan *et al.*, 2015), as is expected under the conditions of increasing  $\alpha$ -particle self-heating. Stability control with increased implosion speed allowed higher hot-spot temperatures, pressures, and Lawson metric; see Fig. 14(b). As the implosion speed was pushed to 390 km/s by thinning the initial ablator thickness, the ART instability growth increased (Clark *et al.*, 2016), leading to increased sensitivity to the tent membrane (see Fig. 15), an engineering feature needed to hold the capsule in the hohlraum that also seeds localized vorticity and undesirable instability during implosion (Nagel *et al.*, 2015; Tommasini

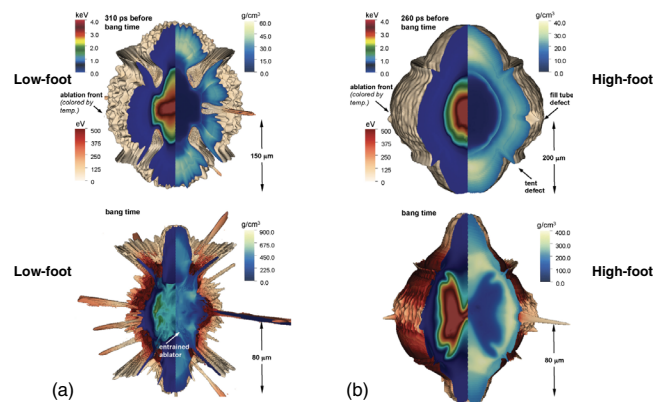


FIG. 17. High resolution 3D simulations of (a) the LF implosion N120405 and (b) the HF implosion N130927 showing the impact of instability, asymmetry, and the tent perturbation. The reduced sensitivity of the HF to ART instability and tent perturbation growth is clear. Both implosions exhibit a mode-2 asymmetry, which manifest itself as a toroidal hot spot in the HF implosion, albeit the degree of hot-spot asymmetry seen in the 3D simulation is exaggerated compared to the data. Adapted from Clark *et al.*, 2016.

High-foot DT repeatability tests	N131219	N140225 (N131219 repeat)	N141106 (N131219 repeat)	N140520	N141016 (N140520 repeat, bundle misfire)	N150121 (N140520 repeat)	N150409 (N140520 repeat)
X-ray emission at 78-degree view, 100x100 microns							
Neutron emission at 315-degree view (red=13-17 MeV, blue=6-12 MeV)							
$E_{\text{laser}}$ (MJ)	1.62	1.57	1.62	1.76	1.69	1.74	1.73
$Y_{\text{total}}$ (kJ)	9.83	9.14	9.11	25.4	10.0	20.4	22.9
$T_{\text{DT}}$ (keV)	$4.91 \pm 0.15$	$4.51 \pm 0.15$	$4.44 \pm 0.13$	$5.54 \pm 0.15$	$4.07 \pm 0.13$	$5.21 \pm 0.11$	$5.5 \pm 0.15$
$T_{\text{DD}}$ (keV)	$4.16 \pm 0.21$	$3.95 \pm 0.17$	$4.04 \pm 0.17$	$4.8 \pm 0.2$	$3.65 \pm 0.17$	$4.55 \pm 0.17$	$4.6 \pm 0.17$
DSR(%)	$3.8 \pm 0.33$	$3.7 \pm 0.2$	$3.82 \pm 0.21$	$4.08 \pm 0.2$	$3.73 \pm 0.15$	$4.02 \pm 0.18$	$4.21 \pm 0.18$
$BT_{\text{x-ray}}$ (ns)	$16.03 \pm 0.02$	$16.28 \pm 0.02$	$16.25 \pm 0.05$	$15.71 \pm 0.02$	$16.17 \pm 0.03$	$15.86 \pm 0.02$	$15.93 \pm 0.02$
$BW_{\text{x-ray}}$ (ps)	$147.49 \pm 21.9$	$112.89 \pm 33.7$	$130.16 \pm 7.18$	$110.93 \pm 25.1$	$156.0 \pm 40.0$	$109.96 \pm 19.6$	$117.16 \pm 8.71$

FIG. 18. Two sets of repeat shots were performed using the 175  $\mu\text{m}$  ablator thickness capsule variant of the high-foot design in high-gas-fill DU hohlraums (Ma *et al.*, 2015; Hurricane, Callahan, and Patel, 2016). Top row: equatorial (i.e., side) view time-integrated x-ray emission at  $> 6$  keV photon energy (Ma *et al.*, 2012). Second row: equatorial view neutron imaging system data (Volegov *et al.*, 2014). Except for one experiment (N141016, where the NIF laser misfired), the experiments exhibit oblate hot-spot symmetry with indications of DT fuel mass accumulation, inferred from the down-scatter neutrons, at the poles of the implosion. Scalar performance metrics are as labeled in the other rows. Fusion yield repeats to within 25%, while most other metrics repeat to better than 10%.

*et al.*, 2015; Ralph *et al.*, 2020), which ultimately limited any further increase in performance. The tent membrane was inferred to perforate the shell for the highest velocity (i.e., lower mass remaining) high-foot implosions (Clark *et al.*, 2016; Hurricane *et al.*, 2016; Springer *et al.*, 2019; Ralph *et al.*, 2020).

Focused experiments to measure capsule symmetry during the implosion and to measure ART growth rates using the hydrodynamic growth radiography platform (Raman *et al.*, 2014; Smalyuk *et al.*, 2014) were introduced at the same time as the high-foot design in order to test the code predictions of ART growth. The simulation models reproduced the measured perturbation growth for the low- and high-foot platforms (see Fig. 16) from modes 30 to 160 (Casey *et al.*, 2014; Smalyuk *et al.*, 2014; Peterson, Casey *et al.*, 2015). During this same period it was recognized that ultraviolet- (UV-) light-induced oxygen uptake in the first few outer microns of the glow discharge polymer and CH ablaters resulted, over time, in significant nonuniformity of ablation, effectively increasing the capsule surface roughness (Baxamusa *et al.*, 2015; Haan *et al.*, 2015), a result that rationalized why low-foot implosions appeared, from simulations, to behave as if the surface roughness were  $\sim 4$  times worse than capsule metrology indicated.

While the high-foot tactic managed hydrodynamic instability of the ablator and reasonable repeatability between like shots was observed, low-mode asymmetries for many high-foot implosions were observed directly in imaging data (see Fig. 18) and asymmetries were also inferred from time-of-flight nuclear spectra data (Spears *et al.*, 2014; Chittenden *et al.*, 2016; Gatu Johnson *et al.*, 2016). Ultimately, the tent membrane and the low-mode asymmetries that grew upon implosion were implicated as the basis for the observed performance-limiting cliff observed in experiments.

Attempts to use longer hohlraums to mitigate the observed  $P4$  asymmetry resulted in more difficulty with  $P2$  symmetry control, as a result of trouble in propagating the inner-beam laser to the waist (Pak *et al.*, 2017). Rugby-shaped hohlraums were also attempted as a tactic for better symmetry control (Leidinger *et al.*, 2016), but experiments did not show any special advantages. Somewhat better hot-spot symmetry control was obtained with gold-lined DU hohlraums (Döppner *et al.*, 2015). This better control enabled the use of longer duration laser pulses needed for a coast-time study.

It was found that lowering coast time in addition to velocity strongly correlated with hot-spot performance (Hurricane *et al.*, 2016) by reducing premature shell decompression (Zylstra *et al.*, 2014), thereby enhancing the stagnation

pressure, which scales as  $p_{\text{hs}} \sim T_r^{7/5} v_{\text{imp}}^3$  (Hurricane *et al.*, 2017b). With a fixed target geometry, a lower coast time is obtained by increasing the duration of late-time laser power, thus delivering additional laser energy to the target. Longer duration laser pulses keep the hohlraum hotter at late times relative to a long coast-time drive, reducing the drop of the late-time ablation pressure [Eq. (38)] and reducing the radius at which the peak velocity  $R_{\text{pv}}$  is obtained (Hurricane *et al.*, 2022). The reduced  $R_{\text{pv}}$  shortens the deceleration distance of the implosion, thus increasing the rate at which kinetic energy is converted into internal energy as the implosion stagnates, which has beneficial effects [Eq. (41)]; see Sec. III.D. The effectiveness of lowering the coast time was experimentally noted across ablator types and implosion designs (Hurricane, 2016), and thus became a principal design goal for most of the subsequent experiments.

### 3. Adiabatic-shaped design: 2014–2015

Adiabatic-shaped designs (Clark *et al.*, 2014; Milovich *et al.*, 2015; Peterson, Berzak Hopkins *et al.*, 2015), in which the laser pulse was tailored to achieve similar resistance to ART instability growth as the high-foot design, but with a lower fuel adiabat to achieve higher compression similar to the low-foot design, were performed in HGF hohlraums. For the four-shock version, reducing the ablation-front instability growth resulted in a 3–10 times increase in neutron yield with no loss of fuel compression (Casey *et al.*, 2015) compared to the low-foot implosion, but lower yield (by half) compared to the most equivalent high-foot implosion. For the three-shock version, reducing the fuel adiabat resulted in a 36% increase in fuel compression, but with similar yield (and other hot-spot metrics) to the corresponding high-foot implosions (Baker *et al.*, 2015; Smalyuk *et al.*, 2015, 2016; Robey *et al.*, 2016) and below that expected from analytic 1D scaling. Low-mode areal density inhomogeneity remained high, confirming that drive asymmetry and tent-induced capsule perforation would need to be mitigated for CH designs.

### 4. Low-gas-fill hohlraum designs: 2016–present

Symmetry control and reduced x-ray coupling because of high levels of inner-cone SRS remained a performance-limiting problem for HGF hohlraum experiments (Kritcher *et al.*, 2016). Reducing the hohlraum gas fill provided a new avenue for symmetry control and coupling. Research started in 2013 on an indirect-drive exploding pusher for neutron diagnostic calibration used hohlraum gas fills that were 50 times less than previous designs. These near-vacuum hohlraums efficiently converted laser power to x rays because of minimal levels of SRS and other LPI (Le Pape *et al.*, 2014; MacKinnon *et al.*, 2014). Using high-density carbon (HDC) ablaters, with density 3 times higher than previous CH ablaters, shorter laser pulses were used that could tolerate more hohlraum-wall motion that occurs with lower hohlraum gas fills. Low levels of backscatter were confirmed in two- and three-shock designs (Berzak Hopkins *et al.*, 2015a) and symmetry control was achieved in small capsules (Berzak Hopkins *et al.*, 2015b; Turnbull *et al.*, 2016), but symmetry was harder to achieve at larger scales (Le Pape *et al.*, 2016) and was difficult to predict, possibly due to kinetic and/or

plasma inner-penetration effects (Berzak Hopkins *et al.*, 2015b; Higginson *et al.*, 2019) that are absent in radiation-hydrodynamic codes such as HYDRA (Marinak *et al.*, 2001).

Mode-2 symmetry predictability and control was improved without the onset of LPI by increasing the hohlraum helium gas-fill density from 0.03 to between 0.3 and 0.6 mg/cm<sup>3</sup> and led to an improvement in stagnation pressure and fusion yield. In particular, a threshold in gas fill for SRS was observed in a series of experiments that varied gas fill, demonstrating a significant reduction in SRS with gas fills below 0.6 mg/cm<sup>3</sup> (Hall *et al.*, 2017). Low-gas-fill hohlraums favor thinner higher-density ablaters (due to the shorter timescale needed for shocks to transit the material, and thus shorter pulse lengths). Three designs were pursued to assess low-gas-fill (LGF) hohlraums: a high-foot CH design (Hinkel *et al.*, 2016; Döppner *et al.*, 2020), a three-shock HDC design (Divol *et al.*, 2017), and the BigFoot design (Baker *et al.*, 2018). The CH design improved symmetry control, reduced LPI, and reduced levels of hot electrons (Hinkel *et al.*, 2016). By further reducing the CH capsule radius and thickness by 10%, more complete symmetry control, as well as record stagnation pressure for plastic ablator implosions, was obtained with CH (Döppner *et al.*, 2020). In general, for LGF designs the discrepancies between simulated and measured radiation production were markedly reduced and, for a fixed laser energy, improved capsule performance was attained compared to HGF hohlraum implosions.

Using a subscale HDC design (0.844 mm inner radius capsule in a 5.75 mm diameter DU hohlraum), the  $P2$  symmetry control over the duration of the laser pulse was demonstrated to be better than  $\pm 5 \mu\text{m}$ . Based on a detailed RKE analysis (Kritcher *et al.*, 2014) for this implosion, it was concluded that intrinsic asymmetry was a minor source of yield degradation (Divol *et al.*, 2017). Scaling up this design by 8% (to a 0.910 mm inner radius capsule in a 6.20 mm diameter hohlraum) resulted in a neutron yield of  $1.88 \times 10^{16} \pm 5 \times 10^{14}$  whose output fusion energy was estimated to be twice the peak kinetic energy of the imploding shell (Le Pape *et al.*, 2018). The HDC design extended the Lawson  $\rho r$  metric [see Fig. 19(a)] with a significant increase in stagnation pressure compared to earlier plastic ablator designs, but burn-averaged temperatures remained limited to the vicinity of the ignition temperature. Performance-limiting x-ray emission features associated with jetting of ablator material into the hot spot coming from hydrodynamics seeded by the fill tube (Pak *et al.*, 2020) (see Fig. 15) were also first clearly identified in the HDC campaign.

The BigFoot (BF) approach traded off high convergence, and therefore areal density, in favor of high implosion velocity, good energy coupling to the hot spot, and reduced hydrodynamic instability growth (Casey *et al.*, 2018). The design pioneered the “cone and quad split” pointing scheme, which smooths the azimuthal intensity variations and reduces the average laser intensity on the hohlraum wall. This design was scaled up by 12% (to a 0.950 mm inner radius capsule in a 6.00 mm diameter hohlraum) and achieved a marginally higher record yield of  $1.95 \times 10^{16} \pm 5 \times 10^{14}$  at an implosion speed of 425 km/s. The performance of the BigFoot design in

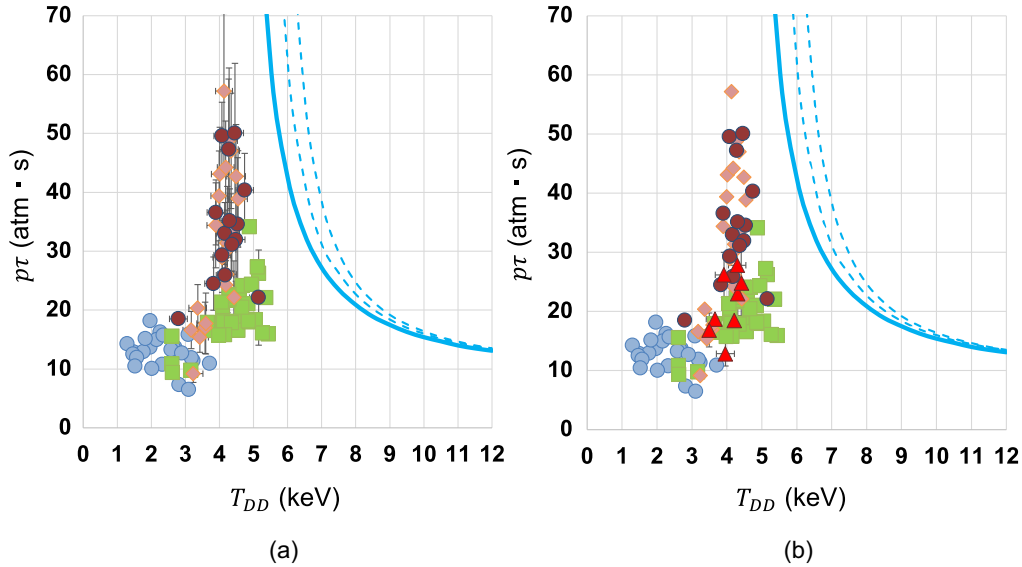


FIG. 19. NIF DT shot data (dots) in the space of the inferred Lawson parameter and the hot-spot thermal temperature. (a) Data from the HDC (diamonds) and BigFoot (dark circles) series of experiments. (b) Data from the Hybrid-E 1100  $\mu\text{m}$  radius capsule series (dark triangles).

Lawson parameter space [see Fig. 19(a)] and the yield closely mirrored that of the contemporary HDC design despite the differences in the designed adiabat ( $\alpha_{if} \sim 4$  for BF versus  $\alpha_{if} \sim 2.5$  for HDC). Attempts to lower the adiabat of BF, to increase convergence, and to further increase the velocity (using a DU hohlraum) showed a decrease in nuclear performance due to suspected ablator-fuel instability during deceleration. In fact, all HDC and BF designs seem to exhibit less convergence for the same adiabat than CH ablator designs and show a lack of compression response to varying  $\alpha_{if}$  (Landen *et al.*, 2021). Understanding the physics origin of this problem is a topic of current research, with the leading (but not only) hypothesis being small-scale hydrodynamic instability of the fuel-ablator interface.

Using the database generated from these and other LGF experiments [such as the two-shock CH design (Hall *et al.*, 2017) and beryllium ablator designs (Zylstra *et al.*, 2018)], a simple underlying pattern for symmetry control was discovered in cylindrical-geometry hohlraums (Callahan *et al.*, 2018). The data from these experiments indicated that the ingress of hohlraum-wall plasma, which was generated by the outer beams at the NIF during the early-time (picket) part of the laser pulse, blocked the inner beams from reaching the hohlraum wall (Ralph *et al.*, 2018). The key connection between design parameters and mode-2 symmetry control was reasoned to be (Callahan *et al.*, 2018)

$$\Delta P_2 \sim -\sqrt{\frac{E_{\text{picket,outer}} t_{\text{laser}} R_{\text{cap}}}{A_{\text{outer}} \rho_{\text{fill}} R_{\text{hohl}} R_{\text{hohl}}}}, \quad (42)$$

where  $E_{\text{picket,outer}}$  is the laser energy in the outer beams during the early-time part of the laser pulse,  $A_{\text{outer}}$  is the surface area the outer laser beams make on the inside of the hohlraum wall,  $t_{\text{laser}}$  is the laser pulse duration,  $R_{\text{hohl}}$  is the initial inner radius of the hohlraum, and  $R_{\text{cap}}$  is the initial outer radius of the

capsule. There are some regimes of hohlraum gas-fill density (such as  $<0.3 \text{ mg/cm}^3$ ) where this simple plasma-ingress picture and Eq. (42) break down (Izumi *et al.*, 2018), and the impact of the LEH on mode-2 symmetry is not fully understood.

In 2017, anticipating that the HDC and BigFoot designs would soon be operating at their limits of performance, the LLNL ICF program developed three new designs (Hybrid-B, Hybrid-C, and Hybrid-D), to be fielded in 2018, that incorporated the understanding and best features of existing designs and capitalized on what was learned about scaling parameters for both neutron yield and hohlraum symmetry control. The principal aspect of the high-yield, big radius implosion design (HYBRID) idea is to increase energy delivery to the hot spot of the implosion since it was noted across the database of NIF experiments that  $Y \sim E_{\text{hs}}^{3.3}$  (Hurricane *et al.*, 2019b). From Eq. (27), we see that  $E_{\text{hs}} = c(\alpha_{if}) m_{\text{shell}} v_{\text{imp}}^2 (1 - f^2)/2$  in the limit of low levels of alpha heating, so the essential elements needed to increase fusion yield were shell mass, implosion velocity, and good low-mode symmetry. Additionally, a higher adiabat directs a larger fraction of the fuel KE into the hot spot [i.e., the  $c(\alpha_{if})$  factor]. Hence, a higher adiabat can help push the hot spot over the tipping point of ignition, with the downside being that the ultimate gain will be reduced because of reduced fuel compression.

It is more favorable to increase  $m_{\text{shell}}$  by increasing shell thickness because of the favorable impact on hydrodynamic stability (see the IFAR discussion in Sec. II.C), but maintaining  $v_{\text{imp}}$  with a thicker shell requires a higher hohlraum  $T_{\text{rad}}$ , necessitating a more efficient hohlraum or more laser energy. Moreover, a thicker shell can complicate symmetry control due to the longer duration laser pulse required to drive it, i.e., Eq. (42). Increasing  $m_{\text{shell}}$  by increasing initial radius, without increasing thickness, absorbs more energy from a given x-ray bath due to the increased capsule surface area, so no additional laser energy or hohlraum efficiency is required.

By increasing the capsule inner and DT fuel radius, controlling implosion symmetry based upon Eq. (42) and CBET if needed while keeping other aspects of the implosion ( $v_{\text{imp}}$ , coast-time, fuel adiabat, hydrostability, etc.) fixed as much as possible (Hurricane *et al.*, 2017a, 2019a, 2019b), it was expected that the hot-spot energy could be increased without lowering the hot-spot pressure. By forcing a fixed coast time (and therefore  $R_{\text{pv}}$ ) despite increased radius, the HYBRID strategy is not equivalent to pure hydrodynamic scaling, which has a less favorable scaling of yield with capsule absorbed energy (Clark *et al.*, 2019).

The Hybrid-B (Hohenberger *et al.*, 2020; Zylstra *et al.*, 2020a) design used a 1.000-mm-inner-radius HDC capsule in a 6.72-mm-diameter gold-lined DU hohlraum, about a 10% increase above the HDC capsule radius used in record-setting shots in 2017, and retained some elements of the HDC and BigFoot pulse shapes. The Hybrid-B design was developed in coordination with a new 2.1 MJ NIF laser capability that materialized only recently in 2022. (In 2018 a 2.1 MJ test shot without a target was performed at the NIF. Unexpected laser optics damage was generated from filamentation instability, so the capability could not be used for ICF experiments.) As a result, the Hybrid-B design was underdriven with the standard NIF energy of 1.8 MJ, but experiments were performed anyway in order to explore how implosion properties changed with capsule scale.

The Hybrid-B experiments were also compromised by unexpected HDC capsule quality issues generated during fabrication; see Fig. 15(d). Nevertheless, the Hybrid-B implosions demonstrated the highest yield for their velocity ( $\sim 360$  km/s) at the time, consistent with expectations of improvement with an increased capsule scale (Hohenberger *et al.*, 2020), which results in an increase in energy delivered to the hot spot that compensates energy losses due to asymmetry and radiation. Building upon earlier work (Kritcher *et al.*, 2018b), the Hybrid-C design (Pickworth *et al.*, 2020), which used CH ablaters that previously struggled with symmetry control in a low-gas-fill hohlraum, tested the efficacy of using small amounts of laser wavelength tuning (for instance,  $\Delta\lambda \sim 1$  Å) to control symmetry by minimizing CBET. The Hybrid-D design, which used Be ablaters, tested the efficacy of using picketless laser pulses to minimize the growth of the outer-beam plasma bubble inside the hohlraum that can occlude the inner-beam propagation.

## 5. Experimental demonstration of burning plasmas and ignition

These initial Hybrid experiments led to the Hybrid-E experimental series, which uses small amounts of wavelength tuning (i.e., CBET) to enable implosions of 1.1 mm inner radius capsules with adequate symmetry, which further increased the energy coupled to the capsule to 270 kJ (inferred). In November 2019 a Hybrid-E experiment attained a yield of  $2 \times 10^{16}$  and a hot-spot energy record of  $\sim 14$  kJ at a modest implosion speed of 360 km/s (Zylstra *et al.*, 2021), albeit these early versions of Hybrid-E occupied the same location in Lawson parameter space as the HDC and BF implosions; see Fig. 19(b). In November 2020, using slightly smaller 1.05 mm inner radius capsules, Hybrid-E achieved a yet higher yield performance of  $3.6 \times 10^{16}$  (thus making it the

first to obtain  $\sim 100$  kJ at an ICF facility) and, along with similarly performing “I-raum” (Robey *et al.*, 2018) experiments (which tested an I-beam cross-section-shaped hohlraum), subsequently entered into the burning-plasma regime (Kritcher *et al.*, 2021, 2022a; Ross *et al.*, 2021; Zylstra *et al.*, 2022a) in winter 2021.

A burning plasma is a fusion plasma where alpha-particle self-heating exceeds the heating from external sources. This definition has existed in the magnetic fusion community for decades but was not commonly considered in ICF until recently (Betti *et al.*, 2015). For an ICF plasma, Eq. (14) implies an energy inequality statement that denotes when a burning-plasma state is achieved. At stagnation, the time rate of the change of the hot-spot volume is  $dV/dt$ , and therefore the heating rate is nearly zero, so time integration of Eq. (14) is needed to define an ICF burning plasma. Mathematically, a statement of a burning plasma appropriate for ICF is (Hurricane *et al.*, 2019a, 2019b; Zylstra *et al.*, 2022a)

$$\int_0^{t_{\text{pf}}} Q_{\alpha} dt > - \int_0^{V_{\text{min}}} \frac{p}{m} dV, \quad (43)$$

where  $t_{\text{pf}}$  is the time of the peak fusion rate and  $V_{\text{min}}$  is the minimum hot-spot volume. Several metrics that represent Eq. (43) exist (Zylstra *et al.*, 2022a), allowing one to test burn-averaged data from implosion experiments. A burning plasma is a physically identifiable threshold just shy of ignition, so knowing that an experiment is in the burning-plasma regime is an indication of that experiment being close to ignition.

Hybrid-E and I-raum burning-plasma experiments finally demonstrated burn-averaged hot-spot temperatures notably above  $T_{\text{ign}}$ , thereby edging the implosions closer to the expected ignition boundary; see Fig. 19(b). After a design modification that allowed access to even shorter coast-time duration than the winter 2021 Hybrid-E experiments (see Fig. 21) in addition to a fortuitous improvement in capsule quality (reducing the number of seeds for hydrodynamic instability), the Lawson ignition criterion was exceeded in a Hybrid-E experiment on August 8, 2021 [see Fig. 20(a)], with  $\sim 220$  kJ of capsule absorbed energy ( $G_{\text{cap}} \sim 6$ ). The ignition conclusion was supported by testing multiple formulations of the Lawson criterion (Abu-Shawareb *et al.*, 2022), examining other data such as the inferred hot-spot power balance and the observed hot-spot volume (Zylstra *et al.*, 2022b), simulation analysis (Kritcher *et al.*, 2022b), and qualitative study of the dramatic jump in burn-averaged temperature and yield observed for the experiments [see Fig. 20(b)], as well as by independent analysis (Wurzel and Hsu, 2022). Further increasing the laser energy and capsule thickness of the design by 8% resulted in the achievement of  $G_{\text{target}} \sim 1.5$  (Lawrence Livermore National Laboratory, 2022). Over the past decade of indirect-drive experiments at the NIF, fusion yields have increased by a factor of more than 1000 times and the central pressures in the implosions have exceeded twice the pressure at the center of the Sun (see Fig. 22), albeit high gains at high  $\rho R$  [see Fig. 2(b)] continue to be a challenge.

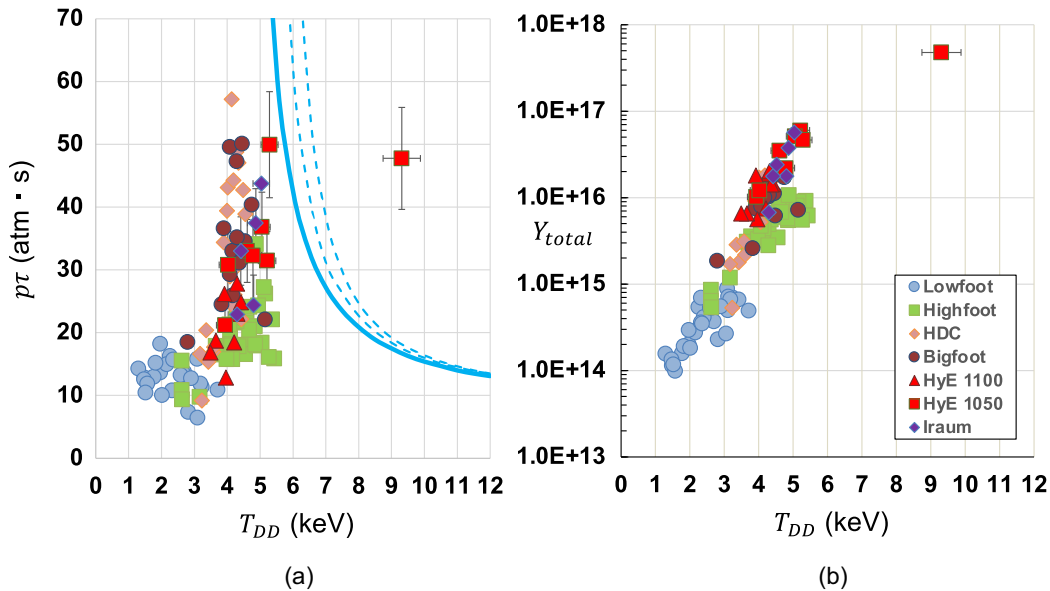


FIG. 20. (a) NIF DT shot data (dots) plotted in the space of an inferred Lawson parameter and hot-spot thermal temperature including the I-raum series (dark diamonds) and Hybrid-E 1050  $\mu\text{m}$  capsule (dark squares) series. (b) Total fusion yield vs temperature across several experimental series with a legend. The significant jump in temperature and yield, setting aside the point associated with experiment N210808 (the rightmost point), is a qualitative indication of ignition reflecting that thermal instability indeed occurred.

## 6. Alternate indirect-drive concepts

Yet to be tested in potentially high-yield DT experiments are a number of novel concepts that attempt to build upon what has been learned or to explore a new part of implosion design parameter space. Namely, designs such as the “hot-thick” one (Young *et al.*, 2020) drive a thick HDC capsule (for improved hydrodynamic stability and better inertial confinement) using a hot hohlraum ( $\sim 320$  eV compared to the more typical  $\sim 300$  eV) with a small case-to-capsule ratio  $CCR = R_{\text{hohl}}/R_{\text{cap}}$ . The hot-thick approach effectively couples more energy to the implosion via increased x-ray drive and greatly reduced coast time. The energy absorbed by the capsule ( $\sim \int T_{\text{rad}}^4 R_{\text{cap}}^2 dt$ ) can be

increased with increased  $T_{\text{rad}}$ , as well as by increasing the capsule surface area  $R_{\text{cap}}^2$ , as is done in designs like the Hybrids, I-raum, and Frustratum (Amendt *et al.*, 2019) (which tests a double-frustum-shaped hohlraum). Another thick-capsule design is the “pushed-single-shell” design (MacLaren *et al.*, 2021), which uses a massive graded-dopant shell to lower the requirements on stagnation pressure and temperature, yet still satisfies Lawson’s ignition criteria via increased inertial confinement (longer  $\tau$ , which from Newton’s law scales as the square root of the shell mass).

Resurrecting an old idea of colliding concentric shell implosions [for instance, the “Apollo” capsules of the late 1970s, as mentioned by (Lindl (1995), albeit the idea predates

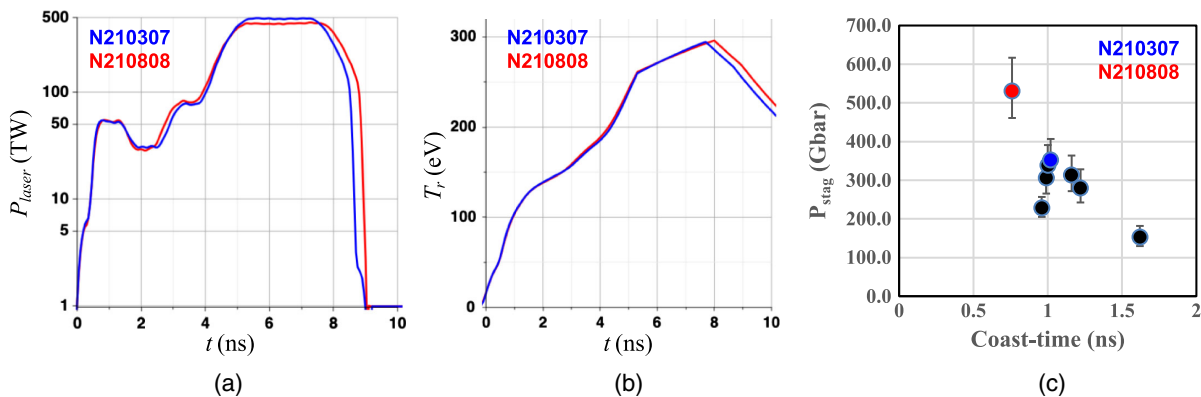


FIG. 21. (a) As-shot laser power vs time for a burning-plasma Hybrid-E experiment (N210307) and the first ignited one (N210808). The peak laser power was reduced and extended in time (conserving total laser energy) for N210808. (b) The model (Callahan *et al.*, 2020) inferred hohlraum radiation temperature vs time for the same two experiments. The  $T_r$  for N210808 was higher than for N210307 due to the reduction in laser entrance hole size and the extension of the late-time laser pulse, despite the reduction in peak power. (c) As seen in previous series of experiments (Fig. 13), the reduction in coast time results in an increase in stagnation pressure. The black points are from other Hybrid-E experiments in the series from late 2020 to mid 2021 and use the same 1050  $\mu\text{m}$  inner radius capsule scale as N210307 and N210808.

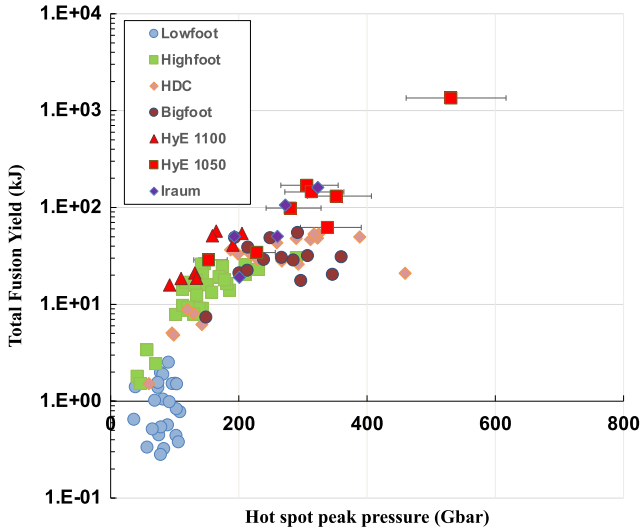


FIG. 22. NIF DT shot data of total measured fusion yield is plotted against data-inferred peak hot-spot pressure with a legend. The pressure at the center of the Sun is estimated to be between 200 and 250 Gbar.

the 1970s], double-shell experiments (Merritt *et al.*, 2019) explore a potential low-to-medium gain design that may be suitable for burning-plasma studies. In a double shell, an outer shell of mass  $m_{\text{outer}}$  is accelerated inward by ablation to a velocity  $v_{\text{outer}}$ . This outer shell then impacts a high- $Z$  inner shell of mass  $m_{\text{inner}}$ , impulsively accelerating the inner shell to a velocity  $v_{\text{inner}}$ . From conservation of energy and momentum, the following velocity and kinetic energy of the inner shell can be obtained:

$$v_{\text{inner}} = \frac{2v_{\text{outer}}}{1 + m_{\text{inner}}/m_{\text{outer}}}, \quad (44)$$

$$\text{KE}_{\text{inner}} = \text{KE}_{\text{outer}} \frac{4m_{\text{inner}}/m_{\text{outer}}}{(1 + m_{\text{inner}}/m_{\text{outer}})^2}, \quad (45)$$

where  $\text{KE}_{\text{inner,outer}} = m_{\text{inner,outer}}v_{\text{inner,outer}}^2/2$ . As seen in Eq. (44), in the limit of  $m_{\text{inner}} \ll m_{\text{outer}}$  a near doubling of the implosion speed can be obtained in a double-shell implosion, but it comes at the cost of kinetic energy [Eq. (45)]; by induction these relations can be applied to multiple shells. When compressed, the high- $Z$  inner shell of a double-shell configuration is designed to be opaque to x rays, essentially stopping bremsstrahlung losses [reducing the  $f_B$  parameter in Eq. (14)], which in principle would allow access to ignition at lower temperature than a standard hot-spot ignition design. Hydrodynamic instability of the inner shell of a double-shell configuration is a major concern because of the shell-shell collision and because there is no ablative stabilization of the inner shell.

## IV. LASER-DRIVEN IMPLOSIONS

### A. A history of direct drive

Direct spherical laser illumination of a DT fuel pellet [laser direct drive (LDD); see Fig. 23] was envisioned in the early



FIG. 23. Schematic of laser-direct-drive ICF. Multiple laser beams symmetrically illuminate a spherical shell containing DT fuel.

days of laser fusion as a means to achieving ignition conditions with moderate laser energy. In the seminal paper of Nuckolls *et al.* (1972), a solid DT sphere was isentropically compressed to high densities and temperatures by a shaped laser pulse with monotonically increasing power to achieve ignition and gain at laser energies as low as a few kilojoules. The theory of homogeneous isentropic compression was later developed by Kidder (1974), who assumed a time-dependent pressure from laser illumination applied on the surface of a DT sphere. As shown by Nuckolls *et al.* (1972) and Kidder (1974), ignition of a solid DT sphere requires extremely high power levels in the late stage of the implosion (Nuckolls estimated levels up to 1 PW) to achieve ignition temperatures and densities in the center. This is problematic for laser-driven implosions because the coupling of the laser energy to the capsule is degraded late in the implosion, when the smaller capsule surface and the enhanced coronal refraction reduce the overall driving force. As shown by Kidder (1976), these power requirements are significantly relaxed (by a factor of  $\sim 1/5$ ) if a hollow shell is used in place of a solid sphere. Since then, the research effort in ICF has focused on implosions of a layer of DT fuel enclosed within a spherical shell of ablator material. Even though one-dimensional hydrodynamic studies of direct-drive implosions indicated the possibility of ignition and energy gain at the kilojoule level of laser energy, major obstacles were found in the physics of laser-plasma interaction and three-dimensional effects.

Initial experiments using longer wavelength lasers [such as  $\text{CO}_2$  with  $\lambda_L = 10.6 \mu\text{m}$  (Kephart, Godwin, and McCall, 1974) and Nd:glass lasers with  $\lambda_L = 1.053 \mu\text{m}$  (Ceglio and Larsen, 1980)] found poor energy coupling to the target and copious amounts of energetic “hot” electrons produced by LPIs. Hot electrons incident on the imploding shell raise the entropy of the shell material in flight (preheat), thereby reducing the final compression. The relevant parameter for the hot-electron energy is the product  $I\lambda_L^2$ , where  $I$  is the laser intensity on target and  $\lambda_L$  is the laser wavelength (Lindman, 1977). This parameter represents the oscillation energy of an electron in the electric field of the light wave. It became clear that, for direct-drive ICF to be a viable fusion scheme, the magnitude of  $I\lambda_L^2$  has to be reduced. This led to the development of Nd:glass lasers frequency tripled to  $0.351 \mu\text{m}$  using the tripling scheme of Craxton (1981). There are multiple

benefits to shorter wavelength lasers: (a) increased laser energy absorption from inverse bremsstrahlung due to higher critical densities (Fabre *et al.*, 1981), (b) lower hot-electron energies due to reduced  $I\lambda_L^2$ , (c) higher thresholds for laser-plasma instabilities (Kruer, 2003), and (d) increased coupling of the laser energy to the target due to the closer proximity of the critical surface and laser absorption region to the ablation front. All current ICF laser implosion facilities use Nd:glass lasers with UV light at 0.351  $\mu\text{m}$ . The Naval Research Laboratory has successfully pursued the development of even shorter wavelength drivers by exploiting the properties of excimer lasers (Obenschain *et al.*, 1996) to generate deep UV light at 0.248  $\mu\text{m}$  with an electron-beam pumped KrF gas (the Nike laser) or 0.193  $\mu\text{m}$  with ArF gas (Wolford *et al.*, 2020).

While hot-electron generation and fuel preheat was greatly reduced with UV laser drivers, there were still crucial open issues pertaining to the interaction of UV light with the target surface and the coronal plasma. When the laser initially interacts with the target surface, short wavelength modulations (speckles) in the laser-beam intensity produce local spatial variations in the ablation pressure, thereby launching a rippled shock wave into the target (Gardner and Bodner, 1981; Ishizaki and Nishihara, 1998; Goncharov, Skupsky *et al.*, 2000). This phenomenon is called laser imprinting, as the rippled shock leaves behind a nonuniform target surface similar to an imprinted image of the laser speckles. Since imploding shells are hydrodynamically unstable to the Rayleigh-Taylor instability, such perturbations grow exponentially at first and then saturate, producing a mixing layer that advances inside the shell at a velocity growing linearly in time (for a constant shell acceleration) (Alon *et al.*, 1995; Dimonte *et al.*, 2004). Reducing laser imprinting became of paramount importance for the viability of LDD. A straightforward reduction in on-target nonuniformities was first accomplished by maximizing the number of overlapping beams  $N_{\text{beam}}$  as the rms standard deviation over the entire speckle spectrum decreases as  $1/\sqrt{N_{\text{beam}}}$  (Pawley *et al.*, 1997). A further improvement was obtained by installing random or distributed phase plates at the end of each beamline to break the spatial coherence of the beam before the focal lenses (Kato *et al.*, 1984; Kessler *et al.*, 1993). Phase plates greatly reduced the low-mode-intensity nonuniformities while enhancing the high frequency modulations. Those high frequency modulations were subsequently suppressed by smoothing from phase-modulated bandwidth obtained from color variations across the beam driven by two electro-optical modulators in orthogonal directions and dispersed by gratings [smoothing by spectral dispersion (SSD) (Skupsky *et al.*, 1989)]. An alternative temporal laser smoothing scheme [induced spatial incoherence (ISI) (Lehmberg and Obenschain, 1983)] applied earlier in the laser chain using broad bandwidth light is currently adopted in KrF lasers and offers the additional benefit of dynamic control of the laser spot profile (zooming). Though limited to a few terahertz, the bandwidth introduced by SSD or ISI also played an important role in mitigating the growth of parametric instabilities coming from the laser-plasma interaction by reducing the light coherence. In particular, low frequency laser-plasma instabilities such as stimulated Brillouin scattering are suppressed by modest

levels of bandwidth (Berger *et al.*, 1999; Moody *et al.*, 2001; Maximov *et al.*, 2004). Instead, higher frequency LPIs such as SRS and two-plasmon decay (TPD) instability (Kruer, 2003) remained a serious threat since their growth time is faster than beam smoothing temporal modulation. In current direct-drive experiments, SRS and TPD instabilities are controlled by limiting the laser intensity on target and using target-based mitigation strategies such as mid-Z doping (such as Si) of the ablator material (typically CD or CH) (Craxton *et al.*, 2015).

Motivated by indirect-drive models of two crossing laser rays (Michel *et al.*, 2009), another degradation mechanism recently identified in direct-drive ICF is CBET, a SBS-mediated transfer of laser energy from incoming light rays to outgoing ones in the coronal plasma (Igumenshchev *et al.*, 2010). CBET reduces the laser energy absorption and lowers the ablation pressure. Most of the issues arising from laser-plasma instabilities can be fully overcome by rapidly and randomly varying the laser speckle patterns through the proposed spike trains of uneven duration and delay pulse scheme (Afeyan and Hüller, 2013) or with the new-generation lasers currently under development (Campbell *et al.*, 2021), promising 10 times higher bandwidth than current lasers and expected to suppress both low and high frequency LPIs (Follett *et al.*, 2019; Bates *et al.*, 2020).

Multibeam UV lasers with enhanced smoothing have been the standard drivers for ICF research since the 1980s, with direct-drive lasers such as OMEGA and Nike featuring the highest bandwidth (a few terahertz) to minimize laser-plasma instabilities and laser imprinting. Since the 1990s, direct-drive experiments have mostly been carried out at the University of Rochester Laboratory for Laser Energetics, home of the OMEGA laser, at the Osaka University Institute for Laser Engineering, home of the Gekko XII laser, and at the Naval Research Laboratory, home of the Nike laser. Recently direct-drive LPI and imprinting experiments have also been fielded at the NIF. Other smaller laser facilities have also greatly contributed to the exploration of specific aspects of direct-drive physics. Cryogenic DT implosions on the OMEGA 60 laser have been fielded since 2008 using thin plastic shells of about 1 mm in diameter and DT ice layers of several tens of microns thickness. These targets were imploded by shaped laser pulses of a few nanoseconds with energies of 20–30 kJ. The fusion yield of OMEGA DT-layered implosions has steadily increased over the years, starting with  $10^{11}$  neutrons in the early DT implosions of  $\sim 80$   $\mu\text{m}$  thick ice to  $10^{14}$  neutrons of the most recent implosions from targets with thinner ice layers of  $\sim 40$   $\mu\text{m}$  (Gopaldaswamy *et al.*, 2019). When hydrodynamically scaled to NIF energies of symmetric illumination, the best performing OMEGA implosions are projected to produce over 0.5 MJ of fusion yield, but they still fall short of achieving ignition conditions at 2 MJ of laser energy (Gopaldaswamy *et al.*, 2019).

In addition to integrated implosion experiments at OMEGA, many crucial aspects of direct-drive physics are being investigated through dedicated experiments ranging from laser-plasma interactions in the coronal plasma to hydrodynamic instabilities of accelerated targets, from microphysics of extreme pressure states of matter to kinetic effects

and magnetic fields in the compressed core of implosions. While OMEGA experiments can address and resolve many issues related to the physics of direct drive, aspects of implosion physics related to laser-plasma interactions are strongly affected by the scale length of the plasma and need to be studied on megajoule-class lasers capable of imploding larger scale capsules and generating larger scale plasmas. This is the goal of the current direct-drive effort at the NIF, with its main objectives being the study of the generation and transport of hot electrons and the laser-to-capsule energy coupling at ignition scale.

To adapt the existing asymmetric polar-beam configuration of the NIF laser, direct-drive implosions are designed with optimized pointing to minimize the low-mode nonuniformities from the NIF illumination geometry. Polar direct drive (PDD) (Skupsky *et al.*, 2004) requires different pulse shapes and laser intensities for beams with different angles of incidence on target. This leads to lower collisional absorption and cross-beam energy transfer, thus making PDD more challenging than symmetric direct drive (Craxton *et al.*, 2015). Wavelength detuning between different laser beams has been successfully implemented in PDD implosions at the NIF to mitigate CBET and augment the ablation pressure (Marozas *et al.*, 2018b). Furthermore, flat foil NIF experiments using Si layers demonstrated a significant reduction in hot electrons produced by SRS (Rosenberg *et al.*, 2018b). Such laser- and target-based solutions are examples of the multifaceted effort to advance direct-drive ICF at the NIF.

Advanced laser fusion schemes such as shock ignition (Betti *et al.*, 2007; Perkins *et al.*, 2009; Atzeni *et al.*, 2014; Batani *et al.*, 2014) and fast ignition (Tabak *et al.*, 1994; Atzeni, 1999; Kodamai *et al.*, 2002; Azechi *et al.*, 2013) also use direct laser illumination. Shock and fast ignition are considered two-step schemes because they decouple the fuel assembly from ignition using external means such as a laser-driven strong shock or an energetic particle beam to ignite the compressed fuel. These promising schemes have two potential advantages over conventional direct drive: higher gains and lower hydrodynamic stability requirements. Since shock ignition is pursued mostly in Europe and fast ignition is pursued mostly in Asia, these fusion schemes are not included in this review of the U.S. ICF effort. A detailed review of laser direct drive including shock and fast ignition was given by Craxton *et al.* (2015).

## B. Key differences between direct- and indirect-drive ICF

When compared to indirect drive, direct laser illumination leads to greater coupling of the laser energy to the capsule by avoiding the inefficient intermediate step of converting laser light into blackbody radiation and reducing the laser energy absorbed by the capsule (about 10% of the laser energy for typical indirect-drive targets). On the other hand, direct-drive targets absorb about 70% of the laser energy. The laser energy is absorbed via inverse bremsstrahlung in the plasma below the critical density. The critical density surface is the location where the laser frequency equals the plasma frequency. Light waves can propagate in plasmas, but not past the critical density in a monotonically increasing density profile.

For typical low- $Z$  ablaters (CH, CD and DT ice) used in direct-drive targets, the dominant mechanism of energy transport from the laser absorption region to the outer shell surface is electronic heat conduction. The region between the critical surface and the ablation front is called the conduction zone, where the low- $Z$  ablated plasma is close to full ionization and its properties are similar to an ideal plasma, with the heat conductivity given by Spitzer's formula ( $\kappa_{Sp} \sim T^{5/2}$ ). The plasma with a density below the critical density expands isothermally and is referred to as the plasma corona. The coronal plasma is where all the laser-plasma interactions occur and where all the laser-plasma instabilities develop. Figure 24 illustrates the schematics of the density profile in a laser accelerated target with the different plasma regions.

The ablation pressure on a laser illuminated surface can be estimated using a simple planar ablative flow model, assuming that laser light with intensity  $I$  is absorbed near the critical surface and that heat is conducted to the ablation front through an ideal fully ionized plasma. The ablation pressure depends mostly on the laser intensity and the laser wavelength (Manheimer, Colombant, and Gardner, 1982), leading to

$$p_{abl,D} = \frac{m_p^{1/3}}{2^{1/3}} n_{cr}^{1/3} \left(\frac{A}{Z}\right)^{1/3} (I_L^{abs})^{2/3}, \quad (46)$$

where  $m_p$  is the proton mass,  $A$  is the mass number,  $Z$  is the atomic number,  $n_{cr} \simeq 1.1 \times 10^{21} / \lambda_L^2 \text{ cm}^{-3}$  is the critical density,  $\lambda_L$  is the laser wavelength in microns, and  $I_{abs}$  is the absorbed laser intensity. Using parameter values typical of current direct-drive experiments, Eq. (46) can be rewritten as

$$p_{abl,D}(\text{Mb}) \simeq 10^2 \left(\frac{0.35}{\lambda_L^{\mu\text{m}}}\right)^{2/3} \left(\frac{A}{2.5Z}\right)^{1/3} (I_L^{15})^{2/3}, \quad (47)$$

where the absorbed intensity is in units of  $10^{15} \text{ W/cm}^2$  and the ablation pressure is in megabars. This shows that current UV lasers with 351 nm light can produce  $\sim 100 \text{ Mb}$  pressure

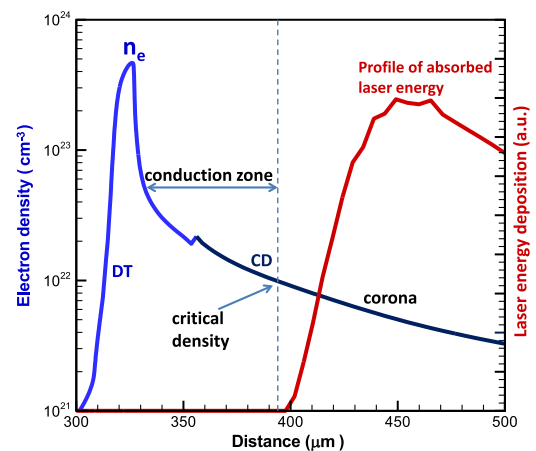


FIG. 24. Typical electron density profile (blue line for DT and gray line for CD) for a direct-drive target. The conduction zone separates the ablation front from the critical surface. The region beyond the critical surface is the coronal plasma. Laser energy deposition (red line) occurs in the CD plasma.

at intensities of  $10^{15}$  W/cm<sup>2</sup>, which is similar to the ablation pressure from x rays in indirect drive for radiation temperatures  $T_{\text{rad}} \approx 300$  eV.

While the ablation pressure is similar, the mass ablation rate is larger for indirect drive due to the deeper penetration of x rays closer to the ablation front. For direct laser illumination, the specific mass ablation rate can be derived from the planar ablative flow model, leading to

$$\dot{m}_a (\text{g/cm}^2 \text{ s}) \approx 2 \times 10^6 \left( \frac{0.35}{\lambda_L^{\text{nm}}} \right)^{4/3} \left( \frac{A}{2.5Z} \right)^{2/3} (I_L^{15})^{1/3}, \quad (48)$$

which is about 5 times less than for indirect drive.

The fraction of ablated mass determines the conversion of the absorbed energy by the capsule to inward kinetic energy of the shell. This can be shown using a simple rocket model (Lindl, 1995; Nora *et al.*, 2014) of the imploding shell leading to

$$\eta_H \equiv \frac{E_{\text{kin}}}{E_{\text{abs}}} = \frac{1}{4} \frac{R_M (\ln R_M)^2}{1 - R_M}, \quad (49)$$

where  $R_M = M_f/M_0$  is the ratio of the final to the initial ablator mass. The maximum hydrodynamic efficiency  $\eta_H \approx 0.16$  occurs at  $R_M \approx 0.2$ , with about 80% of the initial shell mass ablated, which is typical of indirect-drive targets. For direct-drive targets, the ablated mass is about 50% of the initial mass and the hydrodynamic efficiency is only about 9%. However, because of the larger laser absorption fraction (60%–70% for direct drive versus 10% for indirect drive) the overall conversion of laser energy into kinetic energy for direct drive is about 6%, while it is for about 1.5% for indirect drive.

Because of the lower ablation rate, direct-drive targets use a relatively thin ablator that is about 6 times thinner than indirect-drive targets (for the same ablator material). Figure 25 shows a typical DT-layered target used on the OMEGA laser. OMEGA targets use 860–1000  $\mu\text{m}$  outer diameter shells with a 7 to 8  $\mu\text{m}$  thick CD plastic shell and DT ice layers of 40–50  $\mu\text{m}$  thickness. A typical laser pulse is shown in Fig. 25(b). It consists of four parts: (a) an initial spike (or multiple spikes) in the laser power called the picket, (b) a flat pulse called the foot, (c) the power ramp to full power, and (d) a slow varying pulse at peak power called the main drive. The initial picket pulse launches a decaying shock into the target. The foot launches the second

shock. The ramp adiabatically compresses the capsule thickness, and the main drive then accelerates the shell inward to its peak implosion velocity.

The thin plastic shell is quickly ablated when the laser intensity reaches its peak value at the beginning of the main drive, and ablation takes place in the DT fuel that becomes the main ablator material. Because of the highest value of  $Z/A$ , tritium and deuterium-tritium mixtures are the best ablator materials for direct drive, with the highest ablation pressure and ablation rate, as shown by Eqs. (46) and (47). The downside of DT ablators is the low laser energy absorption occurring in DT due to low  $Z$ . To optimize laser absorption, direct-drive targets at OMEGA are designed with a CD layer thick enough to sustain a CD plasma in the underdense corona up to one-quarter critical density through the entire laser pulse. To optimize the ablation pressure, the CD layer is thin enough to be ablated when the main drive starts, so DT becomes the main ablator. Because of the higher  $Z$ , the presence of carbon in the absorption region of the coronal plasma enhances collisional absorption of the laser energy and heat flux toward the ablation front. Having DT as the ablator during the main drive enhances the ablation pressure, the ablation rate, the ablation velocity, and the hydrodynamic efficiency (Goncharov *et al.*, 2014). Optimized OMEGA implosions use 860–1000  $\mu\text{m}$  outer diameter capsules with a CD ablator thickness of 7.5–8.5  $\mu\text{m}$  and an ice thickness of 40–50  $\mu\text{m}$ .

Differences in ablation rate and laser energy coupling to the capsules between direct- and indirect-drive targets have profound implications for the hydrodynamic stability properties, fusion yield, and energy required for ignition. In addition to the previously mentioned hydrodynamic properties, direct- and indirect-drive targets differ with respect to LPI related issues such as hot-electron preheat and cross-beam energy transfer. A detailed description of the hydrodynamic stability and LPI properties of direct-drive targets is presented in Sec. IV.B.3.

### 1. Direct-drive scaling advantages

Because of fourfold higher energy coupling for direct drive versus indirect drive, the pressure requirements for ignition are significantly relaxed. This can be shown by starting with the Lawson ignition criterion

$$\chi \equiv P_{\text{ign}} \tau / S_f \approx 1, \quad (50)$$

where  $S_f = 24T^2 / \langle \sigma v \rangle E_\alpha$  and  $P_{\text{ign}}$  is the pressure required for ignition; see Sec. II.A. Assuming that the onset of ignition occurs at temperatures of about 5 to 6 keV, where the fusion reactivity scales as  $\langle \sigma v \rangle \sim T^3$ , leads to an ignition threshold proportional to the triple product  $\chi \sim \tau T$  (Betti *et al.*, 2010). Since the hot-spot temperature scales approximately linearly with the implosion velocity (Zhou and Betti, 2007) and the pressure confinement time scales with the compressed core radius and the shell implosion velocity ( $\tau \sim R_{\text{hs}} / v_{\text{imp}}$ ), the pressure required for ignition scales inversely proportionally to the core radius ( $P_{\text{ign}} \sim 1/R_{\text{hs}}$ ). Assuming that the hot-spot internal energy  $E_{\text{hs}} \approx (3/2) P_{\text{hs}} V_{\text{hs}}$  is approximately proportional to the shell kinetic energy  $E_{\text{hs}} \sim E_{\text{kin}}$ , the hot-spot radius

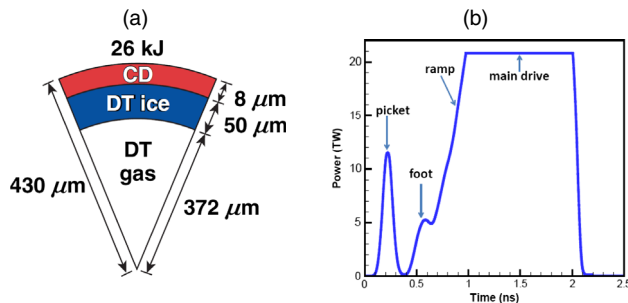


FIG. 25. Typical (a) OMEGA DT-layered target and (b) laser pulse shape. The laser pulse shape is divided into four parts: the picket, the foot, the ramp, and the main drive.

can be written as  $R_{\text{hs}} \sim (E_{\text{kin}}/P_{\text{hs}})^{1/3}$  and the pressure required for ignition is found to scale as (see also Sec. I.B.2)

$$P_{\text{ign}} \sim \sqrt{\frac{1}{E_{\text{kin}}}}. \quad (51)$$

Therefore, for the same laser energy and an about 4 times greater conversion to kinetic energy, direct-drive targets require about half the core pressure of indirect-drive targets to achieve the ignition conditions. Lower pressure requirements translate into lower convergence requirements for the same implosion velocity. Current direct-drive ignition targets are designed for moderate convergence ratios  $C_R \equiv R_0/R_{\text{hs}} \sim 23\text{--}25$  and relatively high in-flight adiabats  $\alpha_F \simeq 3$  to 4 when compared to the more severe indirect-drive requirements of  $C_R \simeq 35\text{--}40$  and  $\alpha_F \simeq 1$  to 2. As mentioned in Sec. IV.B.2, the higher adiabat in direct drive is also a requirement to preserve good hydrodynamic stability, and its effects on the core pressure are consistent with the ignition requirements in Eq. (65). This is shown using the familiar scaling of the pressure (Kemp, Meyer-ter-Vehn, and Atzeni, 2001; Basko and Meyer-ter-Vehn, 2002; Zhou and Betti, 2007; Goncharov *et al.*, 2014) with the Mach number that leads to

$$P_{\text{hs}} \sim p_{\text{abl},D} \text{Mach}^3 \sim p_{\text{abl},D}^{2/5} \frac{v_{\text{imp}}^3}{\alpha_F^{9/10}}, \quad (52)$$

which indicates that, for the same implosion velocity and ablation pressure, the hot-spot pressure in direct-drive implosions is about half of the indirect-drive pressure due to the higher adiabat. Therefore, one must notice that, with respect to achieving the ignition conditions, the direct-drive advantage in energy coupling over indirect drive is balanced by the higher adiabats required to improve the hydrodynamic stability properties in direct-drive implosions.

Unless improvements are made to the uniformity of direct-drive implosions to enable carrying out lower-adiabat implosions ( $\alpha_F \sim 1$  to 2), the larger energy coupling in direct drive is not expected to bring direct-drive implosions closer to ignition than indirect-drive implosions. However, the larger direct-drive targets are expected to achieve significantly higher yields than indirect-drive targets for the same implosion velocity and for the same proximity to ignition as determined by the Lawson parameter.

In the absence of alpha heating, the scaling of the yield with the coupled energy, adiabat, and implosion velocity is  $Y \sim v_{\text{imp}}^4 E_{\text{kin}}^{1.4}/\alpha_F^{0.8}$  (Betti *et al.*, 2010). Therefore, for the same implosion velocity, Lawson parameter, and yield amplification from alpha heating, direct-drive implosions with 4 times the kinetic energy and 2 times the adiabat of indirect drive lead to about 4 times higher fusion yields. In ignited capsules, the fusion yield scales with the DT mass and the burnup fraction, and it will again be larger by about 4 times in direct-drive targets due to the 4 times larger fuel mass than in indirect drive (for the same burnup fraction).

## 2. Hydrodynamic instabilities in direct-drive implosions

Hydrodynamic instabilities develop during the shock-transit phase, the acceleration phase, and the deceleration phase of both direct- and indirect-drive implosions. The Rayleigh-Taylor instability (Rayleigh, 1883; Atzeni and Meyer-ter-Vehn, 2004) is the most deleterious of the hydrodynamic instabilities because it undergoes exponential growth during the linear phase. In the classical description of two superimposed fluids in a gravitational field with the heavy fluid on top and the light fluid at the bottom (Rayleigh, 1883), a single RT Fourier mode exhibits a bubble of light fluid rising into a heavy one, and a “spike” of heavy fluid falling through the light one. RT bubbles are of particular interest during the acceleration phase because they penetrate into the shell while in flight, thus compromising the integrity of the spherical piston. Instead, RT spikes are of interest during the deceleration phase when cold RT spikes from the dense shell penetrate into the hot spot, thereby reducing the temperature and preventing the onset of ignition (Kishony and Shvarts, 2001; Bose *et al.*, 2015).

The ablation front in low-Z laser irradiated targets typical of direct drive exhibits a sharp density profile with a characteristic thickness  $L_0$  set by the thermal conductivity of the cold shell (Kull, 1989; Sanz, 1994),

$$L_0 = \frac{2}{5} \frac{m_i \kappa(T_{\text{sh}})}{\dot{m}_a (1 + Z)}, \quad (53)$$

where  $m_i$  is the ion mass and  $\kappa(T_{\text{sh}})$  is Spitzer thermal conductivity evaluated at the temperature of the ablation front just inside the cold shell ( $T_{\text{sh}}$  is the cold shell temperature). Soft x rays from the ablated plasma smooth out the density profiles, but their effect is small, especially when the ablation front is in DT. The minimum density gradient scale length is  $L_m = (\nu + 1)^{\nu+1}/\nu^\nu L_0$ , where  $\nu = 5/2$  is the temperature power index in Spitzer heat conductivity. For typical direct-drive targets ( $L_0 \simeq 0.07\text{--}0.1 \mu\text{m}$ ), the ablation velocity is  $\sim 5$  to  $6 \mu\text{m/ns}$  and the acceleration  $g \simeq 200 \mu\text{m/ns}^2$ . Early work on the effect of mass ablation on the growth of the RT instability used heuristic closure equations to include the effect of ablation, indicating that ablation is stabilizing but incorrectly capturing the magnitude of the effect (Bodner, 1974; Kull, 1986; Mikaelian, 1992). Fitting the numerical solutions of the full set of linearized equations of motion (Takabe *et al.*, 1985) led to an approximation of the growth rate with the simple formula

$$\gamma \simeq \alpha \sqrt{kg} - \beta kv_a, \quad (54)$$

with  $\alpha \simeq 0.9$  and  $\beta \simeq 3$  for typical direct-drive conditions. Equation (54) was later generalized to different ablator materials and different plasma conditions through explicit dependencies of the coefficients  $\alpha$  and  $\beta$  on the power index for thermal conductivity  $\nu$  and Froude number Fr (Betti *et al.*, 1998). The Froude number ( $\text{Fr} = v_a^2/gL_0$ ) determines the type of RT unstable modes. X-ray radiography experiments at OMEGA measured the growth of optical depth modulation in laser accelerated flat foils (Knauer *et al.*, 2000) and found good agreement for the RT growth rates with 2D

radiation-hydrodynamic simulations and with the theoretical growth rates in Eq. (54). The first analytic self-consistent derivations of the ablative RT growth rate appeared in the literature in the mid 1990s. Since  $Fr > 1$  for typical ablation fronts in DT, the unstable modes have an angular and radial structure much wider than the thickness of the ablation front, and the cutoff in the spectrum from ablative stabilization occurs for  $k_{\text{cut}}L_0 < 1/Fr^{\nu/(\nu-1)} < 1$  (Bychkov, Golberg, and Liberman, 1994; Sanz, 1994; Betti *et al.*, 1995; Goncharov *et al.*, 1996). For wave numbers above the cutoff, the instability is fully suppressed. There are several stabilizing mechanisms at play in the RT growth when  $Fr > 1$ . The self-consistent derivation of the ablative RT growth rate for direct-drive targets (Sanz, 1994; Goncharov *et al.*, 1996; Piriz, Sanz, and Ibanez, 1997; Betti *et al.*, 1998) led to

$$\gamma \simeq \sqrt{A_T k g - A_T^2 k^2 v_a^2 / r_\rho} - (1 + A_T) k v_a, \quad (55)$$

where  $A_T = (1 - r_\rho)/(1 + r_\rho)$  is the Atwood number at the ablation front and  $r_\rho \simeq (2/\nu)^{1/\nu} (kL_0)^{1/\nu} \ll 1$  is the ratio between the density in the conduction zone at a distance of  $\sim 1/2k$  from the ablation front and the peak density of the shell. As shown in Eq. (55), the instability is driven by the classical RT term  $A_T k g$ , while the ablative stabilization enters through two terms inside and outside the square root. The stabilizing term proportional to  $k^2 v_a^2 / r_\rho$  is the dynamic pressure representing the restoring force from the enhanced “rocket effect” on the RT spikes when one moves toward the laser absorption region (Sanz, 1996). The term proportional to  $k v_a$  represents the fire-polishing effect from enhanced ablation of the spikes versus the bubbles and also the effect of vorticity convection away from the ablation front. The normalized growth rates of the ablative RT instability from Eq. (55) for different values of the Froude number are shown in Fig. 26. Note that higher values of  $Fr$  lead to greater stabilization and smaller cutoff wave numbers.

With respect to indirect drive, direct-drive targets exhibit lower ablation rates, leading to lower ablation velocities ( $v_a = \dot{m}_a / \rho_{\text{sh}}$ , where  $\rho_{\text{sh}}$  is the in-flight shell density) and therefore higher growth of the Rayleigh-Taylor instability at the ablation front. Since the in-flight density of DT  $\rho_{\text{sh}}$  depends on the adiabat through the relation

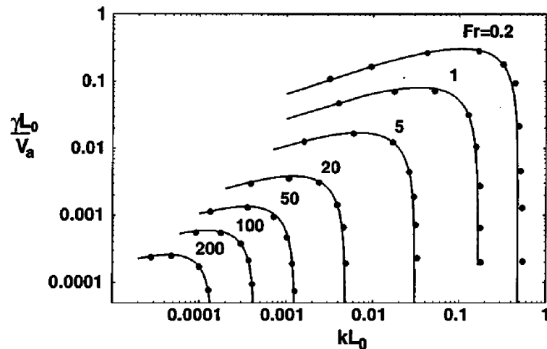


FIG. 26. Normalized linear growth rates of the ablative RTI vs the normalized wave number for different Froude numbers. From Goncharov *et al.*, 1996.

$\rho_{\text{abl},D}(\text{Mb}) \simeq 2.2\alpha_F[\rho_{\text{sh}}(\text{g/cm}^3)^{5/3}]$ , where  $\alpha = 1$  implies a plasma in its Fermi degenerate state, the ablation velocity can be approximated using Eqs. (46) and (47) as

$$v_a(\mu\text{m/ns}) \simeq 5 \left(\frac{\alpha_F}{4}\right)^{3/5} \left(\frac{0.35}{\lambda_L^{\mu\text{m}}}\right)^{14/15} \left(\frac{A}{2.5Z}\right)^{7/15} \left(\frac{1}{I_L^{15}}\right)^{1/15}. \quad (56)$$

Therefore, direct-drive targets need to be driven on an adiabat higher than indirect-drive targets to make up for the lower ablation rate and to maintain acceptable levels of ablative stabilization and RT growth mitigation.

In addition to reducing the linear growth rates, mass ablation affects the RT growth in the nonlinear phase. In the linear phase, a single Fourier mode grows exponentially until its amplitude reaches about  $0.1\lambda$ . After that, the RT bubble advances at a constant velocity denoted as the terminal bubble velocity. As shown by Yan *et al.* (2016), the terminal velocity depends on the buoyancy-drag balance and the fluid vorticity inside the bubble

$$U_b \approx \sqrt{\frac{g(1 - r_\rho)}{C_D k} + r_\rho \frac{\Omega^2}{4k^2}}, \quad (57)$$

where  $C_D = 3$  in two dimensions and  $C_D = 1$  in three dimensions and  $\Omega$  is the vorticity. In ideal fluids without external sources of vorticity, the potential flow description is valid and vorticity is generated only by the RT instability and localized at the interface between the two fluids. In this case  $\Omega = 0$  everywhere outside the interface, including inside the bubble, and Eq. (57) with  $\Omega = 0$  reduces to the classical terminal velocity of Layzer (1955), Hecht, Alon, and Shvarts (1994), and Goncharov (2002). However, in the presence of mass ablation the interfacial vorticity is convected by the ablative flow into the ablated plasma that fills the bubble, thereby accumulating vorticity inside the bubble (Fig. 27). In the ablative RT, the vorticity scales with the ablation velocity

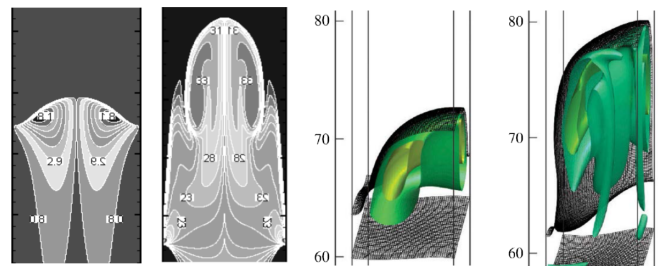


FIG. 27. Contour plots of ablation-induced vorticity inside the bubble of single-mode simulations of the ablative RTI. Left panels: snapshots at 1 and 2.25 ns from 2D simulations of a velocity perturbation with  $\lambda = 10 \mu\text{m}$  wavelength and  $\tilde{v} = 1 \mu\text{m/ns}$  in an accelerated planar target with  $g \simeq 110 \mu\text{m/ns}^2$  and  $v_a \simeq 3.5 \mu\text{m/ns}$  from 2D simulations. From Betti and Sanz, 2006. Right panels: similar snapshots from 3D simulations (Yan *et al.*, 2016). There is no color scale, but the outer (inner) surface of the top color plot corresponds to vorticity values 12.5/ns (19/ns), and the outer (inner) surface of the bottom color plot corresponds to vorticity values 25/ns (40/ns).

as  $\Omega \sim 2kv_a/r_\rho$  leading to a terminal velocity, Eq. (57), enhanced by ablation. The nonlinear single-mode theory of the ablative RT instability given by Sanz *et al.* (2002) described all modifications due to ablation except for the terminal bubble velocity augmentation.

Of particular importance to the acceleration phase is the penetration of the RT bubble front into the imploding shell. Unless dominated by a single mode, the seeds of the RT instability have a broad spectrum. In direct drive, a high-mode broad nonuniformity spectrum comes from laser imprinting (Sec. IV.B.3). In this case, the multimode nonlinear coupling and evolution is most relevant. Many studies of the multimode RT instability have been carried out, mostly for the classical case without mass ablation. It was found that, when the RT instability is seeded by a broad multimode perturbation, small bubbles merge into larger bubbles (bubble merger regime) or a faster growing bubble overcomes the others, developing a self-similar wavelength shift to larger sizes (bubble competition regime). In both cases, the time-dependent mode spectrum exhibits a skew toward longer wavelengths, as predicted by multimode theories and experiments (Shvarts *et al.*, 1995; Ofer *et al.*, 1996; Casner *et al.*, 2016). Figure 28 shows x-ray radiography snapshots of the multimode RT instability seeded by laser imprinting at three different times. The measured and simulated RT mode spectra for a broadband initial perturbation shown in Fig. 28 also indicate a shift of the peak toward longer wavelengths and larger bubbles, as also predicted by Haan's model (Haan, 1989).

Dimensional analysis indicates that, in the deeply nonlinear phase, the RT bubble front should advance proportionally to the distance traveled by the shell

$$h_b \simeq \alpha_b A_T g t^2, \quad (58)$$

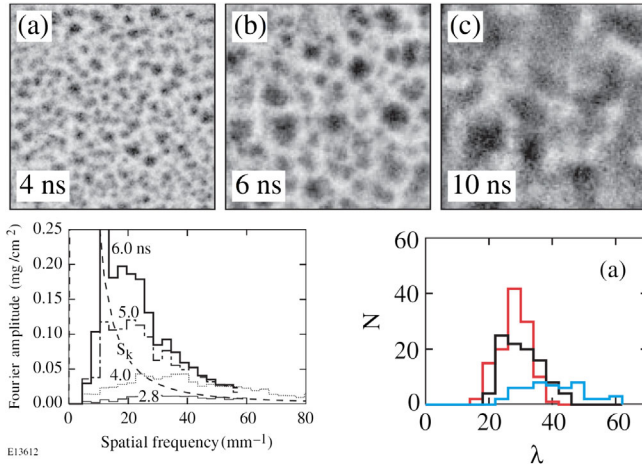


FIG. 28. X-ray radiographs of the 3D broadband modulations, initially produced by imprinting of the laser beam and measured at (a) 4, (b) 6, and (c) 10 ns (Smalyuk *et al.*, 2005). Bottom left panel: mode spectrum from the x-ray radiographs at 3 times (Smalyuk *et al.*, 2005). Bottom right panel: simulated distributions of the bubble sizes (number of bubbles  $N$  vs bubble size  $\lambda$ ) at three different distances traveled: 1  $\mu\text{m}$  (red curve), 18  $\mu\text{m}$  (black curve), and 67  $\mu\text{m}$  (blue curve). From Sadot *et al.*, 2005.

where  $h_b$  is the bubble front width and  $gt^2$  is twice the distance traveled for a constant acceleration. For a time-dependent acceleration,  $gt^2$  should be replaced by  $(\int_0^t \sqrt{g} dt)^2$ . The value of the constant  $\alpha_b$  has been the subject of intense studies, including dedicated experiments (Dimonte and Schneider, 2000) and 2D and 3D simulations (Dimonte, 2004), indicating that  $\alpha_b$  depends on the initial seed values of the perturbations. Zhang *et al.* (2018, 2020) found that for small initial seeds ablation reduces the value of  $\alpha_b$  with respect to the classical case

$$\alpha_b^{\text{abl}} \simeq (1 - \beta v_a \sqrt{k_0/g}) \alpha_b^{\text{cl}}, \quad (59)$$

where  $\beta \simeq 4.2$  and  $k_0 \simeq 0.06 \mu\text{m}^{-1}$  is introduced to normalize the initial amplitudes. For values of  $g$  and  $v_a$  typical of direct drive,  $\alpha_b$  can be significantly reduced by about 30% with respect to the classical value. However, the stabilizing effect of ablation occurs only at sufficiently small initial perturbation amplitudes. Figure 29 compares values of  $\alpha_b$  for the classical RT, ablative RT, and different initial seed amplitudes. Note that in the classical RT ( $v_a = 0$  curve), the value of  $\alpha_b$  saturates at about 0.05 when the bubble front transitions from the bubble competition to the bubble merger regime at large initial amplitudes. Instead, in the ablative case ablation-induced vorticity prevents saturation and  $\alpha_b$  exceeds the classical value at large enough initial perturbations.

If the RT bubble front penetrates through the entire shell and reaches the inner shell surface, the spherical piston is greatly decompressed and cannot efficiently compress the hot spot. An efficient energy transfer from the shell to the hot post requires a thin high-density shell whose inner and outer surfaces stagnate almost simultaneously. A turbulent shell is equivalent to an ultrahigh entropy plasma resulting in a thick low-density shell with an inner surface stagnating well before the outer surface, thus preventing an efficient transfer of energy. Therefore, it is crucial to control the growth of the RT bubble front to a width less than the in-flight shell thickness.

The shell thickness determines the in-flight aspect ratio  $\text{IFAR} = R/\Delta_{\text{sh}}$ , which is defined as the ratio of the shell radius  $R$  and its thickness  $\Delta_{\text{sh}}$ . The IFAR is a crucial parameter determining the hydrodynamic stability to short wavelength perturbations and the penetration of the bubble front into the imploding shell. For a thin shell and in the absence of ablation,

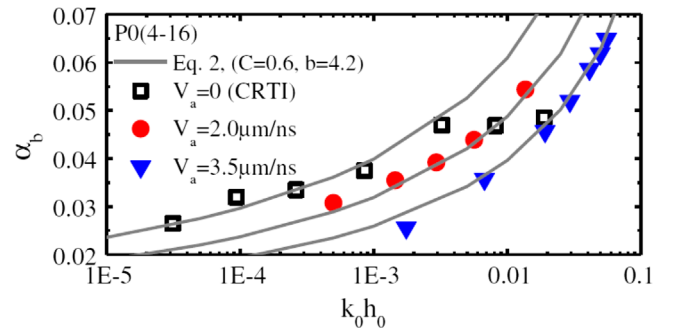


FIG. 29. Results from 2D simulations showing the dependence of  $\alpha_b$  on the initial rms multimode perturbation amplitude  $h_0$  for different ablation velocities. From Zhang *et al.*, 2018.

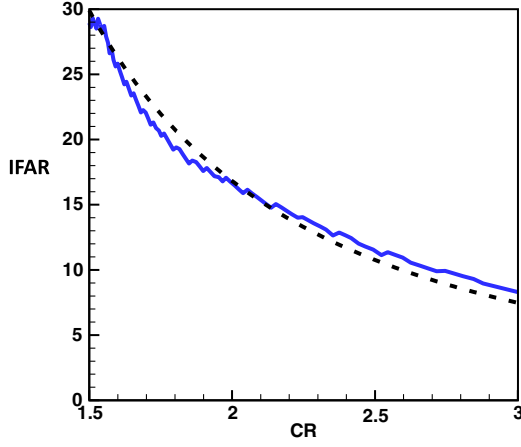


FIG. 30. Simulated evolution of the IFAR vs the convergence ratio ( $C_R$ ) for a typical OMEGA DT-layered target. The solid line is the simulated IFAR, while the dashed line is the  $C_R^{-2}$  approximation.

mass conservation requires that during the implosion the shell thickness will increase like  $C_R^2$ , while the IFAR will decrease like  $C_R^{-3}$ .

Mass ablation reduces the shell thickness and the IFAR scaling with  $C_R$  for typical direct-drive implosions is  $\text{IFAR} \sim \text{IFAR}_{\text{max}}/C_R^2$ , where  $\text{IFAR}_{\text{max}}$  is the maximum IFAR at the beginning of the acceleration phase  $\text{IFAR}_{\text{max}} = R_0/\Delta_{\text{sh}}^{\text{min}}$  (Fig. 30). The figure of merit for the stability against broadband short wavelength RT instability is the ratio  $h_b/\Delta_{\text{sh}}$  representing the relative penetration of the bubble front. If this ratio exceeds unity during the implosion, the shell breaks up. The penetration of the bubble front can be approximated with  $h_b \simeq 2\alpha_b(R_0 - R)$ , where  $R_0$  is the initial radius and  $R_0 - R(t)$  is the distance traveled by the shell. Using the IFAR scaling leads to a relative bubble penetration

$$\frac{h_b}{\Delta_{\text{sh}}} \simeq 2\alpha_b \text{IFAR}_{\text{max}} \frac{1}{C_R} \left(1 - \frac{1}{C_R}\right). \quad (60)$$

Since the maximum value of the right-hand side occurs for  $C_R = 2$ , the constraint on the IFAR to maintain  $h_b < \Delta_{\text{sh}}$  is

$$\text{IFAR}_{\text{max}} < \text{IFAR}_{\text{cr}} = 40 \left(\frac{0.05}{\alpha_b}\right) \quad (61)$$

and the IFAR must be kept below  $\simeq 40$  for  $\alpha_b \simeq 0.05$ . Note that by controlling the initial seeds and/or by increasing the ablation velocity,  $\alpha_b$  can be reduced below 0.05 and the  $\text{IFAR}_{\text{max}}$  can be increased. For  $\text{IFAR}_{\text{max}} > \text{IFAR}_{\text{cr}}$ , shell breakup occurs when the shell is at half the initial radius or earlier. The IFAR scales with the implosion Mach number [ $\text{IFAR} \simeq \text{Mach}^2$  (Lindl, 1995)] and its value is determined by three variables: the in-flight adiabat, the final implosion velocity, and the ablation pressure,

$$\text{IFAR}_{\text{max}} \simeq 41 \left(\frac{v_{\text{imp}}^{\text{km/s}}}{400}\right)^2 \left(\frac{4}{\alpha_F}\right)^{3/5} \left(\frac{100}{p_{\text{abl},D}^{\text{Mb}}}\right)^{2/5}. \quad (62)$$

Higher adiabats and/or lower velocities lead to lower IFARs for a given ablation pressure. At OMEGA and the NIF, higher velocity implosions have been successfully carried out to increase the fusion yield, but at the expense of the adiabat that had to be increased in order to maintain stability by controlling the IFAR. Using Eq. (62) for the maximum IFAR into the minimum kinetic energy required for ignition, it is found that  $\text{IFAR}_{\text{max}}$  sets the minimum ignition energy. This can be shown using the minimum ignition energy derived by Levedahl and Lindl (1997) and Herrmann, Tabak, and Lindl (2001),

$$E_{\text{kin}}^{\text{ign}} > 126 \left(\frac{\alpha_F}{4}\right)^{1.88} \left(\frac{400}{V_{\text{imp}}^{\text{km}}}\right)^{5.89} \left(\frac{100}{p_{\text{abl},D}^{\text{Mb}}}\right)^{0.77}. \quad (63)$$

Equation (63) can be rewritten using the IFAR from Eq. (62), leading to

$$E_{\text{kin}}^{\text{ign}} > 136 \left(\frac{40}{\text{IFAR}_{\text{max}}}\right)^3 \left(\frac{100}{p_{\text{abl},D}^{\text{Mb}}}\right)^2. \quad (64)$$

Since the maximum value of the IFAR is limited by the penetration of the RT bubble set by Eq. (60), the energy required for ignition must satisfy

$$E_{\text{kin}}^{\text{ign}} > 136 \left(\frac{\alpha_b}{0.05}\right)^3 \left(\frac{100}{p_{\text{abl},D}^{\text{Mb}}}\right)^2. \quad (65)$$

Equation (65) shows that the RT stability to short wavelength modes sets the minimum energy required for ignition. For a maximum classical RT bubble front penetration (Fig. 29),  $\alpha_b \simeq 0.05$  and the minimum kinetic energy required for ignition is about 130 kJ. The requirements on  $E_{\text{kin}}^{\text{ign}}$  are relaxed if  $\alpha_b$  is reduced below the classical values either through higher ablation velocities or lower RT seeds [Eq. (59)] or, even better, by keeping the RT growth in the linear phase.

When describing the seeds of the RT instability, it is important to recognize that the Rayleigh-Taylor instability (RTI) occurs during the acceleration phase. Before the acceleration starts, the shell is shocked by multiple shocks (the pulse shape in Fig. 25 is a two-shock design) and adiabatically compressed by the ramp in laser power. This is called the shock-transit phase of the implosion. During this phase, the acceleration of the ablation front is mostly impulsive and originates from the shocks. Shocked surfaces are unstable to the Richtmyer-Meshkov instability, which grows linearly in time in a classical fluid. For a single Fourier mode with initial surface perturbation  $\eta_0$ , the classical RM growth in the linear phase is  $\eta_{\text{RM}}^{\text{cl}} \simeq \eta_0 (A_T k U_{\text{ps}} t + 1)$ , where  $k$  is the perturbation wave number and  $U_{\text{ps}}$  is the postshock fluid velocity. While usually referred to as an instability, the RM is simply an initial ‘‘impulse’’ to the perturbation that sets it in motion with a constant initial velocity causing the surface amplitude to grow linearly in time. The RM in ablation fronts (ablative RM) is different from the classical case because, after the impulse, ablation determines the temporal behavior since the acceleration is negligible during the shock transit. This can be observed by setting  $g = 0$  in Eq. (55), leading to damped oscillatory solutions  $e^{i\omega_{\text{RM}}t - \nu_{\text{RM}}t}$ , with  $\omega_{\text{RM}}$  and  $\nu_{\text{RM}}$  given by

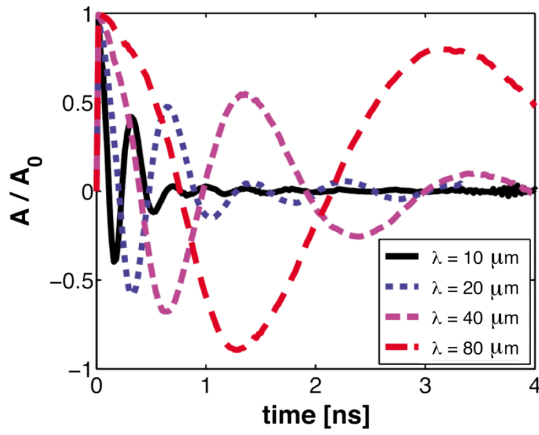


FIG. 31. RM instability at the ablation front. Perturbation evolution is shown for different wavelengths  $\lambda=10,20,40,80\mu\text{m}$ . Simulations refer to a thick  $D2$  target irradiated by  $I = 4 \times 10^{14} \text{ W/cm}^2$ ,  $\lambda_{\text{laser}} = 0.35 \mu\text{m}$ . The target is initialized with a surface amplitude roughness  $A_0 = 0.1 \mu\text{m}$ . From [Marocchino, Atzeni, and Schiavi, 2010](#).

$$\omega_{\text{RM}} \simeq \pm k v_a / \sqrt{r_\rho} \nu_{\text{RM}} \simeq 2k v_a, \quad (66)$$

where  $A_T \simeq 1$  has been used. Therefore, after the initial impulse, ablation turns the linear growth of the RM into damped oscillations ([Goncharov, 1999](#)) with short wavelength modes exhibiting the faster oscillations and the strongest damping (Fig. 31). In the limit of long wavelength modes, the oscillation frequency and the damping vanish and the growth is classical. The wave numbers affected by ablation are those for which the oscillation period  $2\pi/\omega_{\text{RM}}$  and the damping time  $1/\nu_{\text{RM}}$  are shorter than the shock-transit time through the shell. Experiments on Nike (Fig. 32) and OMEGA have confirmed the theoretically predicted behavior of the ablative Richtmyer-Meshkov instability ([Aglitskiy \*et al.\*, 2002](#); [Gotchev \*et al.\*, 2006](#)).

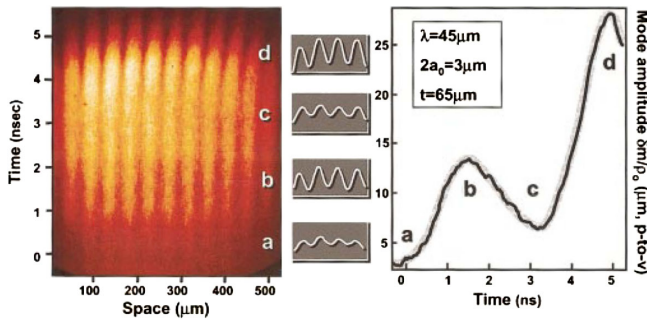


FIG. 32. Richtmyer-Meshkov instability experiments on the Nike laser. Left panel: original streak record along with the amplitude lineouts taken across the ripples at four benchmarking times in the inserts. Right: the time-dependent Fourier amplitude of the dominant mode vs time for a  $65 \mu\text{m}$  thick target with  $\lambda = 45 \mu\text{m}$  and initial peak-to-valley amplitude  $2a_0 \sim 3 \mu\text{m}$ , also marked at four important times: beginning of the pulse, first peak, etc. The origin of time  $t \sim 0$  here and elsewhere corresponds to the instant when the laser-beam intensity reaches half maximum. The thickness of the shaded area approximately corresponds to the experimental uncertainty. From [Aglitskiy \*et al.\*, 2002](#).

Another growth mechanism of surface perturbations in spherical implosions is the Bell-Plesset instability; see Sec. II.C. The Bell-Plesset (BP) instability is not a real instability but rather a secular growth driven by the conservation of mass in a rippled surface in convergent geometry. In spherical geometry and for large mode numbers  $\ell \gg 1$ , the single-mode rippled surface amplitude  $\tilde{\xi}_\ell(t)$  should be replaced by  $\tilde{Q}(t) = \rho R^2 \tilde{\xi}_\ell$ .  $\tilde{Q}$  grows exponentially if the surface is unstable to the Rayleigh-Taylor instability and the surface perturbation would follow,

$$\tilde{\xi}_{\ell \gg 1} \sim \frac{1}{\rho R^2} e^{\int \gamma_{\text{RT}} dt},$$

where  $\gamma_{\text{RT}}$  is the Rayleigh-Taylor growth rate ([Epstein, 2004](#)). During the acceleration phase, the shell density follows the ablation pressure and is approximately constant. Therefore, in addition to the RT exponential growth, surface perturbations exhibit an additional amplification  $1/R^2$  that scales with the square of the convergence ratio. This is usually referred to as the Bell-Plesset growth. Note that the BP growth persists even in the absence of acceleration (coasting phase), and it can be comparable or even exceed the exponential growth for low- $\ell$  modes.

Several mitigation techniques have been developed to reduce the impact of hydrodynamic instabilities. Mitigation strategies can be divided into two categories: (a) reduction of the growth rates and (b) reduction of the initial perturbations (seeds). In this section, we consider only the growth-rate reductions. Ablative RTI growth rates can be reduced by increasing the ablation velocity or by increasing the density gradient scale length at the ablation front. Since the ablation velocity is proportional to  $\alpha_F^{3/5}$ , raising the adiabat is a straightforward remedy to mitigate the ablative RTI; see Sec. III.E.2. However, simply raising the adiabat uniformly throughout the shell degrades the compressibility of the shell and increases the energy required for ignition [Eq. (65)]. Since only the inner portion of the shell contributes to the core confinement, it is possible to shape the adiabat profile such that the ablation front is on a high adiabat (favorable for stability) and the inner shell surface is on a low adiabat (favorable for compression and ignition). Shaping the adiabat can be done in two ways: (a) by using a strong decaying first shock or (b) by launching two shocks, a decaying shock with weak to moderate strength followed by a second shock. The first technique is referred to as adiabat shaping by a decaying shock ([Goncharov \*et al.\*, 2003](#)), and it requires a single-shock laser pulse shape with a strong initial picket followed by the ramp to peak power and the main drive. The strong initial picket launches a decaying shock, leaving behind a monotonically decreasing adiabat profile. The second technique is referred to as adiabat shaping by relaxation ([Anderson and Betti, 2004](#)) and requires a two-shock laser pulse shape with a weak picket followed by a foot, ramp, and main drive. The weak picket launches a decay shock that moderately shapes the adiabat but also drives a rarefaction wave, causing the outer shell surface to expand outward and the density profile to relax. A second shock is launched by the foot of the laser pulse. The second shock travels through the monotonically

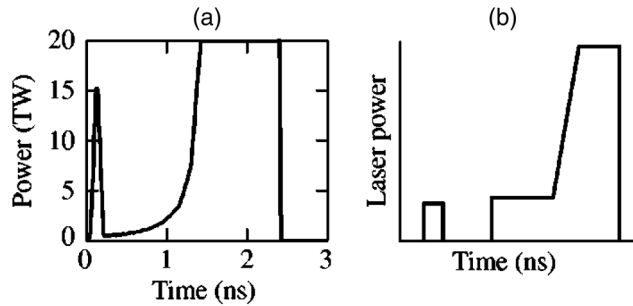


FIG. 33. (a) Laser pulse shapes for a decaying-shock-wave picket and a relaxation picket. The decaying shock wave is created by the short picket at the beginning of the pulse shape. The adiabat is shaped as the shock wave decays. (b) Pulse shape for a relaxation-picket drive. The low-intensity, narrow picket in front creates a spatial density profile that is low at the ablation region and high inside the shell. The strong shock wave resulting from the high-foot intensity then propagates through this density profile, shaping the shell adiabat. From Knauer *et al.*, 2005.

increasing density profile, thereby shaping the adiabat even further. Examples of laser pulses used to perform adiabat shaping are shown in Fig. 33. Figure 34 shows the schematic of the adiabat shape [Fig. 34(a)] and compares adiabat profiles generated by different adiabat shaping techniques [Fig. 34(b)]. Both adiabat shaping techniques have been shown to reduce the RTI growth rates (Fig. 35) and improve implosion performance.

A reduction of the RT growth rates can also be achieved using plastic ablators doped with higher  $Z$  dopants such as bromine (Fujioka *et al.*, 2004). Brominated plastic leads to the formation of double ablation fronts (Sanz *et al.*, 2009) with an outer ablation front driven by electronic heat conduction and an inner front driven by radiation transport. The radiation-heated ablator material between the outer and inner ablation fronts exhibits lower density than the inner portion of the shell, leading to higher ablation velocity and lower RT growth rates at the outer electronic ablation front (Yañez *et al.*, 2011).

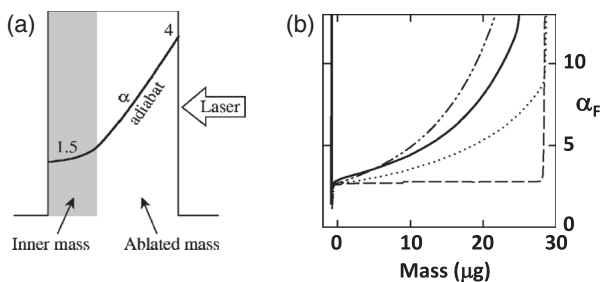


FIG. 34. (a) Schematic of a shell showing a shaped adiabat between the ablation surface and the inner surface. The shaded region is the portion of the shell that is not ablated. The adiabat is higher in the ablated material and therefore reduces the RT growth of ablation-interface perturbations. From Knauer *et al.*, 2005. (b) Simulated in-flight adiabat shapes vs mass coordinates for the three pulses (the dashed curve is flat, the dotted curve is the decaying shock, and the solid curve is the relaxation technique). The dash-dotted curve is an analytic result for adiabat shaping from relaxation. From Anderson and Betti, 2004.

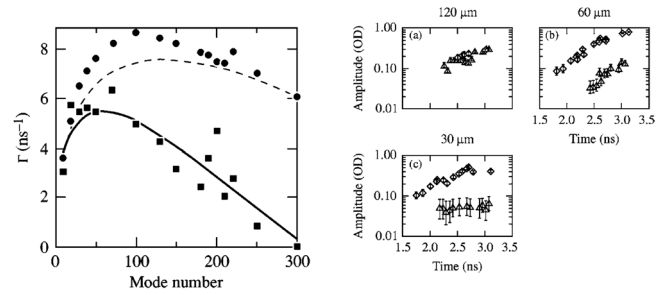


FIG. 35. Left panel: comparison of simulated RT growth rates from flat adiabat (circles) and adiabat-shaped targets (squares) using the relaxation technique. From Anderson and Betti, 2004. Right panels: measurements of the temporal evolution of the optical depth (OD) from laser imprinting perturbations driven by a flat adiabat (diamonds) and adiabat-shaped pulse (triangles) using the decaying shock technique. The different plots are for wavelengths 30, 60, and 120  $\mu\text{m}$ . From Smalyuk *et al.*, 2007.

This technique has not yet been tested in direct-drive DT-layered implosions.

### 3. Initial nonuniformity seeding of hydrodynamic instabilities in direct-drive implosions

In laser direct drive, there are multiple sources of symmetry perturbations that are amplified by hydrodynamic instabilities. The Rayleigh-Taylor instability is the most dangerous form because of the fast exponential growth during the linear phase of the instability. It occurs during the main drive portion of the laser pulse when the target is accelerated inward to achieve the maximum implosion velocity at the end of the pulse. There are three types of perturbations in direct drive: low modes ( $\ell < 6$ ), mid modes ( $6 < \ell < 30$ ), and high modes ( $\ell > 30$ ).

*Low modes.*—Low modes are perturbations with a wavelength longer than the shell radius. In a spherical geometry, the wavelength of an angular perturbation is  $\lambda = 2\pi R/\ell$ , where  $\ell$  is the mode number. Only mode numbers  $\ell < 2\pi \approx 6$  exhibit  $\lambda > R$ , thus the name low modes. Because of their long spatial variation (both angular and radial), low modes are not affected by thermal smoothing in the conduction zone or in the absorption region. Instead, they are secularly driven and amplified by convergence effects. Low modes are seeded mostly by laser mispointing, target offset, and beam power imbalance. In the case of polar direct drive, the laser-beam configuration exhibits a large intrinsic  $\ell = 2$  mode that needs to be mitigated with appropriate beam pointing. There are also low-mode asymmetries in the ice layer and in the ablator shell, but they are typically too small to affect implosion performance. Target offset away from the target chamber center is caused by vibrations of the target mount. At OMEGA, a set of high speed cameras tracks the position of the target and measures the target offset at shot time. Target offsets below 10–15  $\mu\text{m}$  are typical at OMEGA, and the resulting degradation in yield is modest ( $\leq 10\%$  for an  $\sim 10 \mu\text{m}$  offset). Occasionally, large vibrations occur, resulting in large target offset with severe consequences on the fusion yield and core compression. The  $\ell = 1$  mode has also been observed as a systematic deformation in an ambient plastic implosion at OMEGA (Shah *et al.*, 2017). The degradation in the fusion

yield from the  $\ell = 1$  mode is assessed by measuring the apparent ion temperature from multiple lines of sight and by measuring the residual flow velocity of the compressed core using nuclear diagnostics (Mannion *et al.*, 2020). Nuclear measurements of the ion temperature using NTOF detectors are affected by the residual isotropic and anisotropic flows (Murphy, 2014; Munro, 2016). The  $\ell = 1$  mode is a shift of the core with respect to the original target center caused by a residual directional flow. This results in varying ion temperature measurements (about sinusoidal variation) depending on the line of sight (LOS) with a minimum and maximum value. Woo *et al.* (2020) showed that the yield degradation from the  $\ell = 1$  is a monotonic function of the ratio  $T_{\max}/T_{\min}$  with

$$YOC_{\ell=1} \sim \left( \frac{T_{\min}}{T_{\max}} \right)^{1.5}. \quad (67)$$

Therefore, by measuring the apparent ion temperature along different LOSs, it is possible to infer the yield degradation from the  $\ell = 1$  mode.

At OMEGA, the velocity associated with the shift of the moving hot spot is inferred by measuring the second moment of the neutron spectrum among different detectors. This measurement is used (Mannion *et al.*, 2020) to determine a preimposed offset of the target to mitigate systematic  $\ell = 1$  from laser mispointing or power imbalance. This mitigation technique has been successfully implemented in DT-layered implosions leading to significant yield increases.

Another low mode of interest in OMEGA implosions is the  $\ell = 2$  mode that is routinely observed in the core self-emission images and leading to elliptical shapes of the hot spot with typical ellipticity values  $\kappa = b/a \simeq 1.1$ – $1.2$ . Measurements of the soft-x-ray emission from the ablated plasma near the ablation front using multiple framing cameras provide a 3D tomographic reconstruction of the ablation front capable of resolving modes  $\ell = 1$ – $3$ . Using these measurements, such low modes can be suppressed by applying power corrections to the individual beams (Michel *et al.*, 2018). This was demonstrated in implosion experiments using both warm CH shells filled with D2 gas and DT-layered implosions where power corrections led to rounder hot spots and modest increases in neutron yield.

Recent 3D ray-tracing simulations of cross-beam energy transfer including the effect of polarization have indicated that CBET can also be a significant source of low  $\ell = 1, 2$  modes. While the amplitude of these CBET-induced modes is target design dependent, their orientation appears to be systematic and can possibly explain observations of the core emission images (Edgell *et al.*, 2021). Without the effect of polarization, CBET was shown to mitigate the  $\ell = 1$  mode through a restoring force acting on the target (Anderson *et al.*, 2020).

*Mid modes.*—Mid modes are moderate mode number perturbations with  $6 \leq \ell \leq \text{IFAR}$  with  $\text{IFAR} \simeq 30$  for typical direct-drive implosions. The lower bound is determined by the condition for thermal smoothing during the main drive requiring that  $kD_c^{\text{main}} > 1$  through the high-intensity portion of the laser pulse. Here  $D_c^{\text{main}}$  is the distance  $D_c$  between the ablation front and the critical surface. Using  $k \simeq \ell/R$ , thermal smoothing during the main drive and decoupling of the mode

from the capsule occurs when  $\ell > R/D_c^{\text{main}}$ . For OMEGA direct-drive implosions,  $D_c^{\text{main}}$  varies between 50 and 100  $\mu\text{m}$  during the main drive and the critical surface radius varies between the initial target radius and just above half its value ( $\sim 300$ – $500 \mu\text{m}$ ), leading to the condition  $\ell > 6$  for mode decoupling during the main drive. This implies that mid modes are not driven secularly during the main drive but instead are seeded during the picket and foot of the laser pulse and then grow due to the Rayleigh-Taylor instability.

The upper bound in mid mode number is set by the penetration of the mode into the shell (feedthrough). Rayleigh-Taylor modes that are localized near the ablation front are called high modes. Mid modes differ from high modes because they radially extend across the imploding shell. The condition  $k\Delta_{\text{sh}}^{\text{in-flight}}$  determines the transmission of the perturbation across a shell of thickness  $\Delta_{\text{sh}}^{\text{in-flight}}$  from the ablation front to the inner surface. When  $k\Delta_{\text{sh}}^{\text{in-flight}} < 1$  (mid modes), the RT modes at the ablation front decay slowly in space (like  $e^{-kx} \sim 1$ , with  $kx < 1$ , where  $x$  is the distance from the ablation front into the shell), and the ablation-front distortion is transferred to the inner shell surface. Approximating  $k \simeq \ell/R$  leads to the mid mode condition  $\ell < R/\Delta_{\text{sh}}^{\text{in-flight}} \simeq \text{IFAR}$ . The mode spectrum from a hard sphere illumination pattern of the OMEGA 60-beam configuration shows the presence of a mid mode  $\ell = 10$  (Fig. 36). The hard sphere illumination can be viewed as the initial laser pattern seen by the target at the beginning of the laser pulse. As soon as the plasma is formed by laser ablation around the target, the mode spectrum and amplitudes seen by the ablation-front change due to the plasma buffer between the ablation front and the critical surface. During the main drive, the distance between the ablation front and the laser absorption region is large enough that mid modes from the laser illumination pattern are smoothed out before reaching the ablation front. Smoothing occurs due to the large spatial distribution of the absorbed laser energy and the diffusive effects of heat conduction [the cloudy day effect (Bodner, 1981; Craxton *et al.*, 2015)]. Therefore, the source of mode  $\ell = 10$  nonuniformities occur mostly during the picket of the laser pulse shape, to a minor degree during the foot, and rarely during the main drive. In the hard sphere illumination, the amplitude of mode  $\ell = 10$  depends mostly on the ratio

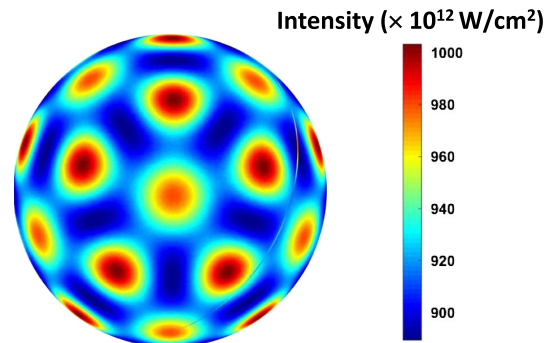


FIG. 36. Hard sphere projection of the laser illumination pattern on a typical target for 60-beam OMEGA. Courtesy of A. Shvydky [Laboratory for Laser Energetics (LLE)].

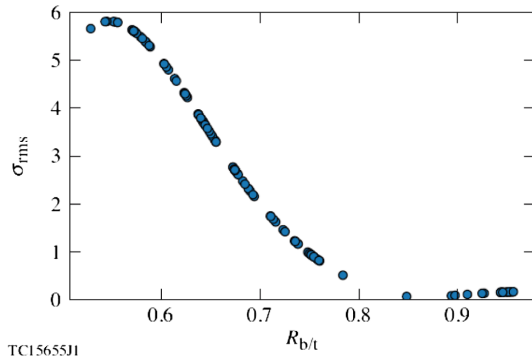


FIG. 37. The rms variation of the on-target illumination vs the ratio  $R_{beam}/R_{target}$  for OMEGA phase plates with super-Gaussian profile exponent 5. Courtesy of V. Gopalaswamy (LLE).

between the laser-beam size and target size ( $R_b/R_t$ ). Figure 37 shows that, at OMEGA, the amplitude of mode  $\ell = 10$  is small for  $R_b/R_t \geq 0.85$ . For  $R_b/R_t < 0.85$ , the amplitude grows monotonically and implosion performance becomes dominated by a mode  $\ell = 10$ . There is some indirect experimental evidence that significant degradation occurs even at higher values of  $R_b/R_t$ , but this has not been confirmed by direct probing of the mode  $\ell = 10$  evolution.

*High modes.*—The main source of short wavelength non-uniformities in direct drive is laser imprinting. Laser imprinting comes from the high frequency modulations of the laser intensity in each beam. In direct drive, high modes have mode numbers  $\ell > IFAR \approx 30$  and are driven by the Rayleigh-Taylor instability. Because of their short wavelength, they are decoupled from the source in the laser speckles during the main drive and they are instead seeded during the initial phase of the laser interaction with the target surface. Using Eq. (46) to determine the local ablation pressure from the laser speckle pattern leads to a modulated ablation pressure launching a rippled shock in the ablator when the laser light first interacts with the target surface. Equation (46) leads to an overestimation of imprinting because it assumes that local spatial and temporal variations of the laser intensity result in local variations of the ablation pressure on the target surface (this is equivalent to 100% imprint efficiency). Instead, the imprint efficiency is reduced by the initial development of the conduction zone between the critical surface and the ablation front. Initially, the conduction zone width increases with time as more laser energy is absorbed near the target surface. In the conduction zone of width  $D_c$ , the temperature rises from tens of eVs, characteristic of the cold imploding shell, to a few keV at the critical surface. Since the absorption region is beyond the critical surface, short wavelength perturbations with wave numbers  $k > 1/D_c$  are smoothed by thermal conductivity (Bodner, 1981; Goncharov, Skupsky *et al.*, 2000). Smoothing by thermal conduction is particularly effective due to the strong temperature dependence of Spitzer thermal conductivity for ideal plasmas ( $\kappa_{Sp} \sim T^{5/2}$ ). It follows that laser imprinting occurs only during the initial picket, when  $D_c$  is small, the plasma temperature is relatively low, and thermal smoothing is ineffective. After the initial development of the conduction zone, imprinting ceases and the growth of short wavelength modes at the ablation front is driven only by

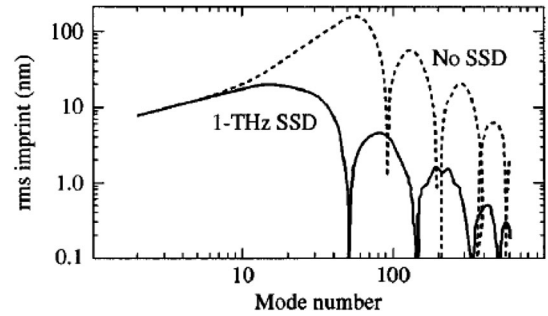


FIG. 38. Simulated ablation-front mode spectrum from laser imprinting at the start of the main drive for OMEGA targets with 1 THz SSD and without SSD. From Goncharov, Skupsky *et al.*, 2000.

hydrodynamic instabilities. Laser smoothing, developed to mitigate laser imprinting, must therefore be effective only during the picket of the laser pulse. Two-dimensional SSD currently implemented on OMEGA is effective in reducing laser imprinting, as shown in Fig. 38, which compares the target nonuniformity spectrum seeded by laser imprinting with and without SSD. SSD varies the interference speckle pattern of a laser beam focused using a phase plate. The smoothing requirements on SSD are set by the speckle variation being shorter than the characteristic hydrodynamic timescale of imprinting. This is achieved by adding bandwidth, typically of a few terahertz, to the fundamental laser frequency using an electro-optical modulator. Spectral dispersion is then introduced, causing the interference structure to vary in time, and the time-averaged intensity is smoothed.

The imprinting level is also dependent on the shape of the initial portion of the laser pulse. Igumenshchev *et al.* (2019) found that laser pulse shapes with a picket develop less imprinting than laser pulses without a picket and with the same adiabat (Fig. 39). The difference comes from the first shock that decays in space and time when launched by a picket, as opposed to a supported shock launched by a foot that travels at constant velocity and strength. This occurs because the penetration depth of the ablation-front perturbation into the shell is reduced by the rarefaction wave following

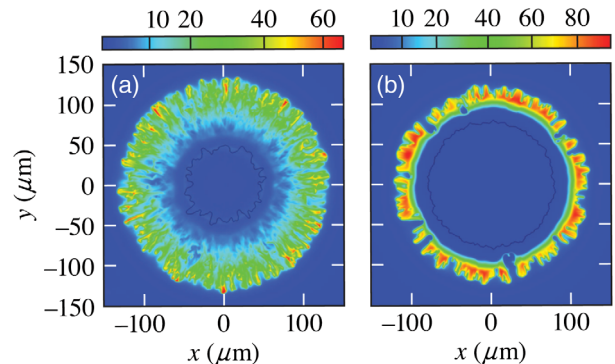


FIG. 39. Cross sections of the density (in  $g/cm^3$ ) from 3D simulations of (left image) a nonpicket and (right image) a single-picket pulse. Images are shown at  $t = 2.45$  and  $2.55$  ns, respectively, in the moment prior to deceleration of the implosion. From Igumenshchev *et al.*, 2019.

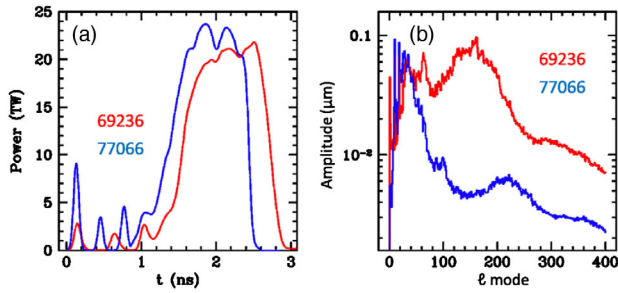


FIG. 40. (a) Laser pulses and (b) simulated spectra of surface modulations. The strong picket pulse is displayed in blue and the reduced picket pulse is shown in red. Spectra are taken at the time corresponding to the shells' initial acceleration. From [Igumenshchev \*et al.\*, 2019](#).

a decaying shock. In this case, the imprinted perturbations remain localized near the ablation front, where they are more effectively suppressed by mass ablation. Figure 40 shows the 3D simulated surface modulation spectra for pulse shapes with strong and weak pickets. The strong picket (and higher-adiabat) pulse shape exhibits significantly lower perturbation amplitudes. The target adiabat plays a major role in governing the growth of laser imprinting after being seeded during the initial part of the laser pulse. This was observed in controlled plastic-target experiments at OMEGA, where the adiabat was varied between  $\alpha_F = 2$  and 6. The measured yield degradation was a strong function of the adiabat, with the lowest adiabats leading to the most severe degradation ([Hu \*et al.\*, 2016](#); [Michel \*et al.\*, 2017](#)).

Three promising approaches to reduce laser imprinting seeds have been explored in the last few years. The first was

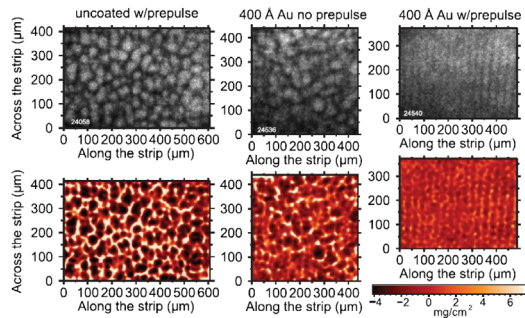


FIG. 41. Imprinting mitigation using a preexpanded Au overcoat. Framing camera images from three shots are shown (left to right): uncoated with a prepulse, 40 nm Au without a prepulse, and 40 nm Au with a prepulse. Frame times are at 4.4 ns. The top row shows the linearized film images in gray scale. The bottom row shows the images processed using Wiener filtering with modulation transfer function correction and converted to areal mass fluctuation, displayed using the color map shown. All three shots had a preimposed 30  $\mu\text{m}$  wavelength and a 0.5  $\mu\text{m}$  amplitude ripple (grooves are oriented vertically). The uncoated shot is dominated by RT-amplified imprint from the laser speckle, while the Au-coated shots with a prepulse show much lower imprint, with the preimposed ripple amplified by RT instability as the prominent feature. The shot with 40 nm Au without a prepulse shows some imprint reduction but is still broken up by the imprint. From [Karasik \*et al.\*, 2021](#).

developed at NRL and uses a thin overcoat of high-Z material on the target outer surface. The high-Z layer is several tens of nanometers thick and needs to be preexpanded before the laser pulse. Preexpansion can be induced by heating the high-Z layer with a uniform source such as an externally generated low-level soft-x-ray prepulse of about 10 J/cm<sup>2</sup>. The heated layer expands, thereby generating a buffer zone between the laser deposition region and the ablation front. The effectiveness of this technique was shown in recent experiments on the OMEGA EP laser (Fig. 41) using Au and Pd coating of CH targets, where the imprinting level was reduced by over an order of magnitude ([Karasik \*et al.\*, 2021](#)).

Another mitigation strategy uses an outer thin Au-coated plastic shell surrounding the capsule. The thin shell consists of a 0.5–1  $\mu\text{m}$  thick outer membrane of CH at a distance of about 300  $\mu\text{m}$  from the capsule and coated with 40–60 nm of Au. A strong picket in the laser pulse heats up the gold and generates enough x-ray flux to drive the first shock into the capsule. The main drive portion of the laser pulse starts when the membrane is fully ablated and subcritical. The first shock is driven by x rays and therefore highly uniform. The acceleration phase of the implosion is driven directly, but a plasma buffer is left by the initial x-ray pulse and the laser is never in direct contact with the dense shell. This scheme is denoted as hybrid. The growth of target nonuniformities from laser imprinting was measured in hybrid targets designed for planar experiments on OMEGA EP (Fig. 42). The evolution of the imprinting spectrum in hybrid targets was compared to standard direct drive, showing strong suppression of mass modulations in hybrid targets ([Ceurvorst \*et al.\*, 2020](#)). Another mitigation technique uses a supercritical CH foam overcoat on the capsule. The growth of imprinting is suppressed by reducing the growth rate of the Rayleigh-Taylor instability through an increased ablation velocity and density scale length at the ablation surface ([Hu \*et al.\*, 2018](#)). Two-dimensional simulations of imploding CH shells are used to study the evolution of nonuniformities seeded by laser imprinting for bare CH shells and for CH shells with a 40  $\mu\text{m}$  thick layer of 40 mg/cm<sup>3</sup> CH foam. As shown in Fig. 43, the foam target exhibits a reduced level of nonuniformities with respect to the standard CH shell. A reduction of laser imprinting was also observed in CH targets doped with higher Z elements such as

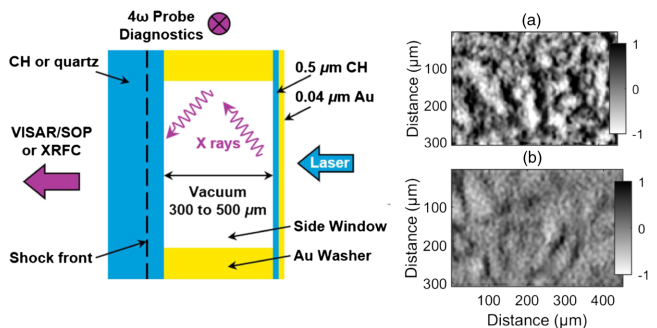


FIG. 42. Left image: schematic of the hybrid direct-drive target design in planar geometry. Optical depth images of (a) a bare target and (b) a hybrid target after 4.2 ns. The hybrid target exhibits greatly reduced mass modulation. From [Ceurvorst \*et al.\*, 2020](#).

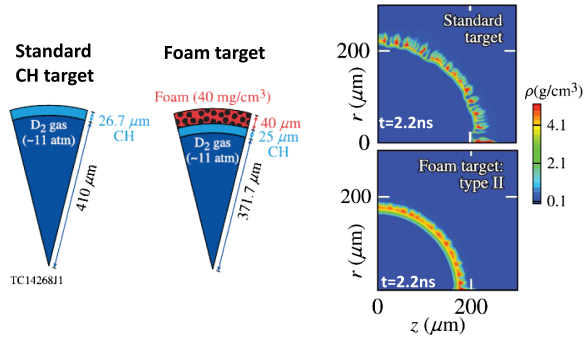


FIG. 43. Left images: schematic diagrams for CH targets displaying both standard bare CH shells and CH shells with a layer of foam added. Right panels: two-dimensional simulations including laser imprinting, performed with the code DRACO, showing significantly improved uniformity in foam targets with respect to standard targets. From Hu *et al.*, 2018.

silicon and germanium (Hu *et al.*, 2012). While this is an easily implementable imprint mitigation technique, it may not be sufficient to enable low-adiabat direct-drive implosions with  $\alpha_F < 3$ , thus requiring strict limitations on the initial imprint.

Direct measurements of the nonuniformities of the first shock front launched by direct laser irradiation in flat foils are good indicators of the seed level of laser imprinting before the amplification from hydrodynamic instabilities. These experiments were carried out using the two-dimensional velocity interferometer for any reflector (VISAR) technique (Celliers *et al.*, 2010), which measures the fluctuations in velocity of the propagating shock front. 2D-VISAR measurements of shock-front nonuniformities were carried out on OMEGA (Peebles *et al.*, 2019) and Nike (Oh *et al.*, 2021) to assess the benefits of the aforementioned imprint mitigation techniques.

Finally, nonuniformities of the inner surface of the DT ice layer can also seed hydrodynamic instabilities occurring at the ablation front through a transfer of perturbations mediated by the rarefaction waves propagating from the inner to the outer shell surface after shock breakout. This transfer is called feedout, and the perturbations exhibit a phase reversal before undergoing exponential RT growth (Betti, Lobatchev, and McCrory, 1998). Feedout measurements with perturbation phase reversal followed by subsequent RT growth were carried out on the NIKE laser (Aglitskiy *et al.*, 2001).

#### 4. Hot-electron preheat in direct-drive implosions

The electric field of nonlinear electron plasma waves driven by laser-plasma instabilities such as SRS and TPD accelerate plasma electrons with velocity of the order of the phase velocity of the wave (Krueer, 2003). Such energetic hot ( $\sim 30$ – $100$  keV) electrons intersect the imploding shell and deposit their energy in the DT fuel, thereby raising the adiabat in flight (preheat) and reducing the fuel compressibility. Understanding and quantifying preheat due to electrons from LPs has been a long-standing effort. In OMEGA direct-drive implosions, the main instability producing hot electrons is the TPD that originated from the decay of a light wave

with frequency  $\omega_0$  into two plasma waves (plasmons) with half the frequency of the pump wave ( $\omega_{pe} = \omega_0/2$ ). The condition  $\omega_{pe} = \omega_0/2$  is satisfied at the quarter critical density  $n_{cr}/4$ . Strong wave-particle interactions occur through Landau damping for wave vectors  $k\Lambda_{De} \simeq 0.2$ – $0.3$ , where  $k$  is the electron plasma wave number and  $\Lambda_{De}$  is the plasma Debye length. The electron plasma wave energy is transferred to energetic electrons through Landau damping and to the background plasma through collisional damping. In a nonuniform plasma, the TPD instability is excited above a convective threshold determined by the parameter  $I\lambda_L L_n/T_e$  depending on the laser wavelength  $\lambda_L$ , the laser intensity  $I$ , the electron temperature  $T_e$ , and the density gradient scale length  $L_n$ , all evaluated at the quarter critical density. As Simon *et al.* (1983) described, the TPD threshold can be approximated as  $\eta_{TPD} = 1$ , where

$$\eta_{TPD} = \frac{I_{14} L_n^{\mu m}}{230 T_e^{\text{keV}}}, \quad (68)$$

with  $I_{14}$  in units of  $10^{14}$  W/cm $^2$ ,  $L_n$  in  $\mu\text{m}$ , and  $T_e$  in keV. In direct-drive implosions, the local laser intensity driving the TPD instability depends on the overlap of several beams that share a common plasma wave vector component. This was recognized both in multibeam experiments and in multibeam simulations (Michel, Maximov *et al.*, 2012; Myatt *et al.*, 2014) and led to a general threshold parameter that depends on the quarter critical plasma properties and a polarization-adjusted sum of the intensities of each beam sharing the same angle with the plasma wave. The conversion of laser energy into hot-electron energy was measured by the hard-x-ray emission from hot electrons slowing down as well as from  $K\alpha$  emission from hot-electron excitation in Mo layers embedded inside the target (Yaakobi *et al.*, 2012). Figure 44, from D. T. Michel *et al.* (2013), shows the measured conversion efficiency ( $f_{\text{hot}}$  is the energy into hot electrons per laser energy) as a function of the overlapping laser intensity (left panel) and as a function of the common

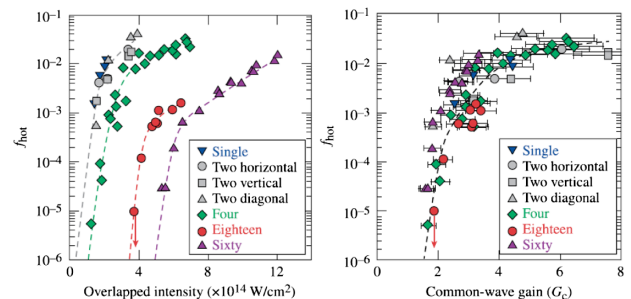


FIG. 44. Left panel: hot-electron fraction ( $f_{\text{hot}}$ ) as a function of vacuum overlapped laser intensity. Single, two, and four correspond to OMEGA EP planar experiments where the beams are linearly polarized; eighteen (sixty) corresponds to OMEGA planar (spherical) experiments where the beams have polarization smoothing. For each configuration, the overlapping intensity is given by the vacuum intensity of the laser beams on the target surface. Right panel: hot-electron fraction vs the common wave gain for each experimental configuration tested. From D. T. Michel *et al.*, 2013.

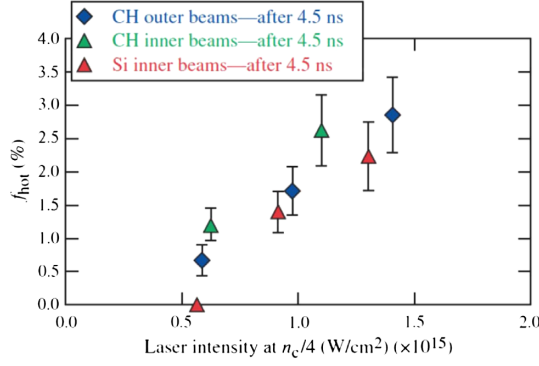


FIG. 45. Planar hot-electron measurements at the NIF. Fraction of laser energy converted to hot electrons as a function of simulated quarter critical laser intensity, for laser drive using outer beams (diamonds) and inner beams (triangles), for CH ablators (blue, green) and Si ablators (orange). Uncertainty in  $f_{hot}$  is based on statistical uncertainty in the hard-x-ray data propagated through EGSNRC modeling. From Rosenberg *et al.*, 2018a.

wave gain (i.e., gain on the beam intensity) for different experimental configurations (planar and spherical) on the OMEGA laser facility.

In large-scale-length plasmas typical of the NIF direct-drive targets, SRS becomes the dominant instability and the overall conversion of laser energy into hot-electron energy is expected to increase. In direct drive, SRS develops mostly at densities below  $n_{cr}/4$ , and its maximum gain occurs for side-scattered light waves. As for TPD, the SRS instability threshold depends on the plasma scale length, the laser intensity, and the laser wavelength and can be approximated as  $\eta_{SRS} = 1$ , where

$$\eta_{SRS} = \frac{I_{14} \lambda_L^{2/3} L_{n(\mu m)}^{4/3}}{1549}. \quad (69)$$

Recent direct-drive experiments at the NIF using planar plastic targets have shown that SRS dominates over TPD in ignition scale plasmas. The conversion efficiency of laser-to-hot-electron energy was shown to increase with a laser intensity between 0.7% and 2.9%. Figure 45 shows the results of the NIF experiments, including CH and Si targets, with the latter exhibiting a higher threshold for hot-electron production.

Conversion factors from laser-to-hot-electron energy above  $\sim 1\%$  are of concern for the viability of direct drive, as described later in this section. What is critical is not only the total amount of energy transferred to hot electrons but also the amount of energy that such electrons deposit inside the DT fuel and, in particular, that portion of the DT fuel that produces the areal density of the compressed core (hot-electron coupling efficiency  $\theta_h$ ). In direct-drive targets about 50% of the initial fuel mass is ablated and most hot electrons deposit their energy either in the outer ablator (typically CD or CH) or in the ablated DT plasma. Only a fraction of the hot-electron energy is deposited inside the unablated DT fuel, and even a smaller fraction in the inner portion of the fuel that produces most of the areal density. The minimum shell kinetic energy required for ignition is proportional to the square of the in-flight adiabat  $\min[E_{kin}^{ign}] \sim \alpha_F^2 / v_{imp}^6$ , and a significant increase

in adiabat from hot-electron preheat results in more stringent requirements on the energy required for ignition. This degradation occurs because higher adiabats lead to lower hot-spot pressures and lower areal densities in the compressed core. The areal density degradation from hot-electron preheat can be easily quantified for a given preheat energy deposited in the fuel, as shown by Christopherson *et al.* (2021),

$$\frac{\rho R_{hot}}{\rho R_{no hot}} \simeq \left( 1 + 1.16 \frac{E_{stag}^{preheat}}{IE_{sh}} \right)^{-4/3}, \quad (70)$$

where the left-hand side represents the ratio of the areal density with and without preheat,  $E_{stag}^{preheat}$  is the energy deposited by the hot electrons in the portion of the fuel that stagnates at peak fusion rate, and  $IE_{sh}$  is the internal energy of that same portion of the shell while in flight. When one uses an ideal plasma approximation (valid for  $\alpha_F \gg 1$ ), the energy ratio on the right-hand side of Eq. (70) is proportional to  $(E^{preheat}/\text{mass}_{sh})/T_{sh}$ , indicating that the areal density degradation depends on the hot-electron energy deposited for unit mass and that lower-adiabat (for instance, colder shell) implosions are more sensitive to hot-electron preheat. After a straightforward manipulation, the shell internal energy  $IE_{shell}$  can be rewritten in the following simple form:

$$IE_{sh} \simeq \frac{9}{7} \frac{E_{kin}}{IFAR}. \quad (71)$$

By denoting with  $\theta_h$  the fraction of hot electrons depositing their energy into the unablated fuel making up the stagnating mass and assuming small areal density degradations  $\delta\rho R/\rho R \ll 1$ , the relation between areal density degradation and laser-to-hot-electron conversion efficiency  $f_{hot}$  can be written as

$$\frac{\delta\rho R}{\rho R} \simeq \frac{\theta_h f_{hot}}{\eta_k} IFAR, \quad (72)$$

where  $\eta_k = E_{kin}/E_L$  is the laser-to-kinetic-energy coupling efficiency. Equation (72) sets a limit on the maximum hot-electron fraction  $f_{hot}$  based on the maximum tolerable areal density degradation

$$f_{hot} \leq \left( \frac{\delta\rho R}{\rho R} \right)_{\max} \frac{\eta_k}{\theta_h} \frac{1}{IFAR}. \quad (73)$$

Note that the maximum  $f_{hot}$  depends on the fraction  $\theta_h$  of electrons depositing their energy in the stagnating mass.  $\theta_h$  depends on the electron source divergence and the electron transport physics, which is not well understood because of the complicated electron dynamics affected by the coronal electromagnetic fields, refluxing of escaping electrons and the shrinking interaction volume of the imploding shell. Measurements of the electron divergence in imploding capsules using Mo spheres of different radii enclosed within imploding shells were carried out on OMEGA (Yaakobi *et al.*, 2013). Those experiments indicated that the divergence of the electron source is wide enough that the fraction of electrons interacting with the shell at different convergence

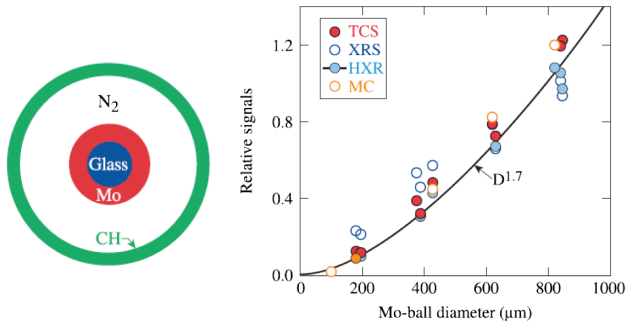


FIG. 46. Left image: target used in divergence experiments on OMEGA. Molybdenum spheres of different sizes are enclosed within a laser-driven plastic shell. Right panel: measured intensity of the Mo- $K\alpha$  line and hard-x-ray radiation. The Monte Carlo (MC) simulation results for a divergent fast-electron beam are also shown. The curve is the best fit to the hard-x-ray data. The increase of the signals with the Mo-shell diameter indicates a wide-angle divergence of fast electrons. From [Yaakobi \*et al.\*, 2013](#).

ratios decreases with the shell surface as  $\sim 1/R^2$ . Figure 46 shows the schematics of the targets used in the divergence experiments and the relative  $K\alpha$  signals for different sizes of the inner Mo sphere.

Recently direct measurements of the hot-electron energy deposited in the DT layer of cryogenic implosions and its distribution across the imploding shell mass were carried out on OMEGA ([Christopherson \*et al.\*, 2021](#)). Those experiments used two implosions: one of a DT-layered target with a CD ablator, and one with a mass-equivalent all-CD shell, both imploded by the same laser pulse. Those implosions were designed to exhibit the same coronal conditions at the quarter critical surface, and therefore the same hot-electron source. The differences in hard-x-ray signals in the two implosions were caused by the slowing down of electrons in DT versus CD. Since electron slowing down in DT produces about 5 times fewer hard x rays than in CD, the subtraction of the two hard-x-ray signals is proportional to the hot-electron energy deposited in DT. Figure 47, from [Christopherson \*et al.\* \(2021\)](#), compares the measured hard-x-ray signal of a DT-layered

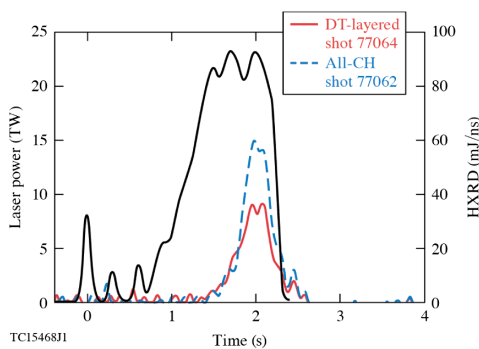


FIG. 47. The laser pulse (black line) and the hard-x-ray signals for DT-layered shot 77064 (red line) and all-CH shot 77062 (blue line) are plotted as a function of time. The difference in hard-x-ray signals is proportional to the hot-electron energy deposited in the DT layer. From [Christopherson \*et al.\*, 2021](#).

implosion to an all-CD mass-equivalent implosion driven by the same laser pulse. The hard-x-ray signal is lower in a layered target due to the hot electrons slowing down in DT rather than CD.

Other experiments using a payload of Cu-doped plastic of different thicknesses and similar preheat measurements were used to infer the distribution of the preheat energy within the unablated payload ([Christopherson \*et al.\*, 2021](#)). That enabled researchers to accurately determine  $\theta_h$  in OMEGA implosions. While  $\theta_h$  varies for different targets, it was found that, for high performance, OMEGA implosions the preheat energy is uniformly distributed through the payload mass, and only about 10% of the total hot-electron energy is deposited in the stagnating mass ( $\theta_h \simeq 0.1$ ). Therefore, when characteristic values typical of direct drive are used, the limit on the hot-electron fraction  $f_{\text{hot}}$  can be rewritten as

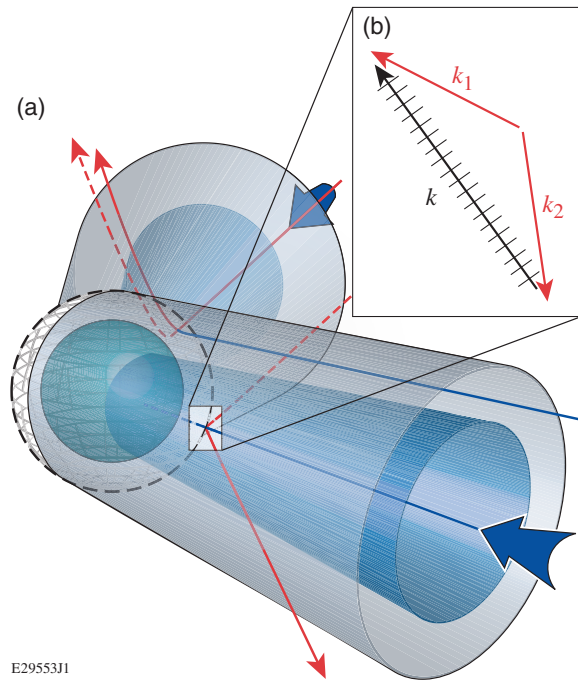
$$f_{\text{hot}}(\%) \leq 0.4 \left( \frac{\delta\rho R}{0.2\rho R} \right)_{\text{max}} \left( \frac{\eta_k}{0.06} \right) \left( \frac{0.1}{\theta_h} \right) \left( \frac{30}{\text{IFAR}} \right), \quad (74)$$

indicating that to prevent areal density degradation greater than 20% the fraction of hot electrons should not exceed 0.4%. In high performance OMEGA implosion experiments, the hot-electron temperature is  $T_{\text{hot}} \simeq 50\text{--}60$  keV and their total energy is about 40–60 J corresponding to a conversion efficiency  $f_{\text{hot}} \sim 0.2\%$  for a 26 kJ laser pulse at peak intensity of about  $9 \times 10^{14}$  W/cm<sup>2</sup>. According to [Christopherson \*et al.\* \(2021\)](#), the preheat energy in the stagnating mass is about 5–7 J, leading to a  $\rho R$  degradation of 10%–20% for an adiabat  $\alpha \simeq 3$  to 4 and IFAR  $\simeq 25\text{--}30$ .

Because of thin ablators used in direct-drive targets, hot electrons from LPs penetrate deep into the DT fuel. Since the threshold of such instabilities is proportional to the plasma scale length, preheat is expected to occur primarily toward the end of the pulse when the ablator material is fully ablated and the DT fuel is exposed to hot electrons, even those with moderate energies  $\sim 40\text{--}60$  keV. Since the instability threshold for SRS and TPD is lower in long-scale-length plasmas, hot-electron preheat is of great concern for ignition scale direct-drive implosions. Ablator materials with higher atomic numbers have been shown to exhibit a higher threshold for LPs. For instance, SiO<sub>2</sub> and Si ablators ([Smalyuk \*et al.\*, 2010](#); [Rosenberg \*et al.\*, 2018a](#)), Si doping of CH shells ([Smalyuk \*et al.\*, 2009](#)), and buried Si layers ([Goncharov \*et al.\*, 2014](#)) have significantly reduced the laser-to-hot-electron conversion efficiency. A comprehensive experimental effort is currently under way at the NIF to quantify and mitigate hot-electron preheat for direct drive at ignition relevant scales ([Solodov \*et al.\*, 2020](#)).

## 5. Cross-beam energy transfer in direct-drive implosions

As laser systems have increased their number of beams and become more powerful to drive large plasmas, the transfer of energy between laser beams in the plasma has become one of the challenges in predicting the hydrodynamic conditions of ICF experiments. The energy transferred between beams is maximized when the frequency difference between the beams is equal to the ion-acoustic frequency in the frame of the plasma:  $\Delta\omega = \omega_2 - \omega_1 = (k_2 - k_1)V + |k_2 - k_1|c_s$ , where



E29553J1

FIG. 48. (a) Light rays propagating past the target (blue curve) interact with light rays in the central region of another beam (red curve). (b) The interacting light rays seed an ion-acoustic wave near the Mach-1 surface (dashed curve). The ion-acoustic wave scatters light before it can penetrate deep into the target (dashed curves).

$\omega_1$ ,  $\omega_2$  and  $k_1$ ,  $k_2$  are the frequencies and wave numbers of the crossing laser beams;  $V$  is the plasma flow velocity; and  $c_s$  is the sound speed (Fig. 48) (Randall, Albritton, and Thomson, 1981). For direct-drive experiments, where the laser beams typically have the same frequency ( $\Delta\omega = 0$ ), the maximum energy transfer occurs near the Mach-1 surface ( $V = c_s$ ), and this energy transfer leads to a significant reduction in the transfer of laser energy to kinetic energy of the imploding shell (6%  $\rightarrow$  4%) (Igumenshchev *et al.*, 2010; Froula *et al.*, 2012). CBET reduces the incident energy in the central portion of the laser beams, making it possible for the incoming light to bypass the high-absorption region near the critical surface (Edgell *et al.*, 2017). Laser light in the wings of the laser beams propagates past the target and provides the seed for CBET to drive ion-acoustic waves to large amplitude. Recent work by Edgell *et al.* (2021) also found that polarization effects on CBET can significantly enhance low-mode asymmetries during the main drive of OMEGA implosions.

Early direct-drive hydrodynamic simulations used classical thermal transport models (Spitzer and Härm, 1953) that required an *ad hoc* multiplier to match the physical observables from direct-drive implosion experiments. Many of the early discrepancies were remedied when both nonlocal thermal transport (Goncharov *et al.*, 2008) and CBET (Igumenshchev *et al.*, 2010, 2012) models were implemented in the hydrodynamic codes, but challenges in modeling the laser-beam propagation using geometric optics limited the accuracy of the CBET modeling. Improvements have been suggested to better account for energy conservation and ray caustics, which makes it

challenging to define intensity (Follett *et al.*, 2018; Colaitis *et al.*, 2019). Furthermore, uncertainties in plasma conditions have led to challenges in isolating errors between modeling the laser-plasma-instability physics and experimental observables (Kirkwood *et al.*, 1996), which have made it difficult to understand the limitations of the linear CBET models implemented in the hydrodynamic codes.

Particle-in-cell simulations have suggested that, when the ion-acoustic waves are driven to large amplitude, nonlinear effects will modify the energy transfer, resulting in deviations from linear CBET theory (Cohen *et al.*, 1997; Yin *et al.*, 2019). Early experiments seemed to corroborate this picture, suggesting that nonlinear physics was required to model the interactions, but these experiments relied primarily on hydrodynamic modeling to determine the plasma conditions (Glenzer *et al.*, 2001; Kirkwood *et al.*, 2002) and, due to the uncertainties in plasma conditions, an understanding of the saturation physics was elusive.

To understand if there was significant missing laser-propagation physics within the models implemented in the hydrodynamic codes that could be masked by uncertainties in the CBET modeling, experiments were implemented that used Thomson scattering to separate the hydrodynamic uncertainties from the CBET physics (Turnbull *et al.*, 2017, 2020; Hansen *et al.*, 2021). Two important results came from these studies, which are shaping the way that CBET is modeled in ICF studies, and the conclusions from both suggest that the current linear CBET models used in hydrodynamic codes are sufficient to accurately predict energy transfer, provided that the underlying hydrodynamic conditions are properly determined.

When the product of the intensities of the crossing beams was sufficiently small to limit the total energy transferred between beams, the linear CBET models implemented in the hydrodynamic codes accurately reproduced the measured results, but a sensitivity in the CBET resonance to the shape of the electron distribution function (Afeyan *et al.*, 1998) was identified (Turnbull *et al.*, 2020). The experiments showed that the non-Maxwellian electron distribution functions measured by Thomson scattering (Milder *et al.*, 2020) and inherent to laser produced plasmas (Langdon, 1980; Matte *et al.*, 1988; Milder *et al.*, 2021) modified the CBET resonance [Fig. 49(a)]. When accounting for the modified electron distribution functions in the CBET calculations, the simulations accurately reproduced the measured energy transfer.

The second significant result was obtained by increasing the probe intensity to where the ion-acoustic-wave amplitudes were expected to significantly exceed  $\delta n/n > 1\%$ . These experiments demonstrated the robust nature of the linear CBET models implemented in the hydrodynamics codes, even when nonlinear laser-plasma-instability physics was occurring [Fig. 49(b)]. During the 500 ps high-intensity CBET experiment, the ion temperature was measured to increase by a factor of 7 (120–900 eV), resulting in increased damping of the ion-acoustic waves, which limited the energy transfer to a regime where the linear CBET model accurately reproduced the energy transfer (Hansen *et al.*, 2021). Large vector particle-in-cell (Bowers *et al.*, 2008) simulations demonstrated the physical mechanisms that limited the

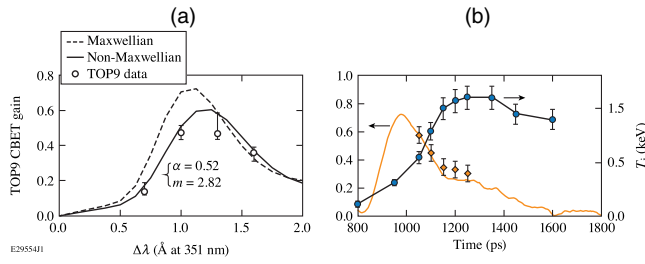


FIG. 49. (a) CBET data (points) measured when energy transfer was relatively low due to the low seed intensities ( $0.4 \times 10^{15}$  W/cm<sup>2</sup>) are shown for conditions where the many overlapping laser beams used to heat the plasma drove non-Maxwellian electron distribution functions. Calculations that assume a Maxwellian electron distribution function (dashed curve) and used the measured non-Maxwellian electron distribution function (solid curve) determined from Thomson scattering (Turnbull *et al.*, 2020). (b) For CBET experiments at higher TOP9 (probe) beam intensities ( $4 \times 10^{15}$  W/cm<sup>2</sup>) where significantly more energy was transferred, the CBET gain was measured (solid curve) to decrease as a function of time. Over this same time period where CBET was active, Thomson-scattering measurements showed a rapid increase in the ion temperature (circles); the final ion temperature was nearly a factor of 2 larger than the electron temperature. When accounting for this increased ion temperature, the linear CBET calculations (diamonds) were in excellent agreement with the measurements (Hansen *et al.*, 2021).

CBET to the linear regime. On fast timescales, the CBET-driven ion-acoustic waves were driven to large amplitudes, where they accelerated ions. The fast ions then equilibrated with the bulk ion distribution function, resulting in an increased ion temperature. Fundamentally, this increase in ion temperature was expected through conservation of energy [Manley-Rowe relations (Manley and Rowe, 1956)] and was explored theoretically in the context of indirect-drive ICF by Michel, Rozmus *et al.* (2012). Although these results show the robustness of linear CBET, one must recognize that CBET inherently transfers energy to the ions, modifying the hydrodynamic conditions, and therefore this physics must be accounted for in hydrodynamic codes to accurately determine the plasma conditions and, subsequently, the laser-plasma instabilities (P. Michel *et al.*, 2013; Strozzi *et al.*, 2017).

Because of the ability of CBET to significantly reduce the hydrodynamic efficiency for direct-drive implosions, concepts for mitigating CBET have been explored (Igumenshchev *et al.*, 2012; Edgell *et al.*, 2017; Bates *et al.*, 2018; Follett *et al.*, 2019). Figure 50 shows the implosion trajectories from direct-drive experiments at the NIF, where the relative frequency of the laser beams was used to reduce CBET and increase the hydrodynamic efficiency by moving the CBET resonances to regions of plasma where energy transfer was less efficient (Marozas *et al.*, 2018b). Although these wavelength detuning concepts are encouraging, they are ultimately complicated by the fact that a reduction in CBET increases the laser intensity near the quarter critical density, making any design using this tactic more susceptible to hot-electron generation by two-plasmon decay or stimulated Raman scattering. To account for both hot-electron

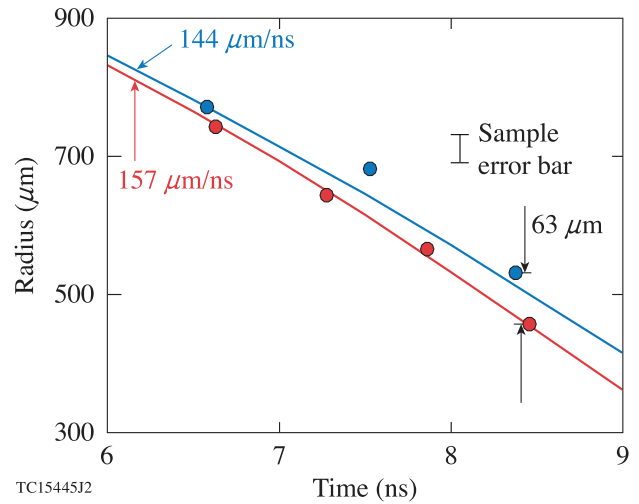


FIG. 50. Equatorial shell trajectories from postprocessed simulated (solid lines) and experimental (symbols) backlit radiographs show improved coupling when the relative frequency between crossing beams is changed. The lower lines and symbols represent the baseline zero frequency detuning experiments. The upper lines and symbols represent the average of the two detuning experiments. From Marozas *et al.*, 2018b.

generation and CBET mitigation, large bandwidth UV lasers (Weaver *et al.*, 2017; Dorrer, Hill, and Zuegel, 2020; Obenschain *et al.*, 2020) are a leading concept (Follett *et al.*, 2019). Significant breakthroughs in both gas laser ( $\Delta\omega/\omega \sim 0.6\%$  at 193 nm) (Obenschain *et al.*, 2020) and solid-state laser technologies ( $\Delta\omega/\omega \sim 5\%$  at 1053 nm) (Dorrer, Hill, and Zuegel, 2020), along with novel broadband frequency conversion concepts ( $\Delta\omega/\omega \sim 1.5\%$  at 351 nm) (Dorrer *et al.*, 2021), are under development. Simulations suggest that increasing the UV bandwidth of the laser beyond  $\Delta\omega/\omega \sim 0.5\%$  (an order of magnitude beyond current UV solid-state laser bandwidths) will mitigate CBET (Bates *et al.*, 2018, 2020), while increasing the bandwidth beyond  $\Delta\omega/\omega > 1\%$  will increase the intensity thresholds for hot-electron generation by factors of several (Follett *et al.*, 2021), allowing current direct-drive designs to be implemented without significant laser-plasma instabilities.

### C. Present status of direct-drive implosion performance and proximity to ignition

Recent progress in direct-drive inertial confinement fusion has considerably improved the prospects for achieving thermonuclear ignition with megajoule-class lasers. When hydrodynamically scaled to laser energies typical of the National Ignition Facility, recent OMEGA implosions are expected to produce about 600 kJ of fusion yield and 74% of the Lawson triple product required for ignition at 1.9 MJ of symmetric illumination. Those implosions have benefited from a significant increase in implosion velocity obtained through larger-diameter targets. A recent statistical approach (Gopalaswamy *et al.*, 2019) used in designing OMEGA targets and laser pulse shapes has demonstrated a considerable predictive capability, thereby enabling the design of targets with improved performance, leading to tripling the fusion

yield, and increasing the areal density. Systematic experiments and statistical modeling were used to identify and quantify the different mechanisms of performance degradation and implosion optimization (Lees *et al.*, 2021), leading to a recent record neutron yield of  $1.74 \times 10^{14}$ .

### 1. Hydrodynamic scaling from OMEGA to megajoule laser energies

Hydrodynamic scaling is a simple way to extrapolate the performance of OMEGA implosions to higher laser energies. This scaling assumes that the same core conditions of hot-spot pressure and shell density achieved at OMEGA can be reproduced at higher energies on a larger spatial scale (Nora *et al.*, 2014).

To keep the hydrodynamics the same at different scales, the target mass and volume must scale with laser energy, the fraction of laser energy coupled to the capsule must be the same, and the shell adiabat must be the same. This leads to scale invariant implosion velocity, stagnation pressure, and shell density. The hydrodynamic scaling relations can be summarized as follows:

$$\text{mass} \sim E_L, \quad R \sim E_L^{1/3}, \quad \frac{E_{\text{kin}}}{E_L} = \text{const}, \quad \alpha = \text{const}, \quad (75)$$

$$v_{\text{imp}} = \text{const}, \quad P_{\text{hs}}^{\text{stag}} = \text{const}, \quad \rho_{\text{sh}}^{\text{stag}} = \text{const}. \quad (76)$$

This simple scaling does not include nonideal effects such as alpha heating, thermal transport, radiation transport, and laser-plasma instabilities. Experimental tests of hydrodynamic scaling from OMEGA to the NIF have been limited and thus far limited to cylindrical geometry (for instability growth diagnosability) (Sauppe *et al.*, 2020). In a spherical geometry, thermal transport is not scale invariant because the heat losses depend on the volume-to-surface ratio. At larger scale the ratio volume/surface  $\sim R$  increases with size  $R$ , leading to lower thermal losses from the hot spot and higher hot-spot temperatures.

This can be shown by using the mass conservation equation for the hot spot (Betti *et al.*, 2001)

$$\dot{M}_{\text{hs}} = 4\pi R_{\text{hs}}^2 \dot{m}_a, \quad (77)$$

where  $M_{\text{hs}}$  is the hot-spot mass and  $\dot{m}_a$  is the ablation rate off the shell inner surface into the hot spot. The ablation rate scales as  $\dot{m}_a \sim \kappa_{\text{Sp}}(T_0^{\text{hs}})/R_{\text{hs}}$ , where  $T_0$  is the hot-spot central temperature,  $\kappa_{\text{Sp}} \sim T^{5/2}$  is Spitzer thermal conductivity, and the hot-spot mass is  $\rho_{\text{hs}} V_{\text{hs}} \sim P_{\text{hs}} V_{\text{hs}}/T_{\text{hs}}$ . Using the previously mentioned scaling relations and substituting the deceleration time scaling  $t_{\text{dec}} \sim R_{\text{hs}}/v_{\text{imp}}$  into Eq. (77) leads to

$$T_{\text{hs}} \sim (P_{\text{hs}} R_{\text{hs}} V_{\text{imp}})^{2/7}. \quad (78)$$

For hydrodynamic equivalent implosions with constant  $P_{\text{hs}}$  and  $v_{\text{imp}}$ , the hot-spot temperature increases with size and laser energy as

$$T_{\text{hs}} \sim R_{\text{hs}}^{2/7} \sim E_L^{2/21}. \quad (79)$$

Equation (79) enables the derivation of the scaling of the fusion yield in the absence of alpha heating ( $Y_{\text{no}\alpha}$ ). For a 50-50 DT plasma, the neutron yield can be written as

$$Y \sim \frac{1}{4} n_i^2 \langle \sigma v \rangle V_{\text{hs}} \tau = \frac{1}{16} P_{\text{hs}}^2 \frac{\langle \sigma v \rangle}{T_{\text{hs}}^2} V_{\text{hs}} \tau, \quad (80)$$

where  $\tau$  is the burn duration or confinement time. For ignition relevant hydrodynamic equivalent implosions, the no- $\alpha$ -particle hot-spot temperature is in the 4–6 keV range where  $\langle \sigma v \rangle \sim T^3$ , the no- $\alpha$ -particle pressure and velocity are invariant, the volume scales as  $V_{\text{hs}} \sim R_{\text{hs}}^3$ , and the confinement time scales as  $\tau \sim R_{\text{hs}}/v_{\text{imp}}$ , leading to

$$Y_{\text{no}\alpha} \sim P_{\text{hs}}^2 T_{\text{hs}} R_{\text{hs}}^4 / v_{\text{imp}} \sim T_{\text{hs}} R_{\text{hs}}^4 \sim R_{\text{hs}}^{30/7} \sim E_L^{10/7}. \quad (81)$$

While the size scaling of the hot-spot thermal transport can be easily taken into account in one-dimensional hydrodynamic scaling, lower heat losses lead to lower ablative stabilization of the deceleration phase Rayleigh-Taylor instability (Betti *et al.*, 2002), thereby affecting the three-dimensional evolution. At larger scales, more bremsstrahlung radiation is trapped by the hot spot and shell. This improves the shell stability during the deceleration phase by increasing the density gradient scale length at larger scales. This stabilizing effect counteracts the destabilization from lower ablation velocity at larger scales such that the overall Rayleigh-Taylor growth factor during the deceleration phase is approximately scale invariant (Bose *et al.*, 2015).

With regard to the thermal transport from the coronal plasma to the ablation front, the diffusive component is approximately scale invariant because it is planar in nature as long as the distance between the critical surface and the ablation front is much smaller than the target radius. Instead, the nonlocal effects vary with scale because the ratio of the electron mean free path to target size is not scale invariant but decreases at larger scales. Changes in coronal thermal transport, laser energy absorption, and cross-beam energy transfer occurring at different scales are combined into a single parameter: the laser-to-capsule energy coupling  $\eta_k = (\text{shell kinetic energy})/(\text{laser energy}) = E_{\text{kin}}/E_L$ . Because of the large uncertainties in the scaling of energy coupling for direct drive and the lack of relevant experimental data at megajoule energies, dedicated experiments are under way at the NIF to assess the value of  $\eta_k$ . Within the frame of the hydrodynamic scaling, the value of  $\eta_k$  is assumed to be scale invariant.

The next step is to assess the effect of alpha heating, which becomes important at megajoule scales. For this, we apply the analytic theory of Betti *et al.* (2015) and Gopalaswamy *et al.* (2019) that approximates the yield amplification from alpha heating using

$$\hat{Y}_{\text{amp}} \equiv \frac{Y_{\alpha}}{Y_{\text{no}\alpha}} \simeq \frac{1}{(1 - 0.96\chi_{\text{no}\alpha})^{0.75}}, \quad (82)$$

where  $\chi_{\text{no}\alpha}$  is the no-alpha normalized Lawson parameter  $P_{\text{hs}} \tau / [P \tau]_{\text{ign}}$  rewritten in terms of the neutron yield and areal density as

$$\chi_{\text{no}\alpha} = \rho R^{0.61} \left( \frac{0.12 Y_{\text{no}\alpha}^{16}}{M_{\text{stag}}} \right)^{0.34}. \quad (83)$$

In Eq. (83)  $\rho R$  is the total neutron-averaged areal density in  $\text{g}/\text{cm}^2$ ,  $Y_{\text{no}\alpha}^{16}$  is the no-alpha-particle neutron yield in units of  $10^{16}$ , and  $M_{\text{stag}}$  is the stagnating DT mass at implosion time in milligrams. For ignition relevant direct-drive targets the stagnating mass is about half of the unablated DT mass ( $M_{\text{stag}} \simeq M_{\text{unabl}}/2$ ).

As shown by Lindl *et al.* (2018), Christopherson, Betti, and Lindl (2019), and Christopherson *et al.* (2020), the normalized Lawson parameter (sometimes rewritten in different forms) is suitable for describing all the different thermonuclear regimes of ICF implosions, from weak alpha heating to burning plasmas and up to the onset of ignition. The scaling of the Lawson parameter with size and energy follows the scaling of the confinement time  $\chi \sim \tau \sim R \sim E_L^{1/3}$ , leading to the following hydrodynamic scaling formulas for the fusion yield from OMEGA to NIF energies of symmetric illumination:

$$Y_{\text{no}\alpha}^{\text{NIF}} = Y_{\text{no}\alpha}^{\text{OMEGA}} E_{\text{ratio}}^{10/7}, \quad (84)$$

$$\chi_{\text{no}\alpha}^{\text{NIF}} = \chi_{\text{no}\alpha}^{\text{OMEGA}} E_{\text{ratio}}^{1/3}, \quad (85)$$

$$\hat{Y}_{\text{amp}} = (1 - 0.96 \chi_{\text{no}\alpha}^{\text{NIF}})^{-0.75}, \quad (86)$$

$$Y_{\alpha}^{\text{NIF}} = Y_{\text{no}\alpha}^{\text{NIF}} \hat{Y}_{\text{amp}}. \quad (87)$$

where  $E_{\text{ratio}} = E_L^{\text{NIF}}/E_L^{\text{OMEGA}}$  is the laser energy ratio between NIF and OMEGA. We emphasize that the OMEGA laser-beam configuration is spherically symmetric, and therefore the aforementioned hydroscaling relations apply only to a spherical symmetric illumination similar to 60-beam OMEGA. This scaling does not account for the polar laser configuration at the NIF, which is expected to significantly degrade the implosion performance.

## 2. Current OMEGA implosion performance and proximity to hydrodynamic scaled ignition

The highest fusion performance of OMEGA DT-layered implosions was achieved in 2018–2021 using larger size capsules with an outer radius 12%–23% larger than the laser-beam radius. Statistical modeling of experimental and simulation databases has enabled the development of an accurate predictive capability (Gopaldaswamy *et al.*, 2019) used to design higher performance implosions.

Figure 51 shows contours of constant fusion yield of high performance OMEGA implosions extrapolated to 1.9 MJ of symmetric illumination using the aforementioned hydrodynamic scaling relations. Three sequential experimental campaigns (“phases”) are shown to indicate the advances in fusion yield since 2015 at OMEGA when the milestone core pressure of 50 Gbar was achieved (Bose *et al.*, 2016; Regan *et al.*, 2016). The neutron yield increased from  $(4\text{--}5) \times 10^{13}$  in 2015 to  $(1.5\text{--}1.7) \times 10^{14}$  in 2018–2021. This increase was accomplished by driving the implosions on high adiabats of about  $\alpha_F \simeq 5$  and using larger size shells with an outer radius

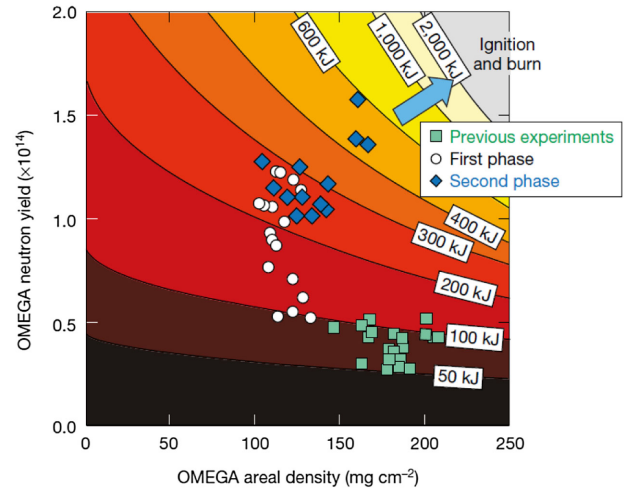


FIG. 51. Results from three sequential implosion campaigns at OMEGA extrapolated to 1.9 MJ of symmetric illumination using the hydrodynamic scaling relations. The contours represent curves of constant extrapolated fusion yield (in kJ) (squares, circles, and diamonds are in a temporal sequence starting in 2015). The arrow points in the direction of future experiments. The increase in yield since 2015 resulted in implosions that would produce about 500–600 kJ of fusion energy at NIF laser energies of 1.9 MJ, with about a third of the yield from hydrodynamic compression and two-thirds from alpha-particle self-heating. From Gopaldaswamy *et al.*, 2019.

larger than the laser-beam radius to improve the laser energy coupling to the capsule, which is partially due to CBET mitigation (Igumenshchev *et al.*, 2013).

As shown in Fig. 51, if the same hydrodynamic no-alpha-particle core conditions of the best OMEGA implosions are achieved at a larger spatial scale (hydrodynamic scaling) to match the higher laser energy of NIF (about 4 times in spatial scale from OMEGA to the NIF), the expected fusion yield at NIF scale is about 600 kJ. While such a yield would represent significant progress in performance, it is still well below the requirements for ignition.

The proximity to ignition is better identified by the value of the no-alpha-particle Lawson parameter requiring  $\chi_{\text{no}\alpha} \simeq 1$  for ignition. Figure 52 shows the fusion yield of OMEGA

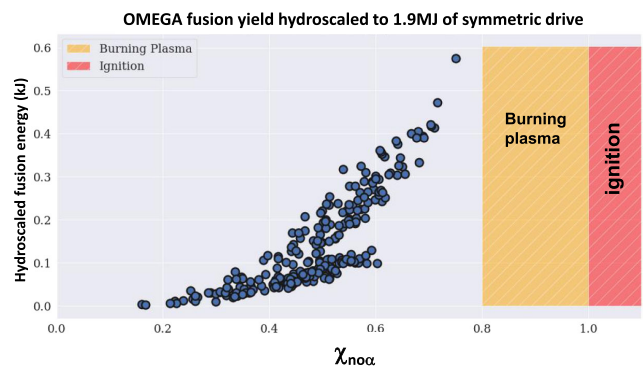


FIG. 52. Fusion yield of OMEGA DT-layered implosions hydrodynamically scaled to 1.9 MJ of symmetric illumination vs the no-alpha-particle Lawson parameter scaled to 1.9 MJ. Courtesy of V. Gopaldaswamy (LLE).

implosions scaled to 1.9 MJ of laser energy versus the no-alpha-particle Lawson parameter. The best performing OMEGA implosions achieved an areal density of about  $0.16 \text{ g/cm}^2$  and a yield of  $(1.5\text{--}1.7) \times 10^{14}$ , with a stagnated mass of  $\sim 0.011 \text{ mg}$  and a laser energy of 27 to 28 kJ. The corresponding Lawson parameter is  $\chi_{\text{no}\alpha} \approx 0.18$ . After scaling  $\chi_{\text{no}\alpha}$  to 1.9 MJ of laser energy using  $E_{\text{ratio}}^{1/3} \approx 4.1$ , the scaled Lawson parameter is  $\chi_{\text{no}\alpha}^{1.9\text{MJ}} \approx 0.74$ . This indicates that about a 50% increase in the Lawson parameter is required to achieve the ignition conditions at the NIF scale for symmetric illumination and hydrodynamic equivalent implosions.

Statistical modeling is also used to quantify the differing degradation mechanisms affecting OMEGA implosions (Lees *et al.*, 2021). The fusion yield is found to be reduced by the ratio of laser beam to target radius (a proxy for the illumination nonuniformities from the OMEGA beam geometry), where the asymmetry in inferred ion temperatures (a measure of the magnitude of the  $\ell = 1$  mode from target offset, laser mispointing, and LPI), the time span over which tritium fuel has decayed (a measure of the  $\text{He}^3$  accumulation from tritium decay) and parameters related to the implosion hydrodynamic stability such as in-flight adiabat and aspect ratio. The recent record fusion yield of  $1.74 \times 10^{14}$  at OMEGA was achieved using a 1.02 mm outer diameter capsule and implementing active mitigation of the  $\ell = 1$  mode using a preimposed target offset (Mannion *et al.*, 2021). When adjusted for tritium decay and  $\ell = 1$  mode, the highest yield in OMEGA cryogenic implosions is predicted to exceed  $2 \times 10^{14}$  fusion reactions (Lees *et al.*, 2021).

### 3. Polar direct drive

An alternative laser-direct-drive approach (Skupsky *et al.*, 2004; Craxton *et al.*, 2005) called polar direct drive is being pursued as a means to perform laser-direct-drive experiments at the National Ignition Facility (Campbell *et al.*, 2017; Goncharov *et al.*, 2017; Regan *et al.*, 2019) without extensive facility modifications. Since a primary goal of the National Ignition Facility is to achieve ignition and modest gain first with laser indirect drive and then with laser direct drive, the facility is optimized only for laser indirect drive (Spaeth *et al.*, 2016). The two approaches have different requirements for the arrangement of laser beams around the target chamber and phase plates controlling the shape of the laser spot on target. The laser beams at the National Ignition Facility are directed through polar-beam ports in each hemisphere of the spherical target chamber [see Fig. 53(a)] to optimize the laser energy coupling to the cylindrical hohlraum for laser indirect drive (Campbell and Hogan, 1999). The hohlraum is positioned at the center of the chamber with its symmetry axis aligned with the vertical axis, and the polar-beam ports have cone angles with respect to the vertical axis of  $23.5^\circ$ ,  $30.0^\circ$ ,  $44.5^\circ$ , and  $50.0^\circ$ , which are referred to as rings 1, 2, 3, and 4, respectively. The phase plates at the National Ignition Facility are designed to form an elliptical focal spot that passes through the laser entrance hole of the hohlraum. For laser direct drive, the optimal beam configuration to maximize on-target laser irradiation uniformity and the energy coupling from the laser to the target is to have the beams uniformly distributed around the target with a normal incidence on the target [i.e.,

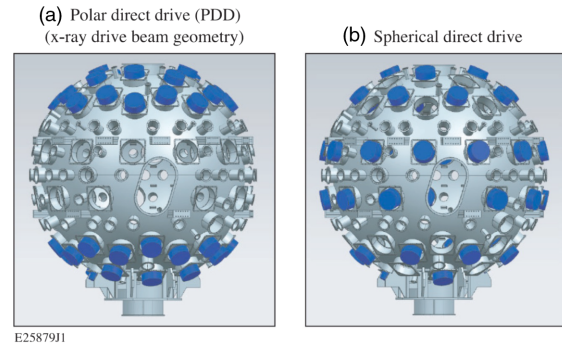
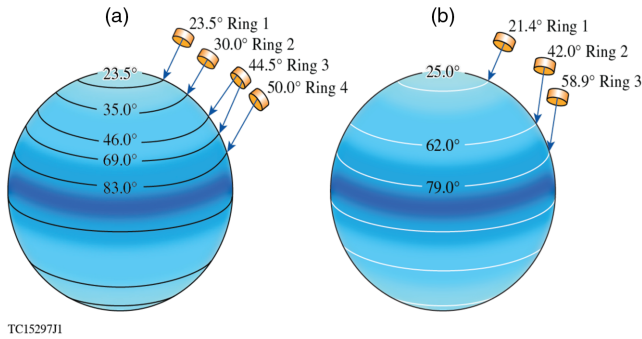


FIG. 53. (a) Mechanical drawing of the target chamber for the National Ignition Facility, with the blue cylinders indicating the beam port positions used for laser indirect drive (i.e., x-ray drive). Polar direct drive uses this beam geometry. (b) Same as (a) except for spherical direct drive, where the beams are spread uniformly around the target chamber. This is the ideal beam arrangement for laser direct drive. From Hohenberger *et al.*, 2015.

spherical direct drive; see Fig. 53(b)], and to have the laser spot size comparable to the target diameter (Craxton *et al.*, 2015). Polar-direct-drive target designs absorb a smaller fraction of the incident laser irradiation than spherical direct-drive designs (Skupsky *et al.*, 2004; Craxton *et al.*, 2005). Although the target chamber of the National Ignition Facility has beam ports for laser direct drive as well as laser indirect drive, switching from the current laser-indirect-drive configuration to the laser-direct-drive one requires a major, resource- and time-intensive engineering effort.

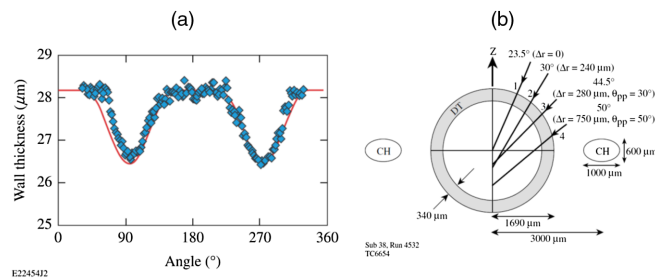
The polar-direct-drive concept was considered during the planning stages of the National Ignition Facility (Eimerl, 1995a, 1995b; Eimerl *et al.*, 1995). In contrast to spherical direct drive, each ring of the NIF polar beams are uniquely repointed toward the equator of the target and defocused for polar direct drive to minimize the laser-driven asymmetry on target (i.e., the elliptical laser spots formed with the laser-indirect-drive phase plates are defocused to match the size of the target diameter). Proof-of-principle polar-direct-drive implosions were performed on the OMEGA laser system (Boehly *et al.*, 1997) using 40 of the 60 beams (Craxton and Jacobs-Perkins, 2005; Marozas *et al.*, 2006; Marshall *et al.*, 2006). The beam repointing schemes for polar direct drive of the National Ignition Facility and the OMEGA laser are shown in Fig. 54. Low-convergence ( $\text{CR} \leq 10$ ) polar-direct-drive implosions that are less susceptible to laser imprint have been conducted on the National Ignition Facility by repointing and defocusing the laser beams (Cobble *et al.*, 2012; Radha *et al.*, 2012, 2016; Hohenberger *et al.*, 2015; Zylstra *et al.*, 2020b; Marozas, 2021; Yeamans *et al.*, 2021). Defocusing a laser beam smoothed with a phase plate is a compromise since it could lead to undesirable modulations in the far-field intensity spatial profile. Assessing implosion performance degradation due to the polar-direct-drive geometry compared to spherical direct drive is a key issue for the laser-direct-drive ignition approach (Radha *et al.*, 2012, 2013, 2016; Hohenberger *et al.*, 2015). In addition, target solutions are being investigated to improve the symmetry of a polar-direct-drive implosion by contouring the shell to alter the mass distribution in the ablator shown in Fig. 55(a) (Marshall *et al.*, 2016) and using a Saturn



TC1529711

FIG. 54. Beam repointing schemes for polar direct drive of (a) the National Ignition Facility and (b) the OMEGA laser. The cylinders to the upper right of each image indicate the beam port locations and ring identifications, and the blue arrows indicate the beam repointing to the polar angles shown on target to achieve optimized laser-driven symmetry in the polar-direct-drive geometry. From Marshall *et al.*, 2016.

target shown in Fig. 55(b) (Craxton and Jacobs-Perkins, 2005; Marshall *et al.*, 2006) (i.e., the addition of a low- $Z$  ring around the capsule equator, where refraction in the plasma formed around this ring permits time-dependent tuning of the capsule drive uniformity). Implosion symmetry, energy coupling (Marozas *et al.*, 2018a, 2018b; Zylstra *et al.*, 2020a), preheat (Rosenberg *et al.*, 2018b, 2020; Michel *et al.*, 2019; Solodov *et al.*, 2020), and laser imprint (Hohenberger *et al.*, 2016) have been investigated at the National Ignition Facility for polar direct drive (Radha *et al.*, 2012, 2013, 2016; Hohenberger *et al.*, 2015; Marozas, 2021). As shown in Fig. 50, proof-of-principle experiments using a modest level of wavelength detuning (i.e.,  $\pm 2.3 \text{ \AA}$  in the ultraviolet) demonstrated an increase in the energy coupling of polar-direct-drive implosions at the National Ignition Facility. Polar-direct-drive implosions of DT-filled capsules at the National Ignition Facility for neutron effect experiments have produced up to



E224542

FIG. 55. Target solutions investigated to improve the implosion symmetry of polar-direct-drive implosions. (a) The measured contoured-shell thickness (diamonds) as a function of polar angle is compared to the ideal contoured profile. Reducing the mass around the equator of the target compensates for the reduced energy coupling of polar direct drive in this region. From Marshall *et al.*, 2016. (b) Depicted addition of a low- $Z$  ring around the capsule equator, where refraction in the plasma formed around this ring permits time-dependent tuning of the capsule drive uniformity. From Craxton and Jacobs-Perkins, 2005.

33.6 kJ of fusion output with 1.26 MJ of ultraviolet laser energy (Yeaman *et al.*, 2021).

The higher convergence ratio ( $CR \geq 20$ ) polar-direct-drive implosions needed for ignition designs at the National Ignition Facility require facility modifications (Campbell *et al.*, 2021; Marozas, 2021). Facility enhancements to the on-target laser-driven uniformity include polar-direct-drive phase plates; high-contrast, multiple-picket pulse shaping; beam smoothing with multifrequency modulation smoothing by spectral dispersion (Hohenberger *et al.*, 2016) or 2D smoothing by spectral dispersion (Skupsky *et al.*, 1989; Regan *et al.*, 2005) and possibly polarization smoothing (Boehly *et al.*, 1999); as well as  $6 \text{ \AA}$  UV wavelength detuning with beam remapping (Collins *et al.*, 2012; Collins and Marozas, 2018; Marozas *et al.*, 2018a, 2018b; Marozas, 2021). Facility enhancements to the DT cryogenic target-handling system are required [i.e., a scaled-up version of the OMEGA fill-tube DT cryogenic target-handling system at the National Ignition Facility (Harding *et al.*, 2018)]. Target solutions to mitigate preheat are needed (Solodov *et al.*, 2020). The use of silicon ablaters was found to mitigate the hot-electron preheat by increasing the threshold laser intensity for hot-electron generation from  $3.5 \times 10^{14}$  in plastic to  $6 \times 10^{14} \text{ W/cm}^2$  in silicon. The overall hot-electron production is also reduced in silicon ablaters when the intensity threshold is exceeded. The laser-beam smoothing, laser pulse shaping, wavelength detuning, and DT cryogenic target-handling system (Gibson *et al.*, 2009; Johal *et al.*, 2009) on the National Ignition Facility (Spaeth *et al.*, 2016) are all optimized for laser indirect drive and do not meet the requirements of laser direct drive (Hansen, 2012; Marozas, 2021). Each of the proposed changes is required for laser direct drive, regardless of whether the National Ignition Facility is configured for polar direct drive or spherical direct drive. The only differences between polar direct drive and spherical direct drive would be the population of optics in the equatorial ports for spherical direct drive and differing phase-plate details between the two approaches.

The strategy for polar-direct-drive research over the next decade on the National Ignition facility is defined by four physics goals (Campbell *et al.*, 2021; Marozas, 2021). The first goal is to optimize symmetry for low-convergence ( $CR \leq 10$ ), warm polar-direct-drive implosion (i.e., DT-filled capsules using plastic or an alternative ablator) using the current National Ignition Facility configuration, pulse shaping, beam pointing, and target solutions (i.e., contouring or shimming and a Saturn ring), with a goal of achieving a 50 kJ fusion yield. The second goal is to improve the energy coupling and symmetry for  $CR \leq 10$ , warm polar-direct-drive implosions using wavelength detuning with beam remapping and polar-direct-drive phase plates. Beam remapping is needed to satisfy the polar-direct-drive requirement that the crossing beams at the target equator have different wavelengths with a wavelength detuning of  $6.0 \text{ \AA}$ . The wavelength detuning is needed to mitigate cross-beam energy transfer and increase the energy coupling (Marozas *et al.*, 2018a, 2018b). The goals for this stage of the research are to achieve a laser absorption exceeding 85% and a fusion yield of 100 kJ with these modifications. The third and fourth goals require the modifications of a laser-direct-drive cryogenic target-handling

system and laser-beam smoothing at the National Ignition Facility to increase the convergence ratio to 15 and then to 20 with a polar-direct-drive DT cryogenic implosion for the alpha burner and burning-plasma regime (i.e., 1 MJ fusion yield) designs, respectively. A ten-year plan is needed to implement polar-direct-drive upgrades at the National Ignition Facility to optimize the performance of polar-direct-drive *DT* cryogenic implosion targets in the burning-plasma regime, and to understand the laser facility requirements (i.e., energy, power, size, laser-beam smoothing, etc.) needed to achieve ignition and multimegajoule yield. The physics program under way at OMEGA and the NIF will inform and validate these modifications (Campbell *et al.*, 2017; Goncharov *et al.*, 2017; Regan *et al.*, 2019).

## V. MAGNETIC-DRIVE IMPLOSIONS

### A. History of pulsed power fusion

#### 1. Development of pulsed power

In this section the developments of pulsed power leading to the Z pulsed power facility (Z) as a driver of fusion experiments are described. This narrative is based on a review by Smith (2006), a Sandia National Laboratories report (Van Arsdall, 2007), and a book by Martin (1996). In addition, Martin (1996) and Van Arsdall (2007) included numerous references to works on the early pulsed power devices that are described in this section. Another recent review of work on the Z pulsed power accelerator was given by Sinars *et al.* (2020).

In 1960 a group at the Atomic Weapons Research Establishment (AWRE) headed by J. C. “Charlie” Martin first developed x-ray sources to radiograph explosive events. The first source used a radio frequency accelerator to generate a 35 MeV electron beam that was focused onto a high-atomic-number target to produce x-ray photons by bremsstrahlung. Although the system worked, much higher intensities were desired. Martin was convinced that a high voltage ( $\sim 6$  MV) delivered to a pair of electrodes separated by a vacuum gap would not simply break down if the pulse length was short (tens of nanoseconds) but would generate an electron beam with  $\sim 100$  kA of current. For this purpose, the AWRE group developed stacked stripline pulse generators. Transmission lines formed by two planar electrodes separated by dielectric insulating material (usually polyethylene) were charged by a simple capacitor bank. These transmission lines stacked in a Blumlein configuration delivered the charge voltage to an electron accelerating gap. The two-way transit time along each of the transmission lines determined the pulse length. An early machine built in 1961 named Dagwood used 10 ft long transmission lines to produce a 1.5 MV voltage pulse of 20 ns duration. In this section we refer to pulsed devices as machines, although they are often referred to as accelerators. Dagwood was used to develop electron tubes. The accelerating gap of an electron tube must operate in vacuum to avoid electric breakdown. The interface between the insulator and the vacuum is subject to surface breakdown. AWRE found that avalanche breakdown could be minimized by orienting this surface at an angle to the electric field, so the electrons were driven away from the surface to avoid

secondary ionization. This work led to the vacuum insulator stack configuration used in modern machines. The AWRE group then built a larger machine named Six Megavolt or Goodbye (SMOG), using 20 solid dielectric Blumlein transmission lines charged in parallel to 200 kV and then switched in series to generate a 4 MV pulse to drive electron tubes to radiograph explosive events.

The need to test the effects of prompt gamma rays and soft x rays on nuclear weapon components grew in the early 1960s. Devices existed that could test small volumes, but larger machines were required to test military components. The U.S. Government agencies contracted the development of nuclear weapons effects simulators (NWES) to industry. Sandia National Laboratories was given the responsibility for the simulation of warhead packages. In 1964, AWRE delivered to Sandia a machine similar to SMOG, which produced a pulse of 4.5 MV and a radiation dose of about 15 rad at 1 m. Prompt gamma-ray simulation work was done with this machine until 1967, but the machine was difficult to operate. The solid dielectric switches had to be replaced after every shot.

At that time, Physics International (PI) was designing an operationally convenient and more powerful machine using Marx banks and Blumlein modules both insulated by transformer oil. At the end of 1964, the Pulserad 730 was operational, producing a 50 kA, 4 MV, 40 ns pulse that could deliver 50 rad at 1 m. PI named this new technology pulsed power.

In 1967 the Defense Atomic Support Agency asked for proposals to build a machine capable of delivering 50 krad. This led to the development of the “Aurora” machine, which had four Marx-oil Blumlein modules delivering power to four electron tubes. Switches with adequate time jitter to synchronize these modules were developed, which led to the modern approach of modular accelerators. Moreover, electrical power was delivered 3 m to the electron tubes via vacuum coaxial transmission lines with electrons not crossing the gap due to the magnetic field generated by the current. This was the first demonstration of self-magnetically insulated transmission lines (MITLs), which are still used in modern pulsed power machines such as Z.

The pulsed power machines described thus far were high impedance, i.e., high voltage and low current. These machines were suitable for simulating the prompt gamma-ray flash from a weapon with many MeV photons, but there was a need for lower energy x rays ( $< 1$  MeV). In 1967, NRL built the low impedance Gamble I machine designed to deliver  $< 1$  MV, 1 MA, 50 ns pulses. Gamble I used water rather than oil for a dielectric in the pulse forming lines, which increased the permittivity by a factor of about 6 and thus reduced their length. The current rise time of a switch at a voltage ( $\mathcal{V}$ ) is limited by the inductive voltage of the switch, i.e.,  $\mathcal{V} = L di/dt$ . Simply increasing the voltage does not help, because the switch gap, and thus  $L$ , will need to be increased. This was not a problem for previous low current machines. Gamble I used switches with multiple channels to overcome this problem. Marx generators charged intermediate storage capacitors that were then discharged into the pulse forming lines. These were switched in 200 ns at 500 kA to 2 MV to a transmission line transformer, which increased the current and lowered the voltage. This scheme further reduced  $di/dt$  in the

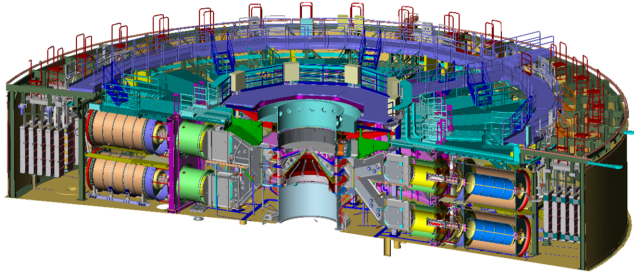


FIG. 56. Z at Sandia National Laboratories.

switches. NRL's 1 TW Gamble II, built in the mid 1970s to generate electron beams at  $1 \text{ MA/cm}^2$ , was based on similar technology.

Dagwood, Aurora, Gamble I, and Gamble II demonstrated several important technologies used in modern modular pulsed power machines. Further developments such as low jitter triggered gas switches developed at Sandia allowed the construction of Particle Beam Fusion Accelerator (PBFA) I (now Saturn) and PBFA II, which was reconfigured to the present Sandia Z machine, which we refer to simply as Z. Z has 36 parallel modules delivering power radially inward; see Fig. 56. Each module starts with a Marx generator that charges an intermediate storage capacitor. Triggered gas switches transfer this energy into pulse forming lines. Multichannel water switches then transfer the energy to transformer transmission lines. The Marx generators are immersed in a tank containing oil, and the rest of the components are immersed in deionized water. At a radius of 1 m, an insulator stack separates the water section from the inner vacuum section. The stack is similar to those designed at AWRE for electron tubes. Four levels of disk-shaped transmission lines propagate the power inward toward the load. These transmission lines use the principle of self-magnetic insulation that was demonstrated on the Aurora machine. These four levels are connected in parallel to increase the current by a posthole convolute at a radius near the load. Power is then delivered to the load by a single MITL referred to as the final feed. The Z machine delivers 18–28 MA, depending on the impedance of the loads.

## 2. Electron-beam-driven fusion

In the 1960s electron-beam-driven bremsstrahlung sources were providing multimegavolt photons, which could be used to simulate the effects of the prompt gamma rays. However, intense x-ray sources at lower photon energies were still needed. Lower voltage high-current machines were being built to provide this need. Winterberg (1968) proposed that such electron beams could be used to drive ICF implosions in a manner similar to that of lasers. Al Narath and Everet Beckner started an electron-beam-driven fusion program at Sandia in 1973, with help from NRL using Gamble I and Gamble II, motivated by NWES and the possible generation of commercial electricity, and hired Gerald Yonas, then at PI, to head that new program. Such fusion explosions would provide the needed soft x rays (Van Arsdaal, 2007). Numerical simulations of capsules driven by 1 MeV electron beams indicated that extremely high electron-beam current

(360 MA), current density on target ( $1400 \text{ MA/cm}^2$ ), and beam intensity on target ( $\sim 1400 \text{ TW/cm}^2$ ) would be needed (Sweeney and Clauser, 1975), but the much higher energy efficiency of pulsed power (5%–10%) as compared to Nd lasers ( $<1\%$ ) was a strong motivation. It was demonstrated that electron beams could be focused to current densities of  $5 \text{ MA/cm}^2$  (Yonas *et al.*, 1973), but the stopping distance was too large to effectively couple to an ablatively driven capsule. The low energy deposition per unit mass resulted in low implosion velocities, even when the beam was allowed to pass through the shell. Nevertheless, a magnetized target driven by an electron beam did produce measurable deuterium-deuterium (DD) fusion neutrons of  $\sim 10^6$  (Chang *et al.*, 1977; Widner *et al.*, 1977). That result may have been the first successful demonstration of magnetoinertial fusion (MIF) (Lindemuth and Kirkpatrick, 1983) because bremsstrahlung generated in the outer shell of the target preheated the fuel, thereby decreasing the hydrodynamic efficiency of the compression of the fuel. However, scaling to higher yields with electron beams did not look promising. Sweeney and Farnsworth (1981) did evaluate a class of high-gain ICF targets that were postulated to be driven by electrons or light ions that included magnetic thermal insulation of the low-density fuel as well as a cryogenic fuel layer. The reduced fuel losses and higher fuel adiabat produced ignition and burn at lower power and intensity than without the magnetic field. The results were somewhat simplistic, however, since the fuel physics would clearly have had two-dimensional features, and such codes were not available at that time.

## 3. Ion-beam-driven fusion

The stopping range of ions is much smaller for electrons at a given voltage, which in principle alleviates this problem. Magnetically insulated diodes demonstrated the feasibility of generating intense ion beams (Dreike *et al.*, 1976). Numerical simulations indicated that a 10 MA, 10 MV proton beam could drive a break-even capsule (Clauser, 1975). Slutz (1995) proposed and provided analytical estimates of performance of a target that converted the light ion beam energy into x rays to drive the capsule. The target consists of a spherical gold shell filled with CH foam that contains a radiation-driven fusion capsule similar to those now being shot on NIF; see Fig. 25. In this design the ion beam, which is focused radially inward, penetrates the gold shell and stops in the foam, where it deposits most of its energy. The hot foam emits x rays that are trapped within the gold shell, forming a radiation-filled hohlraum. The radiation is symmetrized in the same manner as the laser-indirect-drive hohlraums discussed in Sec. III. Furthermore, the radiation intensity is higher than the beam intensity due to a “greenhouse effect.” The light ions have a relatively long range in gold because most of the electrons are bound. Thus, they penetrate easily, as does visible light through glass. The ion range is shorter in the low-atomic-number CH foam because there are more free electrons to interact with the moving ion. Consequently, the ion energy is absorbed in the foam as is the visible light absorbed by the floor of a greenhouse. The gold shell has a high opacity to the x-rays emitted by the foam and so the radiation is trapped just as glass is opaque to the infrared emitted by the heated floor of

a greenhouse. Thus, both the beam intensity and symmetry requirements are reduced. With these promising developments, Sandia switched from an electron beam to a light ion fusion program. During this period Sandia built PBFA-I and PBFA-II to test ion diodes. The most studied ion diode was the applied magnetic-field diode (Johnson *et al.*, 1985), which used external coils that generated a magnetic field of 2–3 T to allow ions, but not electrons, to cross the accelerating gap. Electrons emitted by the cathode formed a cloud of negative space charge that acted as a virtual cathode. The anode surface was designed to break down electrically to form a source of ions. Since the breakdown involved hydrocarbons, the dominant ions were protons. The anode surface had a shape similar to a barrel to focus the ion beam to the cylindrical axis. However, the beams did not form a tight focus due to high emittance and the diode impedance decreased with time, which reduced the coupling of energy to the beam. The beam intensity at the focus was  $1.5 \text{ TW/cm}^2$ , which was much too low to drive ICF capsules since more than  $30 \text{ TW/cm}^2$  would be required.

Protons with an energy of 4 MeV at a nearly optimal range in an indirect-drive ion target design (Slutz, 1995) and lithium ions with 30 MeV have nearly the same range. A new approach was then pursued based on inductive energy storage and plasma opening switches (Cook *et al.*, 1986; Mendel *et al.*, 1987) to accelerate lithium ions to 30 MeV. The idea was to build up magnetic energy over about 100 ns by driving current through the MITLs into a plasma opening switch that would initially be in a conducting mode. The switch would then open quickly to generate high voltage, much like the ignition system in older cars. In principle, this would multiply the power. Unfortunately, the switches did not open quickly into anything but a low impedance load, i.e., not into an ion diode.

There were other problems as well. The beams were not pure lithium, but due to the relatively poor vacuum ( $\sim 10^{-5}$  Torr) were contaminated with hydrocarbons (Quintenz *et al.*, 1996). Cuneo *et al.* (Cuneo *et al.*, 1997) developed cleaning techniques that removed most of these impurities (Cuneo, 1999). Perhaps the most damaging problem was that an instability in the ion accelerating gap led to unacceptably large emittance despite attempts to control that instability (Desjarlais *et al.*, 1991). The instability induced fluctuations allowed the electrons to diffuse toward the anode, which lowered the diode impedance over time. Solutions were proposed (Slutz, 1987), but these were not successful.

A probable explanation is that charge exchange of the beam ions with neutral ions in the anode plasma also contributed to a falling impedance of the diode (Litwin and Maron, 1989; Pointon, 1989). In the end, the beam intensity needed to drive fusion capsules with light ions was not achieved.

#### 4. Z-pinch-driven indirect drive

During the period that light ions were the main approach to pulsed power fusion, a small group at Sandia was studying the generation of x rays with fast Z pinches. The motivation of this research was the need to test the radiation effects of intense soft x rays ( $<5 \text{ keV}$ ) on weapon components. Electron-beam-driven bremsstrahlung sources were not adequate to test these effects, so alternative approaches were

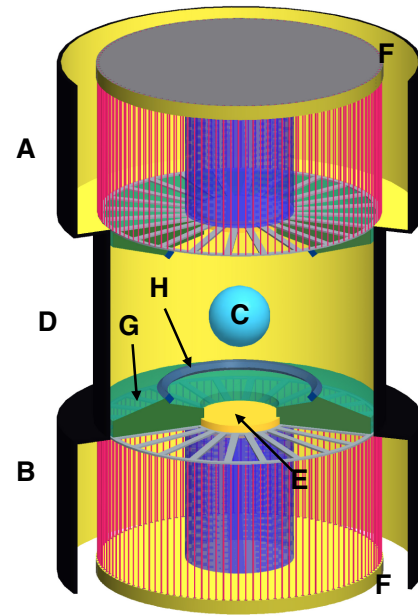


FIG. 57. Double-ended Z-pinch hohlraum concept, with (a) top and (b) bottom primary hohlraums, with each containing a notional wire-array Z pinch with an internal pulse-shaping target, (c) a high-yield fusion capsule, (d) a secondary hohlraum containing the capsule, (e) an on-axis permanent shine shield and radial spoke electrode structures, (f) upper and lower electrical power feeds, (g) secondary entrance tamping foam, and (h) a  $P_4$  symmetry shield.

being pursued. Imploding wire arrays, which formed hollow cylindrical Z-pinch plasmas, were found to be effective radiators (Sanford *et al.*, 1996; Matzen, 1997). Research was started to determine whether these radiation sources could be used to drive ICF implosions, and PBFA-II was converted to the Z machine; see Fig. 56. Hammer *et al.* (1999) proposed a concept to generate highly symmetric radiation fields from these Z pinches to drive ICF capsules. In this approach a capsule is contained in a cylindrical secondary hohlraum that has radiation entrance holes in the two end walls (Matzen *et al.*, 2005); see Fig. 57. That geometry is essentially the same as for the NIF indirect-drive approach described in Sec. III. However, instead of laser beams entering the entrance hole, radiation flows in from two primary hohlraums that each contain a wire-array Z-pinch implosion. At stagnation these Z pinches radiate x rays, which fill the primaries. A shine shield protected the capsule from direct radiation from these Z pinches, while the radiation driving the capsule is symmetrized by radiation smoothing within the secondary hohlraum. Simulations by Hammer *et al.* (1999) indicated that this *double-ended* pinch approach could produce fusion yields of 400 MJ if both Z pinches were driven with 60 MA of current. Experiments based on this configuration were performed on Z with 19 MA driving the two pinches in series (Bennett *et al.*, 2002), which drove a capsule implosion to a convergence of 20 and indicated a highly symmetric radiation drive. Numerical simulations and view-factor calculations also indicated that high radiation symmetry could be obtained within the secondary hohlraum (Vesey *et al.*, 2003).

The simulations of pinches at 60 MA by Hammer *et al.* (1999) indicated that the primary hohlraums would reach a temperature of about 280 eV, while the secondary hohlraum containing the capsule would reach a temperature of 210 eV. Z experiments at 20 MA produced radiation temperatures of 145 eV in a primary hohlraum and 95 eV in a secondary hohlraum (Cuneo *et al.*, 2005). We can show by simple scaling that the measured primary hohlraum temperature is consistent with simulations at 60 MA. The energy in a Z-pinch implosion is determined by the integral of  $\int PdV$ , which is proportional to the square of the drive current  $I$ . The radiation energy lost to the hohlraum walls is given by the time integral of Eq. (33) with Eq. (34). Using these relations and the Z experimental results we can then estimate the drive current needed to reach a primary hohlraum temperature of 280 eV. The result is  $I = 19(280/145)^{5/3} = 57$  MA, which is close to the detailed calculation. As with NIF capsules, the radiation needs to be pulse shaped. Pulse shaping was demonstrated experimentally using nested wire arrays (Cuneo *et al.*, 2005). These results indicate that the double-ended pinch hohlraum could be a viable approach to fusion with pulsed power machines delivering about 60 MA to two pinches. This approach should be revisited when a pulsed power machine is built that can deliver such current.

Although the radiation temperatures achieved on Z were not high enough to get a significant yield from an ICF implosion, they were high enough to study capsule ablation at conditions similar to the foot pulse of a NIF target. Radiographs at 6.151 keV showed a spikey structure to the ablator surface of a CH capsule at a convergence of 4.1 (Cuneo *et al.*, 2012) and the effect of a fill tube on the capsule uniformity (Bennett *et al.*, 2007).

Another indirect-drive approach was studied that could produce much higher radiation temperatures, which was referred to as the *dynamic hohlraum* at Sandia (Matzen, 1997) and as the *flying radiation case* at Los Alamos (Brownell *et al.*, 1998). In this approach, tungsten wire arrays implode onto a foam target, driving a radiative shock into the foam; see Fig. 58. The wire-array plasma would remain relatively cool and trap radiation, generating high radiation temperatures ( $\sim 300$  eV) within the foam (Nash *et al.*, 1999). Simulations (Lash *et al.*, 2000) indicated that this indirect-drive approach might produce high yields on future pulsed power machines with larger drive currents. The collision of the tungsten onto the foam generated a radiative shock (Bailey *et al.*, 2002), while the high opacity tungsten acted as a radiation case. Simulations (Slutz *et al.*, 2003) were used to

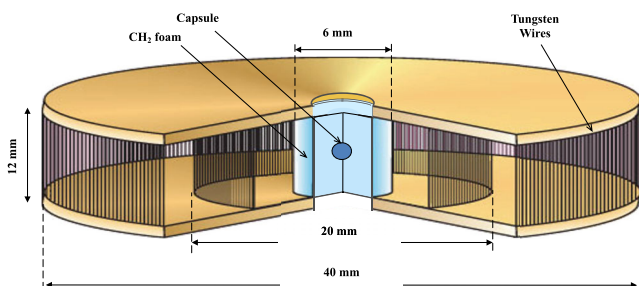


FIG. 58. Schematic of the dynamic hohlraum.

optimize the dynamic hohlraum configuration for driving small plastic capsules filled with deuterium. Experiments with this configuration (Ruiz *et al.*, 2004) generated  $\sim 5 \times 10^{10}$  DD fusion neutrons. Subsequent numerical simulations were in good agreement with these results (Slutz *et al.*, 2006). Generating radiation fields with the high symmetry required for fusion was the greatest challenge for the dynamic hohlraum approach and led to the design of opacity tailored capsules that, according to numerical simulations, could accept nonuniformities as large as 20% and still implode symmetrically (Slutz, Vesey, and Herrmann, 2007). Two dynamic hohlraums were also used in the double-ended pinch configuration (Sanford *et al.*, 1999), which produced a radiation temperature of 130 eV in the secondary hohlraum. The dynamic hohlraum approach is still being used on Z for opacity measurements (Rochau *et al.*, 2014).

Although both of these indirect-drive approaches still have promise, research at Sandia is now focused on magnetic direct-drive concepts that are unique to pulsed power and can deliver large energies to the implosion.

## B. Direct magnetic drive using the MagLIF concept

### 1. Basic principles

Wire arrays driven by Z, which stores 22 MJ, have produced nearly 2 MJ of x rays. This demonstrates the high efficiency of pulsed power, but can fusion implosions be directly driven by magnetic pressure from a pulsed power machine? Since the fuel must be contained, the Z pinch should be a metal tube rather than a wire array, as illustrated in Fig. 59. The axial current within the tube produces an azimuthal  $B$  field given by  $B = \mu_0 I / 2\pi r$ , where in Sec. V units are meters kilogram seconds unless otherwise stated. The  $B$  field exerts

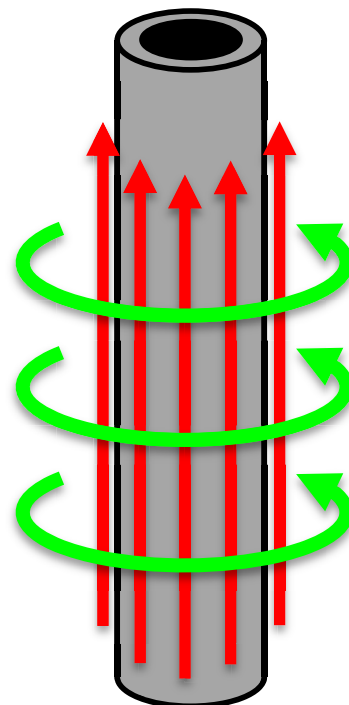


FIG. 59. Schematic of the magnetic implosion of a liner.

a pressure  $P_{\text{mag}} = B^2/2\mu_0 = (\mu_0/8)(I/\pi r)^2$  that can be high: for instance, 100 Mbars for  $I = 25$  MA and  $r = 1$  mm. This pressure is comparable to the ablation pressure of a NIF indirect-drive capsule implosion. The wall thickness  $\Delta r$  of the tube must be thick enough to avoid disruption by the MRT instability (Harris, 1962). We define the aspect ratio  $A_R = r_o/\Delta r$ , where  $r_o$  is the outer radius of the tube, which by convention is called a liner. Experiments and simulations (Dimonte, 2000) showed that bubbles from the Rayleigh-Taylor instability penetrate a distance  $h = \alpha g t^2$ , where  $g$  is the acceleration and  $t$  is the time. The factor  $\alpha$  is about 0.05, so  $A_R < 10$  is needed to avoid bubble penetration through the liner.

We can estimate the liner implosion velocity using the assumption of a thin liner. The total force driving the liner inward is  $F = P_{\text{mag}} 2\pi r L$ , where  $r$  and  $L$  are the radius and length of the liner. Equating this to the liner mass  $M$  times acceleration and putting the resulting equation in dimensionless form, we obtain

$$\frac{d^2 x}{d\tilde{\tau}^2} = \frac{-8(I/I_x)^2}{\sqrt{3}x}, \quad (88)$$

where  $\tilde{\tau} = t/t_p$ ,

$$t_p = \sqrt{\frac{8}{\sqrt{3}} \left(\frac{4\pi}{\mu_0}\right) \left(\frac{r_o}{I_x}\right) \frac{M}{L}}, \quad (89)$$

$x = r/r_o$ ,  $r_o$  is the initial radius of the liner, and  $I_x$  is the peak current. Equation (88) has the simple solution  $x = 1 - \tilde{\tau}^4$  for a current profile given by  $(I/I_x)^2 = (3\sqrt{3}/2)\tilde{\tau}^2(1 - \tilde{\tau}^4)$ . The implosion velocity is then

$$v_{\text{imp}} = -4 \left(\frac{C_R - 1}{C_R}\right)^{3/4} \left(\frac{I_x}{t_p}\right)^{1/2} \left[\frac{\sqrt{3}\mu_0 A_R^2}{32\pi^2 \rho_L (2A_R - 1)}\right]^{1/4}, \quad (90)$$

where  $A_R$  is used only to calculate the mass of the liner, the convergence ratio is defined to be  $C_R = r_o/r_s$ , with  $r_o$  and  $r_s$  the initial and stagnated radius of the liner (as in Sec. II.C.). The implosion velocity decreases with liner density, so a low density is desirable. Some of the liner material could be mixed into the fuel during the implosion, which would enhance radiation losses. Since radiation losses increase with atomic number [see, for instance, Eq. (4)], a low-atomic-number material is advantageous. Lithium would be an optimal choice but is difficult to machine and handle. Beryllium is a practical alternative.

When a beryllium liner with  $A_R = 10$ ,  $I_x = 20$  MA,  $t_p = 120$  ns, and  $C_R = 30$  is assumed, the implosion velocity is 105 km/s, which is too low for conventional ICF. For instance, NIF capsules implode at  $\sim 400$  km/s; see Sec. II. The high implosion velocity of conventional ICF serves two purposes. First, a strong shock wave heats gaseous fuel, which lowers the amount of compression that is needed. Second, the high velocity produces compressive heating that overwhelms loss mechanisms. The temperature of a shocked DT gas is  $\theta_s = 0.0047 v_{\text{shock}}^2$  eV, where  $v_{\text{shock}}$  is the shock velocity in km/s, so  $\theta_s = 750$  eV for a 400 km/s implosion and

$\theta_s = 47$  eV for a 100 km/s implosion. The fuel density will increase by roughly a factor of 4 (strong planar shock limit); hence, during the shock heating phase the liner or capsule will converge by  $C_s = 4^{1/d}$ , where the dimensionality is  $d = 2$  for cylindrical and  $d = 3$  for spherical implosions. Subsequent compression further heats this preheated gas quasiadiabatically to fusion temperatures and forms a hot spot. Ignoring thermal losses, the temperature after compression will be  $\theta_c = \theta_s C_c^{d(\gamma-1)}$ , where  $\gamma = 5/3$  for a monatomic gas and  $C_c$  is the convergence after shock heating. The overall convergence is then  $C_R = 4^{1/d}(\theta_f/\theta_s)^{1/d(\gamma-1)}$ . Assuming a final temperature  $\theta_f = 6$  keV, which is comfortably above the ignition temperature of 4 keV (see Sec. I.B.1), we find that a convergence greater than 76 is required for the 100 km/s cylindrical implosion, but only 4.5 for a 400 km/s spherical implosion. Shock heating is not sufficient for the relatively slow magnetically driven cylindrical implosions, and some kind of fuel preheat is required. This is accomplished by laser heating in the magnetized liner inertial fusion (MagLIF) concept (Slutz *et al.*, 2010), which is presently being studied on Z at Sandia National Laboratories, with a frequency doubled (0.53  $\mu\text{m}$ ) neodymium glass laser (Z-Beamlet) providing the preheat.

Thus far we have considered only adiabatic compression, but radiative and conductive cooling are important during the implosion (as discussed in Sec. I.B.). If we assume a cylindrical implosion with uniform fuel density and use the ideal gas equation of state, the rate of compressive heating is given by  $P(dV/dt) = 5.0 \times 10^{11} \rho \theta r v_{\text{imp}}$  (W/m). Thermal conduction is dominated by electrons due to their low mass and subsequent high velocity. The thermal flux is  $F_{ce} = [9.6 \times 10^{14} \theta^{2.5} \nabla \theta F(\omega\tau)] / \ln(\Lambda)$ . The temperature profile can be found by assuming that the divergence of the thermal flux is independent of the radius. This leads to  $L_{ce} = 5.7 \times 10^{14} \theta^{3.5} F(\omega_{ce}\tau_{ei})$  W/m for the rate of conductive cooling, where we have assumed that  $\ln(\Lambda) = 6$ ,  $\theta$  is the central temperature, and  $F(\omega_{ce}\tau_{ei})$  accounts for the effect of a strong magnetic field. The degree of magnetothermal insulation is a function of the Hall parameter, which is the product  $\omega_{ce}\tau_{ei}$ , where  $\omega_{ce}$  is the cyclotron frequency of the electrons and  $\tau_{ei}$  is the average time between electron-ion collisions. The magnetization term is (Braginskii, 1965)

$$F(\omega_{ce}\tau_{ei}) = \frac{1 + 0.39(\omega_{ce}\tau_{ei})^2}{1 + 3.9(\omega_{ce}\tau_{ei})^2 + 0.26(\omega_{ce}\tau_{ei})^4} \quad (91)$$

$$\approx \frac{1}{1 + 1.5(\omega_{ce}\tau_{ei})^2} \quad (92)$$

for  $\omega_{ce}\tau_{ei} > 10$ , where  $\omega_{ce}\tau_{ei} = 1.28\theta^{1.5} B/\rho$ .

During the liner implosion the compressive power done on the fuel minus the loss rate equals the rate of change in the fuel energy; thus,

$$P \frac{dV}{dt} (1 - f_L) = \frac{3}{2} \frac{d}{dt} (PV) = \frac{3}{2} \left[ P \frac{dV}{dt} + V \frac{dP}{dt} \right], \quad (93)$$

where  $f_L$  is the ratio of the thermal and radiative losses over  $P(dV/dt)$ . In this discussion we assume that  $f_L$  is constant to

illustrate the physics. The basic ideas remain true when more detailed numerical calculations are done. This can be solved to yield  $PV^{\tilde{\gamma}} = \text{const}$ , where  $\tilde{\gamma} = (5 - 2f_L)/3$  [note the similarity to Eq. (23)]. The fuel temperature from compressive heating including losses is then  $\theta = \theta_0(r_0/r)^{2(\tilde{\gamma}-1)}$ , where  $\theta_0$  is the temperature after preheat and before compression. At stagnation the ratio of the temperature after compression over the preheated temperature is thus  $\theta_s/\theta_0 = C_R^{2(\tilde{\gamma}-1)}$ . This ratio is one-half of the adiabatic case for  $f_L = 0.15$ , assuming that  $C_R = 30$ . The loss fraction

$$f_L = \frac{1}{v_{\text{imp}}} \left[ \frac{1.9 \times 10^5 \Gamma}{\theta^{0.5}} + \frac{1.1 \times 10^3 F(\omega_{ce}\tau_{ei})}{\Gamma} \right], \quad (94)$$

where  $\Gamma = \rho r$  needs to remain small. Equation (94) is minimized by setting  $\Gamma = 0.007\theta^{1.5}F(\omega_{ce}\tau_{ei})^{1/2}$  to find the minimum loss fraction  $f_{Ln} = [2.9 \times 10^4 \theta F^{1/2}(\omega_{ce}\tau_{ei})]/v_{\text{imp}} = 1.7F^{1/2}(\omega_{ce}\tau_{ei})$  at stagnation, assuming that  $\theta = 6$  keV and  $v_{\text{imp}} = 100$  km/s. This indicates that magnetization is required for such implusions. A simple axial field is effective since the heat flow in the axial direction is not large due to the small area of the ends and the much lower axial temperature gradient. We estimate the initial fuel density of  $1.4$  kg/m<sup>3</sup> from the expression for  $f_L$  by assuming that  $F(\omega_{ce}\tau_{ei})$  is small,  $f_L = 0.1$ , and  $C_R = 30$ .

External magnetic-field coils are used to provide an initial magnetic field of 10–20 T for MagLIF experiments. A schematic of the MagLIF configuration within  $Z$  is shown in Fig. 60. A more detailed schematic of just the liner is shown in Fig. 61, and the three steps of MagLIF are illustrated in Fig. 62. First, the fuel and liner are magnetized by the external coils over a relatively long timescale of 3 ms. Second, the laser heats the fuel to an average temperature of 100–200 eV. This is followed by the magnetic compression of the liner. On the timescale of the implosion (50–100 ns), the axial magnetic field is nearly frozen into both the fuel and the liner due to the high conductivity of both the fuel and the liner. The magnetic Reynolds number is greater than 1000 in the fuel. Simulations of MagLIF using the code LASNEX (Zimmerman and Krueger, 1975) indicate that about 50% of the initial magnetic flux in

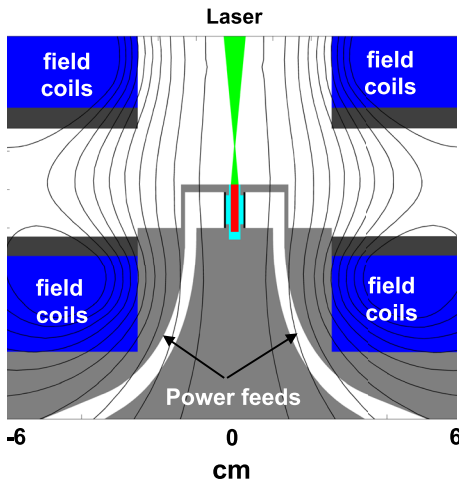


FIG. 60. Schematic of the MagLIF configuration within  $Z$ .

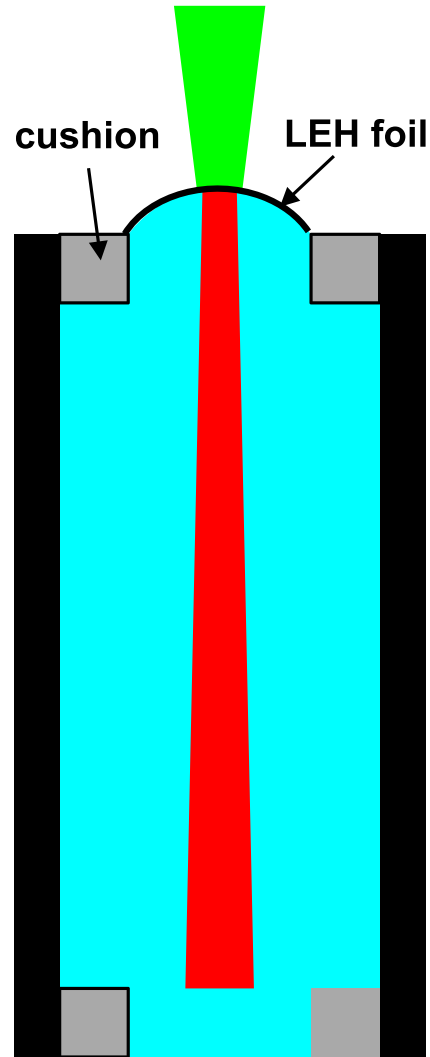


FIG. 61. Schematic of MagLIF. The laser beam is green, the heated fuel is red, and the liner is black.

the fuel inside a beryllium liner is retained until stagnation. Thus, an initial field of 15 T results in a magnetic-field strength of 6000 T and an  $\alpha$ -particle cyclotron radius just 0.4 of the fuel radius at stagnation for  $C_R = 30$ . The field will strongly affect  $\alpha$ -particle heating. The simulations assuming a laser preheat energy of 1 kJ, which Z-Beamlet can provide, indicate a stagnation temperature of about 3 keV and that 50% of the fuel mass is lost out of the open ends during the

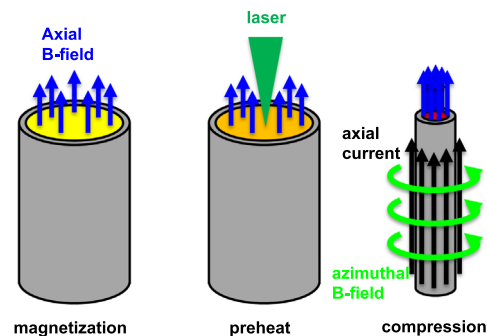


FIG. 62. The three steps of MagLIF.

implosion, so the final fuel density is about  $630 \text{ kg/m}^3$ ; hence,  $\omega_{ce}\tau_{ei} = 63$  and  $F(\omega_{ce}\tau_{ei}) = 0.00037$ , so radial thermal transport is strongly suppressed. The range of an  $\alpha$  particle (Atzeni and Meyer-ter-Vehn, 2004) is  $\Gamma_\alpha = 0.15\theta^{1.5} = 0.8 \text{ km/m}^2$ , which is much smaller than the  $\rho L = 6.4 \text{ km/m}^2$  result for a 1 cm long liner. Therefore, most  $\alpha$  particles will be absorbed in the fuel.

MagLIF is a specific example of MIF. When ICF was proposed (Nuckolls *et al.*, 1972), it was already known that a magnetic field could significantly reduce electron thermal conductivity (Landshoff, 1949). However, it was not until several years later that experiments demonstrated that a magnetic field could improve ICF yields (Chang *et al.*, 1977; Widner *et al.*, 1977), as previously described. Other methods to magnetize and preheat fusion fuel have been proposed. A Soviet proposal Manitnoye Obzhatiye (or magnetic compression) would generate an inverse  $Z$  pinch to inject high velocity plasma into a chamber, where it would be compressed by a liner implosion (Khariton *et al.*, 1976). Subsequently, a joint U.S.-Soviet research effort studied magnetically driven liners for that purpose (Lindemuth *et al.*, 1995). These liners were large compared to MagLIF and imploded in several microseconds. Liner-driven field-reversed plasma configurations (FRCs) have also been proposed (Schoenberg and Siemon, 1998). FRCs were originally developed as magnetic confinement fusion systems (Tuszewski, 1988). It was believed that they are self-sustaining long enough (tens of microseconds) to move them to within a metal liner for subsequent compression (Intrator *et al.*, 2002). FRCs have plasma densities of  $\sim 1 \times 10^{-4} \text{ kg/m}^3$  and plasma temperatures of 250 eV, which make them suitable for liner compression with implosion times of  $\sim 10 \mu\text{s}$  (Intrator *et al.*, 2004). The Air Force Research Laboratory and Los Alamos National Laboratory launched an experimental effort (Intrator, Siemon, and Sieck, 2008) to generate, translate, and compress FRCs using the Shiva Star pulsed power driver. Degnan *et al.* (2013) concluded that the FRCs produced in this experiment did not have a sufficient lifetime for translation and compression. The parameter space for MIF has been explored numerically (Lindemuth and Kirkpatrick, 1983; Lindemuth, 2015). These studies have shown that significant gain could be obtained even for slow implosion velocities ( $< 10 \text{ km/s}$ ) when the initial fuel densities are low ( $\sim 10^{-3} \text{ kg/m}^3$ ). This could allow simple, highly efficient pulsed power drivers and enable a low-cost approach to fusion (Siemon, Lindemuth, and Schoenberg, 1999).

## 2. Experimental demonstration of MagLIF concepts

The first experiments integrating all three phases of the MagLIF concept validated the basic underlying physics. These experiments, which were first designed numerically (Sefkow *et al.*, 2014) and then tested on Z (Gomez *et al.*, 2014, 2015), produced DD neutron yields of  $2 \times 10^{11}$  to  $2 \times 10^{12}$  as measured by activation and time-of-flight techniques (Hahn *et al.*, 2014, 2016). Deuterium plasma temperatures of 1.1–3.0 keV were measured using both neutron time-of-flight and x-ray spectroscopy (Hansen *et al.*, 2015). In addition, secondary DT neutrons produced in the aneutronic branch of

the DD reaction were measured with yields up to  $5 \times 10^{10}$ , indicating a high degree of magnetization (Schmit *et al.*, 2014; Knapp *et al.*, 2015).

The yields in these early experiments were modest for several reasons. First, a large fraction of the laser energy was absorbed in the 1.5–3.5  $\mu\text{m}$  thick polyimide foil covering the LEH; see Fig. 61. The Z-Beamlet laser was obtained from LLNL to provide x rays for backlighting (Rambo *et al.*, 2005). Beam smoothing was not required for this application. Furthermore, Z-Beamlet is a neodymium glass laser with only frequency doubling (0.53  $\mu\text{m}$ ), as compared to NIF and Omega, which are frequency tripled (0.35  $\mu\text{m}$ ). Laser-only experiments using Z-Beamlet (Geissel *et al.*, 2014) indicated that, due to the large variations in laser intensity, only 10% of the 2 kJ of laser energy penetrated a 2.0  $\mu\text{m}$  thick foil in the early MagLIF experiments. Intensity variations drove LPIs that prevented rapid burn-through of the foil. Later experiments using the University of Rochester's OMEGA EP laser and the Z-Beamlet laser at Sandia have shown that the energy coupling could be significantly improved using distributed phase plates to smooth the beam (Harvey-Thompson *et al.*, 2015, 2016; Geissel *et al.*, 2018). Experiments have since been conducted that delivered 1.2 kJ of energy into the fuel. Second, the drive current in these experiments was only about 16 MA because of the relatively high feed inductance (7.2 nH) of these early MagLIF loads as compared to other loads, such as the dynamic hohlraum, which has a feed inductance of only 3.0 nH and peak currents of up to 28 MA.

Increased load inductance raises the voltage on the convolute and increases current loss. The convolute (see Fig. 63) adds the currents from four MITLs, thus delivering 4 times the current of each MITL. A model developed by Hutsel *et al.* (2018) has been incorporated into LASNEX, which can now predict peak drive current as a function of load inductance. New final feed and magnetic coil designs have lowered this inductance (Fig. 64) and increased the current from 16 to 19.5 MA (Fig. 65). Third, 2D simulations (Slutz *et al.*, 2017) indicated that the yield increases with the applied magnetic-field strength. The new field coils have allowed experiments to be conducted with 16.9 T fields, as compared to the early experiments with 7–10 T fields.

All of these improvements have resulted in an order-of-magnitude increase in yield to  $1.1 \times 10^{13}$  DD neutrons and nearly twice the burn-averaged ion temperature to 3.1 keV, both trends predicted by LASNEX simulations (Gomez *et al.*, 2020). Simulations by Slutz *et al.* (2017) indicated that further increases in the drive parameters to a 30 T  $B$  field, 6 kJ preheat energy absorbed, and 22 MA peak load current could enable another order-of-magnitude increase in fusion yield on Z.

The applied magnetic field can be increased to 20–30 T when a set of coils just above the final feed and below the MagLIF liner is implemented; see Fig. 64. Much higher fields could be attained using the automagnetizing (AutoMag) liner concept (Slutz *et al.*, 2017). An AutoMag liner consists of helical conduction paths separated by insulating material; see Fig. 66. The electric field across the insulators is proportional to the rate of current rise ( $dI/dt$ ) of the drive pulse. The drive current is profiled to have a foot that rises to  $\sim 1$  MA in 100 ns, which by design generates an electric field

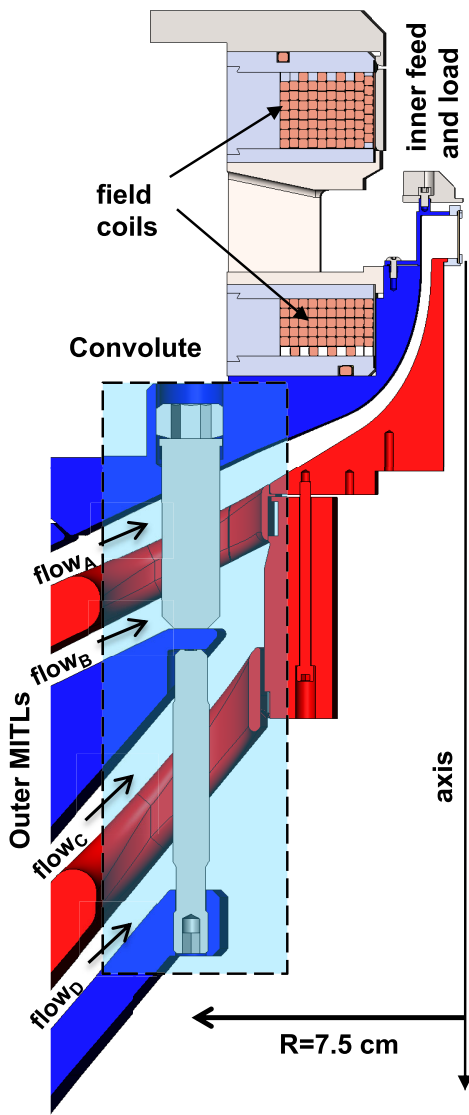


FIG. 63. Schematic of the Z convolute. The convolute adds the four inflow currents into one feed current.

across the insulators that is below the breakdown threshold. Consequently, the drive current flows along the helical conducting paths to magnetize the fuel. The foot is followed by the main pulse, which rises to full current ( $\sim 20$  MA for Z experiments) also in about 100 ns. Since  $dI/dt$  increases by a factor of 20, the insulators break down such that the current flows axially as in a normal liner implosion. Generation of fields as large as 100 T has been demonstrated experimentally with AutoMag (Shipley *et al.*, 2018; Shipley, Jennings, and Schmit, 2019).

Although 2D simulations have predicted the performance trends, the simulated yields are roughly 3 times the experimental yields. These 2D simulations did not include the effects of mix and cannot accurately calculate the 3D nature of the stagnation. Progress is being made on performing 3D simulations of MagLIF.

### 3. The effect of mix

Although 2D simulations have predicted the performance trends, the simulated yields are roughly 2 to 3 times the

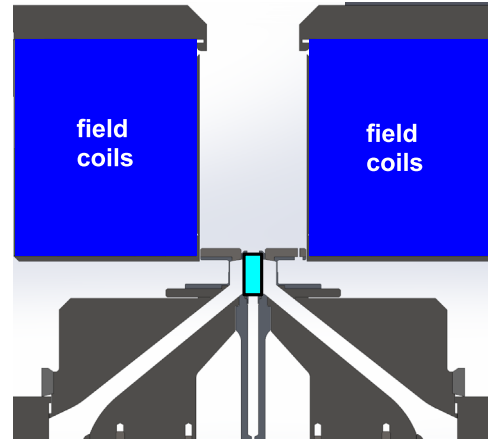


FIG. 64. Schematic of MagLIF with the new lower inductance feed and new magnetic-field coils. This feed geometry approaches the minimal inductance configuration obtained from a variational calculus method (Hurricane, 2004, Waisman and Cuneo, 2009).

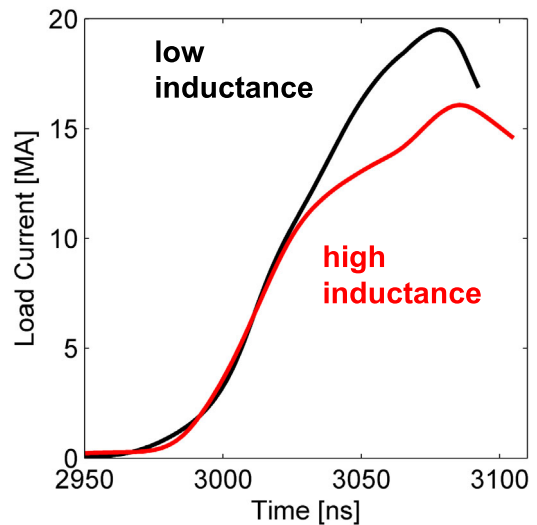


FIG. 65. Measured currents plotted as a function of time for the old (low inductance) and new (i.e., high inductance) MagLIF feeds.

experimental yields. These 2D simulations cannot accurately model the development of the MRT instability (McBride *et al.*, 2012), which could lead to the mixing of liner material into the fuel. Progress is being made on performing 3D simulations of MagLIF, which could, in principle, model such a mixing process.

Materials with an atomic number greater than hydrogen in the fuel will lower performance by enhancing radiation losses. A series of LASNEX simulations were performed by Slutz *et al.* (2018) with various dopants to determine the yield dependence with dopant fraction. The opacities were calculated using the detailed configuration accounting method without assuming local thermodynamic equilibrium (Scott and Hansen, 2010). LASNEX test simulations with this opacity model compared well to the detailed radiation code SCRAM (Hansen *et al.*, 2007). The results indicated that a 0.6%

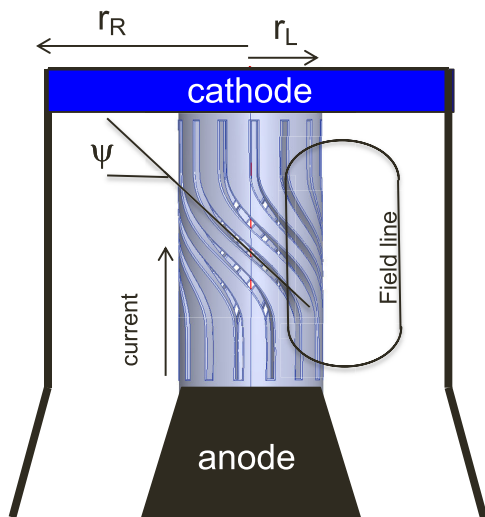


FIG. 66. Schematic of the AutoMag concept. The gaps in the metal would be filled with an insulator such as epoxy.

mixture of beryllium at the start of the simulation decreased the yield by a factor of 2, and a 2.5% mixture would lower the yield by a factor of 10. The effect of other dopant materials scales as the cube of the atomic number; for instance, 1% Be has the same effect as  $(4/13)^3 \times 1\% = 0.03\%$  Al.

The LEH window absorbs a significant fraction of the laser energy and can be injected into the fuel during expansion. This is consistent with observed cobalt spectral lines in experiments performed by [Harvey-Thompson \*et al.\* \(2018\)](#) with thin (1 nm) cobalt layers on the inside of the window. The preheated fuel forms a blast wave that could also mix material from either the liner or the cushion; see Fig. 61. Experiments with coatings on the cushion near the LEH confirm that cushion material is mixed into the fuel. Indeed, experiments with aluminum cushions have had lower yields than experiments with beryllium cushions. As with all ICF approaches, the interface between the metal liner (pusher) and the fuel is unstable to the RT instability when the pressure of the fuel decelerates the liner. Spectral features of iron (a liner impurity of known concentration  $\sim 110$  ppm) have been observed ([Hansen \*et al.\*, 2015](#)) that indicate that beryllium is mixed into the fuel.

A two-pulse laser profile has been used to improve the laser penetration of the LEH foil. Nevertheless, a significant fraction ( $\sim 28\%$ ) ([Harvey-Thompson \*et al.\*, 2018](#)) of the laser energy is still absorbed by the window material, but no mix is observed. An alternative approach ([Slutz \*et al.\*, 2018](#)) is to weaken the foil several microseconds before the main laser pulse so that the fuel pressure of several atmospheres breaks the foil. The window then opens in several microseconds like a gate in response to the pressure of the gaseous fuel. The foil could be weakened by a laser pulse focused to a star pattern on the top of the window or by current-heated wire in contact with the foil around its periphery. Both approaches have demonstrated the desired foil opening ([Miller \*et al.\*, 2020](#); [Galloway, 2021](#)) but have not yet been integrated into MagLIF experiments at Z.

Iron spectral line data indicate a beryllium atomic fraction of about 5% at stagnation ([Hansen \*et al.\*, 2015](#)), assuming

uniform mix into all of the fuel. Simulations predict that such a high uniform mix fraction would essentially negate the yield if it occurred early in the implosion. Analysis of iron helium-like resonance to the lithium-like satellite line ratios indicate a temperature of 50%–70% of the burn temperature, suggesting that Be is not mixed into the central portion of the fuel. A series of LASNEX simulations were performed that introduced Be into a layer of the fuel next to the liner at peak implosion velocity to approximate the effect of RT instability mixing during the deceleration of the liner ([Slutz \*et al.\*, 2018](#)). The layer thickness and the amount of Be were varied. It was found that both the difference between the two measured temperatures and a 50% reduced yield were indicated with a layer thickness roughly 1/3 of the fuel radius at stagnation. These simulations also indicated that the mixing of cold fuel (*DD* or *DT*) instead of Be would have a much smaller effect on the yield. Thus, a cryogenic fuel layer on the inner surface of MagLIF liners should reduce the effect of mixing. *DT* ice layers can be grown through the process of “beta layering” ([Hoffer and Foreman, 1988](#); [Martin, Simms, and Wineberg, 1989](#)), a process that could be used for MagLIF liners as well. Ice layers of strictly deuterium can be made as well and will be used for near term MagLIF experiments. However, at the low temperatures needed ( $< 18$  K) to maintain solid *DT*, the vapor pressure (gas density  $\sim 0.3$  kg/m<sup>3</sup>) is substantially below the gas density needed for MagLIF liners ( $> 1.0$  kg/m<sup>3</sup>). One solution is to form the ice layer and then puff gas into the liner. Another is to provide a foam layer on the inside surfaces of the liner that can wick liquid fuel. We return to this in Sec. V.B.5.

#### 4. Implosions instabilities

The RT instability plays an important role in all ICF approaches; see Sec. II.C. The acceleration phase of a MagLIF implosion is driven by the azimuthal magnetic field produced by the axial current flow. Such implosions are susceptible to the MRT instability. Unlike radiation or laser direct drive, there is no ablative stabilization mechanism; thus, the MRT instability poses a serious threat to liner implosions. A Z pinch with no applied axial field is most susceptible to the  $m = 0$  mode because that mode does not bend the driving azimuthal field lines; i.e., the  $k$  vector is in the axial direction, which is perpendicular to the magnetic field. Therefore, the MRT instability produces bubbles and spikes that form bands around the cylindrical Z pinch. Liner implosion experiments without an axial field exhibited this behavior ([McBride \*et al.\*, 2012](#)), as illustrated in Fig. 67. When an axial field is applied, the  $k$  vector of the fastest growing mode will have an azimuthal component and the bubble and spike bands will be helical, with a pitch angle  $\Phi = B_z/B_\theta$ . The drive current is about 1/2 of the maximum when the liner starts to move ([Slutz \*et al.\*, 2010](#)), so  $B_\theta > 600$  T, while  $B_z = 10$  T when the MRT instability starts to develop. This implies a small pitch angle, which is not consistent with the experimental results ([Awe \*et al.\*, 2013, 2014](#)); see Fig. 68. The leading hypothesis ([Ryutov and Dorf, 2014](#)) for the large pitch angles observed is that low-density plasma is swept from the MITL feed to the liner region. As the current rises, this plasma entrains the axial magnetic field and compresses against the liner. Such a mechanism could make the axial field on the outside of the

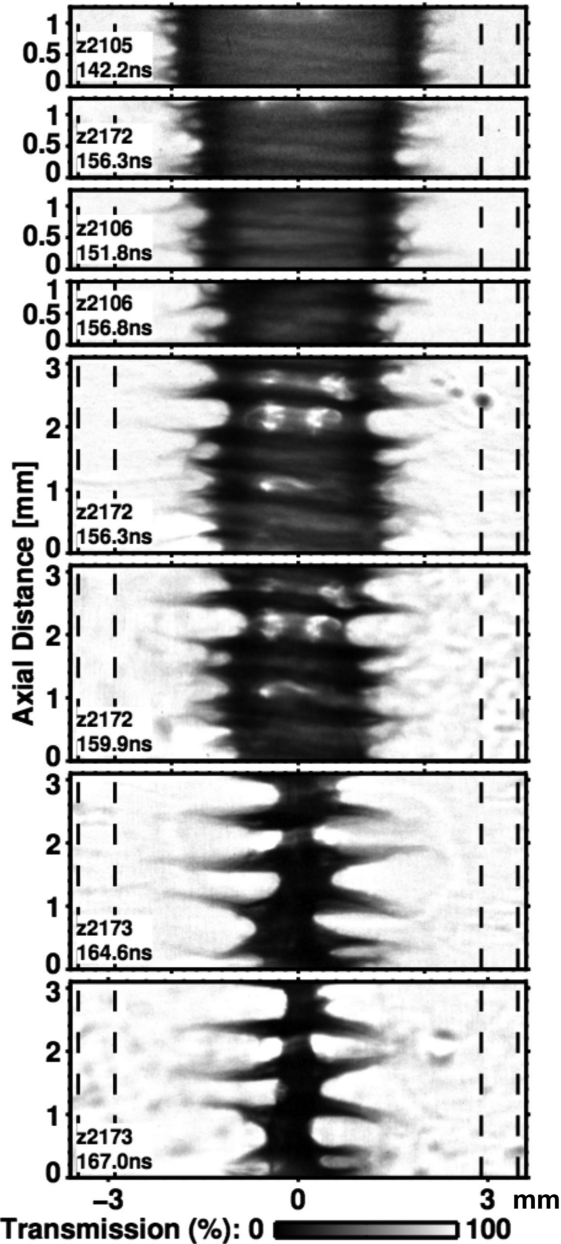


FIG. 77. Radiograph of a beryllium liner implosion at different times without an axial magnetic field.

liner comparable to the azimuthal field. Extended MHD simulations (Seyler, Martin, and Hamlin, 2018) of the power flow have demonstrated this mechanism. The need to include extended MHD terms increases the difficulty of performing 3D simulations that can accurately simulate the effect of MRT on liner implosions. Simulations (Jennings, 2020) using the 3D Eulerian GORGON code, which does not have extended MHD (Chittenden *et al.*, 2004), have qualitatively reproduced the stagnated images in MagLIF experiments at stagnation; see Fig. 69. However, the helical structure is produced only when an initial helical perturbation is applied. Similar results are produced (Weis, 2020) with the 3D ALE code HYDRA (Farmer *et al.*, 2017). Three-dimensional simulations with sufficient physics to exhibit the helical instability without imposing initial helical perturbations are required to determine

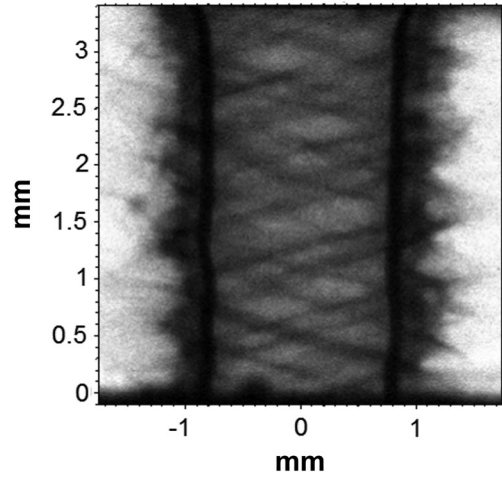


FIG. 68. Radiograph of a beryllium liner implosion at a convergence of 2.7 with an applied 7 T axial magnetic field.

whether the helical MRT instability is better or worse than the  $m = 0$  mode.

The MRT instability can be seeded by both surface roughness and density nonuniformities. Another possible source (Peterson *et al.*, 2012) is an electrothermal instability (ETI) that is caused by positive feedback when current is driven through a material that has a temperature-sensitive resistivity. ETI can be seeded by temperature, current density, or resistance variations. Experiments performed with aluminum and copper rods machined to be as smooth as possible have exhibited initial growth due to ETI that was larger than that expected from the MRT instability. Later, when the ETI has produced significant density variations, the MRT instability becomes important. These rods had rms surface roughness of 11 nm for Cu and 27 nm for Al and also had some pits and bumps on the surface. Simulations show that development of the ETI is not strongly affected by the surface roughness over a range of 37–296 nm (Peterson *et al.*, 2013).

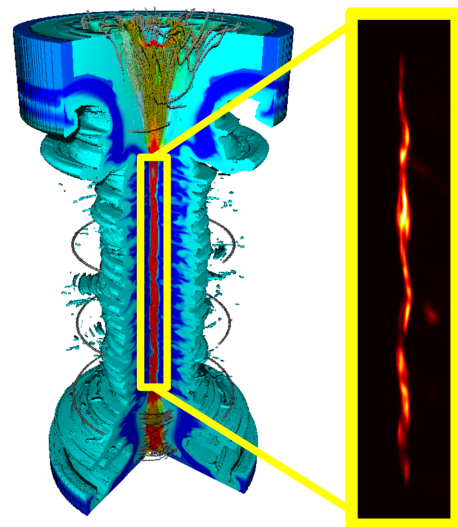


FIG. 69. A 3D GORGON simulation compared to a self-emission x-ray image of the stagnated fuel in a MagLIF experiment at Z.

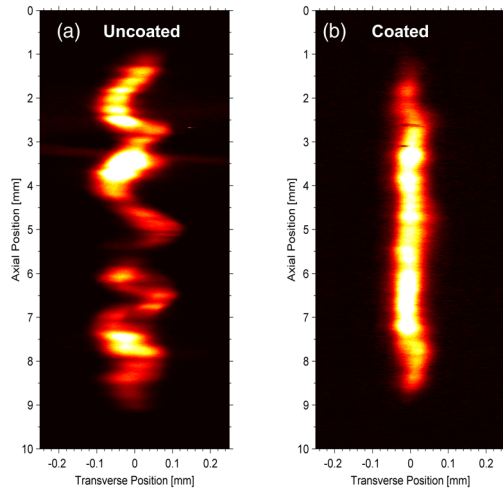


FIG. 70. X-ray images of stagnated fuel for MagLIF experiments with and without a dielectric coating on the liner.

A thin coating of dielectric material can reduce the ETI, and hence the MRT instability, significantly (Peterson *et al.*, 2014; Awe *et al.*, 2016). This technique has been used to improve the stagnation stability of MagLIF. Figure 70 shows x-ray images of the stagnated fuel from an  $A_R = 6$  liner implosion (a) without (Knapp *et al.*, 2019) and (b) with a dielectric coating (Gomez *et al.*, 2020) on the outside of the liner. The coating has improved stability, but the DD neutron yield decreased from  $3.2 \times 10^{12}$  to  $7.6 \times 10^{11}$ . Liners with  $A_R = 9$  have produced higher yields with coatings than without coatings (Ampleford, 2020). There is not presently a good explanation for the decreased yield on the  $A_R = 6$  shots.

There are other options for reducing the effect of the MRT instability on MagLIF that have not yet been tried. The growth rate of the MRT instability would be reduced in a liner with density profile that is low at the outer surface and increases toward the inner surface (Velikovich *et al.*, 1998). The magnetic pressure will then drive a snowplowlike implosion with nearly constant velocity. Another possibility is the dynamic screw pinch (Schmit *et al.*, 2016; Shipley, Jennings, and Schmit, 2019), which produces a time-dependent axial magnetic field. We have already mentioned that a dense cryogenic layer of fuel would help mitigate the effects of mixing.

### 5. High yield and gain from MagLIF on future pulsed power machines

When MIF was first being studied, it was thought that, although a magnetic field would improve volume burn, it would inhibit the propagation of a deflagration burn wave into any surrounding fuel (Jones and Mead, 1986). This would limit MIF to modest gains. Later Slutz and Vesey (2012) found numerically that propagating burn and gains approaching 1000 were possible for MagLIF with drive currents exceeding 60 MA. A layer of cryogenic (frozen) DT on the inside surface of the liner was included in these simulations. The optimum thickness of this layer increases with drive current. Several conditions are required for burn propagation. First,

modest initial fields ( $\sim 10$  T) are optimum. Larger fields inhibit propagation, while smaller fields result in poor hot-spot performance. Second, the liner areal density must be large ( $\Gamma_L \sim 50$  kg/m<sup>2</sup>) to provide sufficient confinement time. Finally, the fuel areal density  $\Gamma_F$  also needs to be sufficiently large. This requirement depends on the  $\Gamma_L$  for  $\Gamma_L = 50$  kg/m<sup>2</sup>, which is attained in simulations of MagLIF liners driven by 60 MA ( $\Gamma_F > 0.7$  kg/m<sup>2</sup>). Note that the fusion rate is proportional to  $P^2V$ , which is proportional to  $\Gamma_F^2$ . Simulations indicate that optimal initial gas densities are 3 kg/m<sup>3</sup> at 60 MA and rise to  $\sim 5$  kg/m<sup>3</sup> at 70 MA (Slutz *et al.*, 2018). We later discuss how to get such gas densities that are not in equilibrium with an ice layer.

Z has enabled research on dynamic material equations of state, opacities, and inertial fusion and has also provided radiation and neutron sources for weapon component testing. The maximum current delivered by Z ranges from 20 MA for high impedance loads such as MagLIF to 28 MA for low impedance loads such as the dynamic hohlraum. All of this research would benefit from higher currents. Work is presently under way to design a new pulsed power machine capable of delivering 40–60 MA. One possible approach is to use linear transformer driver (LTD) technology (Douglass *et al.*, 2018). Two LTD-based pulsed power machines have been designed to deliver 48 and 65 MA to high impedance loads such as MagLIF (Stygar *et al.*, 2015). An equivalent circuit of these two designs has been used in 2D LASNEX simulations to find optimal MagLIF designs as a function of the driver current (Slutz *et al.*, 2016). These 2D simulations indicate that propagating burn could be possible for currents greater than 55 MA, with a yield of 1 GJ at 60 MA. The simulations indicate that the optimum preheat energy increases with current from several kilojoules at 20 MA to 30 kJ at 50 MA. This level of preheat has been demonstrated by experiments (Pollock *et al.*, 2023) performed at the NIF. Although the effects of the MRT instability and mix were not included, the simulation scaling is encouraging.

The energy delivered by a 60 MA machine is 9 times the energy delivered by the 20 MA Z machine, while the simulated yields increase by a factor of 1000 without propagating burn. The physical parameters of the fuel and implosion change significantly for this predicted scaling. Recently a more conservative scaling was presented (Schmit and Ruiz, 2020) that holds most of the dimensionless physical quantities constant. This scaling predicts the yield increases with drive current as  $(I^3 - I^4)$  if alpha-particle heating is ignored. This corresponds to a yield increase of about 80, but according to simulations the yield would be increased another factor of 10 by including alpha-particle heating. Thus, both scalings indicate that 50–100 MJ yields may be possible with a 60 MA driver even without propagating burn into a dense fuel layer. Additional work on similarity scaling for MagLIF was conducted and published in 2023 that explored the concept and implications for next-generation pulsed power capabilities. Ruiz, Schmit, Yager-Elorriaga *et al.* (2023) presented the reduced theoretical model for MagLIF implosions in terms of dimensionless parameters, with Sec. X introducing our latest thinking on similarity scaling. Ruiz *et al.* (2023) discussed the scaling to peak

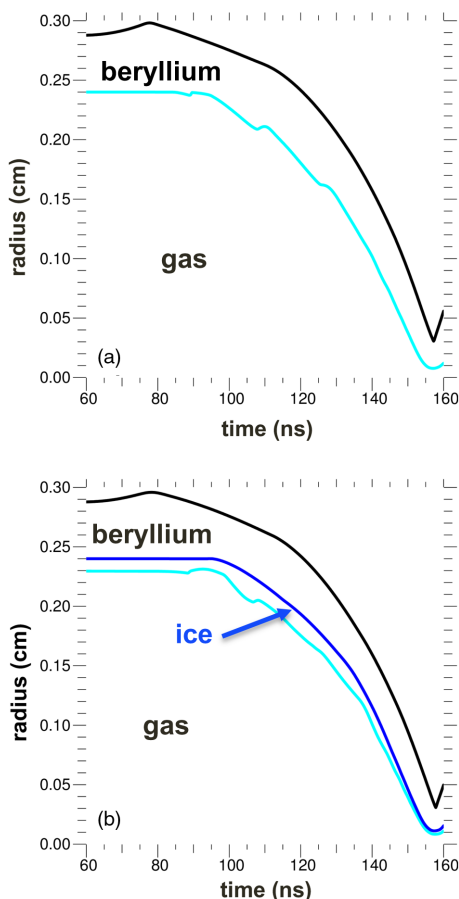


FIG. 71. Interface positions as a function of time from LASNEX simulations with and without a layer of cryogenic fuel on the inside of the liner.

current and how MagLIF “gas burning” loads perform at 60 MA. They showed how the theory works in practice to design the MagLIF current-scaling experimental series on Z and a comparison to computer simulations. Ruiz, Schmit, Weis *et al.* (2023) introduced a second application of the theory (i.e., MagLIF scaling with respect to rise time of the current pulse), showing that MagLIF scales unfavorably, in terms of preheat and electrical energy, to longer current pulses.

One-dimensional LASNEX simulations of MagLIF liners without and with a cryogenic fuel layer are shown in Fig. 71. The trajectory of the inner surface of the liner is strongly affected by the blast wave induced by laser heating when no cryogenic layer is present, while the trajectory of the inner surface is smooth when a layer is included. A new set of simulations has been performed with a cryogenic DT wetted foam (CH) layer on the inside of the liner. The results for several foam densities are shown in Fig. 72. The layer serves as a mix mitigation layer for “gas burners” and as extra fuel for high gain “cryo burners.” The layer was 100  $\mu\text{m}$  thick for the gas burner and increases from this value with current for the cryo burners. Note that the optimum liner radius is smaller for cryo burners than gas burners. Wetted foam has an advantage in that the gas density is determined by the temperature; for instance, the vapor density of liquid DT is

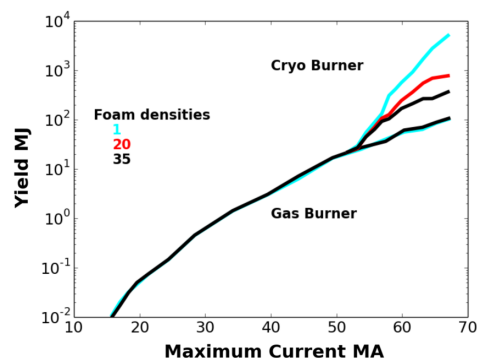


FIG. 72. LASNEX simulated yields of optimized MagLIF with a cryogenic wetted foam layer on the inside of the liner.

4  $\text{kg}/\text{m}^3$  at 23 K. The disadvantage is that the layer is mixed with carbon, which makes it harder to burn. Foam densities of 35  $\text{kg}/\text{m}^3$  have been used in NIF capsules. Lower foam densities may be possible: for instance, a density of 14  $\text{kg}/\text{m}^3$  is used for dynamic hohlraum experiments. The wetted foam has essentially no effect on the gas burners but reduces the yield of cryo burners as the foam density increases. Yet, even for the highest foam density (35  $\text{kg}/\text{m}^3$ ) the simulated yields are significantly greater than for gas burners at high-current drive.

## VI. SUMMARY AND OUTLOOK

Across the U.S. ICF program, our understanding of what physics and engineering principles are key is improving at a rapid pace. There are many commonalities to the problems that indirect drive, direct drive, and magnetic drive face. The underlying physics principles of ICF are the same regardless of the approach. Given that we now have an existence proof of fusion ignition and scientific breakeven in the laboratory, the future of ICF looks bright.

While the initial predictions for indirect drive at the NIF appear to have been optimistic, a strategy of identifying and addressing the physics and engineering obstacles in steps has paid off in terms of understanding the physics and demonstrating increased fusion performance. Using a strategy of leveraging we increased the capsule scale with what has been learned about implosion symmetry and instability control. A key turning point was achieved at the NIF, where the record fusion yields discussed in Sec. III.D. were increased to 170 kJ, exceeding  $G_{\text{fuel}} > 6$  (Fig. 2), and a major fusion physics milestone was achieved with a burning plasma (Ross *et al.*, 2021; Kritcher *et al.*, 2022a; Zylstra *et al.*, 2022a), then shortly thereafter ignition by Lawson’s criterion (Abu-Shawareb *et al.*, 2022; Kritcher *et al.*, 2022b; Zylstra *et al.*, 2022b) with 1.37 MJ total fusion yield  $G_{\text{fuel}} > 70$  and  $G_{\text{capsule}} \sim 6$ . Most recently  $G_{\text{target}} \sim 1.5$  followed (Lawrence Livermore National Laboratory, 2022), with a modest and incremental increase in laser drive (the development of which was set in motion in 2015) and a corresponding increase in capsule thickness. Since the early indirect-drive experiments at the NIF a decade ago, fusion yields have increased by a factor of more than 1000 times. What remains is to build upon these recent results by increasing energy coupling to the indirect-drive

targets and then understanding and correcting the limitations presently observed with respect to compression.

In conjunction with the mainline indirect-drive approaches at the NIF that have led to tangible gains, a number of higher-risk concepts are also being explored in the hopes of accelerating both learning and progress toward yet higher gains. Machine learning has been used to great effect to improve the fusion performance of direct-drive implosions at LLE and teased out key sensitivities that were not previously recognized. When scaled to NIF energies with an assumption that the NIF is reconfigured to a spherical direct-drive configuration, the best performing OMEGA implosions are projected to produce over 0.5 MJ of fusion yield.

Pulsed power has evolved since the 1960s and is still evolving. Z can deliver megajoules to a load with a relatively high efficiency of 5%. Future pulsed power machines are now being designed to deliver 10 MJ to a load. Pulsed power is used to efficiently generate x rays with wire-array and gas puff implosions. These x rays are used for weapon component testing and for studying the properties of materials. For instance, the dynamic hohlraum approach is currently being used to measure the opacity of materials relevant to understanding our Sun.

Concepts to produce fusion in the laboratory using pulsed power are also continuing to evolve. That research started with electron beams. Although the stopping distance of electron beams was too long, the principles of magnetoinertial fusion were first demonstrated with electron-beam-driven capsules. The program then switched to ion beams, which have a more favorable deposition but were found to be difficult to focus. Pulsed power research then focused on generating x rays to indirectly drive the capsules. Two approaches were developed using wire-array implosions. These are the double-ended pinch and the dynamic hohlraum, which could be viable on a future pulsed power machine. The research was then redirected toward the possibility of direct magnetic drive to deliver much more energy to the implosion. This change was motivation for the development of MagLIF. The principles of MagLIF have been demonstrated experimentally and fusion yields have improved by increasing the  $B$  field, the preheat energy, and the drive current. Simulations indicate that high fusion gain and yields could be possible with MagLIF on a future pulsed power machine that delivers more current.

## ACKNOWLEDGMENTS

We appreciate the helpful manuscript comments from the ICF publications committee. O. A. H. thanks Debbie Callahan, Dan Casey, Tom Dittrich, M. John Edwards, Jim Hammer, Denise Hinkel, John Kline, Annie Kritcher, Tammy Ma, Steve MacLaren, Art Pak, Hye-Sook Park, Bruce Remington, Mordy Rosen, Brian Spears, Paul Springer, Tod Woods, Alex Zylstra, and the NIF operations team, as well as the target fabrication teams at Livermore and General Atomics. This work was performed under the auspices of the U.S. Department of Energy by Lawrence Livermore National Laboratory under Contract No. DE-AC52-07NA27344. R. B. thanks S. Hu and S. Obenschain for their suggestions. This material is based on work supported by the Department of

Energy National Nuclear Security Administration under Awards No. DE-NA0003856 and No. DE-NA0001944, the Department of Energy Office of Fusion Energy Sciences under Award No. DE-FC02-04ER54789, the University of Rochester, and the New York State Energy Research and Development Authority. S. A. S. thanks Tom Mehlhorn, Matt Weis, and the MagLIF team at Sandia. Sandia National Laboratories is a multimission laboratory managed and operated by National Technology and Engineering Solutions of Sandia, a wholly owned subsidiary of Honeywell International, for the U.S. Department of Energy's National Nuclear Security Administration under Contract No. DE-NA-0003525. This document was prepared as an account of work sponsored by an agency of the U.S. Government. Neither the U.S. Government, nor Lawrence Livermore National Security, nor the University of Rochester, nor National Technology and Engineering Solutions of Sandia, nor any of their employees makes any warranty, expressed or implied, or assumes any legal liability or responsibility for the accuracy, completeness, or usefulness of any information, apparatus, product, or process disclosed, or represents that its use would not infringe upon privately owned rights. Reference herein to any specific commercial product, process, or service by trade name, trademark, manufacturer, or otherwise does not necessarily constitute or imply its endorsement, recommendation, or favoring by the U.S. Government or any agency thereof. The views and opinions of the authors expressed herein do not necessarily state or reflect those of the U.S. Government, Lawrence Livermore National Security, the University of Rochester, or National Technology and Engineering Solutions of Sandia, and shall not be used for advertising or product endorsement purposes.

## REFERENCES

- Abu-Shawareb, H., *et al.* (Indirect Drive ICF Collaboration), 2022, *Phys. Rev. Lett.* **129**, 075001.
- Afeyan, B. B., A. E. Chou, J. P. Matte, R. P. J. Town, and W. J. Kruer, 1998, *Phys. Rev. Lett.* **80**, 2322.
- Afeyan, Bedros, and Hüller, Stefan, 2013, *EPJ Web Conf.* **59**, 05009.
- Aglitskiy, Y., A. L. Velikovich, M. Karasik, V. Serlin, C. J. Pawley, A. J. Schmitt, S. P. Obenschain, A. N. Mostovych, J. H. Gardner, and N. Metzler, 2001, *Phys. Rev. Lett.* **87**, 265002.
- Aglitskiy, Y., A. L. Velikovich, M. Karasik, V. Serlin, C. J. Pawley, A. J. Schmitt, S. P. Obenschain, A. N. Mostovych, J. H. Gardner, and N. Metzler, 2002, *Phys. Plasmas* **9**, 2264.
- Ali, S. J., *et al.*, 2018, *Phys. Plasmas* **25**, 092708.
- Alon, U., J. Hecht, D. Ofer, and D. Shvarts, 1995, *Phys. Rev. Lett.* **74**, 534.
- Amendt, P., *et al.*, 2019, *Phys. Plasmas* **26**, 082707.
- Ampleford, D., 2020 (private communication).
- Anderson, K., and R. Betti, 2004, *Phys. Plasmas* **11**, 5.
- Anderson, K. S., *et al.*, 2020, *Phys. Plasmas* **27**, 112713.
- Atzeni, S., 1999, *Phys. Plasmas* **6**, 3316.
- Atzeni, S., and J. Meyer-ter-Vehn, 2004, *The Physics of Inertial Fusion* (Oxford University Press, Oxford).
- Atzeni, S., X. Ribeyrei, G. Schurtzi, A. Schmitti, B. Canaudi, R. Betti, and L. Perkins, 2014, *Nucl. Fusion* **54**, 054008.
- Awe, T. J., *et al.*, 2013, *Phys. Rev. Lett.* **111**, 235005.
- Awe, T. J., *et al.*, 2014, *Phys. Plasmas* **21**, 056303.

- Awe, T. J., *et al.*, 2016, *Phys. Rev. Lett.* **116**, 065001.
- Azechi, H., *et al.*, 2013, *Nucl. Fusion* **53**, 104021.
- Bailey, J. E., *et al.*, 2002, *Phys. Rev. Lett.* **89**, 095004.
- Baker, K. L., *et al.*, 2015, *Phys. Plasmas* **22**, 052702.
- Baker, K. L., *et al.*, 2018, *Phys. Rev. Lett.* **121**, 135001.
- Ballabio, L., J. Källne, and G. Gorini, 1998, *Nucl. Fusion* **38**, 1723.
- Basko, M. M., and J. Meyer-ter-Vehn, 2002, *Phys. Rev. Lett.* **88**, 244502.
- Batani, D., *et al.*, 2014, *Nucl. Fusion* **54**, 054009.
- Bates, J., *et al.*, 2020, *High Energy Density Phys.* **36**, 100772.
- Bates, J. W., J. F. Myatt, J. G. Shaw, R. K. Follett, J. L. Weaver, R. H. Lehmberg, and S. P. Obenshain, 2018, *Phys. Rev. E* **97**, 061202.
- Baxamusa, S., T. Laurence, M. Worthington, and P. Ehrmann, 2015, *Polym. Degrad. Stab.* **122**, 133.
- Bell, G., 1951, Los Alamos Scientific Laboratory Technical Report No. LA-1321.
- Benedict, L. X., K. P. Driver, S. Hamel, B. Militzer, T. Qi, A. A. Correa, A. Saul, and E. Schwegler, 2014, *Phys. Rev. B* **89**, 224109.
- Bennett, G. R., *et al.*, 2002, *Phys. Rev. Lett.* **89**, 245002.
- Bennett, G. R., *et al.*, 2007, *Phys. Rev. Lett.* **99**, 205003.
- Berger, R. L., E. Lefebvre, A. B. Langdon, J. E. Rothenberg, C. H. Still, and E. A. Williams, 1999, *Phys. Plasmas* **6**, 1043.
- Berzak Hopkins, L. F., *et al.*, 2015a, *Phys. Plasmas* **22**, 056318.
- Berzak Hopkins, L. F., *et al.*, 2015b, *Phys. Rev. Lett.* **114**, 175001.
- Betti, R., K. Anderson, V. N. Goncharov, R. L. McCrory, D. D. Meyerhofer, S. Skupsky, and R. P. J. Town, 2002, *Phys. Plasmas* **9**, 2277.
- Betti, R., P. Y. Chang, B. K. Spears, K. S. Anderson, J. Edwards, M. Fatenejad, J. D. Lindl, R. L. McCrory, R. Nora, and D. Shvarts, 2010, *Phys. Plasmas* **17**, 058102.
- Betti, R., A. R. Christopherson, B. K. Spears, R. Nora, A. Bose, J. Howard, K. M. Woo, M. J. Edwards, and J. Sanz, 2015, *Phys. Rev. Lett.* **114**, 255003.
- Betti, R., V. N. Goncharov, R. L. McCrory, and C. P. Verdon, 1995, *Phys. Plasmas* **2**, 3844.
- Betti, R., V. N. Goncharov, R. L. McCrory, and C. P. Verdon, 1998, *Phys. Plasmas* **5**, 1446.
- Betti, R., and O. A. Hurricane, 2016, *Nat. Phys.* **12**, 435.
- Betti, R., V. Lobatchev, and R. L. McCrory, 1998, *Phys. Rev. Lett.* **81**, 5560.
- Betti, R., and J. Sanz, 2006, *Phys. Rev. Lett.* **97**, 205002.
- Betti, R., M. Umansky, V. Lobatchev, V. N. Goncharov, and R. L. McCrory, 2001, *Phys. Plasmas* **8**, 5257.
- Betti, R., C. D. Zhou, K. S. Anderson, L. J. Perkins, W. Theobald, and A. A. Solodov, 2007, *Phys. Rev. Lett.* **98**, 155001.
- Bodner, S. E., 1974, *Phys. Rev. Lett.* **33**, 761.
- Bodner, S. E., 1981, *J. Fusion Energy* **1**, 221.
- Bodner, S. E., 1995, *Comments Plasma Phys. Controlled Fusion* **16**, 351.
- Boehly, T., *et al.*, 1997, *Opt. Commun.* **133**, 495.
- Boehly, T. R., V. A. Smalyuk, D. D. Meyerhofer, J. P. Knauer, D. K. Bradley, R. S. Craxton, M. J. Guardalben, S. Skupsky, and T. J. Kessler, 1999, *J. Appl. Phys.* **85**, 3444.
- Bosch, H.-S., and G. Hale, 1992, *Nucl. Fusion* **32**, 611.
- Bose, A., R. Betti, D. Shvarts, and K. M. Woo, 2017, *Phys. Plasmas* **24**, 102704.
- Bose, A., K. M. Woo, R. Nora, and R. Betti, 2015, *Phys. Plasmas* **22**, 072702.
- Bose, A., *et al.*, 2016, *Phys. Rev. E* **94**, 011201(R).
- Bose, A., *et al.*, 2018, *Phys. Plasmas* **25**, 062701.
- Bowers, K. J., B. J. Albright, L. Yin, B. Bergen, and T. J. T. Kwan, 2008, *Phys. Plasmas* **15**, 055703.
- Braginskii, S., 1965, in *Reviews of Plasma Physics*, Vol. 1, edited by M. A. Leontovich (Consultants Bureau, New York).
- Brown, L. S., D. L. Preston, and R. L. Singleton, Jr., 2005, *Phys. Rep.* **410**, 237.
- Brownell, J. H., R. L. Bowers, K. D. McLenithan, and D. L. Peterson, 1998, *Phys. Plasmas* **5**, 2071.
- Bychkov, V. V., S. M. Golberg, and M. A. Liberman, 1994, *Phys. Plasmas* **1**, 2976.
- Callahan, D. A., *et al.*, 2012, *Phys. Plasmas* **19**, 056305.
- Callahan, D. A., *et al.*, 2015, *Phys. Plasmas* **22**, 056314.
- Callahan, D. A., *et al.*, 2018, *Phys. Plasmas* **25**, 056305.
- Callahan, D. A., *et al.*, 2020, *Phys. Plasmas* **27**, 072704.
- Campbell, E., *et al.*, 2017, *Matter Radiat. Extremes* **2**, 37.
- Campbell, E. M., and W. J. Hogan, 1999, *Plasma Phys. Controlled Fusion* **41**, B39.
- Campbell, E. M., *et al.*, 2021, *Phil. Trans. R. Soc. A* **379**, 20200011.
- Casey, D. T., *et al.*, 2014, *Phys. Rev. E* **90**, 011102.
- Casey, D. T., *et al.*, 2015, *Phys. Rev. Lett.* **115**, 105001.
- Casey, D. T., *et al.*, 2018, *Phys. Plasmas* **25**, 056308.
- Casey, D. T., *et al.*, 2021, *Phys. Rev. Lett.* **126**, 025002.
- Casner, A., *et al.*, 2016, *J. Phys. Conf. Ser.* **717**, 012010.
- Ceglio, N. M., and J. T. Larsen, 1980, *Phys. Rev. Lett.* **44**, 579.
- Celliers, P. M., D. J. Erskine, C. M. Sorce, D. G. Braun, O. L. Landen, and G. W. Collins, 2010, *Rev. Sci. Instrum.* **81**, 035101.
- Cerjan, C., P. Springer, and S. Sepke, 2013, *Phys. Plasmas* **20**, 056319.
- Ceurvorst, L., *et al.*, 2020, *Phys. Rev. E* **101**, 063207.
- Chang, J., M. Widner, A. Farnsworth, Jr., R. Leeper, T. Prevender, L. Baker, and J. Olsen, 1977, in *Proceedings of the 2nd Topical Conference on High Power Electron and Ion Beam Research and Technology, Ithaca, 1977* (Cornell University, Ithaca), pp. 195–205, <https://www.osti.gov/servlets/purl/6156661>.
- Chang, P. Y., R. Betti, B. K. Spears, K. S. Anderson, J. Edwards, M. Fatenejad, J. D. Lindl, R. L. McCrory, and R. Nora, 2010, *Phys. Rev. Lett.* **104**, 135002.
- Cheng, B., T. J. T. Kwan, Y.-M. Wang, and S. H. Bathe, 2013, *Phys. Rev. E* **88**, 041101(R).
- Cheng, B., T. J. T. Kwan, S. A. Yi, O. L. Landen, Y. M. Wang, C. J. Cerjan, S. H. Batha, and F. J. Wysocki, 2018, *Phys. Rev. E* **98**, 023203.
- Chittenden, J. P., B. D. Appelbe, F. Manke, K. McGlinchey, and N. P. L. Niasse, 2016, *Phys. Plasmas* **23**, 052708.
- Chittenden, J. P., S. V. Lebedev, C. A. Jennings, S. N. Bland, and A. Ciardi, 2004, *Plasma Phys. Controlled Fusion* **46**, B457.
- Christopherson, A. R., R. Betti, A. Bose, J. Howard, K. M. Woo, E. M. Campbell, J. Sanz, and B. K. Spears, 2018, *Phys. Plasmas* **25**, 012703.
- Christopherson, A. R., R. Betti, J. Howard, K. M. Woo, A. Bose, E. M. Campbell, and V. Gopalaswamy, 2018, *Phys. Plasmas* **25**, 072704.
- Christopherson, A. R., R. Betti, and J. D. Lindl, 2019, *Phys. Rev. E* **99**, 021201(R).
- Christopherson, A. R., R. Betti, S. Miller, V. Gopalaswamy, O. M. Mannion, and D. Cao, 2020, *Phys. Plasmas* **27**, 052708.
- Christopherson, A. R., *et al.*, 2021, *Phys. Rev. Lett.* **127**, 055001.
- Clark, D. S., A. L. Kritcher, S. A. Yi, A. B. Zylstra, S. W. Haan, and C. R. Weber, 2018, *Phys. Plasmas* **25**, 032703.
- Clark, D. S., *et al.*, 2014, *Phys. Plasmas* **21**, 112705.
- Clark, D. S., *et al.*, 2016, *Phys. Plasmas* **23**, 056302.
- Clark, D. S., *et al.*, 2019, *Phys. Plasmas* **26**, 050601.
- Clauser, M. J., 1975, *Phys. Rev. Lett.* **34**, 570.
- Cobble, J. A., *et al.*, 2012, *Phys. Plasmas* **19**, 122713.

- Cohen, B. I., B. F. Lasinski, A. B. Langdon, and E. A. Williams, 1997, *Phys. Plasmas* **4**, 956.
- Colaitis, A., R. K. Follett, J. P. Palastro, I. Igumenshev, and V. Goncharov, 2019, *Phys. Plasmas* **26**, 072706.
- Collins, T. J. B., and J. A. Marozas, 2018, *Phys. Plasmas* **25**, 072706.
- Collins, T. J. B., *et al.*, 2012, *Phys. Plasmas* **19**, 056308.
- Cook, D. L., *et al.*, 1986, *Plasma Phys. Controlled Fusion* **28**, 1921.
- Craxton, R., 1981, *IEEE J. Quantum Electron.* **17**, 1771.
- Craxton, R. S., and D. W. Jacobs-Perkins, 2005, *Phys. Rev. Lett.* **94**, 095002.
- Craxton, R. S., *et al.*, 2005, *Phys. Plasmas* **12**, 056304.
- Craxton, R. S., *et al.*, 2015, *Phys. Plasmas* **22**, 110501.
- Cuneo, M. E., 1999, *IEEE Trans. Dielectr. Electr. Insul.* **6**, 469.
- Cuneo, M. E., *et al.*, 1997, *IEEE Trans. Plasma Sci.* **25**, 229.
- Cuneo, M. E., *et al.*, 2005, *Phys. Rev. E* **71**, 046406.
- Cuneo, M. E., *et al.*, 2012, *IEEE Trans. Plasma Sci.* **40**, 3222.
- Degnan, J., *et al.*, 2013, *Nucl. Fusion* **53**, 093003.
- Daughton, W., B. J. Albright, S. M. Finnegan, B. M. Haines, J. L. Kline, J. P. Sauppe, and J. M. Smidt, 2023, *Phys. Plasmas* **30**, 012704.
- d'Escourt Atkinson, R., and F. G. Houtermans, 1929, *Nature (London)* **123**, 567.
- Desjarlais, M. P., T. D. Pointon, D. B. Seidel, R. S. Coats, M. L. Kiefer, J. P. Quintenz, and S. A. Slutz, 1991, *Phys. Rev. Lett.* **67**, 3094.
- Dewald, E. L., J. Milovich, C. Thomas, J. Kline, C. Sorce, S. Glenn, and O. L. Landen, 2011, *Phys. Plasmas* **18**, 092703.
- Dimonte, G., 2000, *Phys. Plasmas* **7**, 2255.
- Dimonte, G., 2004, *Phys. Rev. E* **69**, 056305.
- Dimonte, G., and M. Schneider, 2000, *Phys. Fluids* **12**, 304.
- Dimonte, G., *et al.*, 2004, *Phys. Fluids* **16**, 1668.
- Dittrich, T. R., *et al.*, 2014, *Phys. Rev. Lett.* **112**, 055002.
- Divol, L., *et al.*, 2017, *Phys. Plasmas* **24**, 056309.
- Döppner, T., *et al.*, 2015, *Phys. Rev. Lett.* **115**, 055001.
- Döppner, T., *et al.*, 2020, *Phys. Plasmas* **27**, 042701.
- Dorner, C., E. M. Hill, and J. D. Zuegel, 2020, *Opt. Express* **28**, 451.
- Dorner, C., M. Spilatro, S. Herman, T. Borgerand, and E. M. Hill, 2021, *Opt. Express* **29**, 16135.
- Douglass, J. D., *et al.*, 2018, *Phys. Rev. Accel. Beams* **21**, 120401.
- Dreike, P., C. Eichenberger, S. Humphries, and R. Sudan, 1976, *J. Appl. Phys.* **47**, 85.
- Edgell, D., P. B. Radha, J. Katz, A. Shvydky, D. Turnbull, and D. H. Froula, 2021, *Phys. Rev. Lett.* **127**, 075001.
- Edgell, D. H., R. K. Follett, I. V. Igumenshev, J. F. Myatt, J. G. Shaw, and D. H. Froula, 2017, *Phys. Plasmas* **24**, 062706.
- Eimerl, D., 1995a, Lawrence Livermore National Laboratory Technical Report No. UCRL-ID-120758.
- Eimerl, D., 1995b, Lawrence Livermore National Laboratory Technical Report No. UCRL-JC-121271.
- Eimerl, D., J. E. Rothenberg, M. H. Key, S. V. Weber, C. P. Verdon, S. Skupsky, J. M. Soures, and R. S. Craxton, 1995, in *Solid State Lasers for Application to Inertial Confinement Fusion (ICF)*, SPIE Proceedings Vol. 2633, edited by M. Andre and H. T. Powell (SPIE—International Society for Optics and Photonics, Bellingham, WA), pp. 170–182.
- Epstein, R., 2004, *Phys. Plasmas* **11**, 5114.
- Fabre, E., F. Amiranoff, R. Fabbro, C. Garban-Labaune, J. Virmont, M. Weinfeld, F. David, and R. Pellat, 1981, in *Proceedings of the 8th International Conference in Plasma Physics and Controlled Nuclear Fusion Research, Brussels, 1980* (IAEA, Vienna), pp. 263–272.
- Farmer, W. A., J. M. Koning, D. J. Strozzi, D. E. Hinkel, L. F. Berzak Hopkins, O. S. Jones, and M. D. Rosen, 2017, *Phys. Plasmas* **24**, 052703.
- Follett, R. K., J. G. Shaw, J. F. Myatt, C. Dorner, D. H. Froula, and J. P. Palastro, 2019, *Phys. Plasmas* **26**, 062111.
- Follett, R. K., J. G. Shaw, J. F. Myatt, V. N. Goncharov, D. H. Edgell, D. H. Froula, and J. P. Palastro, 2018, *Phys. Rev. E* **98**, 043202.
- Follett, R. K., J. G. Shaw, J. F. Myatt, H. Wen, D. H. Froula, and J. P. Palastro, 2021, *Phys. Plasmas* **28**, 032103.
- Fratanduono, D. E., *et al.*, 2016, *Phys. Rev. B* **94**, 184107.
- Froula, D. H., *et al.*, 2012, *Phys. Rev. Lett.* **108**, 125003.
- Fujioka, S., *et al.*, 2004, *Phys. Rev. Lett.* **92**, 195001.
- Galloway, B. R., 2021, *Phys. Plasmas* **28**, 112703.
- Gamow, G., 1928, *Nature (London)* **122**, 805.
- Gardner, J. H., and S. E. Bodner, 1981, *Phys. Rev. Lett.* **47**, 1137.
- Gatu Johnson, M., *et al.*, 2016, *Phys. Rev. E* **94**, 021202.
- Geissel, M., L. Ruggles, A. Sefkow, I. Smith, J. Shores, C. Speas, and J. Porter, 2014, in *Proceedings of the 41st European Physics Society Conference on Plasma Physics, Berlin, 2014* (unpublished).
- Geissel, M., *et al.*, 2018, *Phys. Plasmas* **25**, 022706.
- Gibson, C. R., *et al.*, 2009, *Fusion Sci. Technol.* **55**, 233.
- Glenzer, S. H., L. M. Divol, R. L. Berger, C. Geddes, R. K. Kirkwood, J. D. Moody, E. A. Williams, and P. E. Young, 2001, *Phys. Rev. Lett.* **86**, 2565.
- Glenzer, S. H., *et al.*, 2010, *Science* **327**, 1228.
- Glenzer, S. H., *et al.*, 2012, *Phys. Plasmas* **19**, 056318.
- Gomez, M. R., *et al.*, 2014, *Phys. Rev. Lett.* **113**, 155003.
- Gomez, M. R., *et al.*, 2015, *Phys. Plasmas* **22**, 056306.
- Gomez, M. R., *et al.*, 2020, *Phys. Rev. Lett.* **125**, 155002.
- Goncharov, V. N., 1999, *Phys. Rev. Lett.* **82**, 2091.
- Goncharov, V. N., 2002, *Phys. Rev. Lett.* **88**, 134502.
- Goncharov, V. N., R. Betti, R. L. McCrory, and C. P. Verdon, 1996, *Phys. Plasmas* **3**, 4665.
- Goncharov, V. N., J. P. Knauer, P. W. McKenty, P. B. Radha, T. C. Sangster, S. Skupsky, R. Betti, R. L. McCrory, and D. D. Meyerhofer, 2003, *Phys. Plasmas* **10**, 1906.
- Goncharov, V. N., P. McKenty, S. Skupsky, R. Betti, R. L. McCrory, and C. Cherfils-Clérouin, 2000, *Phys. Plasmas* **7**, 5118.
- Goncharov, V. N., S. Skupsky, T. R. Boehly, J. P. Knauer, P. McKenty, V. A. Smalyuk, R. P. J. Town, O. V. Gotchev, R. Betti, and D. D. Meyerhofer, 2000, *Phys. Plasmas* **7**, 2062.
- Goncharov, V. N., *et al.*, 2008, *Phys. Plasmas* **15**, 056310.
- Goncharov, V. N., *et al.*, 2014, *Phys. Plasmas* **21**, 056315.
- Goncharov, V. N., *et al.*, 2017, *Plasma Phys. Controlled Fusion* **59**, 014008.
- Gopalaswamy, V., *et al.*, 2019, *Nature (London)* **565**, 581.
- Gotchev, O. V., V. N. Goncharov, J. P. Knauer, T. R. Boehly, T. J. B. Collins, R. Epstein, P. A. Jaanimagi, and D. D. Meyerhofer, 2006, *Phys. Rev. Lett.* **96**, 115005.
- Gu, J., Z. Dai, Z. Fan, S. Zou, W. Ye, W. Pei, and S. Zhu, 2014, *Phys. Plasmas* **21**, 012704.
- Guderley, G., 1942, *Luftfahrtforschung* **19**, 302.
- Gus'kov, S., O. Krokhin, and V. Rozanov, 1976, *Nucl. Fusion* **16**, 957.
- Haan, S. W., 1989, *Phys. Rev. A* **39**, 5812.
- Haan, S. W., H. Huang, M. A. Johnson, M. Stadermann, S. Baxamusa, S. Bhandarkar, D. S. Clark, V. Smalyuk, and H. F. Robey, 2015, *Phys. Plasmas* **22**, 032708.
- Haan, S. W., *et al.*, 2011, *Phys. Plasmas* **18**, 051001.

- Hahn, K. D., G. W. Cooper, C. L. Ruiz, D. L. Fehl, G. A. Chandler, P. F. Knapp, R. J. Leeper, A. J. Nelson, R. M. Smelser, and J. A. Torres, 2014, *Rev. Sci. Instrum.* **85**, 043507.
- Hahn, K. D., *et al.*, 2016, *J. Phys. Conf. Ser.* **717**, 012020.
- Hall, G. N., *et al.*, 2017, *Phys. Plasmas* **24**, 052706.
- Hammer, J., 2016, *J. Phys. Conf. Ser.* **688**, 012025.
- Hammer, J. H., and M. D. Rosen, 2003, *Phys. Plasmas* **10**, 1829.
- Hammer, J. H., M. Tabak, S. C. Wilks, J. D. Lindl, D. S. Bailey, P. W. Rambo, A. Toor, G. B. Zimmerman, and J. L. Porter, 1999, *Phys. Plasmas* **6**, 2129.
- Hansen, A. M., *et al.*, 2021, *Phys. Rev. Lett.* **126**, 075002.
- Hansen, R., 2012, Lawrence Livermore National Laboratory Technical Report No. LLNL-TR-553311.
- Hansen, S., J. Bauche, C. Bauche-Arnoult, and M. Gu, 2007, *High Energy Density Phys.* **3**, 109.
- Hansen, S. B., *et al.*, 2015, *Phys. Plasmas* **22**, 056313.
- Harding, D., M. Bonino, W. Sweet, M. Schoff, A. Greenwood, N. Satoh, M. Takagi, and A. Nikroo, 2018, *Matter Radiat. Extremes* **3**, 312.
- Harris, E. G., 1962, *Phys. Fluids* **5**, 1057.
- Harvey-Thompson, A. J., A. B. Sefkow, M. S. Wei, T. Nagayama, E. M. Campbell, B. E. Blue, R. F. Heeter, J. M. Koning, K. J. Peterson, and A. Schmitt, 2016, *Phys. Rev. E* **94**, 051201.
- Harvey-Thompson, A. J., *et al.*, 2015, *Phys. Plasmas* **22**, 122708.
- Harvey-Thompson, A. J., *et al.*, 2018, *Phys. Plasmas* **25**, 112705.
- Hecht, J., U. Alon, and D. Shvarts, 1994, *Phys. Fluids* **6**, 4019.
- Heitler, W., 1954, *The Quantum Theory of Radiation* (Clarendon Press, Oxford).
- Herrmann, M. C., M. Tabak, and J. D. Lindl, 2001, *Nucl. Fusion* **41**, 99.
- Hicks, D. G., B. K. Spears, D. G. Braun, R. E. Olson, C. M. Sorce, P. M. Celliers, G. W. Collins, and O. L. Landen, 2010, *Phys. Plasmas* **17**, 102703.
- Higginson, D. P., *et al.*, 2019, *Phys. Plasmas* **26**, 012113.
- Hinkel, D. E., E. A. Williams, R. L. Berger, L. V. Powers, A. B. Langdon, and C. H. Still, 1998, *Phys. Plasmas* **5**, 1887.
- Hinkel, D. E., *et al.*, 2016, *Phys. Rev. Lett.* **117**, 225002.
- Hoddeson, L., P. Henriksen, R. Meade, and C. Westfall, 1993, *Critical Assembly: A Technical History of Los Alamos during the Oppenheimer Years, 1943–1945* (Cambridge University Press, Cambridge, England).
- Hoffer, J. K., and L. R. Foreman, 1988, *Phys. Rev. Lett.* **60**, 1310.
- Hohenberger, M., *et al.*, 2015, *Phys. Plasmas* **22**, 056308.
- Hohenberger, M., *et al.*, 2016, *Phys. Plasmas* **23**, 092702.
- Hohenberger, M., *et al.*, 2020, *Phys. Plasmas* **27**, 112704.
- Hu, S. X., G. Fiksel, V. N. Goncharov, S. Skupsky, D. D. Meyerhofer, and V. A. Smalyuk, 2012, *Phys. Rev. Lett.* **108**, 195003.
- Hu, S. X., D. T. Michel, A. K. Davis, R. Betti, P. B. Radha, E. M. Campbell, D. H. Froula, and C. Stoeckl, 2016, *Phys. Plasmas* **23**, 102701.
- Hu, S. X., *et al.*, 2018, *Phys. Plasmas* **25**, 082710.
- Hurricane, O. A., 2004, *J. Appl. Phys.* **95**, 4503.
- Hurricane, O. A., 2015, <https://lasers.llnl.gov/news/experimental-highlights/2015/may>.
- Hurricane, O. A., 2016, *J. Phys. Conf. Ser.* **717**, 012005.
- Hurricane, O. A., D. A. Callahan, and P. Patel, 2016, Lawrence Livermore National Laboratory Report No. LLNL-TR-692518.
- Hurricane, O. A., S. A. MacLaren, M. D. Rosen, J. H. Hammer, P. T. Springer, and R. Betti, 2021, *Phys. Plasmas* **28**, 022704.
- Hurricane, O. A., *et al.*, 2014a, *Nature (London)* **506**, 343.
- Hurricane, O. A., *et al.*, 2014b, *Phys. Plasmas* **21**, 056314.
- Hurricane, O. A., *et al.*, 2016, *Nat. Phys.* **12**, 800.
- Hurricane, O. A., *et al.*, 2017a, *Bull. Am. Phys. Soc.* **62**, PO7.00001.
- Hurricane, O. A., *et al.*, 2017b, *Phys. Plasmas* **24**, 092706.
- Hurricane, O. A., *et al.*, 2019a, *Plasma Phys. Controlled Fusion* **61**, 014033.
- Hurricane, O. A., *et al.*, 2019b, *Phys. Plasmas* **26**, 052704.
- Hurricane, O. A., *et al.*, 2020, *Phys. Plasmas* **27**, 062704.
- Hurricane, O. A., *et al.*, 2022, *Phys. Plasmas* **29**, 012703.
- Hutsel, B. T., *et al.*, 2018, *Phys. Rev. Accel. Beams* **21**, 030401.
- Igumenshchev, I. V., D. H. Edgell, V. N. Goncharov, J. A. Delettrez, A. V. Maximov, J. F. Myatt, W. Seka, A. Shvydky, S. Skupsky, and C. Stoeckl, 2010, *Phys. Plasmas* **17**, 122708.
- Igumenshchev, I. V., A. L. Velikovich, V. N. Goncharov, R. Betti, E. M. Campbell, J. P. Knauer, S. P. Regan, A. J. Schmitt, R. C. Shah, and A. Shvydky, 2019, *Phys. Rev. Lett.* **123**, 065001.
- Igumenshchev, I. V., *et al.*, 2012, *Phys. Plasmas* **19**, 056314.
- Igumenshchev, I. V., *et al.*, 2013, *Phys. Rev. Lett.* **110**, 145001.
- Intrator, T., *et al.*, 2002, *Nucl. Fusion* **42**, 211.
- Intrator, T., *et al.*, 2004, *Phys. Plasmas* **11**, 2580.
- Intrator, T. P., R. E. Siemon, and P. E. Sieck, 2008, *Phys. Plasmas* **15**, 042505.
- Ishizaki, R., and K. Nishihara, 1998, *Phys. Rev. E* **58**, 3744.
- Izumi, N., *et al.*, 2018, *Rev. Sci. Instrum.* **89**, 10K111.
- Jarrott, L. C., *et al.*, 2018, *Phys. Rev. Lett.* **121**, 085001.
- Jennings, C., 2020 (private communication).
- Johal, Z. Z., J. W. Crippen, A. C. Forsman, E. H. Lundgren, K. A. Moreno, and A. Nikroo, 2009, *Fusion Sci. Technol.* **55**, 331.
- Johnson, D. J., R. J. Leeper, W. A. Stygar, R. S. Coats, T. A. Mehlhorn, J. P. Quintenz, S. A. Slutz, and M. A. Sweeney, 1985, *J. Appl. Phys.* **58**, 12.
- Jones, R., and W. Mead, 1986, *Nucl. Fusion* **26**, 127.
- Karasik, M., J. Oh, S. P. Obenschain, A. J. Schmitt, Y. Aglitskiy, and C. Stoeckl, 2021, *Phys. Plasmas* **28**, 032710.
- Kato, Y., K. Mima, N. Miyanaga, S. Arinaga, Y. Kitagawa, M. Nakatsuka, and C. Yamanaka, 1984, *Phys. Rev. Lett.* **53**, 1057.
- Kemp, A., J. Meyer-ter-Vehn, and S. Atzeni, 2001, *Phys. Rev. Lett.* **86**, 3336.
- Kephart, J. F., R. P. Godwin, and G. H. McCall, 1974, *Appl. Phys. Lett.* **25**, 108.
- Kessler, T. J., Y. Lin, J. J. Armstrong, and B. Velazquez, 1993, in *Laser Coherence Control: Technology and Applications*, SPIE Proceedings Vol. 1870, edited by H. T. Powell and T. J. Kessler (SPIE—International Society for Optical Engineering, Bellingham, WA), pp. 95–104.
- Khariton, Y., V. Mokhov, V. Chernyshev, and V. Yakubov, 1976, *Usp. Fiz. Nauk* **120**, 706.
- Kidder, R., 1974, *Nucl. Fusion* **14**, 53.
- Kidder, R., 1976, *Nucl. Fusion* **16**, 405.
- Kirkwood, R. K., B. B. Afeyan, W. L. Kruer, B. J. MacGowan, J. D. Moody, D. S. Montgomery, D. M. Pennington, T. L. Weiland, and S. C. Wilks, 1996, *Phys. Rev. Lett.* **76**, 2065.
- Kirkwood, R. K., *et al.*, 2002, *Phys. Rev. Lett.* **89**, 215003.
- Kishony, R., and D. Shvarts, 2001, *Phys. Plasmas* **8**, 4925.
- Kline, J. L., *et al.*, 2013, *Phys. Plasmas* **20**, 056314.
- Knapp, P. F., *et al.*, 2015, *Phys. Plasmas* **22**, 056312.
- Knapp, P. F., *et al.*, 2019, *Phys. Plasmas* **26**, 012704.
- Knauer, J. P., *et al.*, 2000, *Phys. Plasmas* **7**, 338.
- Knauer, J. P., *et al.*, 2005, *Phys. Plasmas* **12**, 056306.
- Kodamai, R., *et al.*, 2002, *Nature (London)* **418**, 933.
- Koonin, S., *et al.*, 1997, *Review of the Department of Energy's Inertial Confinement Fusion Program: The National Ignition Facility* (National Academies Press, Washington, DC).
- Kritcher, A. L., *et al.*, 2014, *Phys. Plasmas* **21**, 042708.
- Kritcher, A. L., *et al.*, 2016, *Phys. Plasmas* **23**, 052709.
- Kritcher, A. L., *et al.*, 2018a, *Phys. Plasmas* **25**, 056309.

- Kritcher, A. L., *et al.*, 2018b, *Phys. Rev. E* **98**, 053206.
- Kritcher, A. L., *et al.*, 2021, *Phys. Plasmas* **28**, 072706.
- Kritcher, A. L., *et al.*, 2022a, *Nat. Phys.* **18**, 251.
- Kritcher, A. L., *et al.*, 2022b, *Phys. Rev. E* **106**, 025201.
- Kruer, W., 2003, *The Physics of Laser Plasma Interactions* (Westview Press, Boulder, CO).
- Kull, H. J., 1986, *Phys. Fluids* **29**, 2067.
- Kull, H. J., 1989, *Phys. Fluids B* **1**, 170.
- Kyrala, G. A., *et al.*, 2010, *Rev. Sci. Instrum.* **81**, 10E316.
- Kyrala, G. A., *et al.*, 2011, *Phys. Plasmas* **18**, 056307.
- Landen, O. L., *et al.*, 2010, *Phys. Plasmas* **17**, 056301.
- Landen, O. L., *et al.*, 2011, *Phys. Plasmas* **18**, 051002.
- Landen, O. L., *et al.*, 2012, *Plasma Phys. Controlled Fusion* **54**, 124026.
- Landen, O. L., *et al.*, 2020, *High Energy Density Phys.* **36**, 100755.
- Landen, O. L., *et al.*, 2021, *Phys. Plasmas* **28**, 042705.
- Landshoff, R., 1949, *Phys. Rev.* **76**, 904.
- Langdon, A. B., 1980, *Phys. Rev. Lett.* **44**, 575.
- Lash, J., *et al.*, 2000, *C. R. Acad. Sci. Ser. IV* **1**, 759.
- Lawrence Livermore National Laboratory, 2022, <https://www.llnl.gov/news/national-ignition-facility-achieves-fusion-ignition>.
- Lawson, J. D., 1957, *Proc. Phys. Soc. London Sect. B* **70**, 6.
- Layzer, D., 1955, *Astrophys. J.* **122**, 1.
- Lees, A., *et al.*, 2021, *Phys. Rev. Lett.* **127**, 105001.
- Lehberg, R., and S. Obenschain, 1983, *Opt. Commun.* **46**, 27.
- Leidinger, J.-P., *et al.*, 2016, *J. Phys. Conf. Ser.* **717**, 012035.
- Le Pape, S., *et al.*, 2014, *Phys. Rev. Lett.* **112**, 225002.
- Le Pape, S., *et al.*, 2016, *Phys. Plasmas* **23**, 056311.
- Le Pape, S., *et al.*, 2018, *Phys. Rev. Lett.* **120**, 245003.
- Levedahl, W., and J. Lindl, 1997, *Nucl. Fusion* **37**, 165.
- Li, C.-K., and R. D. Petrasso, 2015, *Phys. Rev. Lett.* **114**, 199901.
- Lindemuth, I. R., 2015, *Phys. Plasmas* **22**, 122712.
- Lindemuth, I. R., and R. C. Kirkpatrick, 1983, *Nucl. Fusion* **23**, 263.
- Lindemuth, I. R., *et al.*, 1995, *Phys. Rev. Lett.* **75**, 1953.
- Lindl, J., 1995, *Phys. Plasmas* **2**, 3933.
- Lindl, J., S. Haan, and O. Landen, 2021 (private communication).
- Lindl, J. D., P. Amendt, R. L. Berger, S. G. Glendinning, S. H. Glenzer, S. W. Haan, R. L. Kauffman, O. L. Landen, and L. J. Suter, 2004, *Phys. Plasmas* **11**, 339.
- Lindl, J. D., S. W. Haan, O. L. Landen, A. R. Christopherson, and R. Betti, 2018, *Phys. Plasmas* **25**, 122704.
- Lindl, J. D., and E. I. Moses, 2011, *Phys. Plasmas* **18**, 050901.
- Lindl, J. D., *et al.*, 2014, *Phys. Plasmas* **21**, 129902.
- Lindman, E., 1977, *J. Phys. (Paris), Colloq.* **38**, C6-9.
- Litwin, C., and Y. Maron, 1989, *Phys. Fluids B* **1**, 670.
- Lyon, S. P., and J. D. Johnson, 1995, Los Alamos National Laboratory Technical Report No. LA-UR-92-3407.
- Ma, T., *et al.*, 2012, *Rev. Sci. Instrum.* **83**, 10E115.
- Ma, T., *et al.*, 2013, *Phys. Rev. Lett.* **111**, 085004.
- Ma, T., *et al.*, 2015, *Phys. Rev. Lett.* **114**, 145004.
- MacGowan, B., *et al.*, 2021, *High Energy Density Phys.* **40**, 100944.
- MacGowan, B. J., *et al.*, 1996, *Phys. Plasmas* **3**, 2029.
- MacKinnon, A. J., *et al.*, 2012, *Phys. Rev. Lett.* **108**, 215005.
- MacKinnon, A. J., *et al.*, 2014, *Phys. Plasmas* **21**, 056318.
- MacLaren, S. A., *et al.*, 2014, *Phys. Rev. Lett.* **112**, 105003.
- MacLaren, S. A., *et al.*, 2018, *Phys. Plasmas* **25**, 056311.
- MacLaren, S. A., *et al.*, 2021, *Phys. Plasmas* **28**, 122710.
- Manheimer, W. M., D. G. Colombant, and J. H. Gardner, 1982, *Phys. Fluids* **25**, 1644.
- Manley, J. M., and H. E. Rowe, 1956, *Proc. IRE* **44**, 904.
- Mannion, O., J. Knauer, V. Glebov, C. Forrest, A. Liu, Z. Mohamed, M. Romanofsky, T. Sangster, C. Stoeckl, and S. Regan, 2020, *Nucl. Instrum. Methods Phys. Res., Sect. A* **964**, 163774.
- Mannion, O. M., *et al.*, 2021, *Phys. Plasmas* **28**, 042701.
- Marinak, M. M., G. D. Kerbel, N. A. Gentile, O. Jones, D. Munro, S. Pollaine, T. R. Dittrich, and S. W. Haan, 2001, *Phys. Plasmas* **8**, 2275.
- Marocchino, A., S. Atzeni, and A. Schiavi, 2010, *Phys. Plasmas* **17**, 112703.
- Marozas, J. A., 2021 (to be published).
- Marozas, J. A., *et al.*, 2006, *Phys. Plasmas* **13**, 056311.
- Marozas, J. A., *et al.*, 2018a, *Phys. Plasmas* **25**, 056314.
- Marozas, J. A., *et al.*, 2018b, *Phys. Rev. Lett.* **120**, 085001.
- Marshak, R. E., 1958, *Phys. Fluids* **1**, 24.
- Marshall, F. J., *et al.*, 2006, *J. Phys. IV (France)* **133**, 153.
- Marshall, F. J., *et al.*, 2016, *Phys. Plasmas* **23**, 012711.
- Martin, A. J., R. J. Simms, and S. B. Wineberg, 1989, *J. Vac. Sci. Technol. A* **7**, 1157.
- Martin, J., 1996, in *On Pulsed Power*, edited by T. H. Martin, A. H. Guenther, and M. Kristiansen (Springer, New York).
- Masse, L., *et al.*, 2019, *Phys. Plasmas* **26**, 062703.
- Matte, J. P., M. Lamoureux, C. Moller, R. Y. Yin, J. Delettrez, J. Virmont, and T. W. Johnston, 1988, *Plasma Phys. Controlled Fusion* **30**, 1665.
- Matzen, M. K., 1997, *Phys. Plasmas* **4**, 1519.
- Matzen, M. K., *et al.*, 2005, *Phys. Plasmas* **12**, 055503.
- Maximov, A. V., J. Myatt, W. Seka, R. W. Short, and R. S. Craxton, 2004, *Phys. Plasmas* **11**, 2994.
- Maynard, G., and C. Deutsch, 1985, *J. Phys. (Paris)* **46**, 1113.
- McBride, R. D., *et al.*, 2012, *Phys. Rev. Lett.* **109**, 135004.
- Mendel, C. W., J. P. Quintenz, L. P. Mix, D. M. Zagar, R. L. Noack, T. Grasser, and J. A. Webb, 1987, *J. Appl. Phys.* **62**, 3522.
- Merritt, E. C., *et al.*, 2019, *Phys. Plasmas* **26**, 052702.
- Meshkov, E. E., 1969, *Fluid Dyn.* **4**, 101.
- Michel, D. T., S. X. Hu, A. K. Davis, V. Y. Glebov, V. N. Goncharov, I. V. Igumenshchev, P. B. Radha, C. Stoeckl, and D. H. Froula, 2017, *Phys. Rev. E* **95**, 051202.
- Michel, D. T., I. V. Igumenshchev, A. K. Davis, D. H. Edgell, D. H. Froula, D. W. Jacobs-Perkins, V. N. Goncharov, S. P. Regan, A. Shvydky, and E. M. Campbell, 2018, *Phys. Rev. Lett.* **120**, 125001.
- Michel, D. T., A. V. Maximov, R. W. Short, S. X. Hu, J. F. Myatt, W. Seka, A. A. Solodov, B. Yaakobi, and D. H. Froula, 2012, *Phys. Rev. Lett.* **109**, 155007.
- Michel, D. T., *et al.*, 2013, *Phys. Plasmas* **20**, 055703.
- Michel, P., W. Rozmus, E. A. Williams, L. Divol, R. L. Berger, S. H. Glenzer, and D. A. Callahan, 2013, *Phys. Plasmas* **20**, 056308.
- Michel, P., W. Rozmus, E. A. Williams, L. Divol, R. L. Berger, R. P. J. Town, S. H. Glenzer, and D. A. Callahan, 2012, *Phys. Rev. Lett.* **109**, 195004.
- Michel, P., *et al.*, 2009, *Phys. Rev. Lett.* **102**, 025004.
- Michel, P., *et al.*, 2011, *Phys. Rev. E* **83**, 046409.
- Michel, P., *et al.*, 2019, *Phys. Rev. E* **99**, 033203.
- Mikaelian, K. O., 1992, *Phys. Rev. A* **46**, 6621.
- Mikaelian, K. O., 1995, *Phys. Fluids* **7**, 888.
- Milder, A., J. Katz, R. Boni, J. Palastro, M. Sherlock, W. Rozmus, and D. Froula, 2021, *Phys. Rev. Lett.* **127**, 015001.
- Milder, A. L., *et al.*, 2020, *Phys. Rev. Lett.* **124**, 025001.
- Miller, S. M., S. A. Slutz, S. N. Bland, S. R. Klein, P. C. Campbell, J. M. Woolstrum, C. C. Kuranz, M. R. Gomez, N. M. Jordan, and R. D. McBride, 2020, *Rev. Sci. Instrum.* **91**, 063507.
- Milovich, J. L., *et al.*, 2015, *Phys. Plasmas* **22**, 122702.
- Moody, J. D., B. J. MacGowan, J. E. Rothenberg, R. L. Berger, L. Divol, S. H. Glenzer, R. K. Kirkwood, E. A. Williams, and P. E. Young, 2001, *Phys. Rev. Lett.* **86**, 2810.
- Moody, J. D., *et al.*, 2012, *Nat. Phys.* **8**, 344.
- Moses, E. I., *et al.*, 2016, *J. Phys. Conf. Ser.* **688**, 012073.

- Munro, D. H., 2016, *Nucl. Fusion* **56**, 036001.
- Murphy, T. J., 2014, *Phys. Plasmas* **21**, 072701.
- Myatt, J. F., *et al.*, 2014, *Phys. Plasmas* **21**, 055501.
- Nagel, S. R., *et al.*, 2015, *Phys. Plasmas* **22**, 022704.
- Nash, T., M. Derzon, R. Leeper, D. Jobe, M. Hurst, and J. Seamen, 1999, *Rev. Sci. Instrum.* **70**, 302.
- Nevins, W., and R. Swain, 2000, *Nucl. Fusion* **40**, 865.
- Nicola, J. D., *et al.*, 2019, *Nucl. Fusion* **59**, 032004.
- Nora, R., *et al.*, 2014, *Phys. Plasmas* **21**, 056316.
- Nuckolls, J., L. Wood, A. Thiessen, and G. Zimmerman, 1972, *Nature (London)* **239**, 139.
- Nuckolls, J. H., 2006, Lawrence Livermore National Laboratory Technical Report No. UCRL-BOOK-219136.
- Obenschain, S. P., A. J. Schmitt, J. W. Bates, M. F. Wolford, M. C. Myers, M. W. McGeoch, M. Karasik, and J. L. Weaver, 2020, *Phil. Trans. R. Soc. A* **378**, 20200031.
- Obenschain, S. P., *et al.*, 1996, *Phys. Plasmas* **3**, 2098.
- Ofer, D., U. Alon, D. Shvarts, R. L. McCrory, and C. P. Verdon, 1996, *Phys. Plasmas* **3**, 3073.
- Oh, J., A. J. Schmitt, M. Karasik, and S. P. Obenschain, 2021, *Phys. Plasmas* **28**, 032704.
- Olson, R. E., *et al.*, 2001, *Rev. Sci. Instrum.* **72**, 1214.
- Pak, A., *et al.*, 2017, *Phys. Plasmas* **24**, 056306.
- Pak, A., *et al.*, 2020, *Phys. Rev. Lett.* **124**, 145001.
- Park, H.-S., *et al.*, 2014, *Phys. Rev. Lett.* **112**, 055001.
- Pawley, C. J., *et al.*, 1997, *Phys. Plasmas* **4**, 1969.
- Peebles, J. L., S. X. Hu, W. Theobald, V. N. Goncharov, N. Whiting, P. M. Celliers, G. D. S. J. Ali, E. M. Campbell, T. R. Boehly, and S. P. Regan, 2019, *Phys. Rev. E* **99**, 063208.
- Perkins, L. J., R. Betti, K. N. LaFortune, and W. H. Williams, 2009, *Phys. Rev. Lett.* **103**, 045004.
- Peterson, J. L., L. F. Berzak Hopkins, O. S. Jones, and D. S. Clark, 2015, *Phys. Rev. E* **91**, 031101.
- Peterson, J. L., D. T. Casey, O. A. Hurricane, K. S. Raman, H. F. Robey, and V. A. Smalyuk, 2015, *Phys. Plasmas* **22**, 056309.
- Peterson, K. J., D. B. Sinars, E. P. Yu, M. C. Herrmann, M. E. Cuneo, S. A. Slutz, I. C. Smith, B. W. Atherton, M. D. Knudson, and C. Nakhleh, 2012, *Phys. Plasmas* **19**, 092701.
- Peterson, K. J., E. P. Yu, D. B. Sinars, M. E. Cuneo, S. A. Slutz, J. M. Koning, M. M. Marinak, C. Nakhleh, and M. C. Herrmann, 2013, *Phys. Plasmas* **20**, 056305.
- Peterson, K. J., *et al.*, 2014, *Phys. Rev. Lett.* **112**, 135002.
- Pickworth, L. A., *et al.*, 2020, *Phys. Plasmas* **27**, 102702.
- Piriz, A. R., J. Sanz, and L. Ibanez, 1997, *Phys. Plasmas* **4**, 1117.
- Plesset, M. S., 1954, *J. Appl. Phys.* **25**, 96.
- Pointon, T. D., 1989, *J. Appl. Phys.* **66**, 2879.
- Pollock, B., *et al.*, 2023, *Phys. Plasmas* **30**, 022711.
- Post, R. F., 1956, *Rev. Mod. Phys.* **28**, 338.
- Putvinski, S., D. Ryutov, and P. Yushmanov, 2019, *Nucl. Fusion* **59**, 076018.
- Quintenz, J., D. Bloomquist, R. Leeper, T. Mehlhorn, C. Olson, R. Olson, R. Peterson, M. Matzen, and D. Cook, 1996, *Prog. Nucl. Energy* **30**, 183.
- Radha, P. B., *et al.*, 2012, *Phys. Plasmas* **19**, 082704.
- Radha, P. B., *et al.*, 2013, *Phys. Plasmas* **20**, 056306.
- Radha, P. B., *et al.*, 2016, *J. Phys. Conf. Ser.* **717**, 012009.
- Ralph, J. E., *et al.*, 2018, *Phys. Plasmas* **25**, 082701.
- Ralph, J. E., *et al.*, 2020, *Phys. Plasmas* **27**, 102708.
- Raman, K. S., *et al.*, 2014, *Phys. Plasmas* **21**, 072710.
- Rambo, P. K., *et al.*, 2005, *Appl. Opt.* **44**, 2421.
- Randall, C. J., J. R. Albritton, and J. J. Thomson, 1981, *Phys. Fluids* **24**, 1474.
- Rayleigh, Lord, 1883, *Proc. London Math. Soc.* **s1-15**, 69.
- Regan, S. P., *et al.*, 2005, in *High Energy Density Laboratory Astrophysics*, edited by G. Kyrala (Springer, Dordrecht), pp. 227–233.
- Regan, S. P., *et al.*, 2013, *Phys. Rev. Lett.* **111**, 045001.
- Regan, S. P., *et al.*, 2016, *Phys. Rev. Lett.* **117**, 025001.
- Regan, S. P., *et al.*, 2019, *Nucl. Fusion* **59**, 032007.
- Richtmyer, R. D., 1960, *Commun. Pure Appl. Math.* **13**, 297.
- Rinderknecht, H. G., D. T. Casey, R. Hatarik, R. M. Bionta, B. J. MacGowan, P. Patel, O. L. Landen, E. P. Hartouni, and O. A. Hurricane, 2020, *Phys. Rev. Lett.* **124**, 145002.
- Robey, H., *et al.*, 2013, *Phys. Plasmas* **20**, 052707.
- Robey, H. F., L. Berzak Hopkins, J. L. Milovich, and N. B. Meezan, 2018, *Phys. Plasmas* **25**, 012711.
- Robey, H. F., *et al.*, 2012a, *Phys. Plasmas* **19**, 042706.
- Robey, H. F., *et al.*, 2012b, *Phys. Rev. Lett.* **108**, 215004.
- Robey, H. F., *et al.*, 2016, *Phys. Plasmas* **23**, 056303.
- Rochau, G. A., J. E. Bailey, R. E. Falcon, G. P. Loisel, T. Nagayama, R. C. Mancini, I. Hall, D. E. Winget, M. H. Montgomery, and D. A. Liedahl, 2014, *Phys. Plasmas* **21**, 056308.
- Rosen, M. D., 1999, *Phys. Plasmas* **6**, 1690.
- Rosenberg, M. J., *et al.*, 2018a, *Phys. Rev. Lett.* **120**, 055001.
- Rosenberg, M. J., *et al.*, 2018b, *Phys. Rev. Lett.* **120**, 055001.
- Rosenberg, M. J., *et al.*, 2020, *Phys. Plasmas* **27**, 042705.
- Ross, J. S., *et al.*, 2021, arXiv:2111.04640.
- Ruiz, C. L., *et al.*, 2004, *Phys. Rev. Lett.* **93**, 015001.
- Ruiz, D. E., P. F. Schmit, M. R. Weis, K. J. Peterson, and M. K. Matzen, 2023, *Phys. Plasmas* **30**, 032709.
- Ruiz, D. E., P. F. Schmit, D. A. Yager-Elorriaga, C. A. Jennings, and K. Beckwith, 2023, *Phys. Plasmas* **30**, 032707.
- Ruiz, D. E., *et al.*, 2023, *Phys. Plasmas* **30**, 032708.
- Rygg, J. R., *et al.*, 2014, *Phys. Rev. Lett.* **112**, 195001.
- Ryutov, D. D., and M. A. Dorf, 2014, *Phys. Plasmas* **21**, 112704.
- Sadot, O., V. A. Smalyuk, J. A. Delettrez, D. D. Meyerhofer, T. C. Sangster, R. Betti, V. N. Goncharov, and D. Shvarts, 2005, *Phys. Rev. Lett.* **95**, 265001.
- Saillard, Y., 2006, *Nucl. Fusion* **46**, 1017.
- Sanford, T. W. L., *et al.*, 1996, *Phys. Rev. Lett.* **77**, 5063.
- Sanford, T. W. L., *et al.*, 1999, *Phys. Rev. Lett.* **83**, 5511.
- Sanz, J., 1994, *Phys. Rev. Lett.* **73**, 2700.
- Sanz, J., 1996, *Phys. Rev. E* **53**, 4026.
- Sanz, J., R. Betti, V. A. Smalyuk, M. Olazabal-Loume, V. Drean, V. Tikhonchuk, X. Ribeyre, and J. Feugeas, 2009, *Phys. Plasmas* **16**, 082704.
- Sanz, J., J. Ram rez, R. Ramis, R. Betti, and R. P. J. Town, 2002, *Phys. Rev. Lett.* **89**, 195002.
- Sauppe, J. P., *et al.*, 2020, *Phys. Rev. Lett.* **124**, 185003.
- Schmit, P. F., and D. E. Ruiz, 2020, *Phys. Plasmas* **27**, 062707.
- Schmit, P. F., A. L. Velikovich, R. D. McBride, and G. K. Robertson, 2016, *Phys. Rev. Lett.* **117**, 205001.
- Schmit, P. F., *et al.*, 2014, *Phys. Rev. Lett.* **113**, 155004.
- Schoenberg, K., and R. Siemon, 1998, Los Alamos National Laboratory Technical Report No. LA-UR-98-2413.
- Scott, H., and S. Hansen, 2010, *High Energy Density Phys.* **6**, 39.
- Scott, R. H. H., *et al.*, 2013, *Phys. Rev. Lett.* **110**, 075001.
- Sefkow, A. B., S. A. Slutz, J. M. Koning, M. M. Marinak, K. J. Peterson, D. B. Sinars, and R. A. Vesey, 2014, *Phys. Plasmas* **21**, 072711.
- Seyler, C. E., M. R. Martin, and N. D. Hamlin, 2018, *Phys. Plasmas* **25**, 062711.
- Shah, R. C., *et al.*, 2017, *Phys. Rev. Lett.* **118**, 135001.
- Shiple, G. A., T. J. Awe, B. T. Hutsel, S. A. Slutz, D. C. Lamppa, J. B. Greenly, and T. M. Hutchinson, 2018, *Phys. Plasmas* **25**, 052703.

- Shibley, G. A., C. A. Jennings, and P. F. Schmit, 2019, *Phys. Plasmas* **26**, 102702.
- Shvarts, D., U. Alon, D. Ofer, R. L. McCrory, and C. P. Verdon, 1995, *Phys. Plasmas* **2**, 2465.
- Siemon, R., I. Lindemuth, and K. Schoenberg, 1999, *Comments Plasma Phys. Controlled Fusion* **18**, 363.
- Sikora, M. H., and H. R. Weller, 2016, *J. Fusion Energy* **35**, 538.
- Simon, A., R. W. Short, E. A. Williams, and T. Dewandre, 1983, *Phys. Fluids* **26**, 3107.
- Sinars, D. B., *et al.*, 2020, *Phys. Plasmas* **27**, 070501.
- Singleton, R. L., 2008, *Phys. Plasmas* **15**, 056302.
- Skupsky, S., R. W. Short, T. Kessler, R. S. Craxton, S. Letzring, and J. M. Soures, 1989, *J. Appl. Phys.* **66**, 3456.
- Skupsky, S., *et al.*, 2004, *Phys. Plasmas* **11**, 2763.
- Slutz, S. A., 1987, *J. Appl. Phys.* **61**, 2087.
- Slutz, S. A., 1995, *Laser Part. Beams* **13**, 243.
- Slutz, S. A., M. C. Herrmann, R. A. Vesey, A. B. Sefkow, D. B. Sinars, D. C. Rovang, K. J. Peterson, and M. E. Cuneo, 2010, *Phys. Plasmas* **17**, 056303.
- Slutz, S. A., C. A. Jennings, T. J. Awe, G. A. Shipley, B. T. Hutsel, and D. C. Lampa, 2017, *Phys. Plasmas* **24**, 012704.
- Slutz, S. A., W. A. Stygar, M. R. Gomez, K. J. Peterson, A. B. Sefkow, D. B. Sinars, R. A. Vesey, E. M. Campbell, and R. Betti, 2016, *Phys. Plasmas* **23**, 022702.
- Slutz, S. A., and R. A. Vesey, 2012, *Phys. Rev. Lett.* **108**, 025003.
- Slutz, S. A., R. A. Vesey, and M. C. Herrmann, 2007, *Phys. Rev. Lett.* **99**, 175001.
- Slutz, S. A., *et al.*, 2003, *Phys. Plasmas* **10**, 1875.
- Slutz, S. A., *et al.*, 2006, *Phys. Plasmas* **13**, 102701.
- Slutz, S. A., *et al.*, 2018, *Phys. Plasmas* **25**, 112706.
- Smalyuk, V. A., V. N. Goncharov, K. S. Anderson, R. Betti, R. S. Craxton, J. A. Delettrez, D. D. Meyerhofer, S. P. Regan, and T. C. Sangster, 2007, *Phys. Plasmas* **14**, 032702.
- Smalyuk, V. A., O. Sadot, J. A. Delettrez, D. D. Meyerhofer, S. P. Regan, and T. C. Sangster, 2005, *Phys. Rev. Lett.* **95**, 215001.
- Smalyuk, V. A., *et al.*, 2009, *Phys. Plasmas* **16**, 056301.
- Smalyuk, V. A., *et al.*, 2010, *Phys. Rev. Lett.* **104**, 165002.
- Smalyuk, V. A., *et al.*, 2014, *Phys. Rev. Lett.* **112**, 185003.
- Smalyuk, V. A., *et al.*, 2015, *Phys. Plasmas* **22**, 080703.
- Smalyuk, V. A., *et al.*, 2016, *Phys. Plasmas* **23**, 102703.
- Smith, I., 2006, *IEEE Trans. Plasma Sci.* **34**, 1585.
- Solodov, A. A., *et al.*, 2020, *Phys. Plasmas* **27**, 052706.
- Spaeth, M. L., *et al.*, 2016, *Fusion Sci. Technol.* **69**, 25.
- Spears, B. K., *et al.*, 2012, *Phys. Plasmas* **19**, 056316.
- Spears, B. K., *et al.*, 2014, *Phys. Plasmas* **21**, 042702.
- Spitzer, L., and R. Härm, 1953, *Phys. Rev.* **89**, 977.
- Spitzer, Jr., L., 2006, *Physics of Fully Ionized Gases* (Dover Publications, Mineola, NY).
- Springer, P. T., *et al.*, 2013, *EPJ Web Conf.* **59**, 04001.
- Springer, P. T., *et al.*, 2019, *Nucl. Fusion* **59**, 032009.
- Strozzi, D. J., D. S. Bailey, P. Michel, L. Divol, S. M. Sepke, G. D. Kerbel, C. A. Thomas, J. E. Ralph, J. D. Moody, and M. B. Schneider, 2017, *Phys. Rev. Lett.* **118**, 025002.
- Stygar, W. A., *et al.*, 2015, *Phys. Rev. ST Accel. Beams* **18**, 110401.
- Suter, L. J., *et al.*, 1996, *Phys. Plasmas* **3**, 2057.
- Sweeney, M. A., and M. J. Clauser, 1975, *Appl. Phys. Lett.* **27**, 483.
- Sweeney, M. A., and A. V. Farnsworth, Jr., 1981, *Nucl. Fusion* **21**, 41.
- Tabak, M., J. Hammer, M. E. Glinsky, W. L. Kruer, S. C. Wilks, J. Woodworth, E. M. Campbell, and M. D. Perry, 1994, *Phys. Plasmas* **1**, 1626.
- Takabe, H., K. Mima, L. Montierth, and R. L. Morse, 1985, *Phys. Fluids* **28**, 3676.
- Takabe, H., L. Montierth, and R. L. Morse, 1983, *Phys. Fluids* **26**, 2299.
- Tarter, C. B., 2018, *The American Lab* (Johns Hopkins University Press, Baltimore).
- Taylor, G., 1950, *Proc. R. Soc. A* **201**, 192.
- Tipton, R., 2015, Lawrence Livermore National Laboratory Technical Report No. LLNL-TR-676592.
- Tommasini, R., *et al.*, 2015, *Phys. Plasmas* **22**, 056315.
- Town, R. P. J., *et al.*, 2011, *Phys. Plasmas* **18**, 056302.
- Town, R. P. J., *et al.*, 2014, *Phys. Plasmas* **21**, 056313.
- Turnbull, D., A. Colaitis, A. M. Hansen, A. L. Milder, J. P. Palastro, J. Katz, C. Dorner, B. E. Kruschwitz, D. J. Strozzi, and D. H. Froula, 2020, *Nat. Phys.* **16**, 181.
- Turnbull, D., C. Goyon, G. E. Kemp, B. B. Pollock, D. Mariscal, L. Divol, J. S. Ross, S. Patankar, J. D. Moody, and P. Michel, 2017, *Phys. Rev. Lett.* **118**, 015001.
- Turnbull, D., *et al.*, 2016, *Phys. Plasmas* **23**, 052710.
- Tuszewski, M., 1988, *Nucl. Fusion* **28**, 2033.
- Van Arsdaal, A., 2007, Sandia National Laboratories Technical Report No. SAND2007-2984P.
- Velikovich, A. L., F. L. Cochran, J. Davis, and Y. K. Chong, 1998, *Phys. Plasmas* **5**, 3377.
- Vesey, R. A., M. E. Cuneo, G. R. Bennett, J. L. Porter, R. G. Adams, R. A. Aragon, P. K. Rambo, L. E. Ruggles, W. W. Simpson, and I. C. Smith, 2003, *Phys. Rev. Lett.* **90**, 035005.
- Volegov, P., *et al.*, 2014, *Rev. Sci. Instrum.* **85**, 023508.
- Waisman, E. M., and M. E. Cuneo, 2009, *Phys. Rev. ST Accel. Beams* **12**, 090401.
- Weaver, J., R. Lehmburg, S. Obenschain, D. Kehne, and M. Wolford, 2017, *Appl. Opt.* **56**, 8618.
- Weis, M., 2020 (private communication).
- Widner, M., C. Chang, A. Farnsworth, Jr., R. Leeper, T. Prevender, L. Baker, and J. Olsen, 1977, *Bull. Am. Phys. Soc.* **22**, 1139.
- Winterberg, F., 1968, *Phys. Rev.* **174**, 212.
- Wolford, M., M. Myers, T. Petrova, J. Giuliani, T. Kessler, M. McGeoch, G. Petrov, A. Schmitt, T. Mehlhorn, and S. Obenschain, 2020, *High Energy Density Phys.* **36**, 100801.
- Woo, K. M., and R. Betti, 2021, *Phys. Plasmas* **28**, 054503.
- Woo, K. M., R. Betti, O. M. Mannion, C. J. Forrest, J. P. Knauer, V. N. Goncharov, P. B. Radha, D. Patel, V. Gopalaswamy, and V. Y. Glebov, 2020, *Phys. Plasmas* **27**, 062702.
- Woo, K. M., *et al.*, 2018, *Phys. Plasmas* **25**, 052704.
- Wurzel, S. E., and S. C. Hsu, 2022, *Phys. Plasmas* **29**, 062103.
- Yaakobi, B., A. A. Solodov, J. F. Myatt, J. A. Delettrez, C. Stoekel, and D. H. Froula, 2013, *Phys. Plasmas* **20**, 092706.
- Yaakobi, B., *et al.*, 2012, *Phys. Plasmas* **19**, 012704.
- Yan, R., R. Betti, J. Sanz, H. Aluie, B. Liu, and A. Frank, 2016, *Phys. Plasmas* **23**, 022701.
- Yañez, C., J. Sanz, M. Olazabal-Loumé, and L. F. Ibañez, 2011, *Phys. Plasmas* **18**, 052701.
- Yeaman, C., G. Kemp, Z. Walters, H. Whitley, P. McKenty, E. Garcia, Y. Yang, R. Craxton, and B. Blue, 2021, *Nucl. Fusion* **61**, 046031.
- Yin, L., B. J. Albright, D. J. Stark, W. D. Nystrom, R. F. Bird, and K. J. Bowers, 2019, *Phys. Plasmas* **26**, 082708.
- Yonas, G., K. R. Prestwich, J. W. Poukey, and J. R. Freeman, 1973, *Phys. Rev. Lett.* **30**, 164.
- Young, C., *et al.*, 2020, in *Bull. Am. Phys. Soc.* **65**, GO09.00004, <https://meetings.aps.org/Meeting/DPP20/Session/GO09.4>.
- Zel'dovich, Y., and Y. Raizer, 2002, *Physics of Shock Waves and High-Temperature Hydrodynamic Phenomena* (Dover Publications, Mineola, NY).

- Zhang, H., R. Betti, R. Yan, and H. Aluie, 2020, *Phys. Plasmas* **27**, 122701.
- Zhang, H., R. Betti, R. Yan, D. Zhao, D. Shvarts, and H. Aluie, 2018, *Phys. Rev. Lett.* **121**, 185002.
- Zhou, C. D., and R. Betti, 2007, *Phys. Plasmas* **14**, 072703.
- Zhou, C. D., and R. Betti, 2009, *Phys. Plasmas* **16**, 079905.
- Zimmerman, G., and W. Kruer, 1975, *Comments Plasma Phys. Controlled Fusion* **2**, 51.
- Zylstra, A. B., and O. A. Hurricane, 2019, *Phys. Plasmas* **26**, 062701.
- Zylstra, A. B., *et al.*, 2014, *Phys. Plasmas* **21**, 112701.
- Zylstra, A. B., *et al.*, 2018, *Phys. Plasmas* **25**, 102704.
- Zylstra, A. B., *et al.*, 2020a, *Phys. Plasmas* **27**, 092709.
- Zylstra, A. B., *et al.*, 2020b, *Phys. Plasmas* **27**, 124501.
- Zylstra, A. B., *et al.*, 2021, *Phys. Rev. Lett.* **126**, 025001.
- Zylstra, A. B., *et al.*, 2022a, *Nature (London)* **601**, 542.
- Zylstra, A. B., *et al.*, 2022b, *Phys. Rev. E* **106**, 025202.